



# Balkan Journal of Electrical & Computer Engineering

An International Peer Reviewed, Referred, Indexed and Open Access Journal

[www.bajece.com](http://www.bajece.com)

Vol :11

No : 2

Year : 2023

ISSN : 2147 - 284X



It is abstracted and indexed in, Index Google Scholarship, the PSCR, Cross ref, DOAJ, Research Bible, Indian Open Access Journals (OAJ), Institutional Repositories (IR), J-Gate (Informatics India), Ulrich's, International Society of Universal Research in Sciences, DRJI, EyeSource, Cosmos Impact Factor, Cite Factor, SIS Scientific Indexing Service, IJIF, iijFactor. ULAKBİM-TR Dizin.

**General Publication Director & Editor-in-Chief**  
Musa Yılmaz, University of California Riverside, US

**Vice Editor**  
Hamidreza Nazarpouya, Oklahoma State University, US

**Scientific Committee**  
Abhishek Shukla (India)  
Abraham Lomi (Indonesia)  
Aleksandar Georgiev (Bulgaria)  
Arunas Lipnickas (Lithuania)  
Audrius Senulis (Lithuania)  
Belle R. Upadhyaya (USA)  
Brijender Kahanwal (India)  
Chandar Kumar Chanda (India)  
Daniela Dzhonova-Atanasova (Bulgaria)  
Deris Stiawan (Indonesia)  
Emel Onal (Turkey)  
Emine Ayaz (Turkey)  
Enver Hatimi (Kosovo)  
Ferhat Sahin (USA)  
Gursel Alici (Australia)  
Hakan Temeltaş (Turkey)  
Ibrahim Akduman (Turkey)  
Jan Izykowski (Poland)  
Javier Bilbao Landatxe (Spain)  
Jelena Dikun (Lithuania)  
Karol Kyslan (Slovakia)  
Kunihiko Nabeshima (Japan)  
Lambros Ekonomou (Greece)  
Lazhar Rahmani (Algerie)  
Marcel Istrate (Romania)  
Marija Eidukeviciute (Lithuania)  
Milena Lazarova (Bulgaria)  
Muhammad Hadi (Australia)  
Muhamed Turkanović (Slovenia)  
Mourad Houabes (Algerie)  
Murari Mohan Saha (Sweden)  
Nick Papanikolaou (Greece)  
Okyay Kaynak (Turkey)  
Osman Nuri Ucan (Turkey)  
Ozgun E. Mustecaplioglu (Turkey)  
Padmanaban Sanjeevikumar (India)  
Ramazan Caglar (Turkey)  
Rumen Popov (Bulgaria)  
Tarek Bouktir (Algeria)  
Sead Berberovic (Croatia)  
Seta Bogosyan (USA)  
Savvas G. Vassiliadis (Greece)  
Suwarno (Indonesia)  
Tulay Adali (USA)  
Yogeshwarsing Calleecharan (Mauritius)  
YangQuan Chen (USA)  
Youcef Soufi (Algeria)

#### **Aim & Scope**

The journal publishes original papers in the extensive field of Electrical-Electronics and Computer engineering. It accepts contributions which are fundamental for the development of electrical engineering, computer engineering and its applications, including overlaps to physics. Manuscripts on both theoretical and experimental work are welcome. Review articles and letters to the editors are also included.

Application areas include (but are not limited to): Electrical & Electronics Engineering, Computer Engineering, Software Engineering, Biomedical Engineering, Electrical Power Engineering, Control Engineering, Signal and Image Processing, Communications & Networking, Sensors, Actuators, Remote Sensing, Consumer Electronics, Fiber-Optics, Radar and Sonar Systems, Artificial Intelligence and its applications, Expert Systems, Medical Imaging, Biomedical Analysis and its applications, Computer Vision, Pattern Recognition, Robotics, Industrial Automation.



ISSN: 2147- 284X  
Vol: 11  
No : 2  
Year: April 2023

#### **CONTENTS**

Ufuk Korkmaz, Deniz Türkpençe; Stabilization and Dissipative Information Transfer of a Superconducting Kerr-Cat Qubit,.....	107-114
Hafize Nurgül Durmuş Şenyapar, Mehmet Rıdâ Tür; Turkey's Domestic Car TOGG in the Framework of New Trends in Electric Vehicles and Consumer Ethnocentrism,.....	115-128
Mehmet Nergiz; Classification of Precancerous Colorectal Lesions via ConvNeXt on Histopathological Images,.....	129-137
Osman Onur Akırmak, Aytaç Altan; Estimation of Extrusion Process Parameters in Tire Manufacturing Industry using Random Forest Classifier,.....	138-143
Murat Ozdemir, Eyüp Emre Ülkü, Kazım Yıldız; Analysis and Comparison of Business Intelligence Tools Most Preferred by Companies in Turkey, .....	144-155
Ahmet Kaymaz; Negative Capacitance and Abnormal Peak Behaviors in GaAs-Based MOS Devices Under Ionizing Radiation, .....	156-162
Ekrem Demir, Ozan Gülbudak, Mustafa Gökdağ; Performance Evaluation of Three-Phase Grid-Connected Inverter with Various Control Methods, .....	163-171
Nazmi Ekren, Bunyamin Sogut; DALI Compatible Smart LED Driver Controller with Wi-Fi Communication, .....	172-183
Sevilay Tüfenkçi, Gürkan Kavuran, Celalettin Yeroğlu; An Approach for DC Motor Speed Control with Off-Policy Reinforcement Learning Method, .....	184-189
Heybet Kılıç, Musa Yılmaz; Sensor and Actuator Fault Tolerant Control of Grid-Tied Microgrid, .....	190-197
Birand Erdogan, Adnan Tan, Murat Mustafa Savrun, Mehmet Uğraş Cuma, Mehmet Tümay; Design and Analysis of a High-Efficiency Resonant Converter for EV Battery Charger, .....	198-206

## **BALKAN JOURNAL OF ELECTRICAL & COMPUTER ENGINEERING**

(An International Peer Reviewed, Indexed and Open Access Journal)

#### **Contact**

Batman University  
Department of Electrical-Electronics Engineering  
Bati Raman Campus Batman-Turkey

**Web:** <http://dergipark.gov.tr/bajece>  
<https://www.bajece.com>  
**e-mail:** [bajece@hotmail.com](mailto:bajece@hotmail.com)

# Stabilization and Dissipative Information Transfer of a Superconducting Kerr-Cat Qubit

Ufuk Korkmaz and Deniz Turkpence


**Abstract**— Today, the competition to build a quantum computer continues, and the number of qubits in hardware is increasing rapidly. However, the quantum noise that comes with this process reduces the performance of algorithmic applications, so alternative ways in quantum computer architecture and implementation of algorithms are discussed on the one hand. One of these alternative ways is the hybridization of the circuit-based quantum computing model with the dissipative-based computing model. Here, the goal is to apply the part of the algorithm that provides the quantum advantage with the quantum circuit model, and the remaining part with the dissipative model, which is less affected by noise. This scheme is of importance to quantum machine learning algorithms that involve highly repetitive processes and are thus susceptible to noise. In this study, we examine dissipative information transfer to a qubit model called Cat-Qubit. This model is especially important for the dissipative-based version of the binary quantum classification, which is the basic processing unit of quantum machine learning algorithms. On the other hand, Cat-Qubit architecture, which has the potential to easily implement activation-like functions in artificial neural networks due to its rich physics, also offers an alternative hardware opportunity for quantum artificial neural networks. Numerical calculations exhibit successful transfer of quantum information from reservoir qubits by a repeated-interactions-based dissipative scheme.

**Index Terms**— Collision model, Information reservoir, Kerr-Cat qubit, Quantum neural network.


## I. INTRODUCTION

THE ERA in which today's computers cope with noise is called the noisy intermediate scale quantum (NISQ) era [1], and various types of research on noise suppression have shown up. One of the most prominent of these searches is that the part of the calculation that provides a quantum advantage is done together with the ordinary quantum circuit model, and classical computers do the part that does not provide a quantum advantage. Although this model is not a complete quantum computing model, there is a quantum acceleration in the

UFUK KORKMAZ, is with Department of Electrical Engineering, Istanbul Technical University, Istanbul, Turkey, (e-mail: ufukkorkmaz@itu.edu.tr).

 <https://orcid.org/0000-0001-5836-5262>

DENİZ TÜRKPENÇE, is with Department of Electrical Engineering, Istanbul Technical University, Istanbul, Turkey, (e-mail: dturkpence@itu.edu.tr).

 <https://orcid.org/0000-0002-5182-374X>

Manuscript received Nov 28, 2022; accepted Mar 28, 2023.

DOI: [10.17694/bajece.1211876](https://doi.org/10.17694/bajece.1211876)

process. That's why this model is called quantum acceleration. In our previous work, we presented a dissipation-based quantum classifier model [2], [3].

Before starting the subject, let's briefly talk about the harmonic oscillator, creator and annihilator processors, which have a very important place in the subject. The quantum Hamiltonian of a simple one-dimensional harmonic oscillator with mass  $m$  and frequency  $\omega_m$  is expressed as:

$$H = \frac{p^2}{2m} + \frac{1}{2}m\omega_m^2q^2 \quad (1)$$

Here,  $p$  and  $q$  are position and momentum operators, respectively, and as it is known,  $[q, p] = i\hbar$  provides the commutation relation. The reduced Planck's constant,  $\hbar$ , is used here.

The operators that provide the commutation relation  $[a, a^\dagger] = 1$  under the  $q = q_0(a^\dagger + a)$  and  $p = p_0(a^\dagger - a)$  transformations are called the annihilation  $a$  and the creation operator  $a^\dagger$ . Here  $q_0 = \sqrt{\hbar/2m\omega_m}$ ;  $p_0 = \sqrt{\hbar m\omega_m/2}$ . When we replace these transformations and the operators that provide the commutation relation in Eq. (1), it turns into

$$H = \hbar\omega_m \left( a^\dagger a + \frac{1}{2} \right). \quad (2)$$

The  $a^\dagger a$  operator is called the number operator because it measures the number of quanta covered by the oscillator. The eigenstates of the number operator are  $n = 0, 1, 2, \dots$  and  $|n\rangle$  number states, which correspond to the presence of exactly  $n$  quanta in the oscillator:

$$a^\dagger a |n\rangle = n |n\rangle. \quad (3)$$

It follows from this that  $|n\rangle$  is also the eigenstates of the Hamiltonian of Eq. (2), so we can express the eigenvalues as:

$$E_n = \hbar\omega_m \left( n + \frac{1}{2} \right) \quad (4)$$

It can be demonstrated that the creation and annihilation operators, respectively, increase and reduce the number of quanta in a number state:

$$a |n\rangle = \sqrt{n} |n-1\rangle, \quad a^\dagger |n\rangle = \sqrt{n+1} |n+1\rangle. \quad (5)$$

"Schrödinger-Cat" states are known as macroscopically recognizable overlapping states of a single-mode quantized electromagnetic field, and in the field of quantum optics, work on the creation of these states and the study of their properties has recently increased. According to the interpretation that is most frequently used in the literature, a macroscopic superposition state (MSS) is a superposition of ordinary coherent states with  $180^\circ$ -differences in their relative amplitudes [4], [5]. In other words,  $|\alpha\rangle$  is the coherent state of the unimodal field, where  $|\alpha\rangle$  is complex, and  $a|\alpha\rangle = \alpha|\alpha\rangle$ ,

where  $\alpha$  is the mod annihilation operator. As a result,  $|\alpha\rangle$  is likewise a coherent field state with  $\alpha|\alpha\rangle = \alpha|\alpha\rangle$ . Superpositions are used to describe Schrödinger-Cat states (or MSSs). In contrast to parametric amplification, a process that uses energy can produce a pure state using a limited amount of energy. Schrödinger-Cat states, which are quantum mechanical superpositions of two coherent out-of-phase states, are these pure states [6]. The superposition states of Schrödinger-Cat states (or MSSs) are expressed as follows:

$$|\psi\rangle = c_+|\alpha\rangle + c_-|-\alpha\rangle \tag{6}$$

Such cases are eigenstates of  $\alpha^2$  such that  $\alpha^2|\psi\rangle = \alpha^2|\psi\rangle$ . The remarkable situations called as the even and odd parity coherent cases (Eqs. (7.a) and (7.b)), respectively, were of great interest.

$$|C_\alpha^+\rangle = \mathcal{N}^+(|\alpha\rangle + |-\alpha\rangle) \tag{7.a}$$

$$|C_\alpha^-\rangle = \mathcal{N}^-(|\alpha\rangle - |-\alpha\rangle) \tag{7.b}$$

Here  $\mathcal{N}^\pm = 1/\sqrt{2(1 \pm e^{-2|\alpha|^2})}$ . There is  $\bar{n} = |\alpha|^2$  relation between  $\alpha$  and average photon number [7], [8].

Logical states in quantum information theory can be represented as two orthogonal pure states, most easily via a single two-level system. Therefore, logical 0 and 1, respectively, can be encoded in the excited state  $|e\rangle$  and ground state  $|g\rangle$ . Qubits, as opposed to just bits, are the name given to logical states since they have the ability to combine coherently [9]. It powers quantum computing thanks to its ability to treat the coherent superposition of large sets of physical systems as units. One need not limit oneself to two-dimensional Hilbert space-codifying physical systems. It is more useful for some cases to code the logical states as a superposition spanning many base cases. An unwelcome and perhaps out-of-control single interaction in the encoded information takes place when a device that permits qubit encoding is connected to a disturbed environment, and this interaction may appear as an error. The type of logical mistake is determined by binding to the logical foundation. Although the binding to the medium is fixed, we have freedom in how we encode the qubits, therefore the foundation for logical encoding can affect the sort of mistake that happens [9].

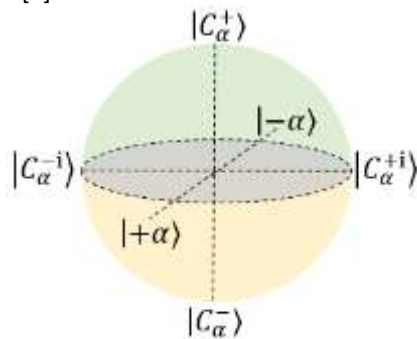


Fig.1. Bloch ball representation of a Cat qubit. Basis state in six different points are labelled.

Schematic of the Cat qubit Bloch representation is shown in Fig. 1. It is simple to confirm that the even-parity Cat state ( $|C_\alpha^+\rangle$ ) contains only even-energy eigenstates and the odd-parity Cat state ( $|C_\alpha^-\rangle$ ) contains only odd-energy eigenstates, regardless of  $\alpha$  [9]. The logical encoding can be represented as

follows for a single qubit due to the orthogonality of the two states.

$$|C_\alpha^+\rangle = |\bar{0}\rangle \tag{8.a}$$

$$|C_\alpha^-\rangle = |\bar{1}\rangle \tag{8.b}$$

A higher-dimensional system's two-dimensional subspace call a logical qubit has been chosen to enable the identification and rectification of specific errors. It frequently takes arbitrary and exact control over the whole system to manipulate encoded information. No matter if logical operations are based on huge dimensional modes like oscillators or multiple physical qubits, constituent parts in actual devices will always have residual interactions that must be taken into consideration when creating logical operations [7], [10].

The potential applications of the Cat-qubit structure are described more clearly in the following statements. These non-classical quantum harmonic oscillator states can be utilized as a system for weak force detection [11], quantum information processing [12], and quantum repeaters [13]. Recently, a study on flying Cat-qubits, which have the potential for use in quantum communication, has also been published [14]. Once the potential implications were expressed in the literature, the feasibility of cat qubits for actual physical systems became significant. Therefore, stabilization and operational proposals have appeared in the literature [15]–[18]. Moreover, advanced protocols including error correction schemes were also reported [19]–[21].

The Kerr-Cat qubit, like the superconducting transmon qubit, is considered bi-level [15], [21]. In the transient dynamics of the Kerr-non-linear resonators (KNR), the Cat states are obtained by connecting a superconducting qubit to a microwave resonator [8]. These obtained states are of great importance in understanding the mismatch in precision measurements in macroscopic systems, which are very important in quantum computing. These states, however, are challenging to produce and manage with high precision because to their vulnerability to undesired interactions and photon loss. To do this, we develop a collisional quantum master equation based on a series of recurrent encounters. Particularly when reservoir states must be clearly stated, as in our current issue, collision models have shown to be very helpful in understanding open quantum dynamics [22]–[26]. Because of the additivity and divisibility qualities of quantum dynamic maps, collision dynamics may yield a stable state given any amount of input data and without the requirement for time-dependent control [27]–[29].

Designing qubits based on atomic structure or superconducting architecture rather than using relatively less stable cat-qubits may be seen as a pitfall that worsens the process. However, as shown by the exciting potential for applications in quantum communication and detection, working on this model is worth it. On the other hand, the ability to be applied by cavity-quantum electrodynamics systems with extensive quantum control experience and network formation capability makes this model suitable as a machine learning architecture.

Currently, quantum machine learning is generally discussed based on the standard quantum circuit model. Artificial neural networks that play an important role in machine learning and the binary classifier, which is the basic processing unit, are simulated using quantum software based on the quantum circuit



[30]–[32]. On the other hand, today's quantum computers are susceptible to noise, so the number of qubits that will provide accurate results is limited. Therefore, noise-resistant algorithms or hardware-efficient solutions are being emphasized [33], [34].

One of these solutions is the dissipation-based quantum computing model that operates with an open quantum system model [35]. It is known that this model type is more advantageous against noise effects. For example, we recently published a study on how a binary classifier quantum perceptron would work according to this model [36]. According to this study, a probe qubit is an open quantum system connected to independent information reservoirs, and the classification result is encoded as a stationary state magnetization. In our current study, where the probe qubit can be described as a cat-qubit, we are numerically testing the stabilization of the cat-qubit and the transfer of information from the information reservoir to the cat-qubit.

In this study, we show that a quantum information classifier can be successfully created with the dissipation-based protocol. A different version of the quantum acceleration model is to use a dissipation-based protocol instead of using a classical computer in the model. Thus, the propose dissipation-based model will both cause less noise and eliminate the difficulty of a classical computer dealing with quantum data.

We numerically examine a dissipation-based information transfer process that would lead to a Cat Qubit-based binary classifier model. Cat-Qubit is an alternative physical qubit model that creates logical bases with appropriate superpositions of so-called coherent states of quantum harmonic oscillator [4], [5], [7], [8]. This physical model, in which the control parameters are richer, has the potential to be evaluated as a quantum neuron, thanks to Kerr non-linearity-based activation possibility. The dissipation model in our study is described by the collision model, which is called the collision model and is based on repeated interactions.

## II. MODEL AND SYSTEM DYNAMICS

### A. Kerr-Cat Qubit Hamiltonian

Some protected qubits, such as these bi-level qubits (a type of bosonic qubit) mentioned in the previous section, are stabilized by a Hamiltonian [21]. Therefore, the following Hamiltonian is used to stabilize the Kerr-Cat qubit.

$$H = \hbar(K\hat{\alpha}^{\dagger 2}\hat{\alpha}^2 - \epsilon_2(\hat{\alpha}^{\dagger 2} + \hat{\alpha}^2) + \Delta_{ar}\hat{\alpha}^{\dagger}\hat{\alpha}) \quad (9)$$

Here,  $K$  is the Kerr nonlinearity,  $\epsilon_2$  is the squeezing-drive strength,  $\Delta_{ar} = \omega_0 - \omega_r$  is the frequency with respect to the rotary coordinate system where  $\omega_0 = 37.7 \text{ GHz}$  is the cavity frequency and  $\omega_r$  is the resonator frequency, respectively.  $\hbar = 1$  throughout the entire study. This interpretation of the Hamiltonian demonstrates that the two states  $|\pm\alpha\rangle$  and  $\alpha = (\epsilon_2/K)^{1/2}$ , the eigenstates of the annihilation operator  $\hat{\alpha}$ , are also degenerate eigenstates of Eq. (9) with energy  $|\epsilon_2|^2/K$ . Equivalently, the even-odd parity states of  $|C_{\alpha}^{\pm}\rangle$  are the eigenstates of  $H$  [8], [15].

### B. Open Quantum System

A subset of supervised learning problems called binary classification tries to create a classification rule that depicts a mapping from  $\mathcal{X} \rightarrow \{0,1\}$  abstract feature spaces to a collection

of binary labels. Here,  $\mathcal{X}$  denotes the  $\mathcal{D} = (\mathcal{X}, \mathcal{Y})$  training set's input data field. The binary labels' associated output data field is  $\mathcal{Y}$ . Another way to state the training set is as follows:

$$(\mathcal{X}, \mathcal{Y}) = \{(\mathbf{x}_i, \mathbf{y}_i)\}^M \quad (10)$$

These pairs in relation to the  $M$  elements,  $\mathbf{x}_i$  is a vector representing the unclassified input data, while  $\mathbf{y}_i$  represents the output vector corresponding to  $\mathbf{x}_i$ . Because the input feature data is a vector in  $N$ -dimensional real space, the  $\mathbb{R}^N \rightarrow \{0,1\}$  map is defined by the binary classification. The perceptron, the primary processing unit of artificial neural networks, is the most basic binary classifier and it is connected with mathematical models [37]. The binary classification model, inspired by a biological neuron,  $\mathbf{x} = [\mathbf{x}_1, \dots, \mathbf{x}_N]^T$  is defined as  $z = f(\mathbf{x}^T \mathbf{w})$  in terms of these vectors representing the input information with the corresponding vector and the weight vector  $\mathbf{w} = [\mathbf{w}_1, \dots, \mathbf{w}_N]^T$ . Here  $f$  is the linear or non-linear activation function, which has an important role in determining the classification rule. The classification is performed by the model as  $z \equiv 1$  if  $z = f(\mathbf{x}^T \mathbf{w})$ , not  $z \equiv 0$ .

A weighted combination of input data samples can be used with the conventional binary classification model.

$$\mathbf{x}^T \mathbf{w} = \sum_i \mathbf{w}_i \mathbf{x}_i \quad (11)$$

We may construct our model using linear combinations of quantum dynamic maps, each of which represents the attachment of the system to a separate reservoir, as motivated by this classical point of view.

$$\Lambda_t[\rho_0] = \sum_i P_i \Phi_t^{(i)}[\rho_0] \quad (12)$$

In this case,  $\rho_0$  stands for the probe qubit from which the output data is read, and  $P_i$  is a positive value that describes the likelihood of the system encountering each reservoir. We imply that every map in Eq. (13) results in a steady state.

$$\Phi_t^{(i)}[\rho_0] = \text{Tr}_{\mathcal{R}_i}[\Lambda_t(\rho_0 \otimes \rho_{\mathcal{R}_i})\Lambda_t^{\dagger}] \quad (13)$$

$\text{Tr}_i$  is partial trace on unit  $i$ th.  $\rho_{\mathcal{R}_i}$  is the quantum state of the  $i$ th reservoir. The completely positive trace-preserving quantum dynamical map (CPTP) [24] represented as  $\Lambda_t[\rho] = -i[H_t, \rho] + \kappa_1 \mathcal{L}_0[\rho] + \kappa_2 \mathcal{L}_0[\hat{\alpha}^2]$  serves as a defining characteristic of the system. Also, a dynamic map that provides  $\Phi_{t+s} = \Phi_t(\Phi_s[\rho])$  complete positivity (CP) for  $t$  and  $s \geq 0$  is called a CP divisible map.  $H_t = K\hat{\alpha}^{\dagger 2}\hat{\alpha}^2 - \epsilon_2(\hat{\alpha}^{\dagger 2} + \hat{\alpha}^2) + \Delta_{ar}\hat{\alpha}^{\dagger}\hat{\alpha}$  is the Hamiltonian that represents a consistent drive on the Kerr-Cat qubit.  $\mathcal{L}[\rho] \equiv 2\rho\sigma\sigma^{\dagger} - \sigma^{\dagger}\rho\sigma - \rho\sigma\sigma^{\dagger}$  is the standard Lindblad super operator. The two super operator constants  $\kappa_1$  and  $\kappa_2$  describe the losses of one photon and two photons.  $\kappa_1 = 1/T_1$  [8]. Eq. (13) is the explicit quantum equivalent of Eq. (12) and is only valid if it satisfies the addition and divisibility conditions of quantum dynamic maps [27], [29], [38]. According to reports, when the weak coupling condition is satisfied, both the complete positivity and the divisibility requirement for quantum dynamic maps hold true [29]. We must focus on two key points in order to comprehend our model more fully. The suggested classifier's dynamics are first presented, which is a collision model in which a probe qubit connects sequentially with identical and non-interacting reservoir units with a limited time  $\tau$ . Second, we refer to these reservoirs as information reservoirs as they are made up of

identical qubits that have been idealized using particular collision model-derived characteristics. These formulations read  $\rho(0) = \rho_S(0) \otimes \rho_{\mathcal{R}_i}$  as the initial quantum state of the entire system. Each information reservoir is made up of a set of identical, non-interacting qubits in pure quantum states, as was already mentioned.

$$\rho_{\mathcal{R}_i} = \bigotimes_{k=1}^n \rho_k(\theta_i, \phi_i) \quad (14)$$

Here,  $\rho_k(\theta_i, \phi_i)$  is the  $k$ th subunit of the  $i$ th information reservoir. The Hamiltonian of the system and the  $i$ th information reservoir is expressed as:

$$H_0 = \hbar \left( K a_0^{\dagger 2} a_0^2 - \epsilon_2 (a_0^{\dagger 2} + a_0^2) + \Delta_{ar} a_0^{\dagger} a_0 + \Delta_{ir} \sum_{i=1}^n a_{k_i}^{\dagger} a_{k_i} \right) \quad (15)$$

and the interaction term is expressed as:

$$H_{int} = \hbar \epsilon_x \sum_{i=1}^n (|C_{\alpha}^+\rangle_0 \langle C_{\alpha}^-| \otimes |C_{\alpha}^- \rangle_1 \langle C_{\alpha}^+| + H.c.) \quad (16)$$

where  $\hbar$  is the reduced Planck constant,  $\Delta_{ar} = \Delta_{ir}$  and  $\epsilon_x$  is the Cat-Rabi driver constant. Rearranging Eq. (13) as cascading partial trace operations to describe dynamic maps via the collision model, we can write it as follows:

$$\Phi_{n\tau}^{(i)}[\rho_0] = Tr_n \left[ \Lambda_{0i_n} \cdots Tr_1 \left[ \Lambda_{0i_1} (\rho_0 \otimes \rho_{\mathcal{R}_{i_1}}) \Lambda_{0i_1}^{\dagger} \right] \otimes \cdots \otimes \rho_{\mathcal{R}_{i_n}} \Lambda_{0i_n}^{\dagger} \right] \quad (17)$$

Here,  $\Lambda_{0i}[\rho] = -i[H, \rho] + \kappa_1 \mathcal{L}_0[a] + \kappa_2 \mathcal{L}_0[a^2]$  is a dynamic map that provides the divisibility of CP where  $H = H_0 + H_{int}$  and  $\rho = \rho_0 \otimes \rho_{\mathcal{R}_i}$ . Here,  $n\tau$  is the amount of time required for  $n$  collisions, and  $\Lambda_{0i}$  is the non-unitary super operator acting on both the system and reservoir qubits.  $n$  is often a finite number that is big enough to stabilize the probe qubit. In the Markov technique, the system state equals that of one of the reservoir units after a sufficient number of interactions. In other words, it is by this discrete dynamic development that the system temperatures get to the thermal reservoir temperature. Quantum homogenization is the name of this procedure [22]. As a result, we simulate our system numerically, which is explained by the following master equation. This process was performed with the Qutip toolbox [39].

$$\dot{\rho}_0 = -i[H, \rho] + \kappa_1 \mathcal{L}_0[a] + \kappa_2 \mathcal{L}_0[a^2] \quad (18)$$

### III. NUMERICAL SIMULATION RESULTS

For numerical computations we use the parameters of superconducting circuits, which has become one of the most successful platforms for quantum information processing applications [40]–[42]. Transmon qubits can be coupled via a resonator bus, where interactions are mediated by the exchange of virtual photons [43]. In this architecture, the coupling forces between the qubits can be controlled through the coupling distributed to the transmission line resonator. A superconducting circuit with weakly coupled transmon qubits typically has resonator frequency  $w_r \sim 1 - 10$  GHz and qubit-resonator coupling  $g \sim 1 - 500$  MHz and effective qubit-qubit coupling  $J \sim 1 - 100$  MHz and qubit energy relaxation time  $T_1 \sim 20 - 60$   $\mu$ s [42], [43].

Fig. 2 shows the variation of the Kerr-Cat qubit populations and magnetization depending on the system parameters. Here our qubit is unstable.

It is seen in Fig. 3 that the oscillation in population states decreases depending on the system parameters. In Figs. 2 and 3,  $T_1 = 15.5 \times 10^{-6}$  s and  $\tau = 3 \times 10^{-9}$  s are scaled with  $w_r = 2\pi \times 10^9$  Hz. Accordingly, it is scaled as  $T_1 w_r = 558 \times 10^3$ .  $\tau_{sc} \cong 113$  corresponds to  $\frac{T_1 w_r}{\tau_{sc}} \cong 5000$  collisions. Thus, 100000 collisions equal  $20T_1$  times, approximately  $30 \times 10^{-5}$  s. This indicates that the qubit remains stable for long enough.

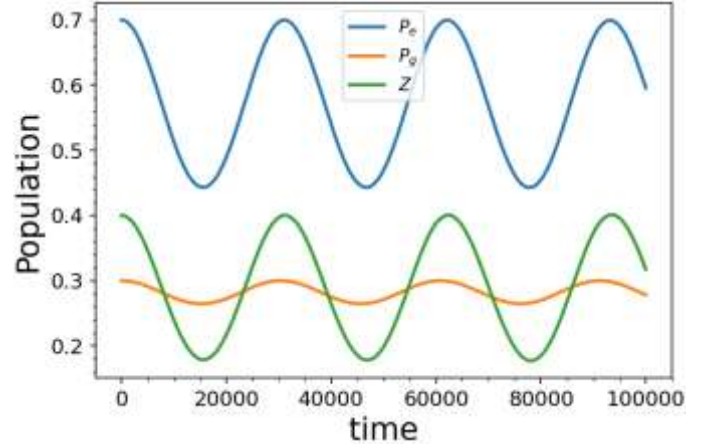


Fig.2. Variation of Kerr-Cat qubit populations and magnetization depending on system parameters. Here,  $P_e$  is the excited state population,  $P_g$  is the ground state population, and  $Z = P_e - P_g$  magnetization.  $K = 1.12 \times 10^{-6}$ ,  $\epsilon_2 = 2.25 \times 10^{-6}$ ,  $\kappa_1 = 1.71 \times 10^{-6}$ ,  $\kappa_2 = 3.34 \times 10^{-5}$  and  $\Delta_{ar} = 1.00 \times 10^{-4}$  are dimensionless and scale with  $w_r$ .

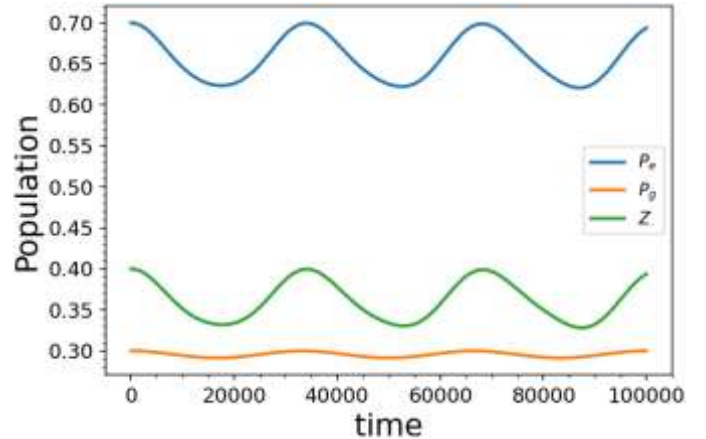


Fig.3. Variation of Kerr-Cat qubit populations and magnetization depending on system parameters. Here,  $P_e$  is the excited state population,  $P_g$  is the ground state population, and  $Z = P_e - P_g$  magnetization.  $K = 1.12 \times 10^{-6}$ ,  $\epsilon_2 = 2.25 \times 10^{-5}$ ,  $\kappa_1 = 1.71 \times 10^{-6}$ ,  $\kappa_2 = 3.34 \times 10^{-5}$  and  $\Delta_{ar} = 1.00 \times 10^{-4}$  are dimensionless and scale with  $w_r$ .

In Fig. 4, it is seen that our qubit has become stable depending on the system parameters. After stabilizing our qubit, we will use the time dependent Hamiltonian to examine the activation states.

$$H(t) = K \hat{a}^{\dagger 2} \hat{a}^2 - \epsilon_2(t) (\hat{a}^{\dagger 2} + \hat{a}^2) + \Delta_{ar} \hat{a}^{\dagger} \hat{a} \quad (19)$$

Here, there are  $t \gg \tau$  and  $\tau K = 5$  relations for  $\epsilon_2(t) = \epsilon_2^0 [1 - \exp(-t^4/\tau^4)]$ ,  $\epsilon_2(t=0) = 0$  and  $\epsilon_2(t) \sim \epsilon_2^0 = 4K$ .

TABLE I  
FIGS. 1, 2, and 3 RESULTS

	$w_r$ , [GHz]	$K/w_r$	$\epsilon_2/w_r$	$\kappa_1/w_r$	$\kappa_2/w_r$	$\Delta_{ar}/w_r$
Fig. 2	$2\pi$	$1.12 \times 10^{-6}$	$2.25 \times 10^{-6}$	$1.71 \times 10^{-6}$	$3.34 \times 10^{-5}$	$1.00 \times 10^{-4}$
Fig. 3	$2\pi$	$1.12 \times 10^{-6}$	$2.25 \times 10^{-5}$	$1.71 \times 10^{-6}$	$3.34 \times 10^{-5}$	$1.00 \times 10^{-4}$
Fig. 4	$2\pi$	$1.12 \times 10^{-6}$	$2.25 \times 10^{-6}$	$1.71 \times 10^{-6}$	$3.34 \times 10^{-6}$	$5.80 \times 10^{-6}$

In Fig. 5, we consider a single information reservoir  $\rho_1 = |\psi(\theta_1, \phi_1)\rangle\langle\psi(\theta_1, \phi_1)|$  in contact with a non-decay probe Kerr-Cat qubit. Bloch vector was expressed using the  $|\psi(\theta_1, \phi_1)\rangle = \cos\frac{\theta_1}{2}|C_\alpha^+\rangle + \sin\frac{\theta_1}{2}e^{-i\phi_1}|C_\alpha^-\rangle$  Kerr-Cat qubit. While following the amplitude parameter for the classification result in our proposal, we monitor the equilibrium dynamics over a steady state. In this simplest case, stationary dynamics yields no classification results, but provides an instructive example of quantum homogenization. As show in Fig. 5 (a) and (b), the probe qubit magnetization converges to the magnetization of the reservoir units with the amplitude parameters  $\theta_1 = 0$  and  $\theta_1 = \pi$ , respectively. The probe prepares as the Kerr-Cat qubit  $\rho_0 = |+\rangle\langle+|$ , which is originally intended to provide a null magnetization. Taken in  $|+\rangle = |\alpha\rangle = 2^{-1/2}[(|C_\alpha^+\rangle + |C_\alpha^-\rangle) + (|C_\alpha^+\rangle - |C_\alpha^-\rangle)]$  form. Without losing generalization, we get  $\phi_i = 0$  in our calculations relative to  $\theta$ .

The smooth and monotonic convergence of the equilibrium curves exhibits a Markov evolution demonstrating the success of CP divisibility collision dynamics. Here homogenization means an equilibration process in which the quantum state of the

system becomes the same as that of the reservoir density matrix with its diagonal inputs [23], [24].

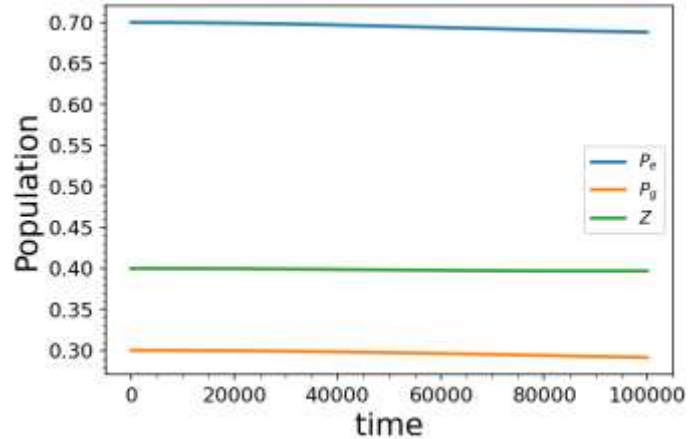


Fig.4. Variation of Kerr-Cat qubit populations and magnetization depending on system parameters. Here,  $P_e$  is the excited state population,  $P_g$  is the ground state population, and  $Z = P_e - P_g$  magnetization.  $K = 1.12 \times 10^{-6}$ ,  $\epsilon_2 = 2.25 \times 10^{-6}$ ,  $\kappa_1 = 1.71 \times 10^{-6}$ ,  $\kappa_2 = 3.34 \times 10^{-6}$  and  $\Delta_{ar} = 5.80 \times 10^{-6}$  are dimensionless and scale with  $w_r$ .

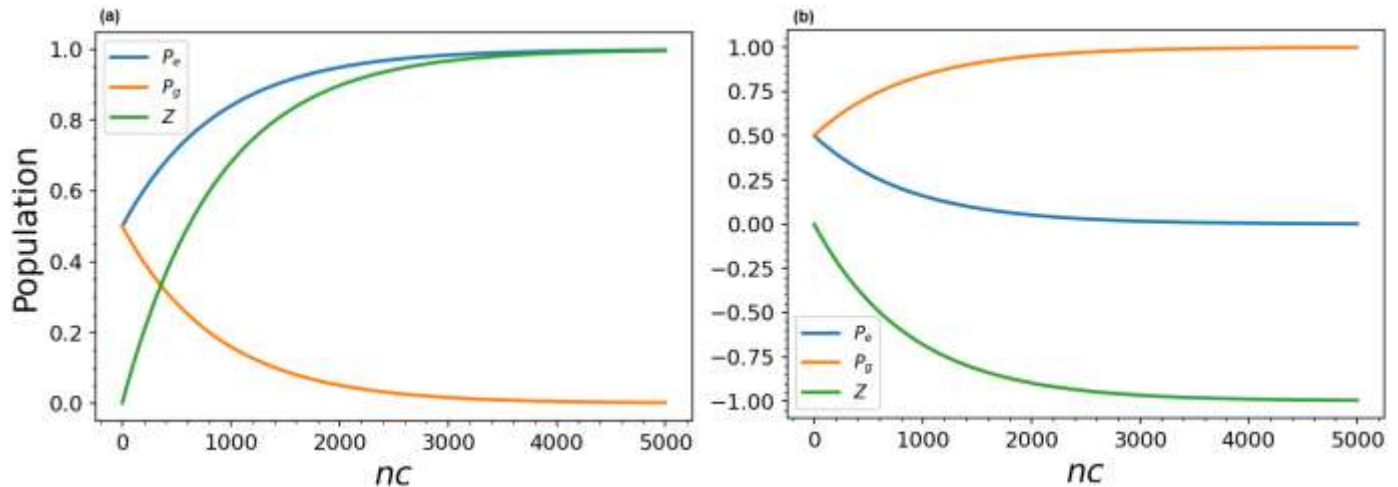


Fig. 5. Variation of Kerr-Cat qubit populations and magnetization depending on system parameters. Here,  $P_e$  is the excited state population,  $P_g$  is the ground state population, and  $Z = P_e - P_g$  magnetization.  $K = 1.12 \times 10^{-6}$ ,  $\epsilon_2 = 2.70 \times 10^{-4}$ ,  $\kappa_1 = 1.71 \times 10^{-6}$ ,  $\kappa_2 = 3.34 \times 10^{-4}$ ,  $\Delta_{as} = 5.80 \times 10^{-6}$  and  $\tau = 113.01$  are dimensionless and scale with  $w_r$ .

As the amplitude parameter of the probe qubit is chosen as the identifying merit of the classification, we introduce the classification rule using the probe qubit's  $Z = Tr[\rho\sigma_z]$  steady state magnetization where  $\sigma_z$  is the Pauli-z operator. Hence, the binary decision of the classifier in steady state with binary labels 0 and 1 reads

$$Decision \begin{cases} 0, & Z \geq 0 \\ 1, & otherwise \end{cases} \quad (20)$$

The above-mentioned work demonstrates the possibility of a dissipative information transfer process for the cat-qubit system using realistic parameters. In this application, a single



information reservoir is repeatedly interacted with a probe cat-qubit system, resulting in open quantum system evolution. The probe system responds with a stable magnetization value in its stationary state. Since the quantum reservoir input represents quantum information, this demonstration is, in fact, the simplest binary classification example for a single input quantum information, according to the classification rule expressed in the text. Eq. (12), expressed in terms of dynamical maps, shows that this process can be easily generalized to multiple quantum information input situations. The convex combination additivity of the density matrix formulation representing open quantum systems suggests that the example in this study, which responds in binary classification form with a single input, has the potential to be a general open quantum classifier for cat-qubits.

#### IV. CONCLUSION

In this study, we investigate whether a quantum neuron model with dissipative information transfer is possible with numerical methods. For this, exact diagonalization methods are used with realistic parameters in the Qutip toolbox. First, as can be seen in Figs. 2, 3, and 4 the stabilization of the Cat-Kerr qubit, which takes an important part, has been provided numerically. Finally, we show in Fig. 5 that reservoir information is successfully transferred to the stabilized Cat-Qubit using the collision method. This model is particularly significant for the energy-dissipative variant of binary quantum classification, which is the fundamental processing unit of quantum machine learning algorithms. Cat-Qubit architecture, on the other hand, provides an alternate hardware possibility for quantum artificial neural networks due to its rich physics and the potential to implement activation-like functions in artificial neural networks.

#### V. APPENDIX

TABLE II  
EXPLANATIONS OF MATHEMATICAL TERMS

Presentation	Explanation
$ \cdot\rangle$	Fock state
$ \alpha\rangle$	Coherent state (Cat state in X basis)
$\mathcal{N}^\pm$	Normalization factor for cat qubit bases
$ C_\alpha^\pm\rangle$	Cat state in standard basis
$ C_\alpha^{i\pm}\rangle$	Cat state in Y basis
$\Phi_t^{(i)}[q_0]$	Dynamical maps
$\Lambda_t[q_0]$	A weighted combination of quantum dynamical maps
$\mathcal{L}[\cdot]$	Lindblad super operator

#### ACKNOWLEDGMENT

The authors thank the funding from TÜBİTAK-Grant No. 120F353. We would also like to thank the Cognitive Systems Laboratory in the Department of Electrical Engineering for providing a suitable environment for the studies.

#### REFERENCES

[1] J. Preskill, ‘Quantum Computing in the NISQ era and beyond’, *Quantum*, vol. 2, p. 79, Aug. 2018, doi: 10.22331/q-2018-08-06-79.

[2] D. Türkpençe, T. Ç. Akıncı, and S. Şeker, ‘A steady state quantum classifier’, *Physics Letters A*, vol. 383, no. 13, pp. 1410–1418, Apr. 2019, doi: 10.1016/j.physleta.2019.01.063.

[3] U. Korkmaz and D. Türkpençe, ‘Transfer of quantum information via a dissipative protocol for data classification’, *Physics Letters A*, vol. 426, p. 127887, Feb. 2022, doi: 10.1016/j.physleta.2021.127887.

[4] C. C. Gerry and E. E. Hach, ‘Generation of even and odd coherent states in a competitive two-photon process’, *Physics Letters A*, vol. 174, no. 3, pp. 185–189, Mar. 1993, doi: 10.1016/0375-9601(93)90756-P.

[5] E. E. Hach III and C. C. Gerry, ‘Generation of mixtures of Schrödinger-cat states from a competitive two-photon process’, *Phys. Rev. A*, vol. 49, no. 1, pp. 490–498, Jan. 1994, doi: 10.1103/PhysRevA.49.490.

[6] L. Gilles, B. M. Garraway, and P. L. Knight, ‘Generation of nonclassical light by dissipative two-photon processes’, *Phys. Rev. A*, vol. 49, no. 4, pp. 2785–2799, Apr. 1994, doi: 10.1103/PhysRevA.49.2785.

[7] M. Mirrahimi *et al.*, ‘Dynamically protected cat-qubits: a new paradigm for universal quantum computation’, *New J. Phys.*, vol. 16, no. 4, p. 045014, Apr. 2014, doi: 10.1088/1367-2630/16/4/045014.

[8] A. Grimm *et al.*, ‘Stabilization and operation of a Kerr-cat qubit’, *Nature*, vol. 584, no. 7820, pp. 205–209, Aug. 2020, doi: 10.1038/s41586-020-2587-z.

[9] P. T. Cochrane, G. J. Milburn, and W. J. Munro, ‘Macroscopically distinct quantum-superposition states as a bosonic code for amplitude damping’, *Phys. Rev. A*, vol. 59, no. 4, pp. 2631–2634, Apr. 1999, doi: 10.1103/PhysRevA.59.2631.

[10] R. W. Heeres *et al.*, ‘Implementing a universal gate set on a logical qubit encoded in an oscillator’, *Nat Commun.*, vol. 8, no. 1, p. 94, Dec. 2017, doi: 10.1038/s41467-017-00045-1.

[11] W. J. Munro, K. Nemoto, G. J. Milburn, and S. L. Braunstein, ‘Weak-force detection with superposed coherent states’, *Phys. Rev. A*, vol. 66, no. 2, p. 023819, Aug. 2002, doi: 10.1103/PhysRevA.66.023819.

[12] H. Jeong, M. S. Kim, and J. Lee, ‘Quantum-information processing for a coherent superposition state via a mixed-entangled coherent channel’, *Phys. Rev. A*, vol. 64, no. 5, p. 052308, Oct. 2001, doi: 10.1103/PhysRevA.64.052308.

[13] P. van Loock, N. Lütkenhaus, W. J. Munro, and K. Nemoto, ‘Quantum repeaters using coherent-state communication’, *Phys. Rev. A*, vol. 78, no. 6, p. 062319, Dec. 2008, doi: 10.1103/PhysRevA.78.062319.

[14] Z. Wang *et al.*, ‘A flying Schrödinger’s cat in multipartite entangled states’, *Science Advances*, vol. 8, no. 10, p. eabn1778, Mar. 2022, doi: 10.1126/sciadv.abn1778.

[15] S. Puri, S. Boutin, and A. Blais, ‘Engineering the quantum states of light in a Kerr-nonlinear resonator by two-photon driving’, *npj Quantum Inf.*, vol. 3, no. 1, p. 18, Dec. 2017, doi: 10.1038/s41534-017-0019-1.

[16] S. Touzard *et al.*, ‘Coherent Oscillations inside a Quantum Manifold Stabilized by Dissipation’, *Phys. Rev.*



- X, vol. 8, no. 2, p. 021005, Apr. 2018, doi: 10.1103/PhysRevX.8.021005.
- [17] S. Puri *et al.*, ‘Stabilized Cat in a Driven Nonlinear Cavity: A Fault-Tolerant Error Syndrome Detector’, *Phys. Rev. X*, vol. 9, no. 4, p. 041009, Oct. 2019, doi: 10.1103/PhysRevX.9.041009.
- [18] S. Puri *et al.*, ‘Bias-preserving gates with stabilized cat qubits’, *Sci. Adv.*, vol. 6, no. 34, p. eaay5901, Aug. 2020, doi: 10.1126/sciadv.aay5901.
- [19] W. Cai, Y. Ma, W. Wang, C.-L. Zou, and L. Sun, ‘Bosonic quantum error correction codes in superconducting quantum circuits’, *Fundamental Research*, vol. 1, no. 1, pp. 50–67, Jan. 2021, doi: 10.1016/j.fmre.2020.12.006.
- [20] Q. Xu *et al.*, ‘Engineering Kerr-cat qubits for hardware efficient quantum error correction’, in *Quantum Computing, Communication, and Simulation II*, Mar. 2022, vol. 12015, pp. 50–63. doi: 10.1117/12.2614832.
- [21] H. Putterman *et al.*, ‘Stabilizing a Bosonic Qubit Using Colored Dissipation’, *Phys. Rev. Lett.*, vol. 128, no. 11, p. 110502, Mar. 2022, doi: 10.1103/PhysRevLett.128.110502.
- [22] V. Scarani, M. Ziman, P. Štelmachovič, N. Gisin, and V. Bužek, ‘Thermalizing Quantum Machines: Dissipation and Entanglement’, *Phys. Rev. Lett.*, vol. 88, no. 9, p. 097905, Feb. 2002, doi: 10.1103/PhysRevLett.88.097905.
- [23] M. Ziman, P. Štelmachovič, V. Bužek, M. Hillery, V. Scarani, and N. Gisin, ‘Diluting quantum information: An analysis of information transfer in system-reservoir interactions’, *Phys. Rev. A*, vol. 65, no. 4, p. 042105, Mar. 2002, doi: 10.1103/PhysRevA.65.042105.
- [24] D. Nagaj, P. Štelmachovič, V. Bužek, and M. Kim, ‘Quantum homogenization for continuous variables: Realization with linear optical elements’, *Phys. Rev. A*, vol. 66, no. 6, p. 062307, Dec. 2002, doi: 10.1103/PhysRevA.66.062307.
- [25] B. Vacchini, ‘General structure of quantum collisional models’, *Int. J. Quantum Inform.*, vol. 12, no. 02, p. 1461011, Mar. 2014, doi: 10.1142/S0219749914610115.
- [26] S. Campbell and B. Vacchini, ‘Collision models in open system dynamics: A versatile tool for deeper insights?’, *EPL*, vol. 133, no. 6, p. 60001, Mar. 2021, doi: 10.1209/0295-5075/133/60001.
- [27] J. Kolodyński, J. B. Brask, M. Perarnau-Llobet, and B. Bylicka, ‘Adding dynamical generators in quantum master equations’, *Phys. Rev. A*, vol. 97, no. 6, p. 062124, Jun. 2018, doi: 10.1103/PhysRevA.97.062124.
- [28] M. M. Wolf and J. I. Cirac, ‘Dividing Quantum Channels’, *Communications in Mathematical Physics*, vol. 279, no. 1, pp. 147–168, Apr. 2008, doi: 10.1007/s00220-008-0411-y.
- [29] S. N. Filippov, J. Piilo, S. Maniscalco, and M. Ziman, ‘Divisibility of quantum dynamical maps and collision models’, *Phys. Rev. A*, vol. 96, no. 3, p. 032111, Sep. 2017, doi: 10.1103/PhysRevA.96.032111.
- [30] T. Yi, J. Wang, and F. Xu, ‘Binary classification of single qubits using quantum machine learning method’, *J. Phys.: Conf. Ser.*, vol. 2006, no. 1, p. 012020, Aug. 2021, doi: 10.1088/1742-6596/2006/1/012020.
- [31] D. Maheshwari, D. Sierra-Sosa, and B. Garcia-Zapirain, ‘Variational Quantum Classifier for Binary Classification: Real vs Synthetic Dataset’, *IEEE Access*, vol. 10, pp. 3705–3715, 2022, doi: 10.1109/ACCESS.2021.3139323.
- [32] M. Schuld, A. Bocharov, K. M. Svore, and N. Wiebe, ‘Circuit-centric quantum classifiers’, *Phys. Rev. A*, vol. 101, no. 3, p. 032308, Mar. 2020, doi: 10.1103/PhysRevA.101.032308.
- [33] R. Dilip, Y.-J. Liu, A. Smith, and F. Pollmann, ‘Data compression for quantum machine learning’, *Phys. Rev. Res.*, vol. 4, no. 4, p. 043007, Oct. 2022, doi: 10.1103/PhysRevResearch.4.043007.
- [34] N. Schetakakis, D. Aghamalyan, P. Griffin, and M. Boguslavsky, ‘Review of some existing QML frameworks and novel hybrid classical–quantum neural networks realising binary classification for the noisy datasets’, *Sci Rep*, vol. 12, no. 1, p. 11927, Jul. 2022, doi: 10.1038/s41598-022-14876-6.
- [35] F. Verstraete, M. M. Wolf, and J. Ignacio Cirac, ‘Quantum computation and quantum-state engineering driven by dissipation’, *Nature Phys.*, vol. 5, no. 9, pp. 633–636, Sep. 2009, doi: 10.1038/nphys1342.
- [36] U. Korkmaz and D. Türkpençe, ‘Quantum collisional classifier driven by information reservoirs’, *Phys. Rev. A*, vol. 107, no. 1, p. 012432, Jan. 2023, doi: 10.1103/PhysRevA.107.012432.
- [37] F. Rosenblatt, ‘The perceptron: A probabilistic model for information storage and organization in the brain.’, *Psychological Review*, vol. 65, no. 6, pp. 386–408, 1958, doi: 10.1037/h0042519.
- [38] M. M. Wolf and J. I. Cirac, ‘Dividing Quantum Channels’, *Commun. Math. Phys.*, vol. 279, no. 1, pp. 147–168, Apr. 2008, doi: 10.1007/s00220-008-0411-y.
- [39] J. R. Johansson, P. D. Nation, and F. Nori, ‘QuTiP 2: A Python framework for the dynamics of open quantum systems’, *Computer Physics Communications*, vol. 184, no. 4, pp. 1234–1240, Apr. 2013, doi: 10.1016/j.cpc.2012.11.019.
- [40] A. Blais, A. L. Grimsmo, S. M. Girvin, and A. Wallraff, ‘Circuit quantum electrodynamics’, *Rev. Mod. Phys.*, vol. 93, no. 2, p. 025005, May 2021, doi: 10.1103/RevModPhys.93.025005.
- [41] P. Krantz, M. Kjaergaard, F. Yan, T. P. Orlando, S. Gustavsson, and W. D. Oliver, ‘A quantum engineer’s guide to superconducting qubits’, *Applied Physics Reviews*, vol. 6, no. 2, p. 021318, Jun. 2019, doi: 10.1063/1.5089550.
- [42] X.-H. Deng, E. Barnes, and S. E. Economou, ‘Robustness of error-suppressing entangling gates in cavity-coupled transmon qubits’, *Phys. Rev. B*, vol. 96, no. 3, p. 035441, Jul. 2017, doi: 10.1103/PhysRevB.96.035441.
- [43] J. Majer *et al.*, ‘Coupling superconducting qubits via a cavity bus’, *Nature*, vol. 449, no. 7161, pp. 443–447, Sep. 2007, doi: 10.1038/nature06184.

## BIOGRAPHIES



**UFUK KORKMAZ** was born in Turkey. He received the BSc, MSc and PhD degrees from the Ondokuz Mayıs University (OMU), Physics Department, in 2006, 2010 and 2014 respectively. He worked as a Postdoctoral Researcher at Istanbul Technical University (ITU) in 2018-2019. He starting researches as

Post-Doc in Istanbul Technical University (ITU) in 2018-2019. His research interests are IR and UV spectroscopy, X-ray single crystal diffraction, Understanding the nature of H bonds in supramolecular structure, Quantum Mechanics and Quantum information theory.



**DENİZ TÜRKPENÇE** Samsun, Turkey in 1977. He completed his primary, secondary and high school education in Samsun. He completed his university education in Samsun Ondokuz Mayıs University, Faculty of Education, Department of Physics in 2000. In 2005, he started his master's

degree in Ondokuz Mayıs University, Faculty of Arts and Sciences, Department of Physics.

In March 2010, he worked as a researcher at Dortmund Technical University for 1 year with a YÖK scholarship to conduct research and examination abroad related to his doctoral thesis. He received his PhD from Ondokuz Mayıs University in June 2013. He worked as a Research Assistant at Koç University in April 2014 and took part in an international project. He completed her studies at Koç University in 2016. He worked as a postdoctoral researcher in the Cognitive Systems Laboratory of the Electrical Engineering Department of Istanbul Technical University between 2017-2018. He started to work as an Instructor in the Department of Electrical Engineering at Istanbul Technical University in March 2018. In November 2019, he was awarded the title of Associate Professor by the Interuniversity Board. It was decided to support the 3501 TÜBİTAK career project proposed in February 2021. Finally, he is the director of Quantum Systems and Cyber Security Laboratory at ITU Faculty of Electrical and Electronics and he still continues his duty as a Lecturer in ITU Electrical Engineering Department.

# Turkey's Domestic Car TOGG in the Framework of New Trends in Electric Vehicles and Consumer Ethnocentrism

H. Nurgul Durmus Senyapar and Mehmet Rida Tur

**Abstract**— Rising energy demands, and technological requirements are causing the world to focus more and more on Electric Vehicles (EVs). Developing technologies for these needs accelerate the development of smart and sustainable transportation and builds smart cities of the future. In this context, Turkey's Automobile Enterprise Group, known as TOGG, was established in Turkey in 2018 with six partners and joined the EV market. In this study, new trends and emerging EV technologies such as wireless charging, smart power distribution, vehicle-to-home and vehicle-to-grid systems, connected vehicles, and autonomous driving for EVs are compared with TOGG technology; and its potential effects on the market are evaluated within the framework of consumer ethnocentrism. It also provides perspectives and recommendations for future smart transportation to serve as a guide for the future technological development and commercialization of EVs.

**Index Terms**— Turkey's Domestic and National Car, TOGG, Electric Vehicles, Battery Systems, Autonomous Operation, Intelligent Systems, Consumer Ethnocentrism.


## I. INTRODUCTION

**A**DOPTION RATES of Electric Vehicles (EVs) are rising all around the globe because of a variety of favorable circumstances, including a reduction in the dependence on energy derived from fossil fuels, increased efficiency, and reduced levels of background noise [1]. In response to the global energy crisis, however, all attention has been focused on the electrification of transportation networks to produce EVs [2]. Up until relatively recently, the high costs involved

**H. NURGÜL DURMUŞ ŞENYAPAR**, is Gazi University Quality Coordinator, Ankara, Turkey, (e-mail: nurguld@gazi.edu.tr).

 <https://orcid.org/0000-0003-0927-1643>

**MEHMET RIDA TUR**, is Electric and Energy Batman University, Batman Technical Sciences Vocational School Batman, Turkey, (e-mail: mrida.tur@batman.edu.tr).

 <https://orcid.org/0000-0001-5688-4624>

Manuscript received Jan 4, 2023; accepted April 6, 2023.

DOI: [10.17694/bajece.1276683](https://doi.org/10.17694/bajece.1276683)

in the development and purchase of EVs left both the consumer and the manufacturer uncertain about the future investment potential of original equipment manufacturers, and with it, customers. This uncertainty was compounded by the fact that EVs were not widely available. However, new companies have provided the automotive industry with a new perspective by rapidly developing new technologies, lowering the prices of batteries and other components of EVs, and opening the possibility of commercializing EVs that have appeal to a mass market. In addition, Original Equipment Manufacturers (OEMs) have been confronted with a significant rise in the level of technical complexity brought on by the proliferation of environmental rules and the growing demand from consumers for more vehicle connections. Over the last century, car manufacturers have become experts in the art of developing and producing cars powered by internal combustion engines. However, to keep up with the development of new technologies, the procedures and tools that are used to create new tools must also continue to advance. Now, there are still a substantial number of cars running throughout the globe that are powered by traditional Internal Combustion Engines (ICEs). These vehicles use a significant quantity of fossil fuels. Because of this, the electrification of automobiles is advancing at a fast pace. In general, pure battery, plug-in hybrid, and fuel cell EVs are the three categories that fall within the category of “green” EVs. Plug-in hybrid EVs are capable of being categorized as a transitional type because they continue to make use of fossil fuels and release pollutants [3]. Although fuel cell EVs offer several benefits, such as high energy efficiency, extended driving range, and rapid hydrogen filling, their technology and market are still not particularly widespread [4]. EVs that run only on the energy generated by their batteries are known as pure battery EVs. These cars emit no emissions whatsoever. Pure battery EVs currently hold much of the market share for EVs and have earned their place as mainstream models [5,6]. This is due to the ongoing development of new battery technologies, the rapid construction of charging facilities, and people's pursuit of low-carbon travel in recent years.

Despite significant advances in fundamental research on battery materials, drivetrains, and technical-level control strategies for EVs, consumers' initial assessment of EVs will

be extremely important. This is something that needs to be done for the successful commercialization of EVs in many developing countries. Research is progressing quickly in the areas of battery technologies [7-9], engine technologies [10,11], charging technologies [12], and power transmission systems [13,14].

The emergence and rapid development of the above-mentioned new technologies and their successful implementation in EVs have initiated a new revolution in the field of EVs. Even though previous analyses and summaries of EVs were extremely comprehensive and detailed, it is believed that the development of new technologies that can be used in EVs would grow the market and motivate more people to start using EVs. Within the framework of EV, the presentation of the new trend takes place in Part 2, and the presentation of typical technical advancements takes place in Part 3 by concentrating on representative instances of technology products developing in various nations. Following that will be a discussion on the new technological possibilities for TOGG, followed by a presentation of future potential and challenges. In conclusion, an investigation of the outcomes as well as projections for the future stages of TOGG's EV development is carried out. This research is very important for increasing TOGG's attractiveness to customers and promoting the growth and maturity of the market. A certain guiding experience and a leadership role for the future courses of EVs may be gained from the prosperous EV development experience that has been presented in this article for several example nations. As a result, this article presents some points of view and suggestions for the development of EVs in the smart cities of the future. In addition, smart cities are searching for innovative answers to various urban problems (environmental, social, and financial) that have surfaced because of the operation of the grid network, development, and fundamental circumstances (such as vehicles, waste, and energy). However, this cooperation is not always detectable, and it is necessary to conduct tests to identify the most significant benefit [15-17].

## II. ELECTRIC VEHICLES AND TREND TECHNOLOGIES

The purpose of the study is to show recent innovations that have emerged in the field of TOGG technology in comparison with other types of electric cars. Emerging technologies, such as wireless charging, smart power distribution, vehicle-to-grid (V2G) and vehicle-to-home (V2H) systems, and autonomous driving are also thoroughly discussed here, along with the obstacles and new possibilities that each present. Following what is shown in Fig. 1, the trend will be segmented into five subgroups that directly correlate to the five new trends.

### A. Wireless Charging Feature

If the induction charging system is in a magnetic resonance coupling state, excellent charging efficiency can still be guaranteed even if the transmit and receive coils are several feet apart [18,19]. This is because magnetic resonance coupling allows magnetic fields to be coupled in a way that is insensitive to distance. Using this approach, automobiles that are parked in garages or on the street may be effectively

charged with 3-7 kW of electrical power across vast range lengths when the induction charging system has well-adjusted hardware components and is positioned at the ideal angle [20,21]. Fig. 2 displays a diagrammatic representation of a typical wireless charging system that is fixed.



Fig. 1. Structure and highlights of this review

Traditional methods of charging have their place, but wireless charging offers many advantages over them, including increased adaptability, longevity, and dependability. It is also more convenient for automobile drivers. These stations not only prevent irreparable damage and corrosion to charging connectors caused by frequent dropping and plugging, but they also provide safe charging in potentially hazardous scenarios, such as explosive gas stations where electric sparks are prohibited [23,24]. In addition, these stations prevent irreparable damage and corrosion to charging connectors caused by frequent dropping and plugging. From the year 2020 until the year 2025, it is anticipated that the worldwide market for EV wireless charging will rise at a compound annual growth rate of 49.38% [25]. Another key component that will continue to drive the market is the sustained growth of rapid EV chargers, which is expected to reach a size of over \$7 billion in 2025. Using predetermined electromagnetic coils buried under the road, the advanced dynamic charging idea intends to continually charge EVs when they are stopped at a signal or even while they are moving. Figure 2 explains the concept of the "smart city" of the future, which is envisioned to include a well-established wireless charging infrastructure.



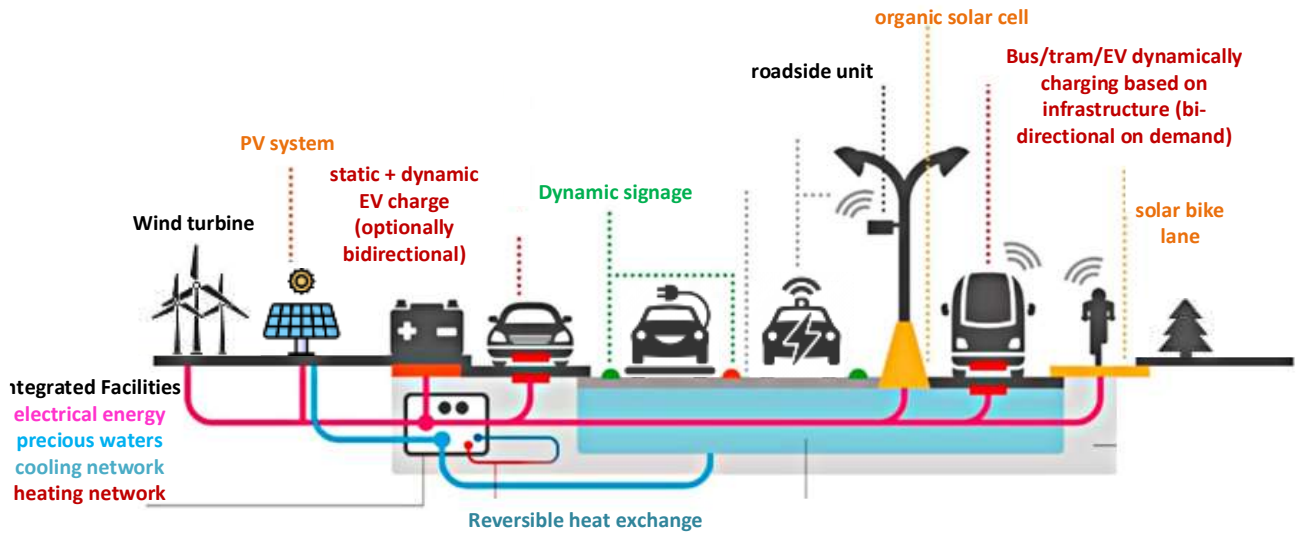


Fig. 2 Fixed wireless charging [22].

TABLE I  
SUMMARY OF CHALLENGES AND OPPORTUNITIES OF WIRELESS CHARGING IMPLEMENTATION IN EVS [26].

Challenges	Opportunities
Misalignment tolerance of charger	Application and development of new materials
Timing of high-speed power transfer	Extended range and battery life on EVs
Multiple vehicles charging per transmitter	Developing autonomous driving
Charger life and durability under real conditions	Renewable energy storage
network effect	Frequency control in grid connection
Grid effect	Cost reduction for EVs
High cost of infrastructure construction and large-scale deployment	Cost reduction and environmental benefits
Interoperability between multiple manufacturers	
Benefits	
Universal standards	
Fast charging	

*B. Smart Power Distribution Technologies*

The efficient distribution of electricity allows for the charging of additional EVs without requiring significant infrastructure improvements. Instead of adding extra physical electrical capacity, the power distribution system may dynamically divide the available power among additional electric vehicle chargers to allow for the charging of a greater number of EVs [27-29]. Figure 3 uses a typical system to highlight the benefits that may be gained by implementing intelligent power distribution. Drivers want information on charging that is communicated openly and honestly, including up-to-date details on the availability of charging stations and the rates charged during peak and off-peak hours. Drivers will have access to sophisticated EV charging management options thanks to a back-end charging centralized control and management system that is comprehensive [30]. These solutions will include demand-side response intelligent energy management.

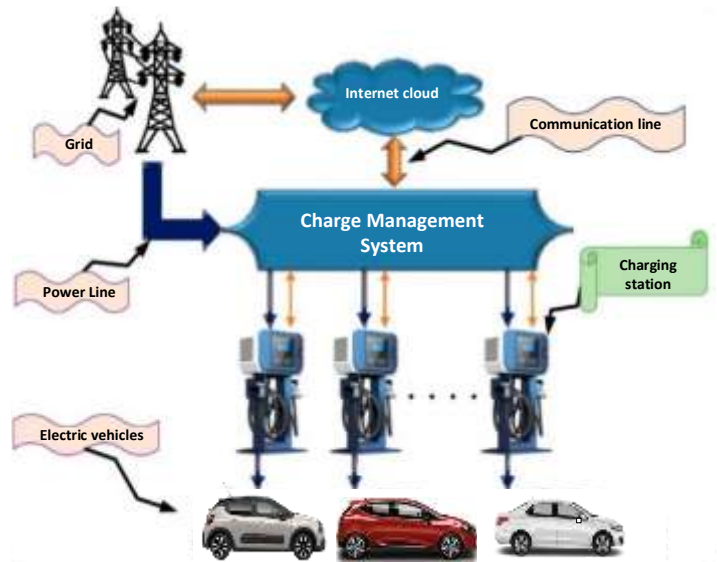


Fig. 3. Schematic diagram of smart power distribution [31].

The integration of secondary batteries and renewable energy sources into the electrical grid is developing into an advanced smart power distribution technology that makes it easier to deploy quick electric vehicle chargers. The capacity of the electrical grid may be increased by re-feeding surplus power output from secondary batteries and renewable energy sources, such as green energy generators. Secondary batteries, which serve as energy buffers, can provide electricity in times of crisis, such as when the grid is overloaded or severed [32].

Table 2 provides a concise summary of the potential and difficulties that lie ahead in the development of intelligent power distribution for EVs.

TABLE II

A SUMMARY OF THE POTENTIAL AND PROBLEMS ASSOCIATED WITH THE IMPLEMENTATION OF SMART POWER DISTRIBUTION FOR EVS [33].

Challenges	Opportunities
Market Framework	New market models enabling active and reactive EV distribution service systems such as load shifting, peak shaving, valley filling, voltage regulation, and distribution system level reactive power control.
Economic aspects	Economic considerations, including benefits analysis for all stakeholders and possible compensation strategies for service providers.
Battery corruption	Integration of battery degradation costs with changes in charge/discharge strategies.

### C. Vehicle Connection Technologies

The connectivity technologies operate together seamlessly with three different networks: the in-car network, the V2G network, and the mobile internet in the vehicle itself. It is a massive, distributed communication system for V2X interaction that incorporates X, and it is also known by its acronym, IoV, which stands for the “Internet of Vehicles”. Vehicle connections offer a multifunctional network that supports intelligent transportation management, intelligent dynamic information services, and intelligent driving control [34]. This comprehensive scenario for the implementation of the Internet of Things (IoT) in the Intelligent Transportation System (ITS) is provided by the Internet of Things (IoT) in the Intelligent Transportation System (ITS). Certain communication protocol standards, such as the IEEE 80211p WAVE standard or cellular data protocols [35], are adhered to throughout the process of exchanging information. Interfaces to WiFi or cellular networks (GSM, HSDPA, LTE, or 5G are projected to be built on a significant scale) and other short-range communication technologies are often included in typical car connection systems [36]. The Global Vehicle Identification (GVI) terminal is without a doubt the technology component that is essential to the connectivity of vehicles and serves as the communication gateway [37]. It allows the vehicle to have global locating and tracking capabilities, as well as a worldwide network connection,

thanks to its integrated information sensors, network communication module, and Global Online Identification (sometimes known as an “online license plate”) [38].

Table 3 provides a summary of the difficulties that may arise and the possibilities that may present themselves throughout the development of Connected Vehicles (CVs) technologies for EAs in the future.

TABLE III

SUMMARY OF CHALLENGES AND OPPORTUNITIES IN IMPLEMENTING CVS IN EAS [39].

Challenges	Opportunities
CV interoperability	Blockchain integration with CVs
CV reliability	Improving the reliability, flexibility, safety, security, and privacy of CVs
Efficient wireless resource allocation in CVs	Implementation and development of artificial intelligence (AI) and machine learning techniques in CVs

### D. V2H and V2G Technologies

While the V2H system makes it possible to utilize the energy that has already been stored in the EV to power a home, the V2G system makes it possible to sell the electricity that has already been stored in the EVs to the grid and charge the EV by buying electricity from the grid [40]. Software for managing the battery, hardware to handle the transfer of power in both directions and communication modules to provide two-way dialogue between the vehicle terminal and the grid operator are the primary components of V2H and V2G systems [41]. Intelligent algorithms keep a constant watch on the working condition of the grid to assess in real-time whether a vehicle is now able to purchase or sell energy from the grid and whether or not a vehicle is qualified to reach the applicable agreement.

In 2013, an example project (Fig. 4) was presented to link EVs, solar power production, and individual consumers via the use of a smart grid and home information management system [42,43]. By using the V2G technology, it was able to communicate the following findings to the public [44-46]:

- Significantly increased energy self-sufficiency, which resulted in an improvement in participants’ zero-emission energy autonomy (from 34% to 65%)
- The frequency of energy exchanges between participants and the grid has been significantly reduced (45%)
- The utilization efficiency of electrical energy storage capacity has reached 93%
- Energy loss from conversion during the process of storing energy in DC batteries and recovering power from them is 80%
- Battery capacity consumption for powering EVs has reached 80%
- Battery capacity consumption for two years of use was negligible (6~7%) [47,48].

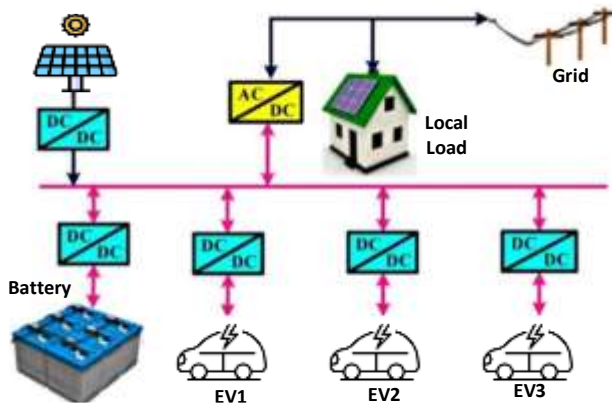


Fig. 4 Representative V2G and V2H systems in different countries [49,50].  
The challenges and opportunities in the future development of V2G and V2H technologies for EVs are summarized in Table 4.

TABLE IV  
SUMMARY OF THE CHALLENGES AND OPPORTUNITIES OF V2G AND V2H FOR EAS [51]

Challenges	Opportunities
Battery corruption	Integration of battery degradation costs with change in charge/discharge strategies
Cyber attacks	New technologies that increase the resilience of V2G and V2H systems against cyber-physical attacks and new security standards
Time delay	Wide bandwidth communication channels such as LAN and WAN networks
Stability issues	Development of robust controllers

E. Autonomous Driving

The Society of Automotive Engineers offers the most widely accepted definition of autonomous driving. Autonomous driving may be broken down into different levels, each corresponding to a different amount of automation. Realizing the potential of autonomous driving will need sophisticated technology across a wide range of fields; and sense will be essential to achieving this goal. These standards define six levels of driving automation, which are “No Automation”, “Driver Assistance”, “Partial Automation”, “Conditional Automation”, “High Automation”, and “Full Automation” [52-54]. “No Automation” is the lowest level of driving automation, and “Full Automation” is the highest level of driving automation.

Wheel speed odometry relies on a rotary encoder to keep track of the rotation of the wheel and estimate the change in position in relation to where it began [55]. However, the wheels do not always have a complete rolling motion to the ground, and they are susceptible to slipping when the driver makes rapid speed changes or while traveling on flat roads. The unrecorded drift will result in cumulative inaccuracies, and as a result, the dependability of odometry will steadily decline over time. It is important to note that visual odometry is not restricted to the form of the movement on the ground since it tries to estimate the vehicle’s location and velocity by analysing the movement of the picture from frame to frame (Figure 5), therefore, it is not limited to the shape of the movement on the ground [56]. The challenges and opportunities in the future development of autonomous driving in EVs are summarized in Table 5.

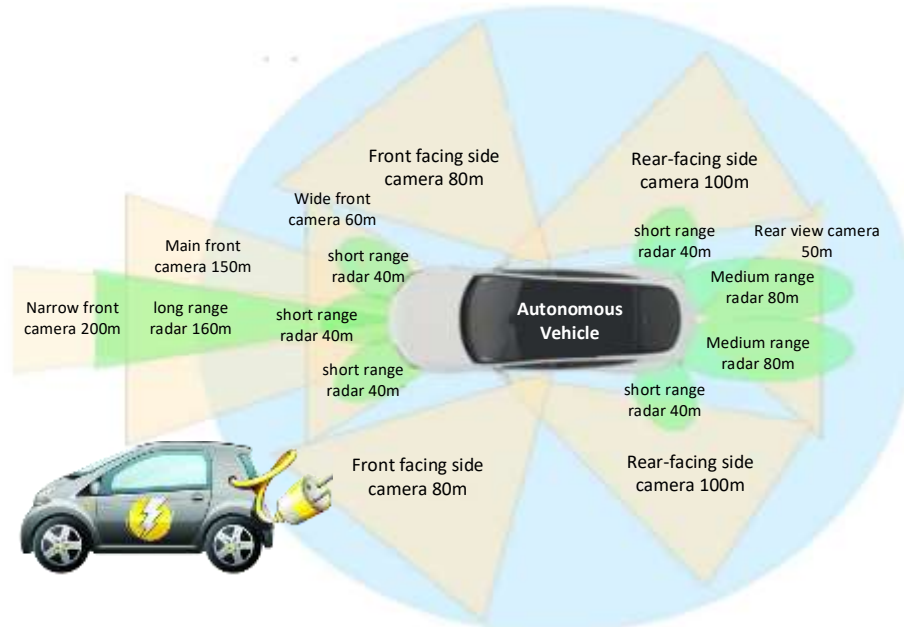


Fig. 5 Locations and scope of sensors installed in an autonomous vehicle [57]

TABLE V  
SUMMARY OF CHALLENGES AND OPPORTUNITIES OF AUTONOMOUS DRIVING IMPLEMENTATION IN EVS  
[58,59].

Challenges	Opportunities
Limited physics-based models	Data-based models and hybrid models
Lack of controller for arbitrary situations	Fully viable methods for numerical control design that can accommodate uncertainties and discover approximately optimal or even viable solutions under real-time operational constraints.
Decision-making algorithms in autonomous vehicles, from powertrain control loops to autonomous driving functionality	Development of large V2X systems and learning-based components
Providing high reliability, low cost, and complexity	Enhanced resilience to sensor and actuator failures, communication interruptions, and cyberattacks
Concerning the positioning of autonomous vehicles, there is a lot of uncertainty about what levels of automation will be brought to public roads and when.	Construction of new physical and cyber infrastructure

### III. ELECTRIC VEHICLES AND TOGG TECHNOLOGY: EXPECTATIONS

#### A. DOMESTIC AND NATIONAL AUTOMOBILE TOGG

Although attempts were made to produce domestically branded automobiles in Turkey in the 1960s, mass production could not be started. On November 2, 2017, Turkey's Automobile Joint Venture Group Promotion Meeting was held at the Presidential Complex. With the protocol signed, Anadolu Group, under the coordination of the Ministry of Science, Industry, and Technology and the Union of Chambers and Commodity Exchanges of Turkey (TOBB), established Turkey's Automobile Enterprise Group to produce the TOGG along with BMC, Kök Group, Turkcell and Zorlu Holding. The prototype of TOGG appeared on August 5, 2019. In 2017, Turkey's Automobile Initiative Group (TOGG) was launched as a domestic and national car. Prototypes of the domestic branded car were produced under the name of Turkey's Automobile and its presentation was made on 27 December 2019. TOGG made its world brand launch at CES 2022. Attending CES, held in Las Vegas, USA, between 5-7 January 2022, with its vision car, TOGG announced its innovations to the world public at a press conference. It is planned to produce 1 million vehicles in 5 different segments by 2030.

The automotive sector leads the way in Turkey's exports. With the expansion of TOGG, it is expected that Turkey will produce one million vehicles in five distinct models by the year 2030. Additionally, it is anticipated that 93 percent of TOGG's supply will be completed, with 78 percent of the supply coming from Turkey and 22 percent coming from countries in Europe and Asia. According to the country's Minister of Industry and Technology, Turkey has gathered more than \$126 million to finance innovation and regional development, and it plans to acquire 30.000 cars by the year 2035. It is anticipated that the electric automobile would reach a yearly production rate of 175.000 units.

Turkish Electric Vehicles (TEV) became the first vehicle whose intellectual property rights belong to a Turkish company. TEV is expected to contribute to the Turkish economy with a USD 7.5 billion decrease in the current account deficit and an increase of USD 50 billion in GDP (TOGG Investment Office, 2020. Within the scope of this discussion, it has been determined that the TOGG battery company, which is anticipated to begin production in 2023, will be responsible for the annual manufacture of 20 GWh worth of lithium-ion batteries. With this capacity, it will be possible for Turkey to create batteries that are enough for an annual average of 250-300 thousand electric automobiles, which would avoid the country from having to import batteries that cost billions of dollars. In this regard, it is thought that meeting the demand for minerals such as lithium, nickel, manganese, and graphene, which are utilized in the creation of batteries, using indigenous resources would become an issue of considerable significance [60].

#### B. TOGG in the International Market

The European market was ahead of the Chinese market in terms of registrations for new Plug-in Hybrid (PHEV) and Battery Electric (BEV) passenger vehicles when we conducted our most recent check at the beginning of 2022. The market in the United States was lagging that in the other two main areas. Now, the picture is a little different, demonstrating once again how dynamic EV sales still are, and for the first half of 2022, the market in China has caught up with the market in Europe. The registration of BEVs accounts for 19% of all new passenger cars, while PHEVs account for an additional 5%. A market share that is eight percentage points more than it was the year before and four times larger than it will be in 2020 is what China has accomplished in terms of market share. Because of this, China has already surpassed the 20% EV share objective outlined in the 14th Five-Year Plan Energy Conservation and Emission Reduction Work Plan, two years earlier than the 2025 deadline that was originally set shown in Figure 6 [61].



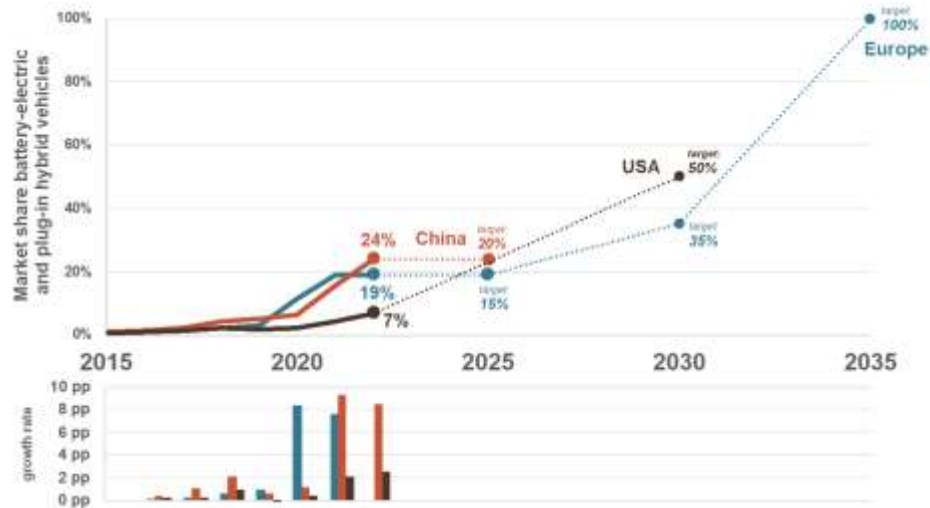


Fig. 6. Market growth rate in EVs

In this context, “Europe” refers to the European Economic Area, and the region presently holds the second-place spot with a 10% proportion of BEVs and a 9% share of PHEVs. As a direct consequence of European CO<sub>2</sub> rules for new automobiles establishing an average goal of 95 grams per kilometers (g/km) for 2020/21, automakers have almost tripled the market share of electric cars in only one year, particularly in 2020. This trend is expected to continue. However, after successfully meeting their CO<sub>2</sub> objectives for 2020/21 without incurring penalties, it seems that car makers’ enthusiasm for EV sales has diminished to some degree. The 2025 standard is the next regulatory goal mark; nevertheless, this standard is not significant enough to have a significant influence on the portfolio plans of manufacturers. The market seems to be growing at a pace of zero percent so far in 2022, although tax benefits for EVs are now beginning to decrease in certain European nations. In addition, there are huge waiting lists for electric cars because of persistent supply constraints.

After falling farther and further behind for a time, the market in the United States had the highest growth rate among the three primary areas during the first half of 2022. During this period, Battery EVs made up 5.5% of all new passenger automobiles, while Plug-in Hybrid EVs made up 1.4%. Sales of light trucks in the United States represent a market share that is three times bigger than it was in 2020, even though it is still lower than in China and Europe. The aim of 50 percent sales of EVs by the year 2030 which was established by the President continues to serve as the leading regulatory signal in the United States.

With the expansion of TOGG, it is expected that Turkey will produce one million vehicles in five distinct models by the year 2030. Additionally, it is anticipated that 93 percent of TOGG’s supply will be completed, with 78 percent of the supply coming from Turkey and 22 percent coming from countries in Europe and Asia. According to the country’s Minister of Industry and Technology, Turkey has gathered more than \$126 million to finance innovation and regional development, and it plans to acquire 30.000 cars by the year 2035. It is anticipated that the electric automobile would reach a yearly production rate of 175.000 units.

In a summary, although the European Union’s aim of having 100% all-electric cars on the road by 2035 is unquestionably the worldwide standard, the area does not have a relevant intermediate target, especially during the years leading up to 2029. As a consequence of this, sales of EVs in Europe will remain flat, mirroring the trend that we saw in the first half of 2022. The new energy vehicle authorization in China, on the other hand, seems to apply ongoing pressure on EV sales; nevertheless, the country’s sales goal for the year 2025 has already been fulfilled, and long-term objectives are still not accessible. It seems that the planned Electric Vehicle objective in the United States is backed by improved light commercial vehicle greenhouse gas emissions requirements for the 2023-2026 model years, making it the most advanced target for EVs anywhere in the world for the timeframe 2030. TOGG engineers will reveal the electric vehicle platform that they have built as their unique work and will patent it. The platform, which will provide a structure for maximum efficiency, comfort, durability, and safety, will see a fixed investment of over 22 billion TL (\$3.21 billion), and the factory will start mass production in 2022 with an annual capacity of 175.000 units [59]. The platform will provide a structure for maximum efficiency, comfort, durability, and safety; the investment in the platform will be over 22 billion TL.

### C. Trend Technologies and TOGG Hardware

Established in 2018, Turkey's Automobile Initiative Group has become the company that produces electric cars in Turkey, and in 2023 it will introduce 20,000 first vehicles from the T10X series to its users. The T10X series can reach 20%-80% occupancy rate in a very short time such as 28 minutes and travel 523 kilometers. The 4-wheel drive AWD model reaches 100 kilometers in 4.8 seconds with 320 kW double engine power, the rear-wheel drive RWD model reaches 100 kilometers in 7.4 seconds with 1660 kW single engine power, the models' torque is 700 Nm and 350 Nm, respectively. produced. [62]. This function is known as regenerative braking and is familiar to many who have used Tesla vehicles.

When the brake is used, kinetic energy is released, which is then captured by the alternator, where it is transformed into electrical energy and stored once again. This technique has the potential to increase the range of a typical domestic automobile by up to twenty percent. It reaches 400 horsepower in variants that include all-wheel drive, and it can go from 0 to 100 kilometers per hour in 4.8 seconds. The homegrown vehicle, which has a 200-horsepower engine and drives the rear wheels, can go from 0 to 100 kilometers per hour in 7.6 seconds. The domestic automobile, which is powered by lithium-ion batteries, offers two alternative possibilities for its range; more than 300 kilometers or more than 500 kilometers [63].

Users will benefit tremendously from the vehicle’s quick-charging technology, which enables the vehicle to achieve a full charge in only thirty minutes. At the same time, the domestic automobile, which can get updates over the internet, is equipped with third-level autonomous driving technology. This is made possible by the car’s sophisticated driving assistance systems. We came upon a feature in Tesla’s automobiles that allowed for an upgrade to be performed via the internet. In the context of the domestic vehicle, the Internet of Things (IoT) was accorded a significant amount of importance. The intelligent energy solutions offered by TOGG provide users with complete control over the charging process and emphasize the user experience before, during, and after

the charging process. Users can enjoy the most effective and convenient experience possible, free from the burden of worrying about battery life or travel distance. All users of EVs will benefit from these solutions since they provide alternatives for ecologically responsible, intelligent driving as well as charging their vehicles. TOGG can stand out from its competitors on a worldwide scale because of its Use Case Mobility methodology and the ecosystem it has developed on this foundation.

Figure 7 provides detailed information on EVs that are manufactured by a variety of companies and are reasonably priced [63]. Additionally, the projected amount of time necessary to charge the car from 0% to 80% capacity according to a variety of charging techniques is included in the figure. In this case, the voltage for the first stage of charging is similar to 110-120 V, the voltage for the second stage of charging is 220-240 V, and the voltage for the third stage of charging, also known as DC Fast Charge (DCFC), is 200-800 V. The amount of charge in an Electric Vehicle’s battery is directly proportional to the vehicle’s driving range. However, depending on the make and model, the range of the battery drops to between 200 and 400 kilometers after traveling 100 kilometers in certain vehicles. On the other hand, the majority of currently available EA models in China can go farther than 400 kilometers. On the other hand, the TOGG was developed for a range of between 300 and 500 kilometers.

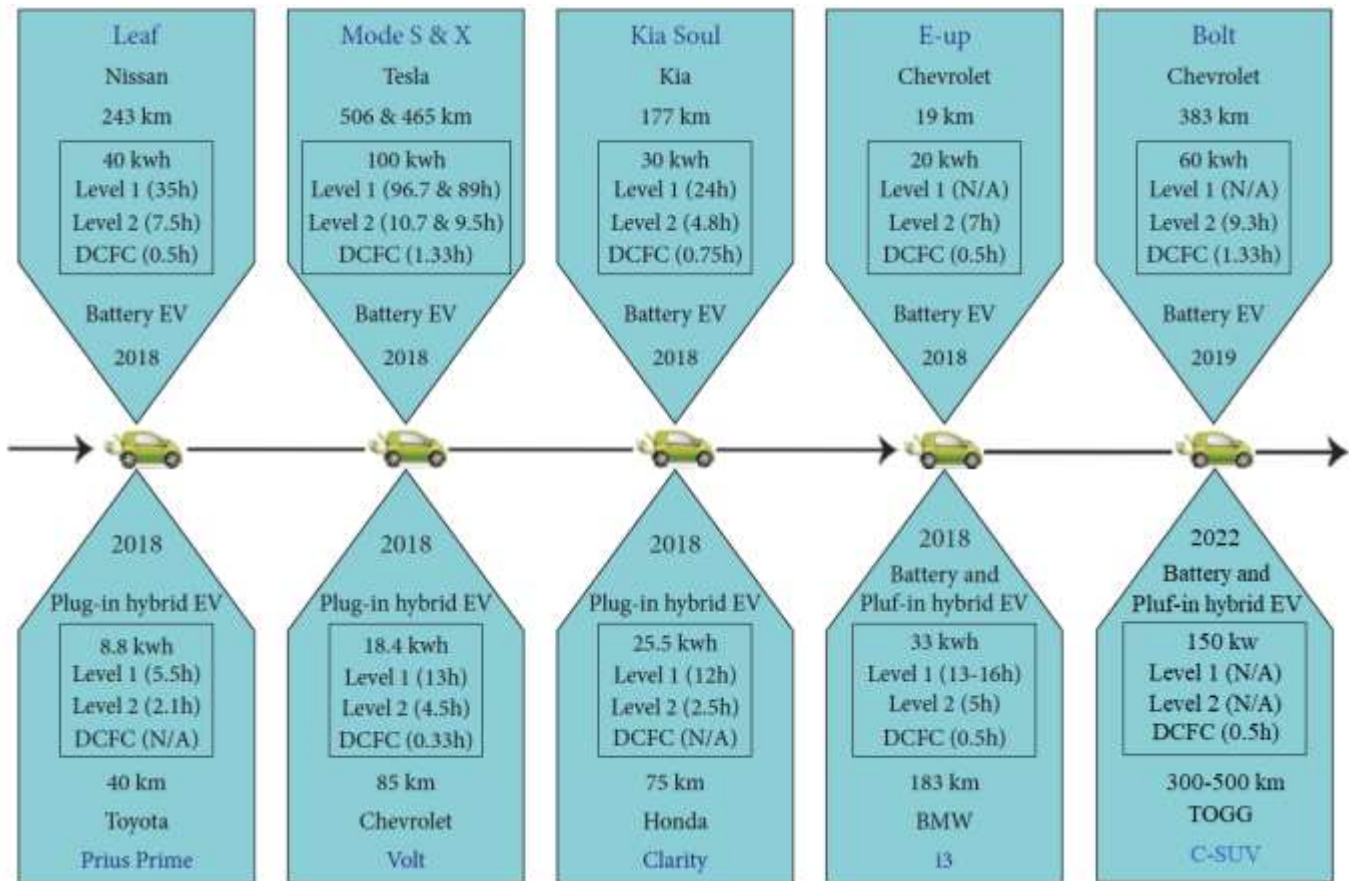


Fig. 7. Comparison of some EVs Produced in the Last 5 Years

The TOGG C-SUV has real-time data on automobiles as well as an intelligent production network that is the Internet of Things compatible. In addition to this, its battery range is sufficient to compete with that of gasoline-powered rivals. When it comes to the design of the battery and the electronic power unit, significant progress has been made. Producing 160 kW / 218 HP and 350 Nm of torque, the T10X RWD (rear drive) will have ranges of 314 and 523 kilometers with two different battery options. While the 52.4 kWh battery option of the rear-wheel drive T10X offers 16.7 kWh/100 km (WLTP) energy consumption, the 88.5 kWh battery option has a consumption value of 16.9 kWh/100 km.

#### D. TOGG Expectations

With its national automobile, the TOGG, Turkey demonstrates that it is not unconcerned by the pace of technological advancement taking place elsewhere in the globe. Electric automobiles, which have recently become more commonplace in many nations, are among the most significant instruments that will be used to meld the world of the future. The most recent action that Turkey has made is related to this sector. TOGG will offer a variety of models, including domestic SUV, sedan, and hatchback versions of its vehicles. The TOGG automobile, which will likely be an electric vehicle when it is constructed, is notable due to the qualities it has. TOGG was conceived to be outfitted with cutting-edge technology, making it a potential contender to be one of the automobiles of the future that has remarkable characteristics. The C-SUV is slated to become the first vehicle of its kind to be manufactured under the TOGG brand. The Mercedes-Benz C-Class is the model that is most popularly purchased in Turkey, which is why this is the case. The capability of maintaining an internet connection at all times is the element of the TOGG domestic automobile that stands out as the most significant and useful characteristic. It is anticipated that the car would take 28 minutes to get an 80 percent charge once the charge has been started. The TOGG is a one-of-a-kind automobile that is of the newest generation and distinguishes out due to the advanced technology it has. The battery of the long-range TOGG may be recharged in a relatively short amount of time.

Surprisingly, the TOGG national automobile comes with two distinct engine choices since this is one of its many impressive qualities. The vehicle's acceleration from 0 to 100 kilometers per hour takes 7.6 seconds with the first engine choice, which produces 200 horsepower; the vehicle's acceleration from 0 to 100 kilometers per hour with the second engine option, which produces 400 horsepower, takes 4.8 seconds. Both sorts of engines have the potential to be quicker than many other cars that are now operating on Turkey's congested roadways when seen from a broader perspective. Despite this, the maximum speed that the domestic automobile TOGG is capable of reaching is limited to 180 kilometers per hour (another characteristic that stands out), which was done

to make driving in traffic safer. The electric TOGG automobile includes several characteristics, including autonomous driving and a chassis that can be customized. In addition, TOGG, which is anticipated to give the domestic and international markets additional momentum because of its cutting-edge technological characteristics, is another significant development that is anticipated to pollute the air less as a consequence of its capacity to produce zero emissions.

In a study that was prepared by using the interview method, various topics such as the first reactions of the participants with the exploratory feature of TOGG, which features of the vehicles they emphasized in their evaluations, price estimates/expectations, purchase intentions, and brand name suggestions were examined [63]. The characteristics of TOGG, both in terms of its design and its implementation, have been discussed in the previous section. In general, the fact that the cars are electric, the ease with which they can be recharged, the technological components, the level of safety, and the range that they can travel on a single charge are among the technical factors that are stressed in the assessments. Notable aspects include the capacity of the cars' batteries, the current charging state of the vehicles, and the infrastructure associated with the charging stations.

When the assessments that were produced by the research are looked at, it can be observed that TOGG is intelligent, autonomous, and has other similar characteristics. It has been noted that the emphases do not seem to have a significant impact on the individuals who were interviewed. Only three of the people who were interviewed highlighted the importance of being intellectual or independent. However, just like in comparisons and explanations with other models in the same category, the TOGG C-SUV is equipped with high-tech batteries that will provide a range of 300 to 500 kilometers with a battery that can compete with alternatives to gasoline, as well as an intelligent production network system that is compatible with the Internet of Things.

During the interviews, 78 people made clear mention of quality, and 52 of those people stated that they believed the tool to be of good quality. Emphasizing the quality of the participants in their evaluations, during the interviews. Some of these 51 individuals discussed quality by assessing it in conjunction with the design. The brand has a significant edge in the worldwide rivalry over electric cars because of the Use Case Mobility strategy that the vehicle takes, as well as the ecosystem that TOGG has built around it. The participants said that the price of the automobiles on the market would determine whether they would make a purchase, although 40.2% of them expressed a willingness to buy.

At the introduction ceremony, the release dates for all the models were disclosed. The TOGG Xcoupe has taken the position of the hatchback, which is likely going to be introduced the following year. It is anticipated that the next model will be introduced in the year 2026.



TABLE VI  
TOGG VEHICLE TYPE AND TURKEY RELEASE DATES

Model	Vehicle type	Introduction date	Turkey release date	European release date	Motor
<b>TOGG SUV</b>	C-segment SUV	27 Dec 019	July 2023	2024 3. quarter	Electric
<b>TOGG Sedan</b>	C-segment Sedan	27 Dec 2019	2025 1-2. quarter	–	Electric
<b>TOGG Xcoupe</b>	C-segment Xcoupe	29 Oct 2022	After 2026	–	Electric
<b>TOGG Kompakt SUV</b>	B-segment SUV	Waiting	by 2030	–	Electric
<b>TOGG MPV</b>	–	Waiting	by 2030	–	Electric

#### IV. CONSUMER ETHNOCENTRISM IN PURCHASE DECISIONS

##### A. Consumer Ethnocentrism and Electric Vehicles

As a result of their irreparable damage to the environment, rising greenhouse gas emissions are identified as a significant issue for economies around the globe. The transportation industry has a considerable effect on the situation. Considering the decline of fossil fuels, EVs are viewed as a key answer. While EV adoption is increasing rapidly, particularly in developing nations, a lack of supportive regulations, infrastructure, consumer knowledge, economic incentives, and cheap prices, among other factors, has a direct impact [64].

In Turkey, for instance, the current share of EVs and hybrids accounted for 0.3% of all registered vehicles by 2020 [65]. Therefore, far more effort is required to achieve the target level of EV adoption. Promoting home brands is another strategy to accelerate the adoption of EVs, as patriotism is emerging as a significant factor in influencing consumer behaviour in nations with high levels of nationalism as well as in more expensive product categories [66]. It is anticipated that it will be adopted as a domestic vehicle after the TOGG and that this adoption rate will increase. Consumer Ethnocentrism (CE) is more likely to affect local purchases of expensive product categories, particularly vehicles because they have a greater economic impact [67-69]

The EV sector is a growing market, and EVs appear to be relatively new to the automobile industry, particularly in developing nations. While many companies on the market produce their own EVs, CE has also been linked to the purchase intentions of EVs in nations with high levels of nationalism. In China, for instance, a positive association was established between CE and Chinese consumers' willingness to purchase Chinese EVs. In a second study with a sample of Chinese consumers, they found comparable outcomes [70-72]. CE, a highly sought-after consumer behavior predictor, has also been disregarded in EV adoption research, except for a few studies, while many nations have had to implement

regulations to promote EV adoption on a national scale and a few automakers are developing their own EVs.

Extensive research has demonstrated that consumers' personality traits, attitudes, and features influence their adoption of EVs [73,74], as well as their instrumental/functional perceptions of EV properties and pro-environmental behaviors [75-77]. In EV adoption research, the authors focused on the idea of Consumer Innovativeness (CI) in terms of personality characteristics, disposition/perceptions, and actual behavior, as EVs are viewed as a novel transportation technology [78]. While environmental behavior influences are largely regarded as a factor in EV adoption, consumer innovation appears to be a far less common component. In addition, there is a lack of a holistic picture of consumer-product interaction [79]. Previous research on the Turkish sample has demonstrated that, on average, Turkish consumers exhibit high-to-moderate ethnocentrism [80-82]

Thus, the ethnocentric approach can be utilized to sell TEVs and promote domestic adoption. We believed that CE could therefore influence EV's purchase intentions. This study aims to contribute to the literature on EV adoption by determining if and to what extent CE and CI influence TEV buying intentions. As TEV is the first EV with a Turkish-branded electric vehicle, we hypothesize that these two primary concepts are likely to affect the adoption of EVs in Turkey [83].

In the literature, EV types are categorized as Battery Electric Vehicles (BEVs), Plug-in Hybrid Electric Vehicles (PHEVs), and Hybrid Electric Vehicles (HEVs). PHEVs and HEVs are EVs with two engines; an internal combustion engine and an electric motor supplied by batteries and the BEV has a single electric motor that is powered by a battery. The TEVs evaluated in this study are battery-powered electric cars. It is referred to as TEV since it is the first electric vehicle produced and manufactured in Turkey. However, the car industry dominates Turkey's exports. Thus, TEV became the first vehicle for which a Turkish corporation owned intellectual property rights. TEV is anticipated to contribute to the Turkish economy by reducing the current account deficit by USD 7.5 billion and increasing GDP by USD 50 billion.



In December 2019, the first two TEV prototypes, a C-SUV, and a Sedan were displayed. It will be distributed by the TOGG. Additionally, TOGG will produce five distinct models by 2030. TOGG is a coalition of four local enterprises, with TOBB (Turkish Union of Chambers and Commodity Exchanges) serving as the coordinator [64]. Long before the introduction of TEVs, it was discovered that perceived hazards had a negative impact on a potential domestic automotive brand's purchase intention, whereas product image had a positive impact [84]. Since TEV is a novel product, few studies have been conducted on it. In the qualitative analysis, 44.6% of respondents deemed the first two prototypes of the TEV to be successful, while 24.1% deemed it to be moderately successful due to its lack of market presence [85]. In addition, the participants emphasized the TEV's functional characteristics (electricity, rapid charging) and its overall design. In another study, CI and CE explain TEV purchasing intent significantly [86].

### *B. Consumer Ethnocentrism in Purchase Decisions and TOGG*

Increasing greenhouse gas emissions are defined as an important problem for economies around the world due to their irreversible damage to the environment. The impact of the transportation sector on the problem is quite remarkable. As fossil energy sources are also declining, EVs are seen as an important solution. While the adoption of EVs is growing rapidly, especially in developing countries, there is a lack of favorable policies, lack of infrastructure, consumer awareness, economic incentives, affordable prices, etc.

For example, in Turkey, as of 2020, the current share of EVs and hybrid cars only accounts for 0.3% of all registered cars in the country. Therefore, much more effort is required to drive EV adoption to the desired level. Another way to increase the adoption of EVs is to promote domestic brands, as the idea of patriotism is emerging as an important factor for influencing consumer behavior in countries with high nationalism as well as in more expensive product categories. It is estimated that TOGG will increase this rate as a domestic automobile. CE is more likely to influence local purchases for expensive product categories, especially automobiles, as they contribute more to the economy. In addition, empirically, it was found that CE explained more variance ( $R^2=0.3$ ) in the purchasing behavior of automobile owners than computer owners ( $R^2=0.1$ ) in comparison to two product categories, automobile, and computer. This relationship has also been empirically confirmed in the Malaysian context. Therefore, CE can be an important determinant of domestic vehicle purchase intentions.

The EV industry is a growing market. EVs seem relatively new to the automotive industry, especially in developing countries. While many brands in the market create their own EVs, EV purchase intentions in countries with high nationalism are also associated with CE. In China, for example, a positive correlation was found between CE and the purchase intentions of Chinese EVs among Chinese consumers. Similar results were obtained in another study on a

sample of Chinese consumers. CE, a widely sought-after determinant of consumer behavior, has also been neglected in EV adoption research, apart from a few studies, while many countries have had to develop policies to promote EV adoption on a national basis, and a few auto brands are creating their own EVs.

Extensive research has also shown that consumers' personality traits, perceptions, and characteristics have an impact on EV adoption and instrumental/functional perceptions of EV attributes and pro-environmental behaviors. Since EV is interpreted as a new technology in transportation, the authors paid attention to the concept of Consumer Innovativeness (CI) in terms of personality traits, disposition/perceptions, or realized behavior in EV adoption research. While pro-environmental behavioral influences are widely accepted factors, it seems quite rare that consumer innovativeness is taken as a determinant in EV adoption. Also, a comprehensive view of the consumer-product relationship is lacking.

This means that the ethnocentric emphasis can be used to market TEV and drive domestic adoption. Therefore, we thought that CE might influence EV purchase intentions. In short, this study aims to contribute to the EV adoption literature by assessing whether and to what extent TEV purchase intentions are affected by CE and CI. We suggest that these two main concepts are likely to influence the adoption of EVs in the Turkish case, as TEV is the first EV with a Turkish-branded Electric Vehicle.

It has been determined that long before the emergence of TEV, perceived risks negatively affect the purchase intention of a possible domestic automobile brand, while product image positively affects it. Since it is a new product, limited research on TEV has been found. In the qualitative study, 44.6% of respondents thought that the first two prototypes of TEV were successful, while 24.1% thought it was somewhat successful because it has not yet been seen on the market. In addition, the participants highlighted some of the functional features of the TEV (electricity, fast charging) as well as its overall design.

## V. CONCLUSIONS

It is anticipated that advancements in the development of electric automobiles as well as contributions to the total sources and facilities of renewable energy would result in an improvement in the reputation of electric cars in the worldwide market. In this sense, additional technological advancements such as appropriate and reasonable pricing rules, smart cities, robust adaptive frameworks, business structures, policy, CO<sub>2</sub> emission reduction, mitigation, and measurement of the impact on the environment, health, and electricity grid are essential.

This research provides an overview of the many components that make up the process of developing electric automobiles. The TOGG market comparison and emerging technologies are investigated once the fundamentals of EVs and the widespread acceptance of these vehicles have been included. To prepare future experts to grasp the solutions that

need to be implemented, known electric vehicle approach guidelines and the various components that make up those guides have been extensively evaluated. In addition, several components of the pre-existing framework that were used to set up TOGG communication and EA sharing networks were investigated and compared. These components included aspects of the framework's characteristics, such as its benefits and drawbacks, consistency, control and coordination strength, and strengths.

Pure battery EVs have emerged as the most popular choice on the market among the many different types of electric vehicle models owing to the modern technology and user-friendly characteristics that they provide. This research looks at some of the most common and significant technologies that are becoming available for EVs, such as wireless charging, intelligent power distribution, V2G and V2H systems, connected vehicles, and autonomous driving. This investigation focuses on the characteristics that define TOGG vehicles, including autonomous control and long-range plucking-aided storage technologies. These characteristics are described.

In October of 2022, an assessment was carried out to see whether the TOGG tool, which had been taken from the band, would be able to live up to the requirements. It has been decided that the vehicle is built for a range of between 300 and 500 kilometers on a single charge using lithium-ion batteries, and the anticipated criteria are that the batteries must be able to charge to 80% in less than thirty minutes. The development of sophisticated technology across a wide range of fields is required to bring fully autonomous driving to the TOGG vehicle. The domestic vehicle, which is equipped with sophisticated driver assistance systems and can get software updates from the internet, is meant to be ready for the technologies required for level 3 autonomous driving.

TOGG, especially in the context of consumer ethnocentrism, should be considered a positive initiative that will enable the adoption of EVs in the market and increase their sales, thus contributing to the country's economy and reducing the environmental pollution. For the vehicle to make a good entry into the sector and ensure its permanence, it should be developed by protecting the technology that can compete with rival imported goods, and the ethnocentric approaches of the consumers should be evaluated as a positive motivating factor in the marketing and sales processes. When supported by legal regulations and economic incentives, Turkey's domestic and national vehicle TOGG has the potential to become an important player in the electric vehicle industry. As a result, Turkey's automobile will always take its place in the internet with its connected infrastructure and will not need a different device to connect to the internet. The car will be in communication with all smart city infrastructure, electrical grid, devices, houses and buildings and will turn into a thinking assistant for its user in many different areas of life. In the coming years, especially with the spread of 5G technology, the connected automobile will become the center of smart life, and new services that will arise within the

mobility ecosystem will provide a different mobility experience that adds value and facilitates the lives of users.

## REFERENCES

- [1] L. Wang, V. Nian, H. Li, & Yuan, J. "Impacts of electric vehicle deployment on the electricity sector in a highly urbanised environment". *Journal of Cleaner Production*, 295, 126386, (2021).
- [2] Y. Luo, Y. Wu, Li, B., Mo, T., Li, Y., Feng, S. P., ... & Chu, P. K. "Development and application of fuel cells in the automobile industry". *Journal of Energy Storage*, 42, 103124, 2021.
- [3] A. Ajanovic, A. Glatt, & R. Haas, "Prospects and impediments for hydrogen fuel cell buses. *Energy*", 235, 121340, 2021.
- [4] V. Vaideeswaran, M. Ragul, V. Keerthana, & M. Prathiksha, "Review on Selection of Battery Packs for Pure Electric Vehicles and Technical Comparison of Battery Packs". 2021 *Innovations in Power and Advanced Computing Technologies (i-PACT)*, pp.1-6, 2021.
- [5] J. C. Ho, & Y. H. S. Huang, "Evaluation of electric vehicle power technologies: Integration of technological performance and market preference". *Cleaner and Responsible Consumption*, 5, 100063, (2022).
- [6] Yilmaz, M. "The Prediction of Electrical Vehicles' Growth Rate and Management of Electrical Energy Demand in Turkey." 2017 Ninth annual IEEE green technologies conference (GreenTech). IEEE, 2017.
- [7] S. Manzetti, & F. Mariasiu, "Electric vehicle battery technologies: From present state to future systems". *Renewable and Sustainable Energy Reviews*, 51, 1004-1012, 2015.
- [8] A. Fotouhi, Auger, D. J., Propp, K., Longo, S., & Wild, M. "A review on electric vehicle battery modelling: From Lithium-ion toward Lithium-Sulphur." *Renewable and Sustainable Energy Reviews*, 56, 1008-1021, 2016).
- [9] A. E. Aliasand, & Josh, F. T. "Selection of motor foran electric vehicle: A review." *Materials Today: Proceedings*, 24, 1804-1815., 2020.
- [10] M. L. De Klerk, & Saha, A. K. "A comprehensive review of advanced traction motor control techniques suitable for electric vehicle applications". *IEEE Access*, 9, 125080-125108, (2021).
- [11] A. Ahmad, Z. A. Khan, Saad Alam, M., & Khateeb, S. "A review of the electric vehicle charging techniques, standards, progression, and evolution of EV technologies in Germany". *Smart Science*, 6(1), 36-53, (2018).
- [12] X. Sun, Z. Li, X. Wang, & Li, C. "Technology development of electric vehicles: A review". *Energies*, 13(1), 90, (2019).
- [13] G. Wu, X. Zhang, & Z. Dong, "Powertrain architectures of electrified vehicles: Review, classification and comparison". *Journal of the Franklin Institute*, 352(2), 425-448, (2015).
- [14] Ş. İnre, F. Cantez & D. Çelebi, "The Adoption Of Electric Vehicles In Turkey: A Multi-Level Perspective." *Proceedings Book*, 121, (2019).
- [15] Y. Gao, C. Duan, Oliveira, A. A., Ginart, A., Farley, K. B., & Tse, Z. T. H. "3-D coil positioning based on magnetic sensing for wireless EV charging." *IEEE Transactions on Transportation Electrification*, 3(3), 578-588, (2017).
- [16] V. P. Galigekere, J. Pries, O. C. Onar, G. J. Su, Anwar, S., Wiles, R., & J. Wilkins, "Design and implementation of an optimized 100 kW stationary wireless charging system for EV battery recharging". In 2018 *IEEE Energy Conversion Congress and Exposition (ECCE)* (pp. 3587-3592). IEEE, (2018).
- [17] A., Ahmad, Alam, M. S., & Chabaan, R. "A comprehensive review of wireless charging technologies for electric vehicles." *IEEE transactions on transportation electrification*. 4(1), 38-63, (2017).
- [18] M. Amjad, Farooq-i-Azam, M., Ni, Q., Dong, M., & Ansari, E. A. "Wireless charging systems for electric vehicles." *Renewable and Sustainable Energy Reviews*, 167, 112730, (2022).
- [19] C. Panchal, S. Stegen & J. Lu, Review of static and dynamic wireless electric vehicle charging system. *Engineering science and technology, an international journal*, 21(5), 922-937, (2018).
- [20] T. Campi, Cruciani, S., De Santis, V., Maradei, F., & Feliziani, M. "EMC and EMF safety issues in wireless charging system for an electric vehicle (EV)." In 2017 *International Conference of Electrical and Electronic Technologies for Automotive* (pp. 1-4). IEEE, (2017).
- [21] Y. Gao, Farley, K. B., Ginart, A., & Z. T. H. "Tse, Safety and efficiency of the wireless charging of electric vehicles." *Proceedings of the Institution of Mechanical Engineers, Part D: Journal of Automobile Engineering*, 230(9), 1196-1207, (2016).

- [22] M. I. Hasan, Mukta, N. A., Islam, M. M., Chowdhury, A. M. S., & Ismail, M. "Evaluation of fuel properties of Sal (*Shorea robusta*) seed and Its oil from their physico-chemical characteristics and thermal analysis". *Energy Sources, Part A: Recovery, Utilization, and Environmental Effects*, 1-12, (2020).
- [23] P. Machura, & Li, Q. "A critical review on wireless charging for electric vehicles". *Renewable and Sustainable Energy Reviews*, 104, 209-234, (2019).
- [24] O. Elma, "A dynamic charging strategy with hybrid fast charging strategy for electric vehicles. *Energy*, 202, 117680, 2020.
- [25] Y. Zheng, & Jian, L. "Smart charging algorithm of electric vehicles considering dynamic charging priority." In 2016 IEEE International Conference on Information and Automation (ICIA) (pp. 555-560). IEEE, (2016).
- [26] J. Hu, Li, J., Hu, Z., Xu, L., & Ouyang, M. Power distribution strategy of a dual-engine system for heavy-duty hybrid electric vehicles using dynamic programming. *Energy*, 215, 118851, (2021).
- [27] Celikel, R., M.Yilmaz, and A. Gundogdu. "A voltage scanning-based MPPT method for PV power systems under complex partial shading conditions." *Renewable Energy* 184 (2022): 361-373.
- [28] Jawad, M., Qureshi, M. B., Ali, S. M., Shabbir, N., Khan, M. U. S., Aloraini, A., & Nawaz, R. (2020). A cost-effective electric vehicle intelligent charge scheduling method for commercial smart parking lots using a simplified convex relaxation technique. *Sensors*, 20(17), 4842.
- [29] Yilmaz, M. "Real measure of a transmission line data with load fore-cast model for the future." *Balkan Journal of Electrical and Computer Engineering* 6.2 (2018): 141-145.
- [30] Sun, X. H., Yamamoto, T., & Morikawa, T. (2015). Charge timing choice behaviour of battery electric vehicle users. *Transportation Research Part D: Transport and Environment*, 37, 97-107.
- [31] Arooj, A., Farooq, M. S., Akram, A., Iqbal, R., Sharma, A., & Dhiman, G. (2022). Big data processing and analysis in internet of vehicles: architecture, taxonomy, and open research challenges. *Archives of Computational Methods in Engineering*, 29(2), 793-829.
- [32] Liu, C., & Ke, L. (2022). Cloud assisted Internet of things intelligent transportation system and the traffic control system in the smart city. *Journal of Control and Decision*, 1-14.
- [33] Tahir, M. N., & Katz, M. (2022). Performance evaluation of IEEE 802.11 p, LTE and 5G in connected vehicles for cooperative awareness. *Engineering Reports*, 4(4), e12467.
- [34] Zhu, T., Ji, G., Jiang, G., Ding, Y., Feng, J., & Wang, C. (2021). Comparing and Analysis of Test and Evaluation Methods for Connected Vehicle Communication Antenna System. In *Journal of Physics: Conference Series* (Vol. 2108, No. 1, p. 012007). IOP Publishing.
- [35] Mihailescu, M. I., Nita, S. L., & Rogobete, M. G. (2021). Authentication Protocol for Intelligent Cars using Fog Computing and Software-Defined Networking. In 2021 13th International Conference on Electronics, Computers and Artificial Intelligence (ECAI) (pp. 1-6). IEEE.
- [36] Kong, X., Wang, K., Hou, M., Hao, X., Shen, G., Chen, X., & Xia, F. (2021). A federated learning-based license plate recognition scheme for 5G-enabled internet of vehicles. *IEEE Transactions on Industrial Informatics*, 17(12), 8523-8530.
- [37] Zhou, H., Xu, W., Chen, J., & Wang, W. (2020). Evolutionary V2X technologies toward the Internet of vehicles: Challenges and opportunities. *Proceedings of the IEEE*, 108(2), 308-323.
- [38] Vadi, S., Bayindir, R., Colak, A. M., & Hossain, E. (2019). A review on communication standards and charging topologies of V2G and V2H operation strategies. *Energies*, 12(19), 3748.
- [39] Wang, Y., Sheikh, O., Hu, B., Chu, C. C., & Gadh, R. (2014). Integration of V2H/V2G hybrid system for demand response in distribution network. In 2014 IEEE International Conference on Smart Grid Communications (SmartGridComm) (pp. 812-817). IEEE.
- [40] Shin, H., & Baldick, R. (2016). Plug-in electric vehicle to home (V2H) operation under a grid outage. *IEEE Transactions on Smart Grid*, 8(4), 2032-2041.
- [41] Tur, M. R., Colak, İ., & Bayindir, R. (2018). Effect of faults in solar panels on production rate and efficiency. In 2018 International Conference on Smart Grid (icSmartGrid) (pp. 287-293). IEEE.
- [42] Wadi, M., Baysal, M., Shobole, A., & Tur, M. R. (2018). Reliability evaluation in smart grids via modified Monte Carlo simulation method. In 2018 7th International Conference on Renewable Energy Research and Applications (ICRERA) (pp. 841-845). IEEE.
- [43] Shobole, A., Wadi, M., Tür, M. R., & Baysal, M. (2017). Real time active power control in smart grid. In 2017 IEEE 6th International Conference on Renewable Energy Research and Applications (ICRERA) (pp. 585-590). IEEE.
- [44] Shobole, A., Ali, M. H., Wadi, M., & Tür, M. R. (2019). Overview of big data in smart grid. In 2019 8th International Conference on Renewable Energy Research and Applications (ICRERA) (pp. 1022-1025). IEEE.
- [45] Wadi, M., Shobole, A., Tur, M. R., & Baysal, M. (2018). Smart hybrid wind-solar street lighting system fuzzy based approach: Case study Istanbul-Turkey. In 2018 6th International Istanbul Smart Grids and Cities Congress and Fair (ICSG) (pp. 71-75). IEEE.
- [46] Tur, M. R., & Bayindir, R. (2019). Project surveys for determining and defining key performance indicators in the development of smart grids in energy systems. *International Journal of Smart Grid*, 3(2), 103-107.
- [47] Tur, M. R., & Bayindir, R. (2019). A review of active power and frequency control in smart grid. In 2019 1st Global Power, Energy and Communication Conference (GPECOM) (pp. 483- 488). IEEE.
- [48] Savio, D. A., Juliet, V. A., Chokkalingam, B., Padmanaban, S., Holm-Nielsen, J. B., & Blaabjerg, F. (2019). Photovoltaic integrated hybrid microgrid structured electric vehicle charging station and its energy management approach. *Energies*, 12(1), 168.
- [49] Islam, S., Iqbal, A., Marzband, M., Khan, I., & Al-Wahedi, A. M. (2022). State-of-the-art vehicle-to-everything mode of operation of electric vehicles and its future perspectives. *Renewable and Sustainable Energy Reviews*, 166, 112574.
- [50] Bejgam, R. (2021). Brief Study and Review on the Next Revolutionary Autonomous Vehicle Technology. In 2021 International Conference on Advance Computing and Innovative Technologies in Engineering (ICACITE) (pp. 34-37). IEEE.
- [51] Sharma, B., & Noida, G. (2021). Online classes experience among students during lockdown. *The Online Journal of Distance Education and e-Learning*, 9(2), 247-254.
- [52] Williams, B. (2021). *Automated Vehicles and MaaS: Removing the Barriers*. John Wiley & Sons.
- [53] Péter, G., Kiss, B., & Tihanyi, V. (2019). Vision and odometry based autonomous vehicle lane changing. *ICT Express*, 5(4), 219-226.
- [54] Esfahani, M. A., Wang, H., Wu, K., & Yuan, S. (2019). AbolDeepIO: A novel deep inertial odometry network for autonomous vehicles. *IEEE Transactions on Intelligent Transportation Systems*, 21(5), 1941-1950.
- [55] Zhang, Y., Sun, H., Zhou, J., Pan, J., Hu, J., & Miao, J. (2020). Optimal vehicle path planning using quadratic optimization for baidu apollo open platform. In 2020 IEEE Intelligent Vehicles Symposium (IV) (pp. 978-984). IEEE.
- [56] Ersal, T., Kolmanovsky, I., Masoud, N., Ozay, N., Scruggs, J., Vasudevan, R., & Orosz, G. (2020). Connected and automated road vehicles: state of the art and future challenges. *Vehicle system dynamics*, 58(5), 672-704.
- [57] Mo, T., Li, Y., Lau, K. T., Poon, C. K., Wu, Y., & Luo, Y. (2022). Trends and Emerging Technologies for the Development of Electric Vehicles. *Energies*, 15(17), 6271.
- [58] 2021 International Council on Clean Transportation, <https://www.ccacoalition.org/en/partners/international-council-clean-transportation-icct>
- [59] Öztürk, S., Taşçı, B. (2019). Son dakika... Yerli otomobil tanıtıldı! İşte ilk fotoğraflar (Last minute... Domestic car introduced! Here are the first photos). *Hurriyet.com.tr*.
- [60] Ertunç, M. A. (2019). Yerli otomobil tanıtıldı! İşte tüm özellikleri. (Domestic car introduced! Here are all the features). *ShiftDelete.net*. Archived from the original on 9 August 2020.
- [61] Peter Mock and Zifei Yang. A 2022 Update On Electric Car Sales: China Taking The Lead, The U.S. Catching Up, And Europe Falling Behind, August 19, 2022
- [62] Hossain, M. S., Kumar, L., El Haj Assad, M., & Alayi, R. (2022). Advancements and future prospects of electric vehicle technologies: a comprehensive review. *Complexity*, 2022.
- [63] Kocagöz, E., İğde, Ç. S., & Çetindağ, G. (2020). Elektrikli ve akıllı, yerli ve milli: Türkiye'nin Otomobili Girişim Grubu'nun tanıttığı araçlara yönelik tüketicilerin ilk değerlendirmeleri (Electric and smart, domestic and national: Consumers' first evaluations of the vehicles introduced by Turkey's Automobile Initiative Group). *Erciyes University Journal of the Social Sciences Institute*, (49), 55-74.



- [64] Turkish Statistical Institute (2020). Road Motor Vehicles, November 2020. Retrieved from <https://turkstatweb.tuik.gov.tr/PreHaberBultenleri.do?id=33938>.
- [65] Guo, X., & Bunchapattanasakda, C. (2020). Impacts of Consumer Ethnocentrism on Purchasing Intention of Electric Vehicles: A Case Study of Henan Province, China. *International Business Research*, 13(3), 1-59.
- [66] Li, W. K., & Wyer Jr, R. S. (1994). The role of country of origin in product evaluations: Informational and standard-of-comparison effects. *Journal of Consumer psychology*, 3(2), 187-212.
- [67] Balabanis, G., & Siamagka, N. T. (2017). Inconsistencies in the behavioural effects of consumer ethnocentrism: The role of brand, product category and country of origin. *International Marketing Review*, 34(2), 166-182.
- [68] Herche, J. (1992). A note on the predictive validity of the CETSCALE. *Journal of the Academy of Marketing Science*, 20(3), 261-264.
- [69] Wel, C. A. C., Alam, S. S., Khalid, N. R., & Mokhtaruddin, S. A. (2018). Effect of Ethnocentrism and Patriotism on the buying intention of Malaysian National Car. *Jurnal Pengurusan*, 52, 169-179.
- [70] Björck, L., & Lu, M. (2019). Consumer Perception of Brand Image: Country of Origin and Country of Ownership in Electric Vehicle Brands.
- [71] Khazaei, H. (2019). The influence of personal innovativeness and price value on intention to use of electric vehicles in Malaysia. *European Online Journal of Natural and Social Sciences*, 8(3), pp-483.
- [72] Morton, C., Anable, J., & Nelson, J. D. (2016). Exploring consumer preferences towards electric vehicles: The influence of consumer innovativeness. *Research in transportation business & management*, 18, 18-28.
- [73] Asadi, S., Nilashi, M., Samad, S., Abdullah, R., Mahmoud, M., Alkinani, M. H., & Yadegaridehkordi, E. (2021). Factors impacting consumers' intention toward adoption of electric vehicles in Malaysia. *Journal of Cleaner Production*, 282, 124474.
- [74] Tu, J. C., & Yang, C. (2019). Key factors influencing consumers' purchase of electric vehicles. *Sustainability*, 11(14), 3863.
- [75] Schuitema, G., Anable, J., Skippon, S., & Kinnear, N. (2013). The role of instrumental, hedonic and symbolic attributes in the intention to adopt electric vehicles. *Transportation Research Part A: Policy and Practice*, 48, 39-49.
- [76] Egbue, O., & Long, S. (2012). Barriers to widespread adoption of electric vehicles: An analysis of consumer attitudes and perceptions. *Energy policy*, 48, 717-729.
- [77] Vandecasteele, B., & Geuens, M. (2010). Motivated consumer innovativeness: Concept, measurement, and validation. *International Journal of Research in Marketing*, 27(4), 308-318.
- [78] Akin, M., Çiçek, R., Gurbuz, E., & İnal, M. E. (2009). Tüketici Etnosentrizmi ve Davranış Niyetleri Arasındaki Farklılığın Belirlenmesinde CETSCALE Ölçeği. (The CETSCALE Scale in Determining the Difference Between Consumer Ethnocentrism and Behavioural Intentions) *Ege Academic Review*, 9(2), 489-512.
- [79] Erdogan, B. Z., & Uzkurt, C. (2010). Effects of ethnocentric tendency on consumers' perception of product attitudes for foreign and domestic products. *Cross Cultural Management: An International Journal*.
- [80] Acikdilli, G., Ziemnowicz, C., & Bahhouh, V. (2018). Consumer ethnocentrism in Turkey: Ours are better than theirs. *Journal of International Consumer Marketing*, 30(1), 45-57.
- [81] Zeren, D., Kara, A., & Arango Gil, A. (2020). Consumer ethnocentrism and willingness to buy foreign products in emerging markets: Evidence from Turkey and Colombia. *Latin American Business Review*, 21(2), 145-172.
- [82] Ö. Gönül, , A. C. Duman, & Ö. Güler, Electric vehicles and charging infrastructure in Turkey: An overview. *Renewable and Sustainable Energy Reviews*, 143, 110913, (2021).
- [83] M. Aktan, Kamuoyunun Yerli Otomobil Projesini Algısı. *Öneri Dergisi*, 10(39), 1-9, (2013).
- [84] İbrahim, A. V. C. I. "Yerli Markalı Otomobil Satın Alma Niyetinde Etnosentrizm, Ülke İmajı ve Yenilikçiliğin Etkisi: Türkiye'nin Otomobili (TOGG) Bağlamında Bir Araştırma" (The Effect of Ethnocentrism, Country Image and Innovation on Intention to Buy Domestic Branded Cars: A Study in the Context of Turkey's Automobile (Togg)). *Bingöl University Journal of the Social Sciences Institute*, (20), 439-466. (2020).
- [85] C. F. Calvillo, Sánchez-Mirallas, A., & Villar, J. "Energy management and planning in smart cities". *Renewable and Sustainable Energy Reviews*, 55, 273-287., 2016.
- [86] C. F. Calvillo, Sánchez-Mirallas, A., Villar, J., & Martín, F., "Impact of EV penetration in the interconnected urban environment of a smart city." *Energy*, 141, 2218-2233, 2017

## BIOGRAPHIES



**HAFIZE NURGUL DURMUS SENYAPAR** In 2005, she obtained her master's degree in communication studies from Ankara University in Ankara, Turkey. In 2012, she earned her doctorate from Gazi University with a dissertation on critical discourse analysis. She completed her undergraduate education in the departments of business and communication and is currently pursuing a third undergraduate degree in health management. As a necessary prerequisite for health, she continues her research on environmental sustainability and the social elements of green energy. She conducts multidisciplinary research to provide a new perspective on topics such as the health co-benefits of renewable energy resources, consumer approaches, incentive mechanisms for economic and social support of green energy transformation, and consumer attitudes and intentions against new and environmentally friendly technologies. She teaches Management and Organization, Quality and Strategic Management, Health Communication, and Social Psychology at Gazi University. At Gazi University, she serves as an assistant quality coordinator.



**MEHMET RIDA TUR** (M'05–SM'10–Ph.D'18) B.S. He received his Master's degree from Marmara University, Istanbul, Turkey in electrical engineering in 2005 and in electrical and electronics engineering from Fırat University, Institute of Science and Technology in 2008. He received his PhD degree from Yıldız Technical University in 2018 with

his thesis on Power Systems. He worked as an Instructor at Mardin Artuklu University Technical Programs from 2010 to 2019. From 2010 to 2019, he held various positions in Artuklu University Electricity and Energy Departments, especially as the Head of the Department. Since 2019, he has been appointed to the Department of Electricity and Energy at Batman University and is still working as an Associate Professor and Head of the Department. He has many books, one of which is the co-author of *Electric Energy in Turkey* (Seta, 1st edition, 2017). He has close to one hundred publications and has worked in power engineering on many different aspects of his career, due to his interest in applying economic analysis and quality methods in power systems. The focus of his career has been public service delivery systems. He is a member of the International Conference on Renewable Energy Research and IEEE Applications committee. His main areas of interest are protection-reliability, power systems quality, power systems economics, renewable energy systems and smart grids.



# Classification of Precancerous Colorectal Lesions via ConvNeXt on Histopathological Images

Mehmet Nergiz


**Abstract**—In this translational study, the classification of precancerous colorectal lesions is performed by the ConvNeXt method on MHIST histopathological imaging dataset. The ConvNeXt method is a modernized ResNet-50 architecture having some training tricks inspired by Swin Transformers and ResNeXt. The performance of the ConvNeXt models are benchmarked on different scenarios such as ‘full data’, ‘gradually increasing difficulty based data’ and ‘k-shot data’. It is shown that the ConvNeXt model outperforms almost all the other studies in the literature which are applied on MHIST by using ResNet models, vision transformers, weight distillation, self-supervised learning and curriculum learning strategy based on different scenarios and metrics. The ConvNeXt model trained with ‘full data’ yields the best result with the score of 0.8890 for accuracy, 0.9391 for AUC, 0.9121 for F1 and 0.7633 for cohen’s kappa. The power of ConvNeXt is found as promising for classifying precancerous histopathological images and may be a good base line for miscellaneous tasks of computational pathology field with respect to the classical convolutional neural networks and vision transformers..

**Index Terms**—ConvNeXt, CNN, Vision Transformer, Colorectal Cancer, Histopathology.

## I. INTRODUCTION

COLORECTAL CANCER is the reported as the world’s third most common cancer type and it’s at the fourth rank in terms fatality whereas there are only 3.94 pathologists per 100000 people in United States [1]–[3]. As a result of this imbalanced burden, classifying colorectal polyps which grow inside the colon lining and may transform to colonic cancer if not treated early enough is one of the time and energy consuming tasks in pathology [4]. The classification task of the colorectal polyps in which the inter-rater variability is significantly high mainly targets to identify hyperplastic polyps (HPs) and sessile serrated adenomas (SSAs) which are respectively benign and precancerous lesions to be treated immediately [4].

MEHMET NERGİZ, is with Department of Computer Engineering University of Dicle, Diyarbakır, Turkey, (e-mail: [mnergiz@dicle.edu.tr](mailto:mnergiz@dicle.edu.tr)).

 <https://orcid.org/0000-0002-0867-5518>

Manuscript received January 21, 2023; accepted February 23, 2023.  
DOI: [10.17694/bajece.1240284](https://doi.org/10.17694/bajece.1240284)

The sort of challenges like high-resolution and variable size images as well as costly annotations which do not have clear guidelines constitute a barrier for the researchers that have limited resources to enter the field and apply different approaches and deep learning models. In order to lower that barrier, Wei et al. proposed MHIST which is planned to be an environment where different deep learning models to be benchmarked easily and then applied to large scale datasets acting just like a petri dish for histopathology image analysis [4], [5]. MHIST by having a limited amount of images can be classified as having a low data regime and is also a good fit for benchmarking few-shot learning which is a concept to define the ability of a machine learning model to learn from a restricted amount of data [6], [7]. The idea of few-shot learning on histopathology imaging is worth to be analyzed since collecting, preprocessing and annotating steps of this particular medical field is very costly and time consuming [8], [9]. Additionally, the histopathological imaging datasets which will be proposed in the future for different or rare diseases will probably start with a small number of examples and some of the large scaled current state of the art deep learning methods may not be tuned well for them.

This article is organized as follows: Related Works section includes a review of recent works using ConvNeXt method or MHIST imaging dataset. Material section gives the details about the MHIST dataset. Method section explains the details and tricks proposed by the ConvNeXt method. Results section presents the benchmarking scenarios and the obtained results comparatively. Discussion section presents some analyses about the obtained results for each proposed benchmarks and the compares this study with respect to the related literature. Conclusion boils down the results and figures out the future work.

### A. Related Work

In most of the histopathology images, the dissemination and progression of diseases show a gradually increasing pattern and the levels of difficulty of classification changes on time [10]. MHIST has a natural range of difficulty based on the majority voting of the annotation of the pathologists. Thus, Wei et al. applied curriculum learning strategy in which the training examples are presented in an increasing level of difficulty and a better performance is obtained compared to the random sampling of training examples [4], [5], [10]–[12]. More and more, self-supervised learning based approach which exploits and learns from a relatively large scale

unlabeled in domain data and then fine-tuned in downstream data is used by Wang et al., Srinidhi and Martel [12], [13]. ResNet based deep learning models are used as a gold standard Convolutional Neural Networks (CNN) method for MHIST dataset whereas Wang et al. not only utilized CNN but also added a token-aggregating and excitation module and a transformer to their model [13]. Tasdemir et al., applied ConvNeXt models on data the Colorectal Polyps of UniToPatho, EBHI and Kayseri City Hospital [14]. Alternatively, Zhang et al. proposed a cross knowledge transfer among 9 different histopathological image datasets which is basically composed of downstream fine-tuning and weight distillation procedures aiming to increase the performance of vanilla ResNet-18 model [15].

To sum up, this study proposes the following contributions:

- 1- The ConvNeXt models are benchmarked on MHIST and almost all the other methods are outperformed with respect to various evaluation criteria like Accuracy, F1 score, AUC and Cohen's Kappa.
- 2- The ConvNeXt models are benchmarked to the subsets of MHIST having k-shots of images and different levels of difficulties.
- 3- The AUC of the ConvNeXt model on 'full data' scenario is at least 8.53% higher than of the baseline CNNs such as AlexNet, DenseNet, SqueezeNet, Inception v3 and VGG16.

## II. MATERIAL

This dataset is obtained from scanning 328 Formalin Fixed Paraffin-Embedded (FFPE) WSI of colorectal polyp tissues of the patients at the Dartmouth- Hitchcock Medical Center [4]. Each scanned WSI which is scanned by an Aperio AT2 scanner at 40x resolution is diagnosed as sessile serrated adenomas (SSAs) or hyperplastic polyps (HPs) as shown in Fig. 1., 3152 image tiles which are having 224x224 resolution extracted from the obtained images. The permission for releasing and using this dataset is accepted by the Dartmouth-Hitchcock Health IRB [4].

The annotation process is performed by seven board certified gastrointestinal pathologists at the Dartmouth Hitchcock Medical Center [4]. Each histopathological image tile is classified as SSA or HP with respect to World Health Organization criteria from 2019 [16]. The label class of each image is gathered individually from each of the pathologists and the final gold standard labels are assigned based on the majority vote of the seven labels, as commonly performed at the most of the studies in the literature [6]. In this dataset, 16.7% of the images have 4/7 agreement which implies that there is a discordance among the annotators and a nontrivial challenge on the colorectal polyp classification task. The average Cohen's Kappa of the performance of the per-pathologist is 0.45 [17]. In this study, aligned with the other studies, to propose different training scenarios, four different levels of difficulty are defined based on the agreement of the annotators such as: very easy (VE) (7/7 agreement), easy (E) (6/7 agreement), hard (H) (5/7 agreement) and very hard (VH) (4/7 agreement) [17].

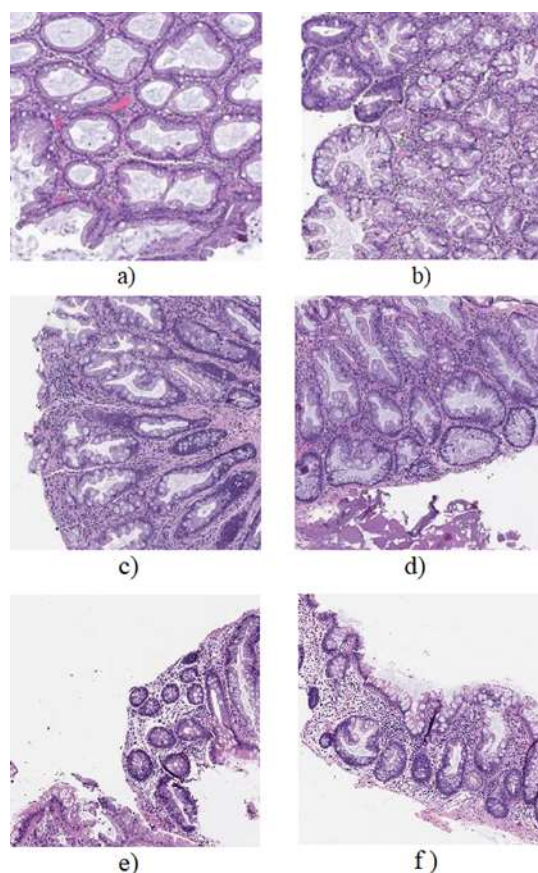


Fig.1. Two characteristic images for both of the classes of MHIST dataset. a) HP (benign) b) SSA (precancerous) c) HP d) SSA

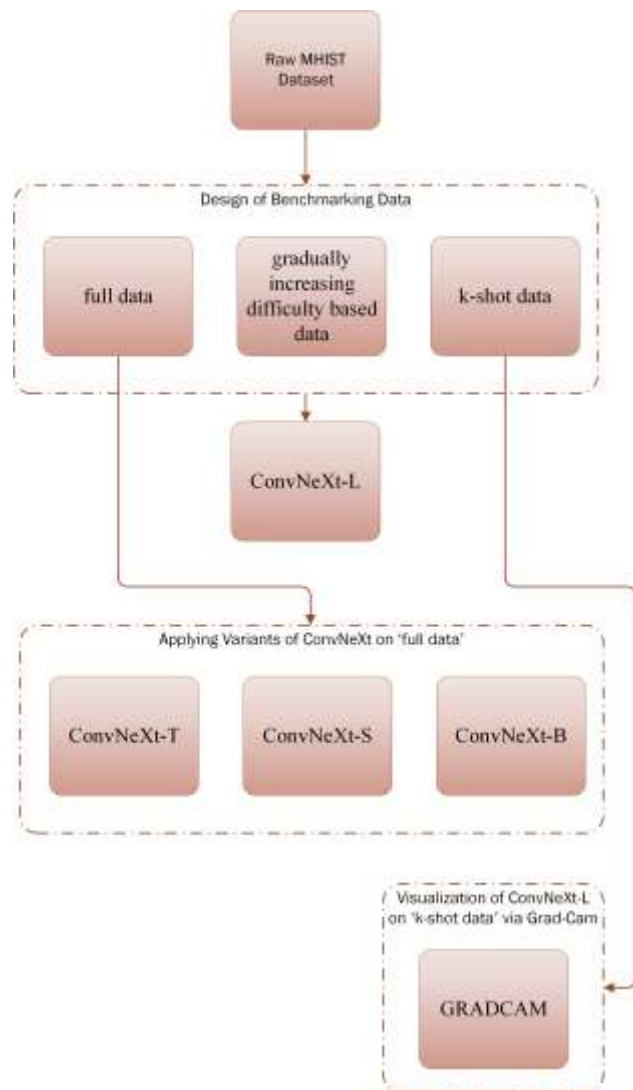
## III. METHOD

The main flowchart of the proposed study is given in Fig. 2. The first procedure is to design benchmarking data for 'full data', 'gradually increasing difficulty based data' and 'k-shot data' and applying ConvNeXt-L to these benchmarking datasets. Then, different variants of ConvNeXt is applied on the 'full data'. Afterwards, the behavior of ConvNeXt is observed on 'k-shot data' by applying Grad-Cam.

### A. ConvNeXt

The Vision Transformer (ViT) based methods have begun to be addressed as one of the best image classifiers since 2020. The ViT methods have no image related inductive bias and are not much different from the Natural Language Processing (NLP) Transformers except for patchifying the input images into a sequence of smaller patches and their global attention design suffers from the quadratic computational complexities during handling high resolution images [18]. The Swin Transformer (ST) methods overcome that computational complexity issue by introducing sliding windows and can easily exceed the standard ResNet

Fig.2. The Main flowchart of the study



models [19]. ConvNeXt method, as a manifestation of ConvNets for 2020s, is the name of the set of pure convolutional methods (ConvNet) modified by taking into account the novel features of ViT and ST [20]. In this study, the ConvNeXt method, which is specifically the implementation of the modernization of the standard ResNet-50 model towards the design of ST methods, is used for the classification of precancerous colorectal lesions on MHIST image dataset [20]. The gradual steps of the modernization of ResNet-50 are outlined in Fig. 3 and explained in detail as below [20]:

### 1) Training procedure

The training procedure of ConvNeXt is similar to ST and Data-Efficient Image Transformers (DeiT) [19]–[21]. The ConvNeXt model used in this study is pretrained on ImageNet-22K for 90 epochs with a warmup of 5 epochs and fine-tuned on ImageNet-1K for 30 epochs with no warmup. AdamW optimizer, cosine learning rate schedule, a learning rate of  $5e-5$ , data augmentation methods like RandAugment, Cutmix, RandomErasing and Mixup [22], and regularization techniques such as Label Smoothing and Stochastic Depth are used [20].

### 2) Macro Design

- **Stage Compute Ratio:** The number of blocks in each stage of ResNet-50 is converted from (3, 4, 6, 3) to (3, 3, 9, 3) like in ST [20].
- **Stem Cell:** The stem cell of standard ResNet which contains a  $7 \times 7$  convolution layer having stride 2 and a max pool is replaced by a patchifying layer using a  $4 \times 4$  non-overlapping, stride 4 convolution [20].

### 3) ResNeXtify

The ResNeXt method, like ViT architectures, has grouped convolution concept in its bottleneck block to separate the spatial and channel mixing. The ConvNeXt method uses depthwise convolution that is a sort of grouped convolution having groups as many as the number of the channels. Additionally, the network width of ConvNeXt is increased from 64 to 96 similar to ResNeXt as shown in Fig. 4 [20], [23].

### 4) Inverted Bottleneck

Each Transformer block is designed as having an inverted bottleneck in which the dimension of the hidden layer is 4 times wider than its input. Inspired by this design, the block shape of ResNet-50 is inverted from a) to b) as in Fig. 4 [20]

### 5) Large Kernel Sizes

- **Moving up depthwise conv layer:** The depthwise conv layer is moved up in order to apply this more complex operation to fewer channels as shown in Fig. 4 b) to c) [20].
- **Increasing the kernel size:** The kernel sizes are increased to  $7 \times 7$  [20].

### 6) Micro Design

- **Changing Rectified Linear Unit (ReLU) with Gaussian Error Linear Unit (GELU):** The ReLU activation functions are replaced with the GELU that is used by the most of the sophisticated Transformers [20].
- **Fewer activation functions:** Except for the one block which is shown in Fig. 5, all the other GeLU layers are removed from the ConvNeXt [20].
- **Fewer normalization layers:** Except for the one layer that is shown in Fig. 5, all the other Batch Normalization (BN) layers are eliminated from the ConvNeXt [20].
- **Substituting BN with Layer Normalization (LN) :** The BN is replaced by the simpler LN that is used in Transformers [20].
- **Separate down sampling layers:** The down sampling strategy of ResNet which is using  $3 \times 3$  convolution layer with stride 2 is changed to a separate  $2 \times 2$  convolution



layer with stride 2 which is plugged between each stage [20].

In this study, the ConvNeXt-L model variant having C = (192; 384; 768; 1536) channels and B = (3; 3; 27; 3) blocks in each stage is used for the classification of precancerous

colorectal lesions on MHIST image dataset with a batch size of 8. The Google Colab environment having Nvidia K80 / T4 GPU, 12 GB Memory and Intel(R) Xeon(R) 2.3 GHz CPU is used for the benchmarking.

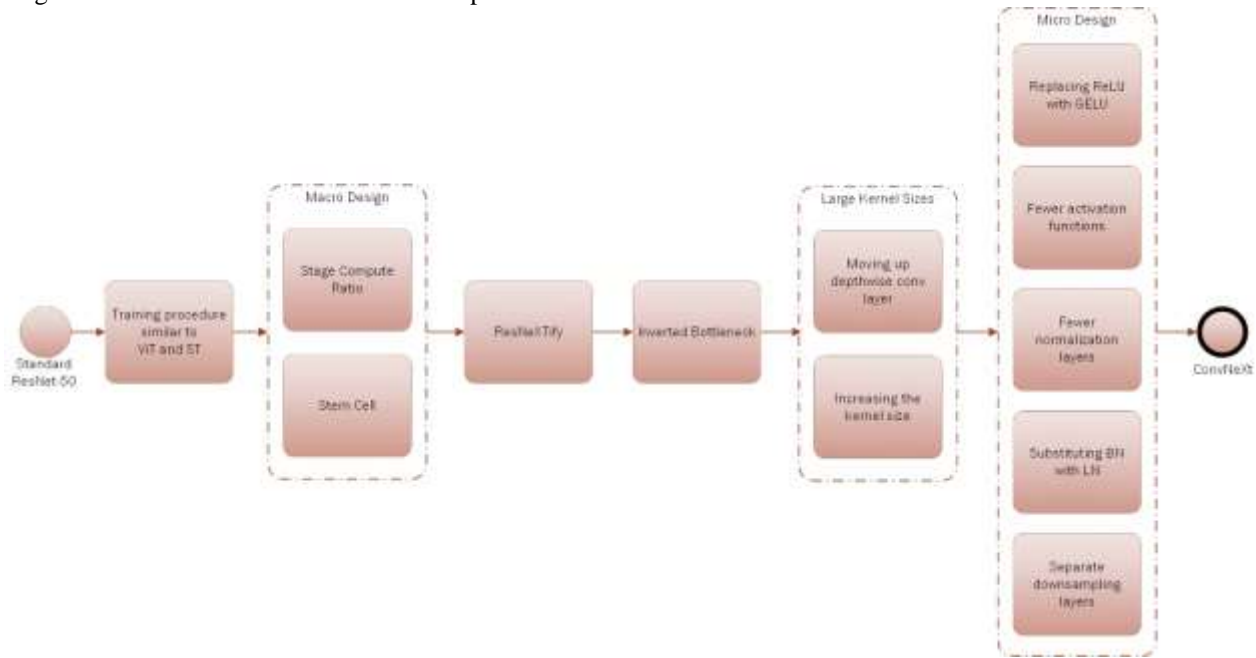


Fig.3. The Modernization Steps of ResNet-50 towards ST to finally get the ConvNeXt model [20]

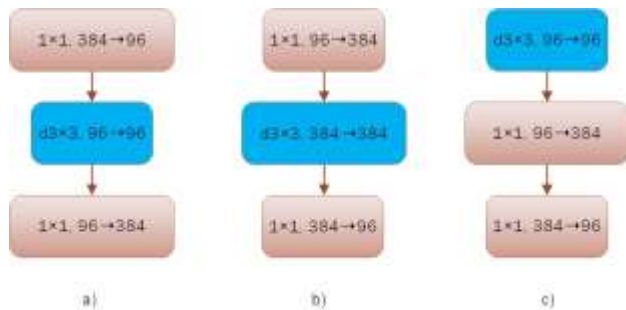


Fig 4. The Bottleneck Inversion and depthwise convolution borrowed from ResNeXt [20], [23] a) ResNeXt block b) Inverted bottleneck block c) Moved up depthwise spatial convolution block

Fig.5. Block and layer architectures of ResNet, ST and ConvNeXt models [19], [20], [23]

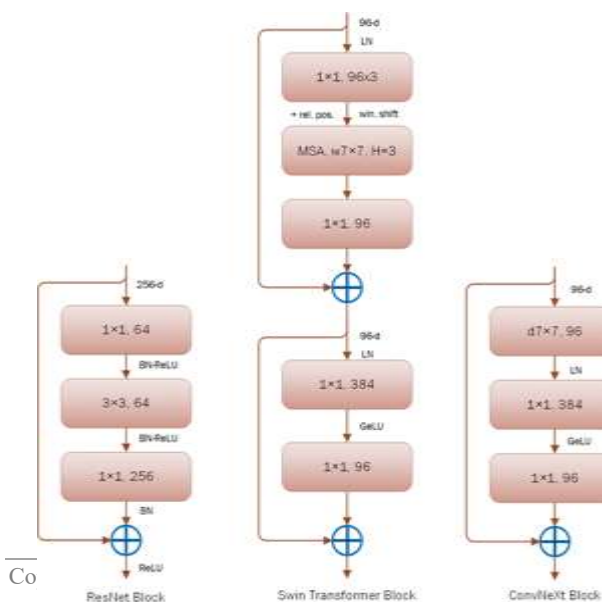
IV. RESULT

In this study, three different benchmarking scenarios such as ‘full data’, ‘gradually increasing difficulty based data’ and ‘k-shot data’ are proposed and the results of ConvNeXt method are shared in Table 1-3. The ‘full data’ scenario is based on using the whole training and testing data as originally provided by MHIST dataset. The ‘gradually increasing difficulty based data’ scenario is set as constituting new data subsets from the original training data by firstly including only VE level data and then adding E, H and VH levels respectively. The ‘k-shot data’ scenario is proposed as the subsets of the original dataset having only k members for each image class. The results of Baseline CNN models using ‘full data’ such as AlexNet, DenseNet, SqueezeNet, Inception v3 and VGG16 are given in Table 4 and Fig. 13. The confusion matrices of k-shots data results and ROC AUC curves of gradually increasing difficulty based data are given in Fig. 10 and 11. The different variants of ConvNeXt is applied on the ‘full data’ and its results are given in Fig. 12 and Table 5.

TABLE I  
ConvNeXt BENCHMARKING ON ‘FULL DATA’

Max ACC	Max F1	Max Cohen Kappa	Max ROC-AUC
0,8890	0,9121	0,7633	0,9391

TABLE II





ConvNeXt BENCHMARKING ON 'K-SHOT DATA'				
K-SHOT	Max ACC	Max F1	Max Cohen Kappa	Max ROC-AUC
40	0,7052	0,7377	0,4128	0,8101
100	0,7554	0,7805	0,5151	0,8617

400 0,7861 0,8088 0,5750 0,8941

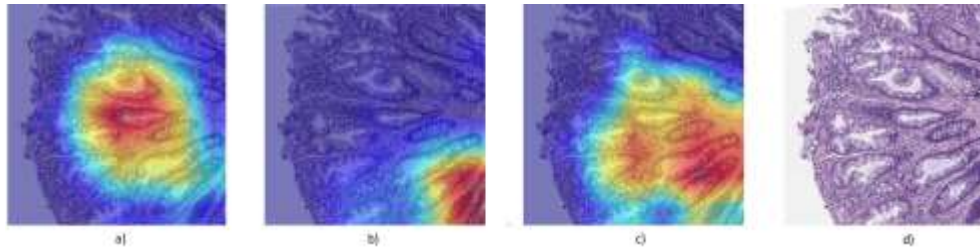


Fig. 6 Grad-Cam Visualizations of positive predictions of ConvNeXt model on an image selected as HP by 7 annotators. a) 40-shots b) 100-shots c) 400-shots d) Original Image

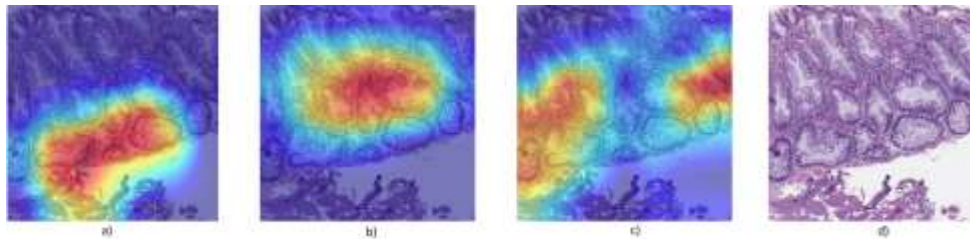


Fig. 7 Grad-Cam Visualizations of negative predictions of ConvNeXt model on an image selected as SSA by 6 annotators. a) 40-shots b) 100-shots c) 400-shots d) Original Image

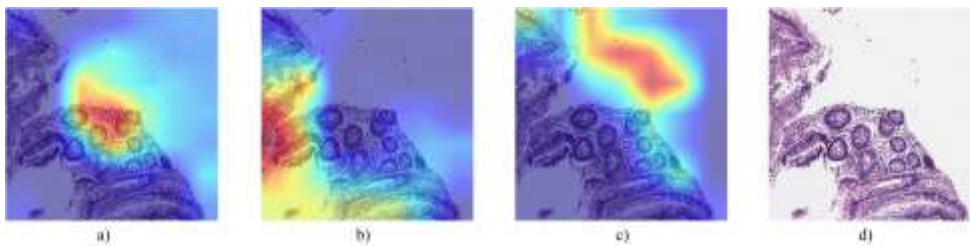


Fig. 8 Grad-Cam Visualizations of positive predictions of ConvNeXt model on an image selected as HP by 5 annotators. a) 40-shots b) 100-shots c) 400-shots d) Original Image

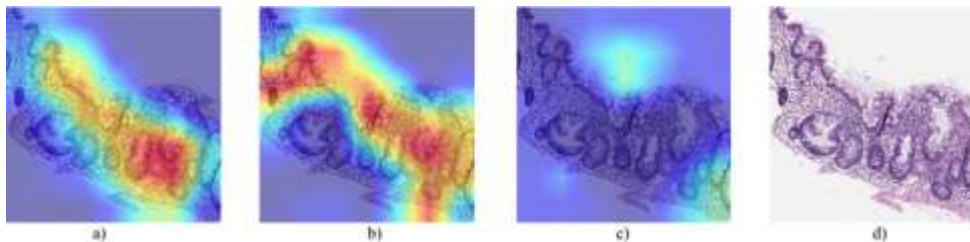


Fig. 9 Grad-Cam Visualizations of positive predictions of ConvNeXt model on an image selected as SSA by 7 annotators. a) 40-shots b) 100-shots c) 400-shots d) Original Image

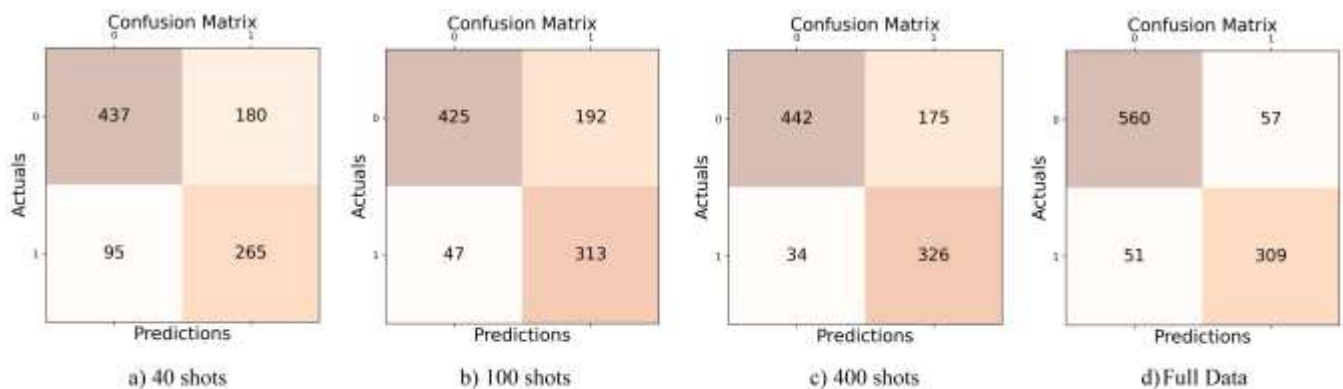


Fig. 10. The Confusion Matrices of ConvNeXt on k-shots data and 'full data' scenarios. a) 40 shots b) 100 shots c) 400 shots d) Full Data

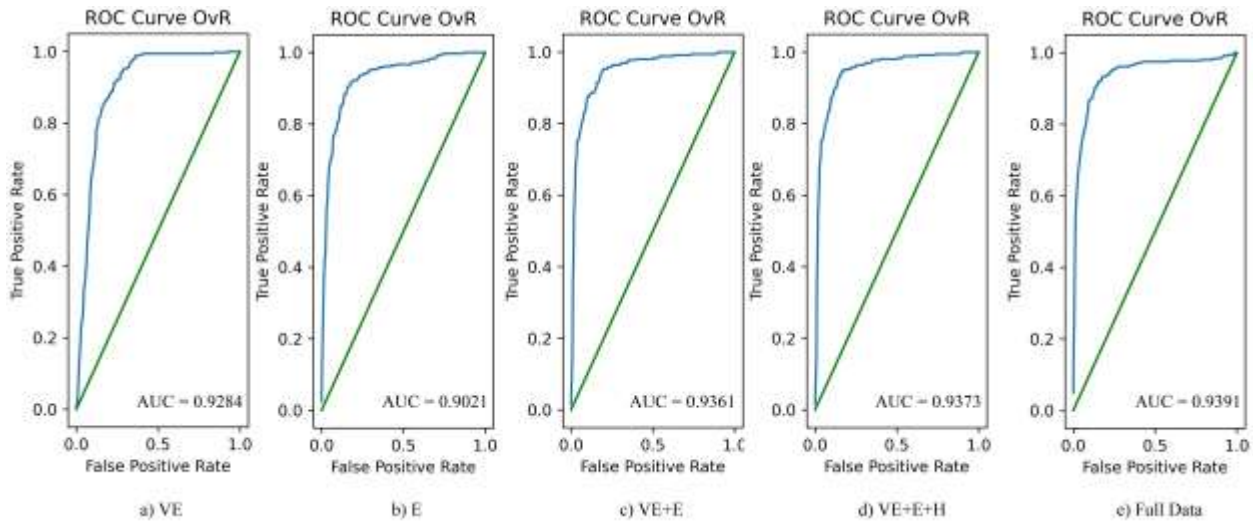


Fig. 11. The ROC graphs of ConvNeXt on difficulty based data and ‘full data’ scenarios. a) VE b) E c) VE+E d) Full Data

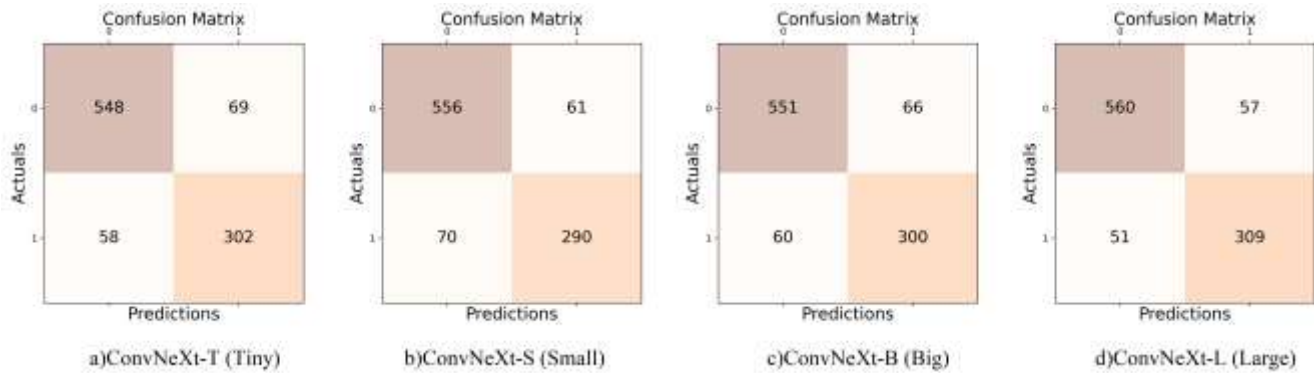


Fig. 12. The Confusion Matrices of different ConvNeXt variants on ‘full data’ scenario. a) Tiny b) Small c) Big d) Large

TABLE III  
ConvNeXt BENCHMARKING ON ‘GRADUALLY INCREASING DIFFICULTY BASED DATA’

DIFF	Max ACC	Max F1	Max Cohen Kappa	Max ROC-AUC
E	0,8690	0,8947	0,7214	0,9284
VE	0,8209	0,8450	0,6372	0,9021
VE+E	0,8843	<b>0,9067</b>	0,7547	0,9361
VE+E+H	0,8865	0,9072	0,7588	0,9373
VE+E+H+VH	0,8890	0,9121	0,7633	0,9391

TABLE IV  
BASELINE CNNs BENCHMARKING ON ‘FULL DATA’

Model	Max ACC	Max F1	Max Cohen Kappa	Max ROC-AUC
AlexNet	0,7292	0,6461	0,3356	0,8243
DenseNet	0,7211	0,6275	0,3081	0,8439
SqueezeNet	0,7005	0,6184	0,2736	0,8049
Inception v3	0,7131	0,6488	0,3346	0,8538
VGG16	0,7041	0,6011	0,2635	0,8268

TABLE V  
ConvNeXt BENCHMARKING ON ‘FULL DATA’ FOR DIFFERENT MODELS

Model	Max ACC	Max F1	Max Cohen Kappa	Max ROC-AUC
Tiny	0,8700	0,8962	0,7225	0,9326
Small	0,8659	0,8946	0,7104	0,9298
Big	0,8710	0,8930	0,7239	0,9305
Large	0,8890	0,9121	0,7633	0,9391

V. DISCUSSION

The comparative table of the state of the art studies applied on MHIST database in literature is summarized on Table 6. The balanced values of ACC, AUC and F1-score values and high Cohen’s Kappa of this study is promising with respect to all related studies. The Kappa metric analysis on the Fig. 7 of Wei et al. states that the average Cohen’s Kappa among the annotations of 7 seven pathologists is 0.45 in the moderate range of 0.41-0.60 [4]. Nearly all the Cohen’s Kappa results of all scenarios and models of this study which are calculated using majority voted ground truth labels and predicted labels as input to the `cohen_kappa_score()` function of sklearn library are over 0.60. Additionally, in this study, 40,100 and 400 shot data settings are curated from all difficulty levels by selecting equally and randomly are shown in Table 2. These results show that the generalization capability of ConvNeXt method on few shot subsets is promising. The 400-shots of not pretrained model of Wei et al. achieved 0.793 whereas the 40-shots of this study achieved 0.8101 for AUC [4]. The 100-shots of pretrained model of Wei et al. achieved 0.837 whereas the 40-shots of this study achieved 0.8617 for AUC [4].

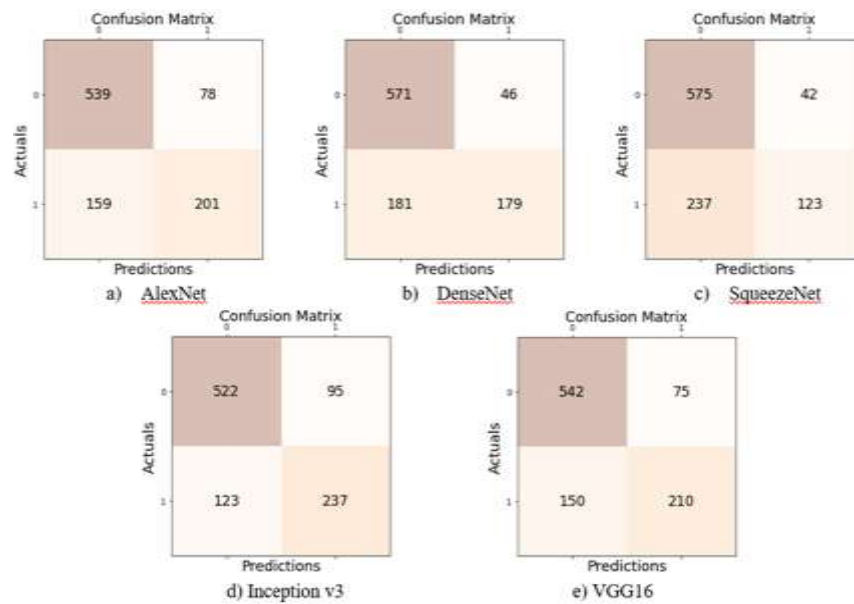


Fig.13. The Confusion Matrices of baseline CNN models on 'full data' scenario

TABLE VI  
COMPARISON OF THIS STUDY AND THE STATE OF ART METHODS  
APPLIED ON MHIST

Study	ACC	AUC	F1	Cohen Kappa	
Wei et. al [5]	-	0,936	-	0,473	
Wei et. al [4]	-	0,927	-	-	
Srinidhi and Martel [12]	0,815	<b>0,887</b>	-	-	
Wei et. al [10]	-	0,862	-	-	
Wang et. al [13]	CNN	0,8095	0,9188	0,7957	-
	CNN+TRANS	0,8302	0,9378	0,8277	-
	CNN+TRANS+TAE	0,8651	<b>0,9476</b>	0,8586	-
Zhang [15]	0,8536	-	-	-	
<b>ConvNeXt (This Study)</b>	<b>0,8890</b>	<b>0,9391</b>	<b>0,9121</b>	<b>0,7633</b>	

This study exceeds the AUC results of the Srinidhi and Martel as can be seen on Table 6. The ConvNeXt model on 'full data' scenario of this study outperforms the AUC of all the ablated model settings of Wang et al. and reached very close to the performance of their best model setting which is 'CNN(ResNet50)+Transformer+TAE module pretrained as SSL' as can be observed in Table 6 (0.9391 versus 0.9188, 0.9378 and 0.9476) [13]. This study outperforms also the ACC and AUC of both pure transformers like ViT and T2T-ViT-24 as well as hybrid CNN-transformer paradigms such as VT-ResNet and BoTNet-50 [13]. On the other hand, it is worth to notice that Wang et al. used millions of histopathology images and trained 100 epochs on 32 Nvidia V100 GPUs during 200 hours. This sort of GPU capacity is very hard to reach for small research groups. On the other hand, this study based on ConvNeXt model can work with very few images and does not have high time complexity.

The superior ACC performance of this study is reasonable and more reliable since the SSA/HP class imbalance ratio of the MHIST dataset is 58%. The performance results and confusion matrices of Baseline CNN methods such as AlexNet, DenseNet, SqueezeNet, Inception v3 and VGG16 models benchmarked on 'full data' scenario are shown in Table 4 and Fig. 13. As it can be clearly understood from the

Table 1 and 4, the AUC value of the ConvNeXt model on 'full data' scenario are 8.53 higher than of the Inception v3 which is reported as the best baseline CNN. The ACC of the ConvNeXt model on 'full data' scenario is 15.98 higher than of the AlexNet as the baseline model having highest accuracy.

The last but not least, the Grad-Cam method is used for visually observing the behavior of the ConvNeXT model in Fig. 6,7,8 and 9 [24]. On the Grad-Cam images, it is observed that the effective regions of the images are more specialized as the number of shots are increased. Additionally, the effective regions of the images are observed as mostly observed as overlapping which supports the consistency of the ConvNeXT model across different shots of images.

The comparison of the change of training losses of the 40, 100 and 400 shots with respect to the full data is shown in Fig. 14. It is observed the loss of the smaller amount of shots starts from higher values as it is expected but they tend to reach to the plateau as the the curve of full data as epoch 40. On the other hand, the comparison of the change of training losses of the VE,E, VE+E and VE+E+H shots with respect to the full data is shown in Fig. 15. It is observed the loss of the easier subsets of the dataset starts from lower values as it is expected but they tend to reach to the plateau as the curve of full data as epoch 40. More comprehensive datasets may give further insights about the ConvNext method.

## VI. CONCLUSION

In this study, the ConvNeXt method is applied on MHIST which is a histopathological imaging dataset having low data regime for the classification of precancerous colorectal lesions. ConvNeXT outperforms the other state of the art methods, which are applied on MHIST with respect to various metrics of different benchmarked training scenarios such as 'full data', 'gradually increasing difficulty based data' and 'k-shot data'. It is observed that the ConvNeXT method is capable of generalization even from a low data regime MHIST histopathological dataset using only limited number



of images. The ConvNeXt method also shows superior performance on the full data with respect to CNNs and ViTs with the score of 0.889, 0.9391, 0.9121 and 0.7633 for accuracy, AUC, F1 and Cohen's kappa. The preferred ConvNeXt-L model is also found as superior with respect to the other variants of ConvNeXt such as Tiny, Small and Big ones in terms of all performance metrics. The ConvNeXt method is found as giving promising results on the computational pathology field and may be used in our future works for different datasets or deep learning based tasks as an alternative to CNNs and ViTs.

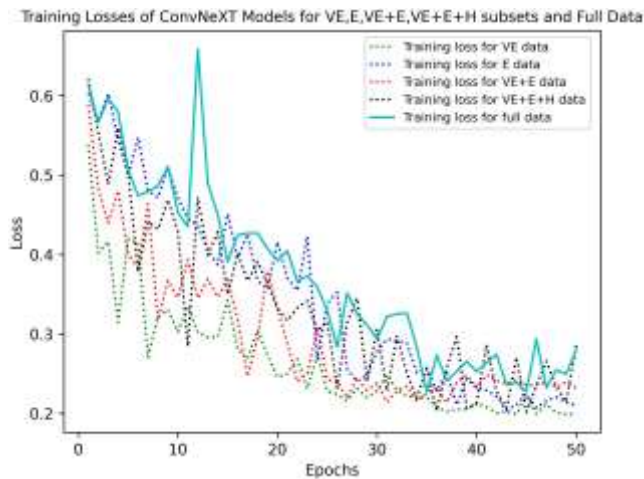


Fig.14. The comparison of the training losses of ConvNeXt models for 40, 100, 400 shots and full data

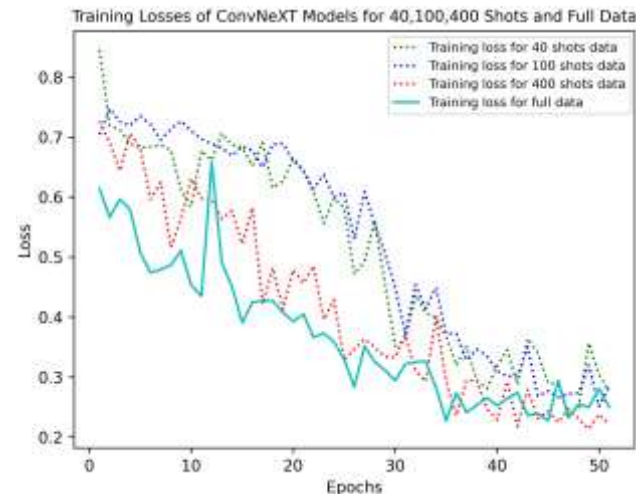


Fig.15. The comparison of the training losses of ConvNeXt models for VE, E, VE+E, VE+E+H subsets and full data

#### ACKNOWLEDGMENT

The author declares no conflict of interest. The dataset analyzed during the current study are provided by the Dartmouth-Hitchcock Health IRB and publically available in the MHIST repository, [https://bmirids.github.io/MHIST/]. This work has been supported by funding from Dicle University (DÜBAP Project No: MÜHENDİSLİK.22.001).

#### REFERENCES

- [1] S. Famitha and M. Moorthi, "Intelligent and novel multi-type cancer prediction model using optimized ensemble learning," *Comput. Methods Biomech. Biomed. Engin.*, 2022, doi: 10.1080/10255842.2022.2081504.
- [2] D. M. Metter, T. J. Colgan, S. T. Leung, C. F. Timmons, and J. Y. Park, "Trends in the us and canadian pathologistworkforces from 2007 to 2017," *JAMA Netw. Open*, vol. 2, no. 5, pp. 1–11, 2019, doi: 10.1001/jamanetworkopen.2019.4337.
- [3] I. Mármol, C. Sánchez-de-Diego, A. P. Dieste, E. Cerrada, and M. J. R. Yoldi, "Colorectal carcinoma: A general overview and future perspectives in colorectal cancer," *Int. J. Mol. Sci.*, vol. 18, no. 1, 2017, doi: 10.3390/ijms18010197.
- [4] J. Wei *et al.*, "A Petri Dish for Histopathology Image Analysis," Jan. 2021, [Online]. Available: <http://arxiv.org/abs/2101.12355>
- [5] J. Wei *et al.*, "Learn like a Pathologist: Curriculum Learning by Annotator Agreement for Histopathology Image Classification," Sep. 2020, [Online]. Available: <http://arxiv.org/abs/2009.13698>
- [6] Y. Wang, Q. Yao, J. T. Kwok, and L. M. Ni, "Generalizing from a Few Examples," *ACM Comput. Surv.*, vol. 53, no. 3, pp. 1–34, 2021, doi: 10.1145/3386252.
- [7] V. Dumoulin *et al.*, "Comparing Transfer and Meta Learning Approaches on a Unified Few-Shot Classification Benchmark," Apr. 2021, [Online]. Available: <http://arxiv.org/abs/2104.02638>
- [8] X. X. Yin, S. Hadjiloucas, Y. Zhang, and Z. Tian, "MRI radiogenomics for intelligent diagnosis of breast tumors and accurate prediction of neoadjuvant chemotherapy responses-a review," *Comput. Methods Programs Biomed.*, vol. 214, p. 106510, 2022, doi: 10.1016/j.cmpb.2021.106510.
- [9] D. Pandey, X. Yin, H. Wang, and Y. Zhang, "Accurate vessel segmentation using maximum entropy incorporating line detection and phase-preserving denoising," *Comput. Vis. Image Underst.*, vol. 155, pp. 162–172, 2017, doi: 10.1016/j.cviu.2016.12.005.
- [10] J. Wei, L. Torresani, J. Wei, and S. Hassanpour, "Calibrating Histopathology Image Classifiers using Label Smoothing," Jan. 2022, [Online]. Available: <http://arxiv.org/abs/2201.11866>
- [11] Y. Bengio, umontrealca Jérôme Louradour, R. Collobert, and J. Weston, "Curriculum Learning."
- [12] C. L. Srinidhi and A. L. Martel, "Improving Self-supervised Learning with Hardness-aware Dynamic Curriculum Learning: An Application to Digital Pathology." [Online]. Available: <https://github.com/srinidhiPY/>
- [13] X. Wang *et al.*, "TransPath: Transformer-Based Self-supervised Learning for Histopathological Image Classification," *Lect. Notes Comput. Sci. (including Subser. Lect. Notes Artif. Intell. Lect. Notes Bioinformatics)*, vol. 12908 LNCS, pp. 186–195, 2021, doi: 10.1007/978-3-030-87237-3\_18.
- [14] S. B. Yengec-tasdemir, "Classification of Colorectal Polyps from Histopathological Images using Ensemble of ConvNeXt Variants Classification of Colorectal Polyps from Histopathological Images using Ensemble of ConvNeXt Variants," pp. 0–26, 2022.
- [15] R. Zhang *et al.*, "HistoKT: Cross Knowledge Transfer in Computational Pathology," Jan. 2022, [Online]. Available: <http://arxiv.org/abs/2201.11246>
- [16] T. Who and T. Who, "The 2019 WHO classification of tumours of the digestive system," pp. 182–188, 2020, doi: 10.1111/his.13975.
- [17] N. A. C. S. Wong, L. P. Hunt, M. R. Novelli, N. A. Shepherd, and B. F. Warren, "Observer agreement in the diagnosis of serrated polyps of the large bowel," *Histopathology*, vol. 55, no. 1, pp. 63–66, 2009, doi: 10.1111/j.1365-2559.2009.03329.x.
- [18] M. Raghu, C. Zhang, J. Kleinberg, and S. Bengio, "Transfusion: Understanding Transfer Learning for Medical Imaging," Feb. 2019, [Online]. Available: <http://arxiv.org/abs/1902.07208>
- [19] Z. Liu *et al.*, "Swin Transformer: Hierarchical Vision Transformer using Shifted Windows," pp. 9992–10002, 2022, doi: 10.1109/iccv48922.2021.00986.
- [20] Z. Liu, H. Mao, C.-Y. Wu, C. Feichtenhofer, T. Darrell, and S. Xie, "A ConvNet for the 2020s," 2022, [Online]. Available: <http://arxiv.org/abs/2201.03545>
- [21] H. Touvron, M. Cord, M. Douze, F. Massa, A. Sablayrolles, and H. Jégou, "Training data-efficient image transformers & distillation through attention," 2020, [Online]. Available:



- <http://arxiv.org/abs/2012.12877>
- [22] H. Zhang, M. Cisse, Y. N. Dauphin, and D. Lopez-Paz, "MixUp: Beyond empirical risk minimization," *6th Int. Conf. Learn. Represent. ICLR 2018 - Conf. Track Proc.*, pp. 1–13, 2018.
- [23] S. Xie, R. Girshick, P. Dollár, Z. Tu, and K. He, "Aggregated residual transformations for deep neural networks," *Proc. - 30th IEEE Conf. Comput. Vis. Pattern Recognition, CVPR 2017*, vol. 2017-Janua, pp. 5987–5995, 2017, doi: 10.1109/CVPR.2017.634.
- [24] R. R. Selvaraju, M. Cogswell, A. Das, R. Vedantam, D. Parikh, and D. Batra, "Grad-CAM: Visual Explanations from Deep Networks via Gradient-Based Localization," *Int. J. Comput. Vis.*, vol. 128, no. 2, pp. 336–359, 2020, doi: 10.1007/s11263-019-01228-7.

## BIOGRAPHIES



**MEHMET NERGİZ** He graduated from the Computer Engineering Department of Boğaziçi University in 2008. He received his M.S and Ph.D. degrees in 2013 and 2017, respectively from the Department of Electrical and Electronics Engineering at Dicle University. He worked as a Postdoctoral Research

Fellow on medical image analysis and artificial intelligence at Harvard Medical School - Massachusetts General Hospital for one year between 2019 - 2020. His research field is machine learning, deep learning, federated learning, computer vision and signal processing. He currently works as an Assistant Professor and also the Head of Computer Engineering Department, the Director of Remote Distance Center and the Advisor of the Rector at the Dicle University.

# Estimation of Extrusion Process Parameters in Tire Manufacturing Industry using Random Forest Classifier

Osman Onur Akırmak, Aytaç Altan

**Abstract**—The extrusion process is a very complex process due to the number of process parameters involved. Throughout the workflow process, the process parameters are determined by trial-and-error method according to the recipe of materials. This technique causes loss of production and time as well as energy consumption. In extrusion, temperature and speed parameters are very important to obtain a homogeneous raw material product input and high-quality extruded products. It is necessary to monitor the temperature changes and process speed control during the flow of the molten raw material between the barrels of the extruder machine, which is the extrusion equipment. By monitoring the extruder in real time, estimating the extrusion process parameters according to the amount of product to be produced will make the extrusion process operations more efficient. In this study, a classification algorithm to process these parameters is developed in the “Pycharm” environment and the model is trained with the supervised learning method using the image processing algorithm outputs. The model is able to estimate the extruder 'speed and temperature parameters' and the 'ready to run' decision of the machine with 93% success for different production quantities entered by the operator.

**Index Terms**— Extrusion process, tire manufacturing, decision support estimation algorithm, surface inspection, random forest algorithm.

## I. INTRODUCTION

THE EXTRUSION process is a manufacturing technique in which materials are moved along a screw and pushed out of a die at a certain speed. It is widely used in different branches in the industry, and one of the most common areas where it is used is the tire manufacturing industries. In this manufacturing process, thermoplastic material (carbon reinforced synthetic

rubber-SBR) is used as raw material. It becomes the final vehicle tire by going through the component preparation, building, curing and inspection production processes, respectively. Tire faces some potential problems throughout its manufacturing processes. Unlike techniques such as injection molding or blow molding, extrusion is continuous. This means that there is a constant change in extruder parameters. Input parameters should be defined, controlled and monitored for variables that have a non-negligible impact on product quality that will disrupt the extruder's stable running process. Control and monitoring are critical in estimating production quality. The focus of this study is the monitoring of the extruder parameters and the estimation of the parameter settings in the production phase of the tire belt, which is formed by the extrusion process of several rows of cord wire, which is an input of the tire making process.

Process parameters include melting temperature, screw speed and pressure. The parameters used in this study are the melting temperature and screw speed setting values and will be used as inputs in the classification model. These parameters indicate that the melt temperature changes in the extruder are important for determining the stability of the extruder, and fluctuations in other process parameters in the process, along with it, cause problems in tire production [1]. One of these problems is that the coating cannot be done properly, the other problem is that the black rubber coating material is not distributed on cord wires homogeneously on the surface, and the color fluctuation that occurs as a cluster. An example of coating defect after extrusion is shown in Fig. 1.

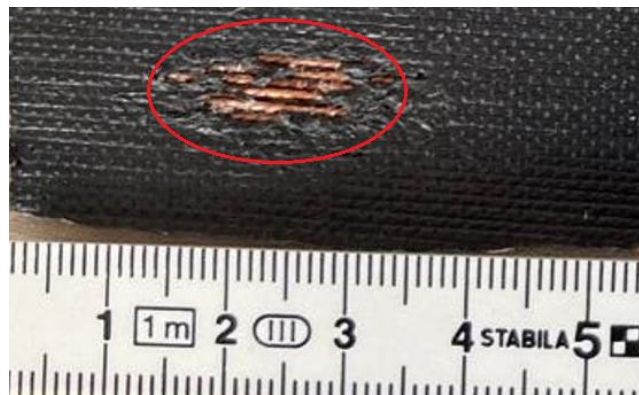




Fig.1. Coating defect after extrusion were shown with red colored marker

Some literature studies that we can pay attention to in extrusion processes regarding a certain product quality

OSMAN ONUR AKIRMAK, is with Department of Electrical Electronics Engineering, Zonguldak Bülent Ecevit University, Zonguldak, Turkey, (e-mail: onur.akirmak@fbe.karaelmas.edu.tr).

 <https://orcid.org/0000-0003-0014-4680>

AYTAÇ ALTAN, is with Department of Electrical Electronics Engineering, Zonguldak Bülent Ecevit University, Zonguldak, Turkey, (e-mail: aytacaltan@beun.edu.tr).

 <https://orcid.org/0000-0001-7923-4528>

Manuscript received January 12, 2023; accepted April 4, 2023.  
DOI: [10.17694/bajece.1232811](https://doi.org/10.17694/bajece.1232811)

situation; optimizing the flow rate of the plastic extrusion process, the characterization of rubber with a multilayer sensor neural network in the rubber extrusion process [2, 3], mapping neuro-fuzzy approach for the hot extrusion process using ANFIS [4], improving the quality of the final product in plastic extrusion with decision trees [5]. In order to detect bubbles and scratches, two-layer feed-forward neural network studies were carried out on the surface of aluminum profiles with co-occurrence matrices [6], temperature response control for the plastic extrusion system to avoid sudden input disturbances [7].

In the tire industry, this study has been a cost-effective and applicable study in factories with more than one extrusion line with low hardware cost, and model training achievements are indicated in the literature studies, since there is no real-time work at the hardware level in the factory environment on calendaring production process on extruder machine, it will be one of the first contributors to work actively in the field in this sector.

The aim of this study is to significantly increase the adequacy value of the process encountered as a result of the studies on surface inspection in the tire industry to develop a decision support estimation algorithm that will contribute to the production of lower cost and high-quality products by reducing the waste significantly, reducing the human factor and related errors and physical inadequacies. In summary, the method is to analyze the extrusion parameters to estimate the product quality appropriate extruder machine operating setting values with a classification model based on these parameters. This study is based on a practical applied solution with the performance of the model estimation, the product quality, and the realization of the field application.

The rest of the paper is organized as follows. Section II describes the extrusion processes of the tire factory and the techniques used to create the forecast model. Field experiments are introduced in Section III, and the experimental results obtained are discussed in Section IV. Section V highlights the results of the study and offers suggestions for future work.

## II. MATERIALS AND METHODS

In this part, respectively; the extrusion process was defined, then the Random Forest Algorithm (RFA) working principle and the most important feature of this algorithm, the Gini index, were defined. In addition, the method of preparation of the data set and the characteristics and success rate of the classifier algorithm used was mentioned.

### A. Extrusion Process

In the extrusion process, the raw material to be processed is fed to the extruder with the help of a hopper. The motor system on the machine is responsible for producing the energy required for propulsion. The transmission, which must be provided for the rotation of the screw produced by the motor, is done with the help of the reducer. The screw system, which rotates with the drive from the motor and reducer, drags the raw materials poured into the hive forward by means of the barrel. Here, the plastic raw material is completely melted by heaters while passing through the feeding, melting and compression zones, respectively, and the extruder machine completes its function

after it is taken out of the nozzle [2]. The steps of the injection process are shown in Fig. 2 [8].

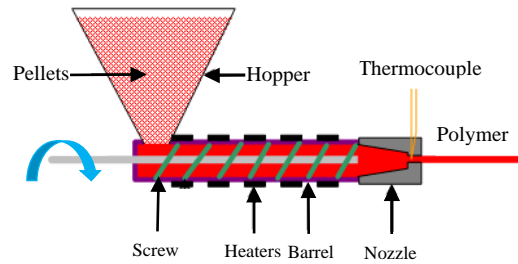


Fig.2. Extrusion process in extruder

### B. Random Forest Algorithm

RFA is one of the supervised classification algorithms. It is used in both regression and classification problems. The algorithm aims to increase the classification value during the classification process by producing more than one decision tree. The RFA is the process of choosing the highest score among many decision trees that work independently of each other. The RFA determines classifications using the majority of multiple trees; so many decision trees must be built. Performance increases with the number of decision trees, requiring memory, and decreases if the number of decision trees is decreased [9].

There are two stages in the RFA, one is the random forest developer and the other is guessing through the random forest classifier responsible for the initial scenario. Pseudocode for generating RFA:

- i. select the  $K$  features randomly from the total  $M$  features (must be  $K < M$ ).
- ii. calculate the  $d$  node using the best split point among the  $K$  features.
- iii. split the node into child nodes using the best split.
- iv. repeat steps *i* and *iii* until the  $L$  node number is reached.
- v. repeat steps *i* and *iv*  $n$  times to create  $n$  number trees.

To know how a RFA works, we need to know decision trees, which are again a supervised machine learning algorithm used for classification and regression problems. Decision trees use a flowchart, such as a tree structure, to show the predictions resulting from a set of feature-based splits. It starts with a root node and ends with a decision made by the leaves are shown in Fig. 3.

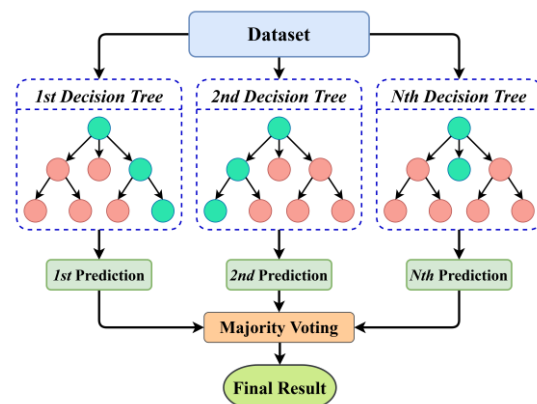


Fig.3. RFA structure

It consists of three components: root node, decision node and leaf node. The node at which the population begins to divide is called the root node. The nodes we obtain after dividing a root node are called decision nodes, and the nodes where further division is not possible are called leaf nodes. The decision of where to start the root node was made by calculating the Gini index.

C. Calculation of Gini Index

It is preferable to choose the feature with at least Gini index as the root node when constructing the decision tree. Another feature of this algorithm is that it can be used for feature selection. The feature evaluations were calculated as the mean and standard deviation of the impurity values in each tree. We defined  $P_i$  is the probability that an object will be classified into a particular class. Where  $P_{i+}$  is the probability of a positive class and  $P_{i-}$  is the probability of a negative class. When we take feature 1 as our root node, we get a pure split whereas when we take feature 2, the split is not pure. To know how much impurity this particular node has can be understood with the help of the ‘‘Gini index’’. Basically, need to know the impurity of dataset and take that feature as the root node which gives the lowest impurity or say which has the lowest Gini index. Mathematically Gini index can be written as:

$$Gini\ index = 1 - [(P_{i+})^2 + (P_{i-})^2] \tag{1}$$

Suppose that try to split a new branch due to  $K$  feature which selected in screw speed window as 30 and temperature feature node value as 75°C to create child nodes. Image processing techniques were used to classify the processing parameters as appropriate '+' and unsuitable '-' shown a sample on Table I. As seen in Table I, we have  $P_{i+}$  two good (+) class element in row and one  $P_{i-}$  as bad (-) in class and  $L$  number reached at once:

$$Gini\ index = 0.45\ where\ P_{i+} = 2/3,\ P_{i-} = 1/3 \tag{2}$$

TABLE I  
DATASET STRUCTURE

Screw (rpm)	Hopper Temp. °C	Barrel Temp. °C	Class
30	30	69	-
30	69	85	+
30	70	83	+

Similarly, this algorithm will try to find the Gini index of all the splits possible and will choose that feature for the root node which will give the lowest Gini index. The lowest Gini index means low impurity. For the final decision, needs to calculate the weighted Gini index that is the total Gini index of this split. Final output is considered based on majority voting if it's a classification problem each tree's classification is combined into a final classification through a 'majority vote' mechanism and repeat steps are shown on pseudocode. By looking at the importance of the feature, it can be decided which features you want to reduce, low features do not contribute enough to the prediction process. This is important because a general rule in

machine learning is that the more features you have, the more likely your model is to be overfitting and vice versa [10]. If a  $D$  data set is divided into two subsets,  $D_1$  and  $D_2$ , on  $S$ , the Gini impurity index is defined as follows and the feature-dependent model classification output is given below for the first 4 nodes of the tree no. Let's define  $P_-$  as class + and  $P_+$  as class -, and

$$GiniS(D) = \frac{D_1}{D} Gini(D_1) + \frac{D_2}{D} Gini(D_2) \tag{3}$$

Tree 1:

- 0 NODE: if feature [1] < 75.0 then next=1 else next=2
- 1 LEAF: return class=0
- 2 NODE: if feature [1] >75 then next=3 else next=4
- 3 LEAF: return class=1

D. Creating of the Dataset

The dataset for use in the model was obtained from the extruder on the production line of a vehicle tire manufacturing plant. The image processing device used is shown in Fig. 4. Due to the high flow rate of the line and the small surface coating defects, a profile sensor, an industrial image processing device, was positioned at the output of the extruder.

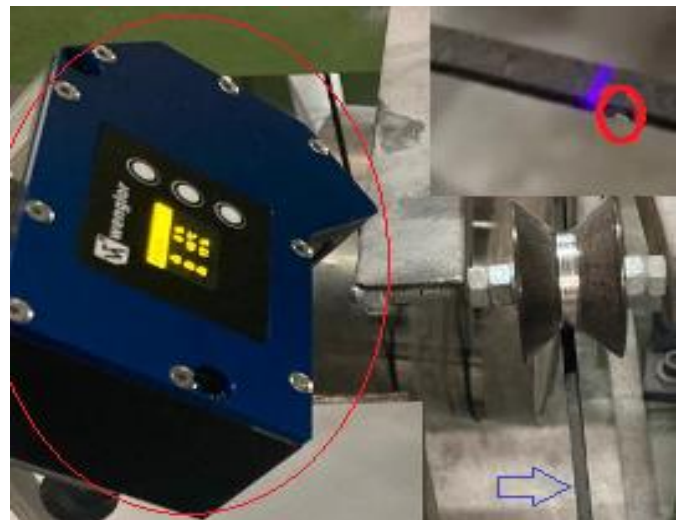


Fig.4. Profile sensor shown on left and defect detailed on top right corner, also can see blue laser light from profile sensor

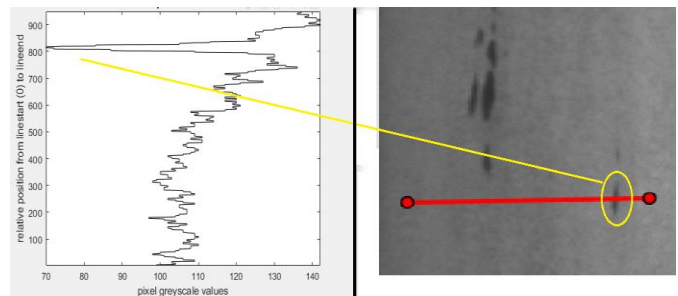


Fig.5. The image values are inverted in grayscale in the (0-255) band, showing the peak value of the laser light's reflection intensity value from the band at the defect point

While the profile sensor was being placed, different camera and laser angles were tried to be mounted at the exit of the extruder according to the layouts shown in Fig. 4. Finally, the



profile sensor is positioned at a distance of 80 mm from the rubber belt piece that reaches with the coating of 3 cord wires with a width of 5 mm to be controlled in the process and inclined 35 degrees horizontally. The two-dimensional images of the area scanned by the profile sensor on the belt were taken and transferred to the computer. The obtained data were analyzed by the developed software and graphics and numerical outputs were created. From the graph created, the peak value of the points with surface defects in the belt was determined and shown in Fig.5.

The temperature values read from hopper, barrel, and nozzle were taken with DS18B20 which connected to microcontroller board. The DS18B20 is a small temperature sensor with a built in 12bit analog to digital convertor (ADC). It can be easily connected to a microcontroller digital input. The sensor communicates over a one-wire bus and requires little in the way of additional components. The sensors have a quoted accuracy of  $\pm 0.5^{\circ}\text{C}$  in the range  $-10^{\circ}\text{C}$  to  $+85^{\circ}\text{C}$ . In the order of preparing the dataset, the data titled '+' and '-' taken from the profile sensor is divided into two classes under the title of "Class" in Table I and the temperature sensors placed on the extruder hopper, barrel, and nozzle respectively. The dataset was created by recording real-time data in .xls format via "Data Streamer" property of excel.

#### E. Classifier Structure

Model parameter optimization is the process of hyperparameter tuning to determine optimal values for a particular random forest classifier. The performance of a model is highly dependent on the value of the hyperparameters. Since there is no way to know the best values in advance for the hyperparameters, ideally, all possible values are determined after the relevant algorithm has been run to know the optimum values, and the model with supervised learning structure has emerged, which is configured as 20 trees and learning coefficient 0.8.

The correlation relationship between the 1369 pieces of data, the mold and hive temperature values increase in direct proportion to the production amount. Another linear relationship was also found to exist between the screw speed data and the amount of product coated as the extruder output. The confusion matrix of the model is shown in Table II. The general accuracies of the applied methods are given in the upper left and lower right corners of the matrix. In addition, the values in the upper right and lower left corners indicate incorrect estimates.

TABLE II  
CONFUSION MATRIX

<b>Positive</b>	True Positive (TP) 397 samples	False Positive (FP) 6 samples
<b>Negative</b>	False Negative (FN) 2 samples	True Negative (TN) 232 samples

### III. FIELD EXPERIMENTS

The system was developed for a low-budget application, and the hardware was selected accordingly. The experimental setup shown on Fig.6 block structure designed to control the mathematical model of an unknown system. The system

consists of three parts, classification model, extruder and image processing system. Depending on the hardware, the limiting criterion in choosing the RFA of the classification model is that it gives higher accuracy 93% than the k-Nearest Neighbor (kNN) algorithm 88%, which is among the model algorithms that can be run on the microcontroller hardware.

Although the model results with 94% trained with the Support Vector Machine (SVM) algorithm whose parameters were optimized on a laptop with a Windows operating system in the "Pycharm" environment, however it was not used in the final tests due to the hardware limitation. One advantage of the RFA is that it can be used for both regression and classification tasks and it is easy to see the relative importance it gives to input properties. It is considered a very useful and easy-to-use algorithm because default hyper parameters usually produce a good prediction result. The number of hyperparameters is also not that high and is easy to understand. The main limitation of the RFA is that a large number of trees can make the algorithm slow and ineffective for real-time predictions. In general, these algorithms can be trained quickly, but are extremely slow to generate predictions once trained [11].

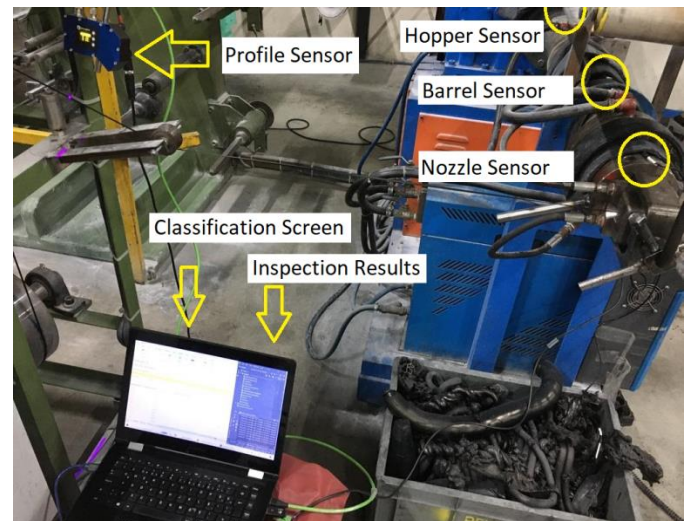


Fig.6. Experimental setup

A more accurate prediction requires more trees, resulting in a slower model. The RFA is fast enough for most real-world applications, but there may be situations where runtime performance is important and other approaches may be preferable. The RFA is a simple algorithm for early training in the model development process and to see how it performs, and it is difficult to create a "bad" RFA due to its simplicity. Overall, the RFA is a fast, simple and flexible tool despite its limitations. The Streaming Random Forest (SRF) algorithm handles multi-class problems successfully as opposed to many stream classification algorithms that are designed and/or tested on only two-class classification algorithms. It is fast enough to handle stream rates of up to  $2.8 \times 10^4$  records/sec, when executed on a fairly small machine such as Pentium 4 machine with 3.2 GHz processor and 512 MB RAM [12].

The success of the classification methods used in the study are shown in Table III. All algorithms are trained with the same training size. The aim is using a low-cost hardware. Due to its small memory size, RFA algorithm was chosen as it has the

highest accuracy and most feasible on the hardware. The F1-score which is machine learning evaluation metric that measures a model's accuracy was calculated. The accuracy metric computes how many times a model made a correct prediction across the entire dataset.

TABLE III  
PERFORMANCES OF ALGORITHMS USED IN THE STUDY

Algorithm	Class	F1-score	Accuracy
Decision Tree	0	0.86	0.83
	1	0.78	
kNN	0	0.90	0.88
	1	0.85	
RFA	0	0.93	0.93
	1	0.92	
SVM	0	0.95	0.94
	1	0.93	

#### A. Experiment 1

According to the prepared the first experiment scenario, without model using, the extruder operator set the barrel and die temperature values as the first initial set value at 85°C and the frequency inverter controlling the screw speed as 20 Hz at the beginning of the workday shift while the system was cold, and loaded the raw material into the extruder system at ambient temperatures without preheating. The cold raw material input to the extruder, whose barrel and mold temperatures reached set values, decreased the average of the barrel and mold temperature value of the single screw extruder with a screw length of 1.5 meters and caused the first 75-meter product to be produced incorrectly. Faulty production was detected by the profile sensor system.

#### B. Experiment 2

According to the prepared the second experiment scenario, the extruder operator set the barrel and die temperature values at 85°C at the beginning of the shift, the frequency inverter controlling the screw speed as 20 Hz, while the system was cold, and preheated the raw material by circulating the product. Meanwhile, the model is running. The operator only manually entered the desired production amount as 42 kg/hour. Nozzle, barrel and hopper temperature information is given to the model in real time by the microcontroller hardware.

The model works on the microcontroller. When the ready information of the extruder is shown on the touch screen, 10 Hz appears to be sufficient according to the “rpm” estimation on the same screen, the operator is asked to adjust the extruder speed, the temperature values, the raw material, barrel, and hopper temperatures 60, 75, and 79°C as soon as the “Machine Ready” information is received. The operator accordingly reduced the heater set value from 85°C to 80°C and terminated the circulation and sent the product to the mold end with the wire for coating. Meanwhile, the image processing system checked the error status of the coated product and no faulty product production was observed. The flow chart of the system is shown on Fig.7.

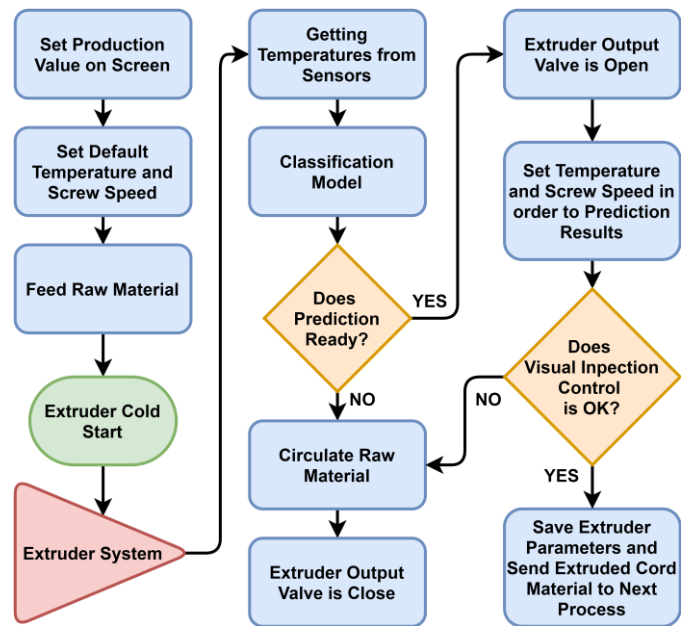


Fig.7. Flow chart of the system

## IV. EXPERIMENTAL RESULTS AND DISCUSSIONS

As seen in the results of Experiment 2, it is possible to set the equipment temperature set values below 85°C in order to produce faultless products. Again, when the results were evaluated, different screw speed rpm values were estimated in order to produce the desired 42 kg/min product amount. By connecting a wattmeter, the instantaneous power was recorded periodically every 5 minutes, and then after 1 hour, the motor consumption was calculated by finding how much power was with an arithmetic average. Here, setting the temperature value as 80°C and setting the inverter speed value as 10 Hz decreased the hourly energy consumption by 25-30% respectively, while the electricity total consumption amount per two workday shifts was 56 Turkish Liras in the previous setting. In addition, since the amount of production counted as faulty waste in the Experiment 1 will decrease/can disappear, an improvement will be achieved in Overall Equipment Efficiency (OEE) calculations in the company's production processes and in quality problems with the real-time image processing system used. Extrusion quality and product quantity at the extruder outlet are directly related to the raw material temperature in the machine feed, machine sleeve temperatures and screw speed data. Accurate estimation of the extruder optimum operating data range increases efficiency in work and energy, and reduces waste.

Although we obtained the result that we achieved an energy gain with a low screw speed in the Experiment 2, we saw that there are reasons that limit our screw speed. It is not possible to reduce to much the speed of the tire winding machine which is connected end of the line and working with the extruder's output material. If we reduce the speed of the tire winding machine, there will be a time-related loss of production. An unpredictable output of this study is that when we set the speed of the tire winding machine to 65 m/min instead of between 25 to 45 m/min at Experiment 2, it is seen in the image processing software output that there is not enough coating on the product

which faulty. Extruder output speed cannot reach this production speed; therefore, the production line speed balance is not properly planned, however an optimum balance can be found with our proposed model. This is necessary for line balancing and stable production planning.

As can be seen from this study, the model can predict the extrusion process parameters with an accuracy of 93%. In future studies, the results can be improved by using different classification algorithms. Experimental hardware has been selected from inexpensive and open-source software available in the market, open-source software, and appropriate hardware. The possibilities of using the neural network in the extrusion process are endless because it is also used for the control of the entire system. When the neural network controller is combined with an extruder, it is sufficient to select the appropriate control input for the plant behavior that can be optimized, the future performance of the system will become predictable. The use of advanced artificial neural networks can eliminate the loss of production due to the individual, the need for learning by trial and error, which is a negative outcome of the process, and improvement can be achieved with more advanced parameter settings by making error classification.

#### V. CONCLUSIONS AND FUTURE WORKS

It can be observed from this study that the use of an classifiers with a low-cost hardware can accurately predict the extrusion process parameters. This can improve the output quality and increase the production rate of tire raw materials. Production workers in tire industries can be equipped with the appropriate tools which can enable them to produce quality tire material while eradicating the need to perform long experiments which can lead to waste of materials and increase the cost of production. The prospects of utilizing the artificial neural network in near future instead of using classifier, will be used for the decision support of the entire system. The neural network controller integrated with an extruder, which enables it to be able to predict future plant behaviors and select appropriate control input can optimize future performance.

#### REFERENCES

- [1] V. García, J.S. Sánchez, L.A. Rodríguez-Picón, L.C. Méndez-González, H.D.J. Ochoa-Domínguez. "Using regression models for predicting the product quality in a tubing extrusion process." *Journal of Intelligent Manufacturing*, vol. 30, 6, 2019, pp. 2535-2544.
- [2] C.Y. Wu, Y.C. Hsu. "Optimal shape design of an extrusion die using polynomial networks and genetic algorithms." *The International Journal of Advanced Manufacturing Technology*, vol. 19, 2, 2002, pp. 79-87.
- [3] S.A. Oke, A.O. Johnson, O.E. Charles-Owaba, F.A. Oyawale, I.O. Popoola. "A neuro-fuzzy linguistic approach in optimizing the flow rate of a plastic extruder process." *International Journal of Science & Technology*, vol. 1, 2, 2006, pp. 115-123.

- [4] R.S. Sharma, V. Upadhyay, K.H. Raj. "Neuro-fuzzy modeling of hot extrusion process." *Indian Journal of Engineering & Materials Sciences*, vol. 16, 2009, pp. 86-92.
- [5] S.H. Hsiang, Y.W. Lin, J.W. Lai. "Application of fuzzy-based Taguchi method to the optimization of extrusion of magnesium alloy bicycle carriers." *Journal of Intelligent Manufacturing*, vol. 23, 3, 2012, pp. 629-638.
- [6] A. Chondronasios, I. Popov, I. Jordanov. "Feature selection for surface defect classification of extruded aluminum profiles." *The International Journal of Advanced Manufacturing Technology*, vol. 83, 1, 2016, pp. 33-41.
- [7] S. Ravi, P.A. Balakrishnan. "Temperature response control of plastic extrusion plant using MATLAB/Simulink." *International J. of Recent Trends in Engineering and Technology*, vol. 3, 4, 2010, pp. 135-140.
- [8] URL: [https://www.substech.com/dokuwiki/doku.php?id=extrusion\\_of\\_polymers](https://www.substech.com/dokuwiki/doku.php?id=extrusion_of_polymers) (Access: Jan 9, 2023).
- [9] Y. Mishina, R. Murata, Y. Yamauchi, T. Yamashita, H.H. Fujiyoshi. "Boosted random forest." *IEICE Transactions on Information and Systems*, vol. 98, 9, 2015, pp. 1630-1636.
- [10] URL: <https://web.stanford.edu/class/archive/cs/cs221/cs221.1186/lectures/learning3.pdf> (Access: Jan 5, 2023).
- [11] G. Leshem, Y.A. Ritov. "Traffic flow prediction using Adaboost algorithm with random forests as a weak learner." *International Journal of Mathematical and Computational Sciences*, vol. 1, 1, 2007, pp. 1-6.
- [12] H. Abdulsalam. "Streaming random forests." Ph.D. Thesis, Queen's University, Canada, July 2008.

#### BIOGRAPHIES



**OSMAN ONUR AKIRMAK** received his B.Sc. degrees in the department of Electrical Electronics and Computer Engineering in 2015 and 2016, respectively. He is studying his M.Sc. degree in the department of Electrical Electronics Engineering from Zonguldak Bülent Ecevit University since 2021. He is currently a Project Engineer at Wenglor Sensoric GmbH. His research interests including software development of sensors and image processing solutions for digitalization of factories.



**AYTAÇ ALTAN** received his B.Sc. and M.Sc. degrees in the department of Electrical Electronics Engineering from Anadolu University in 2004 and 2006, respectively. He is received his Ph.D. degree in the department of Electrical Electronics Engineering from Zonguldak Bülent Ecevit University in 2018. He is currently an Associate Professor at the department of Electrical Electronics Engineering at the Zonguldak Bülent Ecevit University in Turkey. His research interests include signal processing, image processing, optimization techniques, artificial intelligence, data mining, system identification, model-based control, and robotic systems.



# Analysis and Comparison of Business Intelligence Tools Most Preferred by Companies in Turkey

Murat Ozdemir, Eyup Emre Ulku and Kazim Yildiz

**Abstract**— With the development of technology and the increase of the data sources, the size and variety of data collected from these sources has increased considerably. Thus, individuals and institutions have become able to store more data. However, it has become an important need to make meaning from this large and valuable data and transform into information and has become more complex. Business intelligence applications ensure that different types of data collected from different data sources are clustered and separated in a certain order and it provides the creation of reports by establishing a semantic relationship between these stored data. The aim of this study is identifying the business intelligence tools preferred by companies in Turkey. It is also aimed to give ideas to institutions and individual users so that they can choose the right business intelligence tool. Within the scope of the study, first of all, the general definition of business intelligence and the business intelligence applications preferred by the companies in Turkey in recent years are mentioned. Afterwards, the information obtained from the scanned scientific studies are analyzed and the findings are presented and then these tools were compared with the tables and it was aimed to give an idea to individuals and institutions. Scientific studies are very important in terms of revealing the current status of these business intelligence tools and seeing what kind of studies they can be used in the future.

**Index Terms**— Business Intelligence, Qlik, Power BI, SAP BO, Tableau.

## I. INTRODUCTION

STORING AND recording data and records has been one of the important needs since the past. Data recording has become much faster, less costly and safer with the development of technology and the increase in disk speed and size.

**MURAT OZDEMIR**, is with Department of Computer Engineering, Institute of Pure and Applied Sciences, University of Marmara, Istanbul, Turkey, (e-mail: [muratozdemir20@marun.edu.tr](mailto:muratozdemir20@marun.edu.tr)).

 <https://orcid.org/0000-0001-7225-3574>

**EYUP EMRE ULKU**, is with Department of Computer Engineering, Faculty of Technology, University of Marmara, Istanbul, Turkey (e-mail: [emre.ulku@marmara.edu.tr](mailto:emre.ulku@marmara.edu.tr))

 <https://orcid.org/0000-0002-1985-6461>

**KAZIM YILDIZ**, is with Department of Computer Engineering, Faculty of Technology, University of Marmara, Istanbul, Turkey, (e-mail: [kazim.yildiz@marmara.edu.tr](mailto:kazim.yildiz@marmara.edu.tr)).

 <https://orcid.org/0000-0001-6999-1410>

Manuscript received May 30, 2022; accepted March 30, 2023.  
DOI: [10.17694/bajece.1123171](https://doi.org/10.17694/bajece.1123171)

In recent years, it has become possible to store large amounts of data in a computer memory, even in virtual machines that can be accessed remotely, and to access these stored data quickly. In this way, companies can quickly combine this data, which may not have mean on its own, and make sense of historical data and present it to their managers. For this reason, decision support systems have been developed. However, in the future, a new system was needed due to the difficulties in the use of decision support systems, visual deficiencies and incompatibility with applications, and this need was met by designing business intelligence systems [1].

IBM researcher Hans Peter Luhn first used the term business intelligence (BI). It is defined as the ability to make sense of the relationships of existing information to achieve a desired goal [2]. BI is a versatile process that includes techniques, processes and tools that facilitate faster and more effective decision making in businesses according to Sabanovic and Soilen [3]. BI is defined as a mix of collecting, cleaning and integrating data from different sources. It is the process of transforming raw data into useful and meaningful information for decision support purposes in very short time [4].

BI is the process of collecting the exact information in the right format at the right time which produces have a positive impact on operations and strategies in businesses for decision-making purposes [5]. It is critical in the sources where business data is kept, in order to access the data in a short time, process it quickly and make accurate predictions for the future for managers [6]. Business intelligence technology provides the opportunity to perform multidimensional analysis on data in cases where many factors need to be evaluated simultaneously [7]. It can turn into meaningful, summary reports that can be used in decision processes by enabling the search for qualified information, integrating data and obtaining meaningful findings with multidimensional analyzes in a data set consisting of different source [8-9].

## II. BUSINESS INTELLIGENCE TOOLS

The need for business intelligence of companies has become important in terms of extracting analyzes from visual reports and visualizing their future plans and strategies. With the incoming demands, many features such as the number, variety and usability of business intelligence tools have increased and the decision to choose the BI tool to be used has become difficult [10]. Business intelligence applications make sense of

and analyze the data produced by the software, allowing possible risks to be seen and as a result, increase the success of the business and people. For this reason, companies should thoroughly examine their business intelligence applications and make the right choice [11].

While developing websites, these structures can be developed separately from each other by using models such as MVC (Model View Controller), as in the work of Akçay and friends. With this design model, opportunities such as code optimization, code extension, code reuse and code updating are offered [12]. While developing business intelligence projects, each layer can be separated and evaluated separately.

Business Intelligence architecture consists of Data Extraction, Data Transformation, Data Loading, Data Warehouse Layer, Metadata layer and End User Layers [13]. All these layers can be gathered together with the help of business intelligence tools.

185 job postings were listed on the website of kariyer.net [14], which is one of the most used job and employment web site in Turkey, when business intelligence was typed into the search section in Turkish as 'İş Zekası' on January 8, 2022 [15]. It was seen that the newest of these ads was published on the query day and the oldest one 54 days ago. These advertisements were published by various companies in various sectors such as banking, textile, insurance, alcoholic beverage and food. Two of 185 advertisements are the same advertisement. As it was observed that 45 advertisements were irrelevant so that they were removed from the list. And 49 of the remaining postings did not include any business intelligence tool which are not mentioned. As it is shown in Table 1 more than one business intelligence tool can be named in an advertisement, 47 included Power BI, 39 included SAP, 35 included Qlik, 17 included Tableau, 11 included SSRS, 9 included Oracle BI, 9 included Microstrategy, 3 included Cognos, 3 contained IBM Data Stage, 1 contained looker and 1 contained superset.

As a result, it was observed that the name of a business intelligence tool was mentioned 175 times. When calculated as a percentage, we can see that these tags contain Power BI with a maximum of 27% is shown in Fig. 1.

#### A. Power BI

##### 1) About Power BI

Power BI is a cloud-based reporting service developed by Microsoft that enables the creation of reports that make sense of meaningless data [16]. Power BI is intended for users to create their own reports and dashboards without the help of any IT staff. This tool offers the ability to create data warehouses, organize data, and create visual dashboards from that data. One of the best benefits of Power BI is that custom visualizations can be uploaded through its Marketplace app. With Power BI, data from different data providers can be easily retrieved, visualized and shared with other users [17].

Power BI can use different data sources. It can make connection with databases like PostgreSQL, Microsoft SQL, Oracle SQL. Also, it can make connection with cubes like SQL Server Analysis Services or with some folders directly like txt, csv etc. [18].

Power BI consists of three core elements, Power BI Desktop (a Windows desktop application), Power BI Service (an online

software), and Power BI mobile (for mobile devices). It also has two another component, Power BI Report Builder which enables developing paginated reports that can be shared in the Power BI service and Power BI Report Server which is an in-house report server where you can publish your Power BI dashboards created via Power BI Desktop. The process starts by connecting to different types of data sources and creating reports in Power BI Desktop. This report is then published and shared from the Power BI Desktop app to the Power BI service. [17].

TABLE I  
THE NUMBER OF BUSINESS INTELLIGENCE TOOLS IN ADVERTISEMENTS

BI Tool Name	Number of Posting
Power BI	47
SAP	39
Qlik	35
Tableau	17
SSRS	11
Oracle BI	9
Microstrategy	9
Cognos	3
IBM Data Stage	3
Looker	1
Superset	1

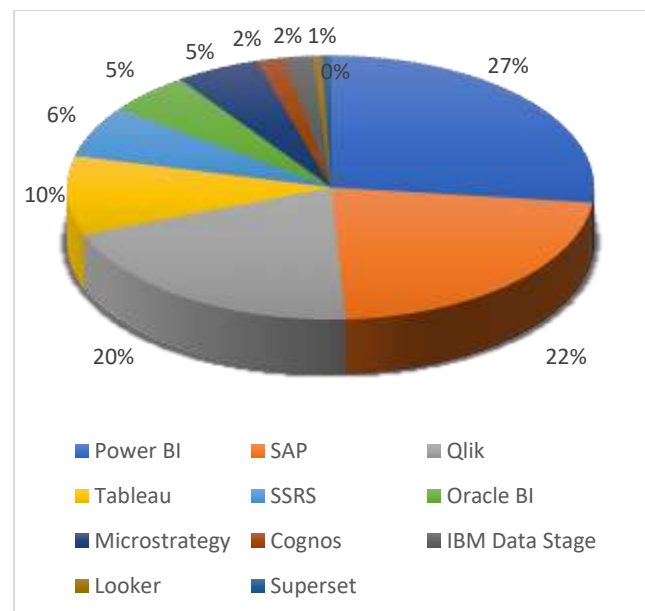


Fig.1. Percentage of business intelligence tool names in advertisements

With dashboards, multiple data can be visualized in a single interface. Tree maps, gauges, combo or funnel charts and fill maps can be used to visualize. The cloud-based Power BI service provides a secure connection without having to move data from Microsoft SQL Server to the cloud. Data can be imported and modeled with Power BI Designer. Real-time control panel can manage updates. Thus, instant and secure connection can be established to data local or in the cloud [10].

##### 2) Power BI versions

In order to share dashboards and reports, license must be purchased. There are 3 different license options for Power BI

Service which are Power BI Pro, Power BI Premium Per user and Power BI Premium Capacity. Power BI Pro provides licenses to users to share data across the organization after converting or visualizing data into a report. Power BI Premium per User allows the use of advanced artificial intelligence features in addition to all the features available with Power BI

Pro. Power BI Premium per Capacity provides data management and enterprise access without per-user licenses. Publishing content to Power BI Premium capacity requires a Power BI Pro license, while viewing content does not require a license [19]. Table 2 shows the comparison of these versions [19].

TABLE II  
COMPARISON of POWER BI VERSIONS

	Power BI Pro	Power BI Premium Per user	Power BI Premium Per capacity
Mobile app access	✓	✓	✓
Paginated (RDL) reports	✗	✓	✓
No license required per user	✗	✗	✓
On-premises reporting with Power BI Report Server	✗	✗	✓
Model size limit	1 GB	100 GB	400 GB
Refresh rate	8/day	48/day	48/day
Advanced AI (text analytics, image detection, automated machine learning)	✗	✓	✓
Dataflows (direct query, linked and computed entities, enhanced compute engine)	✗	✓	✓
Maximum storage	10 GB/user	100 TB	100 TB

### 3) Literature Background of Power BI

Rajesh et al. proposed a data science approach to minimize the time it takes to transfer a player from one team to another depending on the skills and costs of the players. He stated that this would help a football team increase its popularity and profits and create a brand-new club with new players. Using Power BI and Python, performed a statistical analysis of player performance based on capabilities for a new set of gamers while minimizing cost. They suggested that such approaches and analytical results could be useful for building a team of selected players [20].

Ferreira and friends presented research on the design and development of a practical predictive monitoring system. The three main parts are vibration data acquisition, data analytics, and presentation of a report. The data collection is made by STM32F446RE microcontroller. They generated a report using all available information using Microsoft Power BI. Finally, they stored the information using a cloud-based Azure Storage Account [16].

Hewko and friends wanted to analyze the last 6 years of professional basketball data using knowledge discovery tools. The aim was to give an idea of how teams won and what separates these winning teams from the losing teams. They analyzed regular season game data using MSSQL, Microsoft BI, R, and Power BI to find previously unknown trends between winning and losing teams. They used decision trees, Naive Bayesian and association rules. They used defensive and offensive rebounds, blocks, steals, turnovers, 2-point field goal percentage, and 3-point field goal percentage as input for analysis. The results showed that teams with more defensive rebounds won more games, while teams that earned average offensive rebounds lost more games. They claimed this was because teams with more offensive rebounds missed more shots

[21]. Desai and colleagues aimed to help companies selling electronic devices increase productivity and customer satisfaction using Microsoft Power BI [22].

### B. SAP

#### 1) About SAP Business Objects (SAP BO)

SAP BO Business Intelligence is a package available for creating visual reports using data and sharing these reports with other people [23]. SAP BO is a business intelligence application for a business designed for use by companies and employees. It consists of several reporting applications that allow users to visualize the results of their analysis using data from various sources. It provides an easy, personalized and dynamic connection to all necessary structured and unstructured data of the institution's relational database. It aims to simplify reporting and analysis for staff so that users can create, publish, share and use as primary access for analysis within different products without the need for input from data analysts. The data used with it is not integrated at the application layer, but at various back-end resources [24].

Web Intelligence (Webi) allows users to analyze, generate reports, distribute generated reports on BO or PDF or XLS etc. It is a Web browser tool that allows exporting in format. Crystal Reports is a reporting and data analysis tool that allows from various data sources. Business Objects Dashboards is a data visualization tool that allows creating visual tables from reports. SAP Lumira is a visualization tool that allows users to analyze data and create dynamic visual dashboards and analytics applications. SAP BusinessObjects Explorer is a data exploration tool that allows searching large-scale data and creating visual tables from this data. Query as Web Service (QaaWS) is a tool that enables Users to create and publish web services for use in SAP's reporting tools. In addition to existing products, SAP Business Objects is constantly improving its













product line with new integrations, enhancements and new products and constantly supports its portfolio with up-to-date technology [24].

### 2) Lumira Versions

SAP Lumira Desktop has two editions which are Personal and Standard Edition. Personal edition is the version that can be

used for free. CSV, XLS and XLSX and cloud data in SAP HANA One can be connected using this version. Standard Edition is paid, with this version you can connect to various data sources [25]. The comparison of these two versions is shown in Table 3 [26].

TABLE III  
COMPARISON of SAP LUMIRA VERSIONS

	Lumira Desktop Personal Edition	Lumira Desktop Standart Edition
Access of xlsx and csv files		
Access of other data sources		
Data combination and data transformation		
Create storyboards		
Edit storyboards		

### 3) About SAP Analytics Cloud

SAP Analytics Cloud is a tool which is designed specifically for the cloud by SAP to access data and let in analytics straight over business processes to quickly comeback immediate insights into action. It enables real-time Innervisions and exploration of data with self-service data exploration abilities. It offers accurate, locally connected, logical data and tools for data management. It allows to compare data from different data sources, create effective data visualizations and develop instant reports. It can be used directly from a web browser without installation a new program on your computer [27].

### 4) SAP Analytics Cloud Versions

SAP Analytics Cloud offers three different licensing options which are trial, business intelligence and planning. The comparison of these two versions is shown in Table 4 [28].

### 5) Literature Studies Using SAP

Nazarov et al. conducted a study using the SAP Analytic Cloud in Russia to propose models that build predictive analytical models. They suggested that it could ultimately help improve the situation with the development of small and medium enterprises in Russia [29].

Nararya and friends claimed that conclusions could be drawn regarding the application of the predictive analysis model in the SAP Analytics Cloud digital service for the functional dashboard design in the finance module [30].

Nazarov et al. investigated the possibilities of creating data mining models with the help of SAP Analytics Cloud using the data of legal entities and individual entrepreneurs in the Russian Federation, and aimed to determine the effect of state support against COVID19 on the commercial activities of small and medium-sized enterprises [31].

## C. QLIK

### 1) About Qlik

Qlik is a software company founded in Sweden in 1993 and is a provider of Qlik View and Qlik Sense tools for BI. Previously called quick, it later became Qlik [18].

Qlik Sense is an interactive self-service visualization and exploration tool for analyzing, interpreting and visualizing data sources. The drag and drop features of the interface are good for quick creation of dashboards, data visualization and reports. Desktop, server and cloud versions are available. Qlik Sense Desktop is for end users to develop visual dashboards on a their computers. It is free for personal usage. Qlik Sense Enterprise is for organizations which can have big data sources. Qlik Sense Cloud supports is using for data visualization by cloud technology. It provides broad assistance through forums, education materials, webinars and video tutorials [10].

Qlik is memory-based tools for this reason all data is loaded into Random Access Memory. QlikView can connect many different data sources such as ODBC data sources or can connect with folders directly like xlsx, txt, csv and its their data folders called QVD (QlikView Document) files. QlikView and Qlik Sense are free for an individual user. One of the main advantages is that existing selections are saved as bookmarks for later use and users can easily access the bookmarks. Data visualization in QlikView is in the form of charts. Different chart types can be used, such as Bar charts, Radar chart, Line chart, combo chart, Grid chart, Pie chart, Funnel chart, Scatter chart etc. [18].

Qlik View can easily analyze very large datasets, combine data from various sources, and make data quickly accessible via Resource-specific APIs. End users can visualize the data in the browser using plug-ins. The first step is to extract data from specific sources and integrate it into Qlik. Incorrect data fields are cleaned and outliers are identified and preprocessed in the second phase. In the third phase, users are simplified with drag and drop visualizations for reports. Finally dashboards can be shared with other users [18]. Being in-memory tools, reports as excel and pdf, large consultant network, powerful mobile applications, dashboard technologies, simple development cycle and solid integration can be counted as the advantages of Qlik. A good system configuration is required to access large datasets, the need for trained developers, lack of centralized security, difficulty of deploy analytics, and old interface can be evaluated as disadvantages of Qlik [18].

TABLE IV  
COMPARISON of SAP ANALYTICS CLOUD VERSIONS

	SAP Analytics Cloud Trial	SAP Analytics Cloud Business Intelligence	SAP Analytics Cloud Planning
Data Modelling	✓	✓	✓
Data Visualizations	✓	✓	✓
Data Exploration	✓	✓	✓
Augmented Analytics	✓	✓	✓
Live Data Connectivity	✓	✓	✓
SAP BPC integration	✗	✗	✓
Schedules	✗	✗	✓
Currency Translation	✓	✗	✓
Schedule publications	✗	✓	✓
Integrated planning with SAP S/4HANA	✗	✗	✓

### 2) Qlik Versions

There are two versions of Qlik Sense which are Qlik Sense Business and Enterprise. The first one is a cloud solution

developed for use across groups and teams. Qlik Sense Enterprise SaaS is developed for operational usage. The comparison of these two versions is shown in Table 5 [32].

TABLE V  
COMPARISON of QLIK SENSE VERSIONS

	Qlik Sense Business	Qlik Sense Enterprise SaaS
Qlik AutoML	✗	Unlimited ML experiments and 2 ML models included.
Reporting Service	✗	100 reports / month included.
Smart visualizations	✓	✓
Visual data preparation	✓	✓
Single Sign-On	✗	✓
Usage monitoring	✓	✓
API integrations	✓	✓
Support	✓	✓
Qlik SAP Connector	✓	+
Geocoding	✓	+

### 3) Literature Background of Qlik

Kiula and friends conducted a research using the data of an insurance company in Kenya between 2014-2018. QlikView is recommended as a simple and shareable business intelligence application. It was also suggested that it can be used for data analytics and visualization [33]. The healthcare/insurance industry analysis was performed on data from three healthcare/insurance industry ERPs in Kenya. Based on data access and monthly comparison, data were obtained from the

intersection of the three systems for March and April 2018. The comparison and summing are done using functions from QlikView and Microsoft Excel. Inconsistencies of significant monetary value were observed in the data between the three systems. Data analytics using common Microsoft Excel and QlikView tools is proposed to identify inconsistencies and limitations in healthcare/insurance ERPs [34]. Ilieva and friends worked on proposing a method for measuring and analyzing services rendered in information technology

helpdesk teams. The aim of the study was to monitor and optimize these services. QlikView was used to realize this. The results show the satisfaction of the customers with the helpdesk services were carried out and visualized with QlikView [35]. Delgado and friends developed, a web software using SQL server database and QlikView business intelligence tool. As a result, it has been suggested that a system has been developed that can help make the right decisions in order to increase the efficiency of the health institution studied and this system can be used in similar enterprises [36].

#### D. Tableau

##### 1) About Tableau

Tableau was founded in 2003. It is one of the essential tools for data analytics and data visualization. It can be learned easily even without any prior programming knowledge. The amount of data analyzed in Tableau depends on memory capacity. Tableau can connect and access data from different data sources prior to data analysis. SQL, TXT, CSV is some of the data sources which can be access and also Tableau could be accessed from cloud systems such as Azure and Big Data [18].

Connecting and visualizing data is one of the key features of this tool. Sharing of data is facilitated via web and mobile [10].

It has a user-friendly interface, being easily integrated with third-party software, providing mobile support for dashboard reports, user forums, customer service, and low cost can be considered as advantages. Difficulty in initial data preparation and the tables do not provide all statistical features can be considered as disadvantages [18]. Tableau Desktop has two

different editions; Professional which supports all data sources and connects to Tableau server for web-based analytics and Personal supports xls(x), accdb and csv formats of data sources and does not have server support. Both editions can be used for academic or commercial [10]. Tableau Server is a mobile online business intelligence solution. Tableau Online can be used for publish reports with Tableau Desktop. Tableau Public is for interactive data visualization on the web. By connecting to data, it can create dashboards and can be published directly on the web. Tableau Reader is a free desktop application that can be used to view dashboards developed in Tableau Desktop [10].

##### 2) Tableau Versions

In order to publish the work done on the cloud or server, it is necessary to have one of three different versions which are Tableau Creator, Tableau Explorer, Tableau Viewer. The comparison of these three versions is shown in Table 6 [37].

##### 3) Literature Background of Tableau

Musunuru et al. made an analyze with using donation data from the database of AidData.org. They applied the Hadoop data and displayed the results [38]. Mahatma et al. presented a data visualization approach using Tableau and stated that it allows effective creation of dashboards [39]. Erazo and friends determine the degree of indoor air pollution using time series for data collection and to perform the relevant analysis of this data, its consequences and action to prevent exposure risks to pollutants [40].

TABLE VI  
COMPARISON of TABLEAU VERSIONS

	Tableau Creator	Tableau Explorer	Tableau Viewer
Manage users and permissions	✓	✓	✗
Server administration	✓	✗	✗
Set data quality warnings	✓	✓	✗
Download summary data	✓	✓	✓
Download full data	✓	✓	✗
Create and publish new data sources	✓	✗	✓
Publish and run flows	✓	✗	✗
Schedule flows	✓	✓	✗
Export data (.tde, .hyper or .csv)	✓	✗	✗
Download visualizations as images (.pdf, .png)	✓	✓	✓

### III. COMPARISON OF BI TOOLS

Table 7 shows the comparison of SAP Lumira, SAP Analytic Clouds, Power BI, Tableau and Qlik business intelligence tools. When Data Source Connections are compared, it is seen that although they are not developed by SAP as seen in Table 7, connections to SAP ERP and SAP HANA can be made from Power BI, Tableau and Qlik applications [41].

While it is observed that ODBC connection cannot be made through SAP's business intelligence products, it is observed that there is no JDBC connection over Power BI and Tableau. There are some restrictions on making JDBC connection over Qlik application, but there are also restrictions on making direct data source connection to social media applications via SAP BI applications. As seen in Table 8, although they are not applications developed by SAP, direct connections can be made from Power BI, Tableau and Qlik applications to SAP BW Bex



and SAP BW Info Provider data sources. In addition, it is possible to connect to SAP BW Live/Import data sources as restrictions. However, in order to use SAP BOBJ universes as data sources, it is necessary to use SAP BI applications [41].

Table 9 shows the data modeling capabilities of the tools. All of them have append, union, join, merge, dimension, measure, hierarchical capability and data type conversion features, but there are some restrictions to be able to use join, merge and hierarchical capability in SAP Analytic Cloud [41].

Visualization is one of the most important things in BI tools. Since the data models built in the background are not visible to the end user, they may be unimportant for them. In Table 10, visualization options were compared. It is observed that Circle view and Grant visual can only be used in Tableau, Card and Multi Card visuals can only be used in Power BI, Gauge visual only in Power BI and Qlik, Funnel visual only in Power BI and Tableau [41].

TABLE VII  
COMPARISON of BI TOOLS with DATA SOURCE CONNECTIONS

Data Source Connections	SAP Lumira	SAP Analytic Cloud	Power BI	Tableau	Qlik
Social Media(Twitter,Facebook)	+	+	✓	✓	✓
ODBC	✗	✗	✓	✓	✓
JDBC	✓	✓	✗	✗	+
SAP Cloud Apps	✗	✓	✗	✗	✗
SAP ERP	✓	✓	✓	✓	✓
SAP S4/HANA	✓	✓	✓	✓	✓

TABLE VIII  
COMPARISON OF BI TOOLS with SAP DATA SOURCE CONNECTIVITY

SAP Connectivity	SAP Lumira	SAP Analytic Cloud	Power BI	Tableau	Qlik
SAP BW Bex Queries	✓	✓	✓	✓	✓
SAP BW Info Provider	✓	✓	✓	✓	✓
SAP BW Live/Import	✓	✓	+	+	+
SAP BOBJ Universe Access	✓	✓	✗	✗	✗

TABLE IX  
COMPARISON of BI TOOLS with DATA MODELING

Data Modeling	SAP Lumira	SAP Analytic Cloud	Power BI	Tableau	Qlik
Append/Union	✓	✓	✓	✓	✓
Join / Merge	✓	+	✓	✓	✓
Dimension and Measures	✓	✓	✓	✓	✓
Hierarchical Capabilities(Date/Geo vs.)	✓	+	✓	✓	✓
Data Type Conversion	✓	✓	✓	✓	✓

As can be seen in Table 11, the ability to leave comments on the report is available in all tools, but there are limitations in SAP Lumira and Qlik. Notification and adding alerts are available for SAP Analytics Cloud, Power BI and Tableau tools. It is also very important that the reports made in BI tools can be downloaded and distributed, and that they can be transmitted to other users by mail or other methods without the need to connect to BI environments. For this, reports made in BI tools can be downloaded and distributed in various formats.

Reports can be imported as excel, csv and pdf in all the tools we compared, while importing in ppt format is possible in Power BI and Qlik applications [41]. The data which is very important for companies and should not go out from report. It is a great responsibility to ensure the security of this data. Table 12 gives comparisons about security. Companies or individual users want to try the tool before purchasing it. Availability of trial versions is also presented in Table 13 comparatively [41].

TABLE X  
BI TOOLS COMPARISON of BI TOOLS with DATA VISUALIZATION

Data Visualizations	SAP Lumira	SAP Analytic Cloud	Power BI	Tableau	Qlik
Line	✓	✓	✓	✓	✓
Bar	✓	✓	✓	✓	✓
Stacked Bar	✓	✓	✓	✓	✓
Column	✓	✓	✓	✓	✓
Circle View	✗	✗	✗	✓	✗
Area	✓	✓	✓	✓	✓
Scatter	✓	✓	✓	✓	✓
Histogram	✗	✓	+	✓	✓
Stacked Column	✓	✓	✓	✓	✓
Stacked Area	✓	✓	✓	✓	✓
Pie	✓	✓	✓	✓	✓
Waterfall	✓	✓	✓	✓	✓
Scatter	✓	✓	✓	✓	✓
Bubble	✓	✓	✓	✓	✓
Gauge	✗	✗	✓	✗	✓
Bullet	✗	✓	+	✓	✗
Spark Line	+	+	+	✓	✗
Box Plot	✓	✓	✗	✓	✓
Tree Map	✓	✓	✓	✓	✓
Gantt	✗	✗	✗	✓	✗
Funnel	✓	✗	✓	✓	✗
Distribution Plot	✗	✗	+	✓	✓
Line and Bar (Combo)	✓	✓	✓	✓	✓
Donut	✓	✓	✓	✓	✓
Marimekko	✓	✓	+	+	✗
Parallel Coordinates	✓	✗	✗	✗	✗
Text Table / Cross Tab	✓	✓	✓	✓	✓
Time-Series	✓	✓	+	✓	✓
Word/Tag Cloud	✓	+	+	✓	✗
Numeric Point/KPI	✓	✓	✓	✓	✓
Card/Multi Card	✗	✗	✓	✗	✗
Bubble Map	✓	✓	✓	✓	✓
Symbol Maps	✓	✓	✗	✓	✗
Flow Map	✗	✓	✗	+	+

After the product is purchased, training support and assistance in case of any problem are very important in order to learn and use this product more accurately. Companies that are good at these issues can go one step ahead. Comparison of training and support is given in Table 13 and Table 14 [42-47].

There are different languages used in different countries, and users may want to use these tools in their native language. Language support comparison is as in table 15 [42-47].

TABLE XI  
COMPARISON of BI TOOLS with EXPORT CAPABILITY

Exports and alerts	SAP Lumira	SAP Analytic Cloud	Power BI	Tableau	Qlik
Comment/Annotation	+	✓	✓	✓	+
Windows Desktop App	✓	✗	✓	✓	✓
Broadcasting	+	✓	+	+	+
Notification / Alert	✗	✓	✓	✓	✗
Export to Excel or csv	✓	✓	✓	✓	✓
Export to ppt	✗	✗	✓	✗	✓
Export to PDF	✓	✓	✓	✓	✓

TABLE XII  
COMPARISON of BI TOOLS with SECURITY AND TRIAL

Security and Trial	SAP Lumira	SAP Analytic Cloud	Power BI	Tableau	Qlik
Security	Role based security is maintained in the BI Platform.	Role based security is maintained within the tool itself	User is linked to their Office 365 account.SSO and gateways need to configured for data refresh..	Each user has a username and password linked to Tableau	All authentication is managed by Qlik Sense Proxy Service(OPS).The OPS authentication is regardless of Qlik Sense client type for all users.
Trial	Free for 30 days	Free for 30 days	Power BI Desktop is free.	Tableau Creator is free for 14 days. Tableau public and reader are free.	Qlik Sense cloud and Desktop are free. Qlik View Personal edition is free.

TABLE XIII  
COMPARISON of BI TOOLS with SUPPORT

Support	SAP Lumira	SAP Analytic Cloud	Power BI	Tableau	Qlik
Email/Help Desk	✗	✓	✓	✓	✓
Knowledge Base	✗	✓	✓	✓	✓
Phone Support	✗	✓	✓	✓	✓
24/7 (Live Rep)	✓	✗	✓	✓	✓
Chat	✗	✓	✓	✓	✓
HQ Location	Germany	Germany	USA	USA	USA
Ownership	NYSE:SAP	NYSE:SAP	Microsoft	Tableau Software	Qlik
Discussion	SAP Lumira Community	Official SAP Analytics Cloud Community	Microsoft Power BI Desktop Community	Tableau Desktop Community	Official Qlik Sense Community



TABLE XIV  
COMPARISON of BI TOOLS with TRAINING

Training	SAP Lumira	SAP Analytic Cloud	Power BI	Tableau	Qlik
In Person	✘	✘	✔	✔	✔
Live Online	✔	✔	✔	✔	✔
Webinars	✔	✔	✔	✔	✔
Documentation	✔	✔	✔	✔	✔

Other strengths and weaknesses of the tools are presented in tables in Table 16 [41]. Even if companies examine all the features and choose the most suitable vehicle for them, if the budget is not enough, they can afford to cut down on some features. Therefore, price can be one of the most important

criteria. In Table 17 [19,28,32,37,48], price comparisons of the products are given. Access to this price information was made on September 3, 2022 with a computer used over Turkey, and prices may change in the future and differ from country to country.

TABLE XV  
COMPARISON of BI TOOLS with SUPPORTED LANGUAGES

Supported Languages	SAP Lumira	SAP Analytic Cloud	Power BI	Tableau	Qlik
languages	Czech, German, English, French, Hungarian, Japanese, Korean, Portuguese, Russian, Spanish, Turkish, Chinese (Simplified)	Czech, German, English, French, Italian, Japanese, Korean, Polish, Portuguese, Russian, Spanish, Chinese (Simplified)	Arabic, Bulgarian, Catalan, Czech, Danish, German, Greek, English, Estonian, Basque, Finnish, French, Hebrew, Hindi, Croatian, Hungarian, Indonesian, Italian, Japanese, Korean, Latvian, Lithuanian, Malay, Dutch, Norwegian, Polish, Portuguese, Romanian, Russian, Slovak, Slovenian, Spanish, Serbian, Swedish, Thai, Turkish, Ukrainian, Vietnamese, Chinese (Simplified)	German, French, Japanese, Korean, Portuguese, Spanish, Chinese (Simplified)	German, English, French, Italian, Japanese, Korean, Dutch, Polish, Portuguese, Russian, Spanish, Swedish, Turkish, Chinese (Simplified)

TABLE XVI  
BI TOOLS COMPARISON FOR OTHER FUTURES

SAP Lumira	SAP Analytic Cloud	Power BI	Tableau	Qlik
Interoperability with SAP Lumira Designer	Cloud based solution for BI.	Free desktop and integration with office 365 like Microsoft Teams.	New tool for extensive data prep.	Extensive scripting ability within applications
SDK component for custom data Access and visualization	Intuitive collaboration and commenting features	Good connectivity to Microsoft and Azure based data sources	Ease of use and robust data connectivity with support to advanced functions	Powerful in-memory engine with data indexing
Live BW connectivity using native BICS data services	Subscription model with regular updates from SAP	Natural language processing with Q&A features	API's for customizations and collaborate features in server	Extensions in qlik nprinting.

TABLE XVII  
BI TOOLS COMPARISON FOR PRICES

Product	Price
Power BI Desktop	Free
Power BI Pro	\$9.99 Per user/month
Power BI Premium Per user	\$20 Per user/month
Power BI Premium per capacity	\$4,995 Per capacity/month
SAP Lumira Personal edition	free
SAP Lumira, Standard edition	\$185 per user
Qlik Sense Business	\$30USD/user/month. Billed Annually.
Qlik Sense Enterprise Edition	Contact QlikView Pricing per user on Subscription or Perpetual basis
SAP Analytics Cloud Trial	Free for 30 days
SAP Analytics Cloud Business Intelligence	30 EUR per User / Month
SAP Analytics Cloud Planning	Price upon request
Tableau Creator for Cloud	70\$ user/month
Tableau Explorer for Cloud	42\$ user/month
Tableau Viewer for Cloud	15\$ user/month
Tableau Creator for Server	70\$ user/month
Tableau Explorer for Server	35\$ user/month
Tableau Viewer for Server	12\$ user/month

#### IV. DISCUSSIONS

As a result, considering the data taken from a job posting site in Turkey in the first week of 2022, it has been observed that the most used business intelligence tools of companies are Power BI, SAP Business Intelligence tools, Qlik Business Intelligence tools and Tableau. When these 4 business intelligence tools are compared over the tables like chapter III, it has been observed that each business intelligence tool has its own advantages and disadvantages. However, it has been concluded that when choosing the business intelligence tool they will use, companies should consider what field they operate in, why they need a business intelligence tool, and whether mobile access is important. It also emerged that companies have to decide whether visibility, speed, variety of available data sources, export capacity, security or cost were more important and make a choice accordingly.

#### V. CONCLUSION

In this study, the most used business intelligence tools were determined with the help of the data obtained from a job posting site in Turkey and it was aimed to facilitate the decision making of the companies when choosing the business intelligence tool to be used by making comparisons on them. In future studies, the number of these job posting sites and the date range of the postings may be increased.

The research can be expanded not only on a country basis, but also worldwide. By conducting a survey with the companies using these business intelligence tools, their satisfaction can be researched and the companies that will make a choice can be helped more.

#### ACKNOWLEDGMENT

This study has been supported by Marmara University Scientific Research Projects Coordination Unit under grant number FYL-2022-10762.

#### REFERENCES

- [1] H. Ates "Karar Vermede İş Zekasının Önemi: Tekstil Sektöründe Bir Araştırma", T.C. Dokuz Eylül Üniversitesi Sosyal Bilimler Enstitüsü İşletme Anabilim Dalı Üretim Yönetimi ve Endüstri İşletmeciliği Programı Yüksek Lisans Tezi, 2008
- [2] Luhn, Hans P. "The Automatic Creation of Literature Abstracts." IBM Journal of Research and Development, 159-165 (1958).
- [3] Sabanovic, Adis, Klaus Solberg Söilen. "Customers' Expectations and Needs in the Business Intelligence Software Market." Journal of Intelligence Studies in Business 2.1 (2012).
- [4] KARIM, Akram Jalal. The value of competitive business intelligence system (CBIS) to stimulate competitiveness in global market. International Journal of Business and Social Science, 2.19 , (2011).
- [5] Zeng L., Li L., Duan L. "Business intelligence in enterprise computing environment. Information Technology and Management." 13 (4):297-310 (2012).
- [6] Akçetin E., Çelik U., Takçı H. "Lojistik ve Denizcilik Sektörü Açısından Veri Madenciliği Uygulamalarının Önemi". Journal of ETA Maritime Science, 1(2): 73-80 (2013).
- [7] Yılmaz E. "İş Zekası Araçları Ve Ormancılık". İstanbul Üniversitesi Orman Fakültesi Dergisi, 55(1):135-146 (2005).
- [8] Dursun T., Kaya S. "İş Zekası Ve Sosyal Medya Uygulamaları". Maltepe Üniversitesi İktisadi Ve İdari Bilimler Fakültesi Ekonomik, Toplumsal Ve Siyasal Analiz Dergisi, 2015/II(6):174-198 (2015).
- [9] M. Damar, G. Özdağoğlu, A. Özdağoğlu. "İş Zekası ve İlgili Teknolojileri Konu Alan Araştırmalara Küresel Ölçekte Bilimetric Bakış", BEYDER / 2018, 13:2 (197-218)(2018).
- [10] K. Gowthami, M.R. Pavan Kumar. "Study on Business Intelligence Tools for Enterprise Dashboard Development", International Research Journal of Engineering and Technology (IRJET) e-ISSN: 2395 -0056 Volume: 04 Issue: 04 , (2017).
- [11] D. Yıldız. "Bir İş Zekası Uygulaması ve Başarısının Değerlendirilmesi", ASBİ Abant Sosyal Bilimler Dergisi, 2021, Cilt: 21, Sayı: 1/Bahar: 91-111.
- [12] Akçay, M., Kasım Ö., Taşdelen, Z. "ASP. NET And MVC Based Responsive Web Application". Eskişehir Turkic World Application and Research Center Journal of Informatics, 2(1), 34-41.
- [13] Iyer, A., Bali, S., Kumar, I., Churi, P., & Mistry, K. (2019, April). "Presentation Abstraction Control Architecture Pattern in Business Intelligence". In International Conference on Advances in Computing and Data Sciences (pp. 666-679).
- [14] <https://www.kariyer.net/> (January 8, 2022).
- [15] <https://www.kariyer.net/is-ilanlari/?kw=is%20zekasi&is=1> (January 8, 2022).
- [16] R.H.M.S. Ferreira, L.O. Figueiredo, R.B.C. Lima. "IIoT Solution for predictive monitoring based on vibration data from motors using Microsoft Azure machine learning studio and Power BI", 2021 14th IEEE International Conference on Industry Applications.
- [17] <https://docs.microsoft.com/en-us/power-bi/fundamentals/power-bi-overview> (28.04.2022)
- [18] C.S. Reddy, R.S. Sangam , B.S. Rao. "A Survey on Business Intelligence Tools for Marketing, Financial, and Transportation Services", Second International Conference on SCI 2018, Volume 2
- [19] <https://powerbi.microsoft.com/en-us/pricing/> (Sep 4, 2022).
- [20] P. Rajesh, Bharadwaj, M. Alam, M. Tahernezhad. "A Data Science Approach to Football Team Player Selection", 2020 IEEE International Conference on Electro Information Technology (EIT)
- [21] J. Hewko, R. Sullivan, S. Reige, M. El-Hajj. "Data Mining in the NBA: An Applied Approach", 2019 IEEE 10th Annual Ubiquitous Computing, Electronics & Mobile Communication Conference (UEMCON)
- [22] Z. Desai, K. Anklesaria, H. Balasubramaniam. "Business Intelligence Visualization Using Deep Learning Based Sentiment Analysis on Amazon Review Data", 12th International Conference on Computing Communication and Networking Technologies (ICCCNT) | 978-1-7281-8595-8/21/2021.
- [23] <https://www.sap.com/products/bi-platform.html> (May 7, 2022).
- [24] <https://www.techtarget.com/searchsap/definition/SAP-BusinessObjects-BI> (May 7, 2022).
- [25] <https://blogs.sap.com/2013/11/28/sap-lumira-standard-edition-free-for-30-days-heres-how/>(Sep 4, 2022).
- [26] <https://userapps.support.sap.com/sap/support/knowledge/en/2236323> (Sep 4, 2022).
- [27] <https://detayssoft.com/en-US/sap-analytics-cloud-pg-34> (May 7, 2022)
- [28] <https://www.sap.com/turkey/products/technology-platform/cloud-analytics/pricing.html> (Sep 4, 2022).
- [29] D.M. Nazarov, A.D. Nazarov, D.B. KovtunBuilding. "Technology and Predictive Analytics Models in the SAP Analytic Cloud Digital Service", 2020 IEEE 22nd Conference on Business Informatics (CBI)
- [30] S. Nararya, M. Saputra, W. Puspitasari. "Automation in Financial Reporting by using Predictive Analytics in SAP Analytics Cloud for Gold Mining Industry: a Case Study", 2021 International Conference on ICT for Smart Society (ICISS)
- [31] D. M. Nazarov, D. B. Kovtun, T. N. Reichert. "SAP Analytics Cloud: intellectual analysis of small and medium-sized business activities in Russia in the context of COVID-19", 2020 IEEE 14th International Conference on Application of Information and Communication Technologies (AICT)
- [32] <https://www.qlik.com/us/pricing> (Sep 4, 2022).
- [33] M. Kiula, C. Chege, K. Kahenya. "Application of Data Visualization for Improved Healthcare Insurance Management using QlikView", IST-Africa 2019 Conference Proceedings Paul Cunningham and Miriam Cunningham (Eds) IIMC International Information Management Corporation, 2019 ISBN: 978-1-905824-62-2.
- [34] M.Kiula, C. Chege. "Identification of the Limitations of Healthcare Service/Insurance Industry ERPs on Data Flow using QlikView and MS Excel", IST-Africa 2020 Conference Proceedings Miriam Cunningham

and Paul Cunningham (Eds) IST-Africa Institute and IIMC, 2020 ISBN: 978-1-905824-65-6

- [35] R. Ilieva, K. Anguelov, D. Gashurova. "Monitoring and Optimization of e-Services in IT Service Desk Systems", 2016 19th International Symposium on Electrical Apparatus and Technologies (SIELA)
- [36] A. Delgado, F. Rosas, C. Carbajal. "System of business intelligence in a health organization using the kimball methodology", CHILECON 2019, October 29-31, Valpara'iso, Chile
- [37] <https://www.tableau.com/pricing/teams-orgs#online> (Sep 4, 2022).
- [38] H. Musunuru, R. Lee, T. Matsuo. "Improving Lives Through Donation Analysis", 2017 International Conference on Computational Science and Computational Intelligence
- [39] K. Mahatma, B. Waseso, W. Darwin. "The Design and Implementation of Data Visualization for Integrated Referral and Service System", 2018 International Conference on ICT for Rural Development (IC-ICTRuDev)
- [40] B. Erazo, P. Peláez, J. Achig, F.T. León, D. Marcillo. "Analysis of air pollution in single-family homes by using the time series", 2017 12th Iberian Conference on Information Systems and Technologies (CISTI)
- [41] <https://www.youtube.com/watch?v=0QAXIWFton4> (Sep 4, 2022).
- [42] <https://www.softwareadvice.com/bi/sap-lumira-profile/vs/qlik-sense/sap-analytics-cloud/> (Sep 4, 2022).
- [43] <https://www.softwareadvice.com/bi/sap-lumira-profile/vs/microsoft-power-bi/tableau/> (Sep 4, 2022).
- [44] <https://www.g2.com/products/qlik-sense/reviews> (Sep 4, 2022).
- [45] <https://www.g2.com/products/sap-analytics-cloud/reviews> (Sep 4, 2022).
- [46] <https://www.g2.com/products/microsoft-microsoft-power-bi-desktop/reviews> (Sep 4, 2022).
- [47] <https://www.g2.com/products/sap-lumira/reviews#details> (Sep 4, 2022).
- [48] <https://www.g2.com/products/sap-lumira/pricing> (Sep 4, 2022).



**KAZIM YILDIZ** completed his PhD in Marmara University Computer-Control Education in 2014, he completed his PhD. Between 2015 (October) - 2016 (October), He worked as a postdoctoral researcher at Georgia Institute of Technology School of Electrical and Computer Engineering in USA. He received the title of Associate Professor in Computer Science and Engineering in 2020. His research interests are AI, deep learning, machine learning and computer vision.

## BIOGRAPHIES



**MURAT OZDEMIR** In 2019, he completed his undergraduate education at Sakarya University, Department of Computer Engineering. He has been studying for a master's degree in computer engineering at Marmara University since 2021. He worked as a business intelligence engineer in various companies from 2017 to the

end of 2021. He has been working as a senior data engineer in a private company in Turkey since the beginning of 2022.



**EYUP EMRE ULKU** Dr. Eyup Emre Ulku is an Assistant Professor in the Department of Computer Engineering at Marmara University, Turkey. He completed his Ph.D. in Computer Engineering at Marmara University in 2018. His research interests include wireless communications, ad hoc networks, image processing, deep

learning and educational technologies in engineering education.

# Negative Capacitance Phenomenon in GaAs-Based MIS Devices Under Ionizing Radiation

Ahmet Kaymaz

**Abstract**— This study focuses on the abnormal peaks observed in voltage-dependent capacitance graphs and negative capacitance behaviours of the GaAs-based MIS devices for the unirradiated sample and after exposing the device to 5 and 10 kGy ionizing (gamma) radiation doses. Experimental results showed that the amplitude of the abnormal peaks, observed at about 1.75 V, increases with the irradiation dose. The peak point was also shifted toward the positive biases after irradiation. Furthermore, the conductance values increased rapidly and reached their maximum level, while the capacitance values reached their minimum level in the high voltage biases. It is known that this situation is directly related to the inductive behaviour of the MIS devices. However, it has been determined that the MIS device's inductive behaviour is more effective after irradiation. These behaviours can be observed because of the ionization process, the MIS device's series resistance, surface states, and due to some displacement damages caused by ionizing radiation. Therefore, the series resistance and the radiation-induced surface states were obtained to clarify the impact of radiation on the device. It was seen that the radiation-induced surface states changed around  $3 \times 10^{12} \text{ eV}^{-1} \text{ cm}^{-2}$  for the maximum cumulative dose (10 kGy), and the series resistance values changed to less than  $2 \Omega$ . As a result, the degradation in the GaAs-based MIS device was determined to be insignificant for 10 kGy doses. Therefore, this MIS device can be safely used as an electronic component in radiation environments such as nuclear plants and satellite systems.

**Index Terms**— Abnormal/Anomalous peak, GaAs-based devices, Ionizing radiation, MIS devices, Negative capacitance.

## I. INTRODUCTION

IT IS KNOWN THAT Schottky diodes/structures are obtained by contacting metal and semiconductor (M/S) materials with or without oxide/insulator or ferroelectric interlayers [1]. These structures are also the basis of many electronic devices, such as photodiodes, photodetectors, transistors, and solar cells [2]. Interfacial layers can be grown between the M/S interface by native or some special methods [3]–[5]. Many ways are used to deposit an interfacial layer, such as the sol-gel method [6], [7], chemical vapour


deposition [8], electrospinning [9], [10], molecular beam layer deposition [11], and spin coating [12] as well as other techniques [13]. In this study, the oxide layer was grown by a natural method due to the stable behaviour of the Si and SiO<sub>2</sub> combination [5]. The oxide interlayer also controls interdiffusions between the M/S interface and prevents possible chemical reactions. Furthermore, the devices can gain better capacitive features due to the dielectric effect of the oxide interfacial layer [14].

When the interfacial layer obtained using an oxide or an insulating material in the devices is thinner than 500 Å, this device can be used as a diode [15]. Such devices are referred to as Schottky diode/structure due to the critical works in this area proposed by W. H. Schottky. If the thickness of the oxide/insulator interlayer is greater than 500 Å, such a structure is defined as a capacitor rather than a diode. It is well-known that these devices cannot provide carrier conduction at the M/S interface and, therefore, can store electrical charges and energy [15], [16]. In this study, the thickness of the natural oxide layer for the Au/n-GaAs/Au-Ge type Schottky device was obtained as approximately 23.4 Å using Nicollian and Goetzberger calculation method [17]. Therefore, it can be defined as a metal-insulator-semiconductor (MIS) type Schottky diode or MIS device.

GaAs in the III-V semiconductor group have a wide-direct bandgap and high saturation velocity. GaAs-based designs are also high-speed and low-power consumption devices because of their high mobility, which is approximately six times higher than silicon [2], [18]. These properties make it highly suitable for fabricating M/S-type Schottky devices and make GaAs preferable as a semiconductor for high-power devices used at high frequencies [1], [19], [20]. On the other hand, it has been reported in some previous studies that GaAs-based devices are less affected by radiation damage than other devices [21]. Therefore, GaAs-based materials could be critical devices for future improvement technology. As a result, this study, which aims to understand the radiation impact of GaAs-based devices for attractive voltage regions, is crucial because of the need to reliably/safely use devices that can operate under radiation, such as biomedical devices and satellite systems or nuclear plant devices.

As well as optoelectronic applications [22], there are many reports on Schottky devices with various interfacial layers to obtain devices with better electrical and dielectric properties [23]–[28]. However, it is essential to investigate the ionizing radiation effects of such devices, especially GaAs-based devices, because of their superior features and interesting characteristic behaviours, especially at sufficient high positive voltages (accumulation region). When the voltage-dependent

AHMET KAYMAZ, is with Department of Mechatronics Engineering, Karabuk University, Karabük, Turkey (e-mail: [ahmetkaymaz@karabuk.edu.tr](mailto:ahmetkaymaz@karabuk.edu.tr)).

 <https://orcid.org/0000-0003-2262-1599>

Manuscript received Nov 25, 2022; accepted Feb 23, 2023.

DOI: [10.17694/bajece.1210121](https://doi.org/10.17694/bajece.1210121)



capacitance ( $C$ - $V$ ) characteristics of GaAs-based devices are examined at sufficiently forward biases, it becomes possible to encounter negative capacitance values in this voltage region. Negative capacitance phenomenon can occur because of the series resistance, surface states, and minority carrier injection [29], [30]. The relaxation times of the surface states can also affect negative capacitance behaviour depending on frequency [31], [32]. On the other hand, some advantages of the negative capacitance effect in ferroelectric materials and the advantages of this effect have become an important topic in recent years [33]. And many studies have been carried out on these subjects [29]–[34]. However, the ionizing radiation effects of such devices have not been adequately studied, especially in sufficient forward biases where negative capacitance values are observed. Therefore, it is predictable that this study can significantly contribute to the literature to understand the device's radiation dependency, which has negative capacitance and anomalous/abnormal peak behaviour.

The type and dose of the ionizing radiation can affect the devices' electrical, optoelectronic, and dielectric features [28]. Many energetic particles, such as neutrons, alpha, and beta, as well as electromagnetic radiations, such as  $X$  and  $\gamma$  rays, are in the category of ionizing radiation. These high energy sources (ionizing radiation sources), which emit energetic photons of approximately 1 MeV, can cause events called displacement damage in electronic devices [35]. Displacement damage, defined as the separation of atoms from the standard lattice regions in the target material, can lead to new energy levels formation in the semiconductor band gap. Briefly stated, displacement damage caused by ionizing radiations leads to considerable changes in devices' electrical, optoelectronic, and dielectric features, which makes the reliability of devices used in radiation environments questionable. Therefore, the radiation effects of the electronic devices which possible use under ionizing radiation needs to be carefully studied and understood. The best way to understand these effects is to examine the device's voltage-dependent capacitance-conductance ( $C$ - $G/\omega$ - $V$ ) characteristics and other voltage-dependent current ( $I$ - $V$ ) characteristics. Since this study focuses on the negative capacitance behaviour with the abnormal peak phenomenon observed in  $C$ - $V$  graphs, only the  $C$ - $V$  and  $G/\omega$ - $V$  graphs of the GaAs-based MIS device have been discussed with some critical device parameters such as surface states ( $N_{ss}$ ) and the series resistance ( $R_s$ ).

## II. MATERIALS AND METHODS

The fabrication processes of the GaAs-based with a natural oxide layer MIS device can be summarized in several primary stages. The first step is the chemical cleaning process applied to remove organic and metallic impurities from the surface of a (100) oriented n-type GaAs wafer. At this stage, the wafer was first degreased for about five minutes in some organic solvent mixtures well known in the literature and then etched several times in some solutions. At each step, the wafer was quenched in deionized water. Upon completion of the chemical cleaning process, it was quickly dried in a nitrogen gas environment.

In the second stage, before the formation of the ohmic contact, gold (Au) metal was doped with Ge to obtain a high-

quality ohmic contact [36]. Then the Au-Ge mixture (88% Au and 12% Ge) was evaporated onto the matte (back) surface of the n-type GaAs wafer in a high vacuum system. Afterwards, the n-GaAs/Au-Ge wafer was annealed at 450°C for about six-seven minutes in nitrogen ambient to reduce the ohmic contact resistivity, and 200 nm thick ohmic contact was obtained. Before proceeding to the Schottky contact process in the third stage of the production process, the wafer was kept in a clean room for a few days. Thus, the formation of a very thin natural oxide layer ( $\approx 2.3$  nm) was allowed.

In the final stage of the production process, the Au metal with 99.999% purity was evaporated to the masked front surface of the n-type GaAs/Au-Ge wafer using the thermal metal evaporation system. Thus, many Schottky contacts with a thickness of 200 nm and an area of  $7.85 \times 10^{-3}$  cm<sup>2</sup> were obtained. So, the production process of the Au/(n-type GaAs)/Au-Ge with natural oxide layer (GaAs-based MIS devices) was completed. The schematic view of the produced GaAs-based MIS device can be seen in Fig. (1).

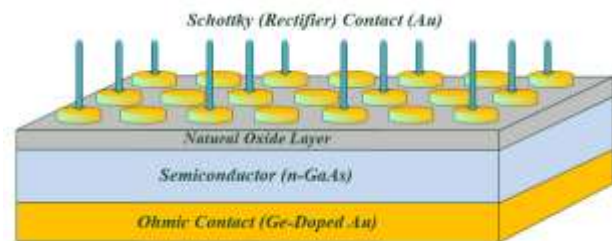


Fig.1. The representative view of the GaAs-based MIS device.

The GaAs-based MIS device's voltage-dependent capacitance and conductance values were obtained for the unirradiated sample (0 kGy) and after 5 and 10 kGy radiation doses for a wide voltage range ( $\pm 4$  V) after the production process. The vpf-475 cryostat was used for measurements to rule out possible external influences, and Hewlett Packard Impedance Analyzer was used to obtain  $C$ - $G/\omega$ - $V$  data. On the other hand, the Ob-Servo Sanguis <sup>60</sup>Co irradiation source located in Ankara was used to expose the devices to ionizing radiation (gamma rays). Detailed information for the measuring system can also be available [37]. The  $C$ - $G/\omega$ - $V$  data for the unirradiated sample and after the irradiation processes were obtained at the high (500 kHz) frequency to eliminate fabrication-induced  $N_{ss}$  [38]. These measurements were carried out in the laboratory located at the Gazi University Photonics Application and Research Center.

## III. RESULTS AND DISCUSSION

Some previous studies have shown that traps/charges can significantly change  $C$ - $G/\omega$  values, especially at low frequencies below 500 kHz, because they can easily track the ac signal [39]. However, at high frequencies ( $f \geq 500$  kHz), these traps/loads cannot track the ac signal and therefore do not cause significant changes in  $C$ - $G/\omega$  values [31]. Another well-known fact is that the  $C$ - $G/\omega$ - $V$  curves of the MIS/MOS devices are highly sensitive to ionizing radiation at high frequencies due to small capacitance/conductance values, mostly in the order of nF/pF. In addition, the disappearance of the effects of fabrication-induced surface conditions can be

shown as another reason for this situation. Therefore, the  $C-G/\omega-V$  data obtained at high frequency can give us essential information about the radiation effects of the MIS devices.

The typical behaviour of the capacitance curves of an MIS/MOS device is given in the reference [40], and there are three regions, known in the literature as depletion, inversion, and accumulation regions, in these characteristics. Typical capacitance characteristics can also be divided into five areas: depletion (voltages around 0 V), weak accumulation-inversion (small positive-negative voltages), and strong accumulation-inversion (high positive-negative voltages) regions. The capacitance values in the high positive voltages can be considered almost independent of voltage in the ideal case. Their values also exhibit a curve behaviour almost independent of the frequency in the weak accumulation/inversion regions [41]. However, because of the surface states and accumulated charges, capacitance values can easily change depending on the frequency in the depletion region. It is known that the GaAs-based MIS devices'  $C-V$  characteristics may exhibit negative behaviour or a concave curvature in the accumulation region due to the surface/dipole polarization, series resistance, and the interlayer growing between the M/S interface.

Voltage- and radiation-dependent  $C-G/\omega-V$  curves given in Fig. (2) show that ionizing irradiation significantly affects the capacitance and conductance curves, especially in the accumulation and depletion regions. Besides, abnormal peak behaviours at about 1.75 V in the capacitance curves are striking for unirradiated measurements after each irradiation dose. On the other hand, all capacitance curves crossed at approximately 3.25 V, and these curves started to take negative values. It can also be seen in Fig. (2) that the peak point of the capacitance curves is shifted towards the positive voltages, and the amplitude of these peaks increases with the increase in gamma-ray amounts. These behaviours can be observed because of the ionization processes, the MIS device's series resistance, and surface states located between the M/S interface, as well as due to some effects (displacement damages) of ionizing radiation [29], [42]–[44].

The capacitance and conductance graphs show that while capacitance values decrease, conductance values increase with increasing biases in the high positive voltages. The conductance values also increase with increasing irradiation doses. Briefly stated, the conductance values increased rapidly and reached their maximum value, while the capacitance values reached their minimum value in the strong accumulation region. It is possible to say that this situation directly shows the inductive behaviour of the MIS devices. The behaviour of the negative capacitance values and increasing conductance values, depending on the increase in the radiation dose, also indicate that the inductive effect of the MIS device becomes more pronounced under ionizing radiation. Nevertheless, it is necessary to thoroughly examine the voltage-dependent resistance curves ( $R_f-V$ ) and radiation-induced surface states to understand which parameter(s) cause these behaviours. Therefore, this issue should be reconsidered when discussing the  $R_f-V$  and radiation-dependent  $N_{ss}-V$  graphs.

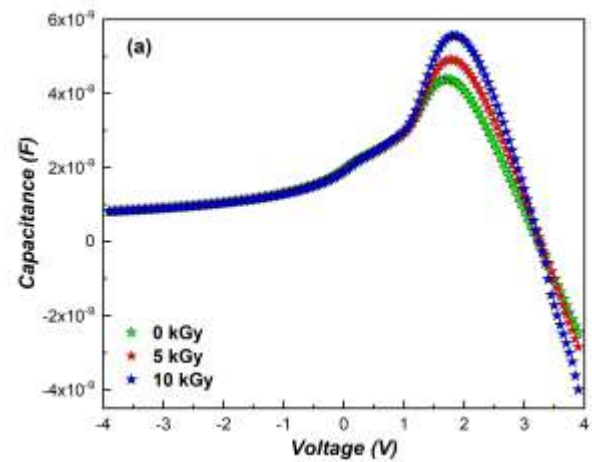


Fig.2a. The behaviour of the GaAs-based MIS device's capacitance curves under radiation.

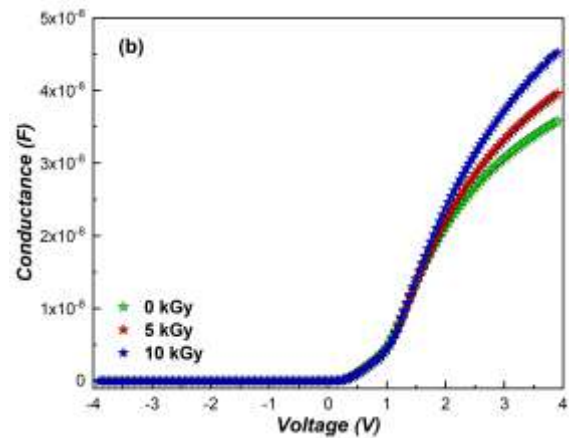


Fig.2b. The behaviour of the GaAs-based MIS device's conductance curves under radiation.

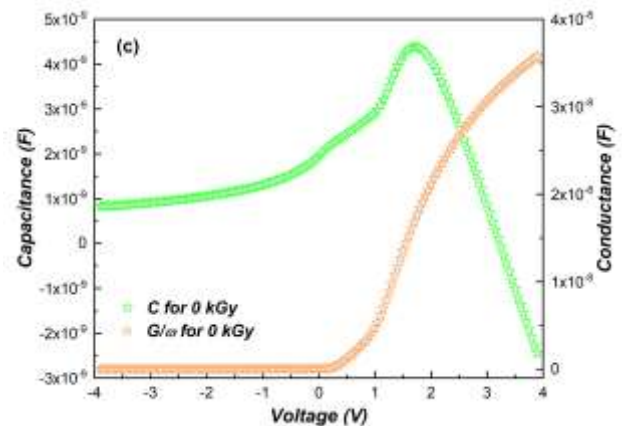


Fig.2c. The capacitance and conductance curves for the unirradiated sample.

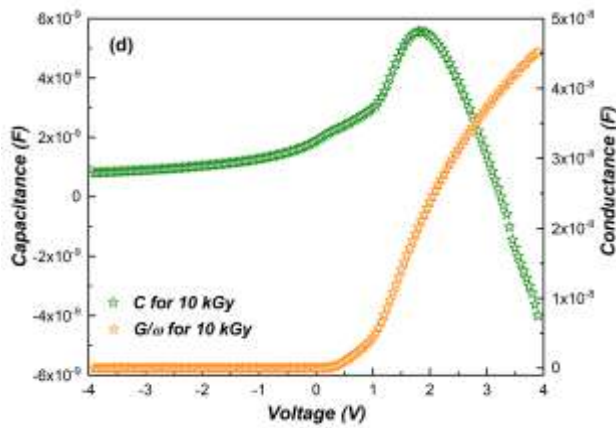


Fig.2d. The capacitance and conductance curves for 10 kGy radiation doses.

The Nicollian and Brews method ( $R_i = G_m / [(G_m)^2 + (\omega C_m)^2]$ ) can be used in order to obtain  $R_i$ - $V$  curves from the  $C$ - $G/\omega$ - $V$  data, and so the actual series resistance values ( $R_s$ ) for MIS devices can be determined from the high positive voltages of these curves [45]. Fig. (3), given  $R_i$ - $V$  curves, shows that  $R_i$  values did not show a significant change depending on the radiation dose when viewed in terms of the curve shape in all regions. Besides, these curves showed peaks in the depletion region and remained almost constant in the high positive voltages where actual series resistance values are obtained. In brief, the  $R_s$  values vary as 8.74, 7.88, and 6.82  $\Omega$  for 0, 5, and 10 kGy ionizing (gamma) radiation doses.

Such a peak behaviour in  $R_i$ - $V$  curves, thought to be due to the particular distribution of  $N_{ss}$ , has occurred in many devices [46]–[48]. However, due to the different effects of gamma irradiation on the devices, it has been determined that the series resistance values and peak amplitude may decrease or increase after the radiation process. The reduction in  $R_s$  values may be due to radiation defects and/or the annealing effect. On the other hand, the increasing behaviour is usually the result of the device's tendency to degrade under radiation. As a result, the reduction in  $R_s$  values under ionizing radiation of this MIS device is meagre and shows that the device is not prone to deterioration. Ionizing radiation changed the carrier mobility and free carrier concentration in the MIS device; therefore, a decrease in  $R_s$  values occurred. These effects have led to an increase in the conductance values in the high positive voltages.

In the previous paragraph, attention has been drawn to some resistance effects. However, it is necessary to obtain correct capacitance-conductance values ( $C_C$ - $G/\omega$ ), which are eliminated  $R_s$  effects, and radiation-induced  $N_{ss}$  to determine all results of the series resistance on the behaviour of the device's electrical characteristics. It is known that the  $C_C$  and  $G/\omega$  values can be obtained from Eqs. (1-3). Thus, the effects of  $R_s$  for each voltage region can be revealed. Therefore some graphs about the correct capacitance-conductance curves are obtained given in Figs. (5a-5d).

On the other hand, the high-low frequency method, which is used to calculate surface states, can also be used to obtain radiation-induced  $N_{ss}$  (provided in Eq. (4)) for all voltage biases [49]. Thus, the graphs of the radiation-induced  $N_{ss}$  that depend on voltage bias are determined and given in Fig. (4).

$$\alpha = G_m - [(G_m)^2 + (\omega C_m)^2] \times R_s \quad (1)$$

$$C_C = [(G_m)^2 + (\omega C_m)^2] \times C_m / [\alpha^2 + (\omega C_m)^2] \quad (2)$$

$$G_C = [(G_m)^2 + (\omega C_m)^2] \times \alpha / [\alpha^2 + (\omega C_m)^2] \quad (3)$$

$$N_{ss} = \left( \frac{1}{qA} \right) \times \left\{ \left( \frac{1}{C_{before}} - \frac{1}{C_{ox}} \right)^{-1} - \left( \frac{1}{C_{after}} - \frac{1}{C_{ox}} \right)^{-1} \right\} \quad (4)$$

Here,  $C_{before}$  represents the capacitance value of the unirradiated device, while  $C_{after}$  corresponds to the capacitance value of the irradiated sample at different doses.  $C_{ox}$  also corresponds to oxide layer capacitance. On the other hand, the interlayer capacitance ( $C_i$ ) can be calculated from the  $C$ - $G/\omega$ - $V$  data, and other parameters are also well-known in the literature ( $C_i = [1 + (G/(\omega C))^2] \times C_m$ ).

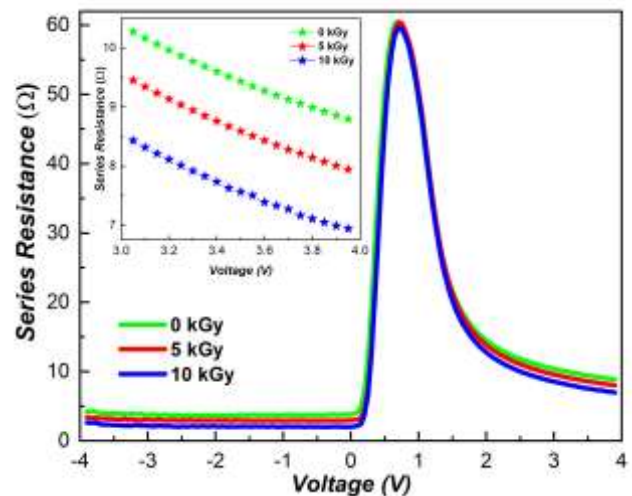


Fig.3. The GaAs-based MIS device's  $R_i$ - $V$  curves under radiation.

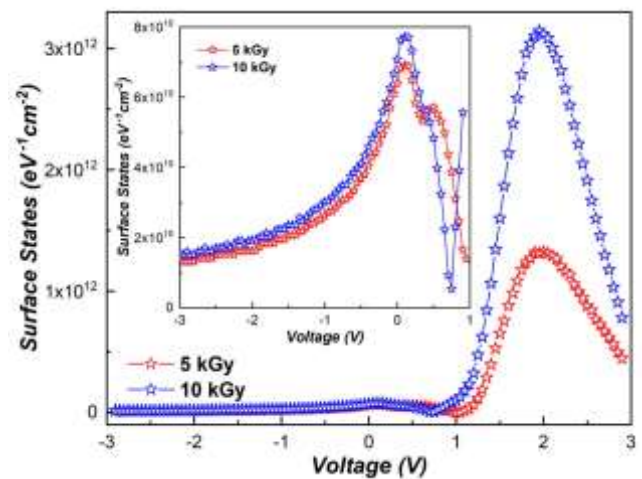


Fig.4. The behaviour of radiation-induced surface states for GaAs-based MIS device.



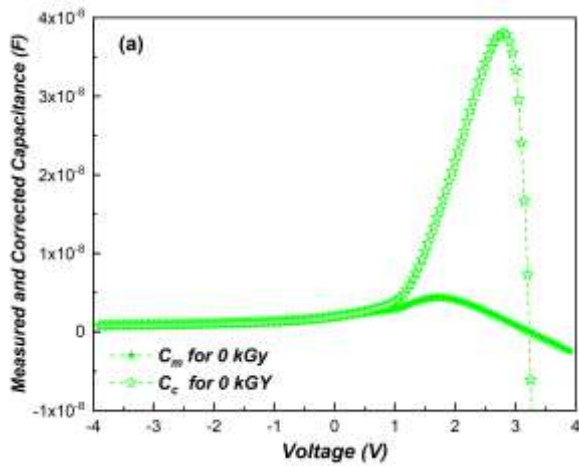


Fig.5a. The  $C_m$ - $C_c$ - $V$  graphs of the GaAs-based MIS device for the unirradiated sample.

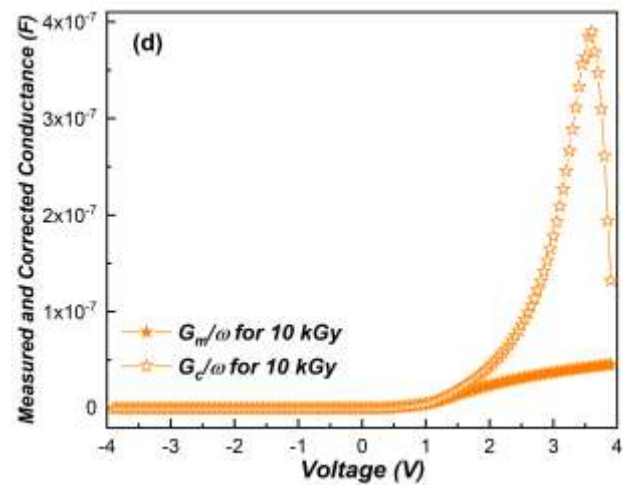


Fig.5d. The  $G_m/\omega$ - $G_c/\omega$ - $V$  graphs of the GaAs-based MIS device after 10 kGy radiation doses.

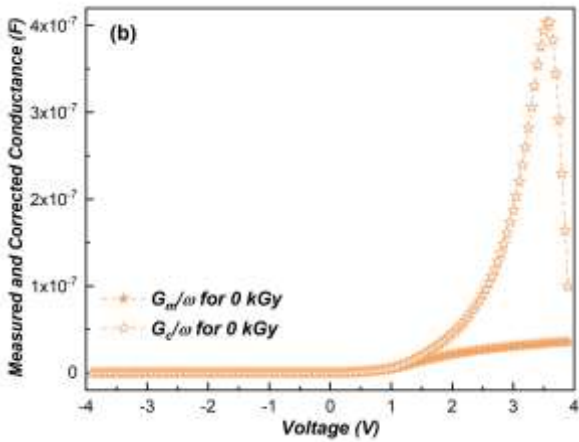


Fig.5b. The  $G_m/\omega$ - $G_c/\omega$ - $V$  graphs of the GaAs-based MIS device for the unirradiated sample.

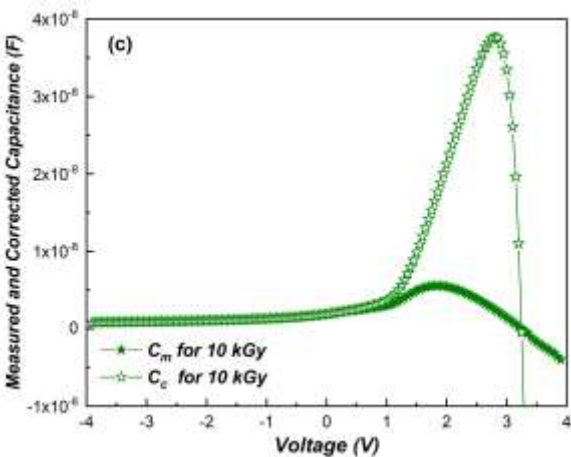


Fig.5c. The  $C_m$ - $C_c$ - $V$  graphs of the GaAs-based MIS device after 10 kGy radiation doses.

As shown in Figs. (5a-5d), the capacitance and conductance values increase significantly when the  $R_s$  effect is neglected in the positive voltages, and the peak points of the capacitance curves shift towards the positive biases. The  $G_c/\omega$ - $V$  features also give a peak before and after irradiation, although there aren't any peaks in the  $G_m/\omega$ - $V$  curves. These peaks in  $G_c/\omega$ - $V$  properties caused by interface traps indicate that charge transfer can occur via diffusion at the M/S interface (mechanical tunnelling mechanism). Briefly, series resistance can seriously affect the devices' capacitance and conductance characteristics. Furthermore, it can hide the interface trap effects, especially in the depletion region.

When the radiation-induced surface states are examined, it can be seen that they increase depending on the radiation dose and give a peak of around two volts depending on the voltage biases. In conclusion, the shifts in the capacitance curves and the peaks in conductance curves indicate the changing trap charge density with the gamma-radiation effect. The shifting of the  $C_c$ - $G_c/\omega$ - $V$  characteristics compared to the measured  $C$ - $G/\omega$ - $V$  curves also indicate charge trapping in the interlayer for the irradiated sample.

The accumulated charges in the interlayer (oxide) result in MIS devices' degradation under ionizing radiation. This degradation is because of the change in silicon dioxide's chemical and physical features as well as the passivation of dangling bonds. The generation of trap centres is also possibly responsible for feature differences [50]. However, when the radiation-induced  $N_{ss}$  is examined (at about  $3 \times 10^{12} \text{ eV}^{-1} \text{ cm}^{-2}$ ), it can be seen that its level is not very high for pinning the fermi energy level [50] under the maximum cumulative dose of gamma-irradiation. The level of the  $R_s$  is also deficient, and it changes less than  $2 \Omega$  (from 8.74 to 6.82  $\Omega$ ) for the maximum radiation doses (10 kGy). Therefore, it is possible to say that the degradation in this MIS device is insignificant, and it can be used as an electronic component in ionizing (gamma) radiation environments with an irradiation dose of around 10 kGy.



## IV. CONCLUSION

The  $C$ - $V$  graphs of MIS/MOS devices, especially GaAs-based devices, may exhibit negative behaviour or a concave curvature in the high voltage biases. Negative capacitance values indicate that the inductive effect of the device is more pressure than the capacitive effect. In this study, the GaAs-based MIS device (Au/n-GaAs/Au-Ge with natural oxide layer) was produced, and its capacitance and conductance data were obtained for 0 (unirradiated sample), 5 and 10 kGy ionizing (gamma) radiation doses. Thus, this study focuses on the negative capacitance phenomenon of MIS devices under ionizing radiation, and experimental results show that abnormal peaks were observed in  $C$ - $V$  graphs, and the peak point shifted toward the positive biases after the device was exposed to gamma irradiation. On the other hand, the conductance values increased rapidly and reached their maximum value, while the capacitance values reached their minimum value in the high voltage biases. This situation is directly related to the MIS devices' inductive behaviour, which was determined to be more effective after irradiation. Such behaviours can be observed because of the ionization process, the MIS devices' series resistance, surface states between the M/S interface, and some displacement damages caused by ionizing radiation.

The actual series resistance values with  $R_i$ - $V$  curves, correct capacitance-conductance graphs, and the radiation-induced surface states were also obtained to clarify the effects of radiation on the device. And results show that the capacitance and conductance values increase significantly when the  $R_s$  effect is neglected (after the correction process), especially in the positive voltages. The peak points of the capacitance curves shift towards the positive biases. Furthermore, the  $G/\omega$ - $V$  graphs give a peak before and after irradiation, although there aren't any peaks in the  $G_m/\omega$ - $V$  curves. Therefore, it can be said that the  $R_s$  can seriously affect the devices' capacitance and conductance characteristics.

In conclusion, the radiation-induced surface states changed around  $3 \times 10^{12} \text{ eV} \cdot \text{cm}^{-2}$  for the maximum cumulative dose (10 kGy), and the actual resistance values changed to 8.74, 7.88, and 6.82  $\Omega$  for 0, 5, and 10 kGy amounts, respectively. Shortly, the degradation rate in the device was found to be negligible. Therefore, this MIS device can be safely used as an electronic component in some radiation environments, such as space, where operating satellite systems, and nuclear plants, at gamma irradiation doses of around 10 kGy.

## ACKNOWLEDGEMENT

The author wishes to thank Prof. Dr Şemsettin Altındal and his research team for making it possible to conduct the application parts of this study at Gazi University.

## REFERENCES

- [1] S. M. Sze and K. K. Ng, *Physics of Semiconductor Devices*. Hoboken, NJ, USA: John Wiley & Sons, Inc., 2006. doi: 10.1002/0470068329.
- [2] R. L. Boylestad and L. Nashelsky, *Electronic Devices and Circuit Theory*, Eleventh Edition. Harlow: Pearson Education Limited, 2014.
- [3] H. Durmuş, A. Tataroğlu, Ş. Altındal, and M. Yıldırım, "The effect of temperature on the electrical characteristics of Ti/n-GaAs Schottky diodes," *Current Applied Physics*, vol. 44, pp. 85–89, Dec. 2022, doi: 10.1016/j.cap.2022.09.015.
- [4] S. Demirezen, Ş. Altındal, Y. Azizian-Kalandaragh, and A. M. Akbaş, "A comparison of Au/n-Si Schottky diodes (SDs) with/without a nanographite (NG) interfacial layer by considering interlayer, surface states ( $N_{ss}$ ) and series resistance ( $R_s$ ) effects," *Phys Scr*, vol. 97, no. 5, p. 055811, May 2022, doi: 10.1088/1402-4896/ac645f.
- [5] A. Kaya, Ş. Altındal, Y. Ş. Asar, and Z. Sönmez, "On the Voltage and Frequency Distribution of Dielectric Properties and ac Electrical Conductivity in Al/SiO<sub>2</sub>/p-Si (MOS) Capacitors," *Chinese Physics Letters*, vol. 30, no. 1, p. 017301, Jan. 2013, doi: 10.1088/0256-307X/30/1/017301.
- [6] A. Amiri, "Solid-phase microextraction-based sol-gel technique," *TrAC Trends in Analytical Chemistry*, vol. 75, pp. 57–74, Jan. 2016, doi: 10.1016/j.trac.2015.10.003.
- [7] B. Akin, J. Farazin, Ş. Altındal, and Y. Azizian-Kalandaragh, "A comparison electric-dielectric features of Al/p-Si (MS) and Al/(Al<sub>2</sub>O<sub>3</sub>:PVP)/p-Si (MPS) structures using voltage-current ( $V$ - $I$ ) and frequency-impedance ( $f$ - $Z$ ) measurements," *Journal of Materials Science: Materials in Electronics*, vol. 33, no. 27, pp. 21963–21975, Sep. 2022, doi: 10.1007/s10854-022-08984-2.
- [8] K. Choy, "Chemical vapour deposition of coatings," *Prog Mater Sci*, vol. 48, no. 2, pp. 57–170, 2003, doi: 10.1016/S0079-6425(01)00009-3.
- [9] R. Asmatulu, "Highly Hydrophilic Electrospun Polyacrylonitrile/Polyvinylpyrrolidone Nanofibers Incorporated with Gentamicin as Filter Medium for Dam Water and Wastewater Treatment," *Journal of Membrane and Separation Technology*, vol. 5, no. 2, pp. 38–56, Jul. 2016, doi: 10.6000/1929-6037.2016.05.02.1.
- [10] H. E. Lapa, A. Kökce, A. F. Özdemir, and Ş. Altındal, "Investigation of Dielectric Properties, Electric Modulus and Conductivity of the Au/Zn-Doped PVA/n-4H-SiC (MPS) Structure Using Impedance Spectroscopy Method," *Zeitschrift für Physikalische Chemie*, vol. 234, no. 3, pp. 505–516, Mar. 2020, doi: 10.1515/zpch-2017-1091.
- [11] H. Zhou and S. F. Bent, "Fabrication of organic interfacial layers by molecular layer deposition: Present status and future opportunities," *Journal of Vacuum Science & Technology A: Vacuum, Surfaces, and Films*, vol. 31, no. 4, p. 040801, Jul. 2013, doi: 10.1116/1.4804609.
- [12] A. Mishra, N. Bhatt, and A. K. Bajpai, "Nanostructured superhydrophobic coatings for solar panel applications," in *Nanomaterials-Based Coatings*, Elsevier, 2019, pp. 397–424. doi: 10.1016/B978-0-12-815884-5.00012-0.
- [13] H. Sawatari and O. Oda, "Schottky diodes on  $n$ -type InP with CdOx interfacial layers grown by the adsorption and oxidation method," *J Appl Phys*, vol. 72, no. 10, pp. 5004–5006, Nov. 1992, doi: 10.1063/1.352027.
- [14] A. Kaymaz, "Ionizing radiation response of bismuth titanate-based metal-ferroelectric-semiconductor (MFS) type capacitor," *Microelectronics Reliability*, vol. 133, p. 114546, Jun. 2022, doi: 10.1016/j.microrel.2022.114546.
- [15] S. Demirezen, A. Kaya, Ş. Altındal, and İ. Uslu, "The energy density distribution profile of interface traps and their relaxation times and capture cross sections of Au/GO-doped PrBaCoO nanoceramic/n-Si capacitors at room temperature," *Polymer Bulletin*, vol. 74, no. 9, pp. 3765–3781, Sep. 2017, doi: 10.1007/s00289-017-1925-2.
- [16] A. Kaymaz, H. Uslu Tecimer, E. Evcin Baydilli, and Ş. Altındal, "Investigation of gamma-irradiation effects on electrical characteristics of Al/(ZnO-PVA)/p-Si Schottky diodes using capacitance and conductance measurements," *Journal of Materials Science: Materials in Electronics*, vol. 31, no. 11, pp. 8349–8358, Jun. 2020, doi: 10.1007/s10854-020-03370-2.
- [17] I. Orak, A. Kocyyigit, and Ş. Alındal, "Electrical and dielectric characterization of Au/ZnO/n-Si device depending frequency and voltage," *Chinese Physics B*, vol. 26, no. 2, p. 028102, Feb. 2017, doi: 10.1088/1674-1056/26/2/028102.
- [18] M. Ambrico *et al.*, "A study of remote plasma nitrided nGaAs/Au Schottky barrier," *Solid State Electron*, vol. 49, no. 3, pp. 413–419, Mar. 2005, doi: 10.1016/j.sse.2004.11.007.
- [19] H. Durmuş, M. Yıldırım, and Ş. Altındal, "On the possible conduction mechanisms in Rhenium/n-GaAs Schottky barrier diodes fabricated by pulsed laser deposition in temperature range of 60–400 K," *Journal of Materials Science: Materials in Electronics*, vol. 30, no. 9, pp. 9029–9037, May 2019, doi: 10.1007/s10854-019-01233-z.
- [20] M. K. Hudait, P. Venkateswarlu, and S. B. Krupanidhi, "Electrical transport characteristics of Au/n-GaAs Schottky diodes on n-Ge at low temperatures," *Solid State Electron*, vol. 45, no. 1, pp. 133–141, Jan. 2001, doi: 10.1016/S0038-1101(00)00230-6.

- [21] D. Ahmad Fauzi, N. K. Alang Md Rashid, M. R. Mohamed Zin, and N. F. Hasbullah, "Radiation Performance of GaN and InAs/GaAs Quantum Dot Based Devices Subjected to Neutron Radiation," *IJUM Engineering Journal*, vol. 18, no. 1, pp. 101–109, May 2017, doi: 10.31436/ijumej.v18i1.653.
- [22] V. Balasubramani, P. v. Pham, A. Ibrahim, J. Hakami, M. Z. Ansari, and T. K. Le, "Enhanced photosensitive of Schottky diodes using SrO interfaced layer in MIS structure for optoelectronic applications," *Opt Mater (Amst)*, vol. 129, p. 112449, Jul. 2022, doi: 10.1016/j.optmat.2022.112449.
- [23] Ş. Karataş, Ş. Altındal, M. Ulusoy, Y. Azizian-Kalendaragh, and S. Özçelik, "Temperature dependence of electrical characteristics and interface state densities of Au/n-type Si structures with SnS doped PVC interface," *Phys Scr*, vol. 97, no. 9, p. 095816, Sep. 2022, doi: 10.1088/1402-4896/ac89bb.
- [24] A. B. Ulsan, A. Tataroglu, Ş. Altındal, and Y. Azizian-Kalendaragh, "Photoresponse characteristics of Au/(CoFe2O4-PVP)/n-Si/Au (MPS) diode," *Journal of Materials Science: Materials in Electronics*, vol. 32, no. 12, pp. 15732–15739, Jun. 2021, doi: 10.1007/s10854-021-06124-w.
- [25] J. R. Nicholls, "Electron trapping effects in SiC Schottky diodes: Review and comment," *Microelectronics Reliability*, vol. 127, p. 114386, Dec. 2021, doi: 10.1016/j.microrel.2021.114386.
- [26] R. M. Sahani and A. Dixit, "A comprehensive review on zinc oxide bulk and nano-structured materials for ionizing radiation detection and measurement applications," *Mater Sci Semicond Process*, vol. 151, p. 107040, Nov. 2022, doi: 10.1016/j.mssp.2022.107040.
- [27] S. Demirezen *et al.*, "Electrical characteristics and photosensing properties of Al/symmetrical CuPc/p-Si photodiodes," *Journal of Materials Science: Materials in Electronics*, Aug. 2022, doi: 10.1007/s10854-022-08906-2.
- [28] A. Tataroglu, Ş. Altındal, M. H. Bölükdemir, and G. Tanır, "Irradiation effect on dielectric properties and electrical conductivity of Au/SiO2/n-Si (MOS) structures," *Nucl Instrum Methods Phys Res B*, vol. 264, no. 1, pp. 73–78, Nov. 2007, doi: 10.1016/j.nimb.2007.07.026.
- [29] Ç. Ş. Güçlü, A. F. Özdemir, A. Karabulut, A. Kökce, and Ş. Altındal, "Investigation of temperature dependent negative capacitance in the forward bias C-V characteristics of (Au/Ti)/Al2O3/n-GaAs Schottky barrier diodes (SBDs)," *Mater Sci Semicond Process*, vol. 89, pp. 26–31, Jan. 2019, doi: 10.1016/j.mssp.2018.08.019.
- [30] E. Arslan, Y. Şafak, Ş. Altındal, Ö. Kelekçi, and E. Özbay, "Temperature dependent negative capacitance behavior in (Ni/Au)/AlGaIn/GaN heterostructures," *J Non Cryst Solids*, vol. 356, no. 20–22, pp. 1006–1011, May 2010, doi: 10.1016/j.jnoncrysol.2010.01.024.
- [31] E. E. Tanrikulu, S. Demirezen, Ş. Altındal, and İ. Uslu, "On the anomalous peak and negative capacitance in the capacitance-voltage (C-V) plots of Al(%7 Zn-PVA)/p-Si (MPS) structure," *Journal of Materials Science: Materials in Electronics*, vol. 29, no. 4, pp. 2890–2898, Feb. 2018, doi: 10.1007/s10854-017-8219-1.
- [32] J. A. M. ALSMAEL, N. URGUN, S. O. TAN, and H. TECİMER, 'Effectuality of the Frequency Levels on the C&w/G/w-V Data of the Polymer Interlayered Metal-Semiconductor Structure', *Gazi University Journal of Science Part A: Engineering and Innovation*, vol. 9, no. 4, pp. 554–561, Dec. 2022, doi: 10.54287/guj.1206332.
- [33] S. Demirezen, E. E. Tanrikulu, and Ş. Altındal, "The study on negative dielectric properties of Al/PVA (Zn-doped)/p-Si (MPS) capacitors," *Indian Journal of Physics*, vol. 93, no. 6, pp. 739–747, Jun. 2019, doi: 10.1007/s12648-018-1355-5.
- [34] J. C. Wong and S. Salahuddin, 'Negative Capacitance Transistors', *Proceedings of the IEEE*, vol. 107, no. 1, pp. 49–62, Jan. 2019, doi: 10.1109/JPROC.2018.2884518.
- [35] S. Demirezen, E. E. Tanrikulu, and Ş. Altındal, 'The study on negative dielectric properties of Al/PVA (Zn-doped)/p-Si (MPS) capacitors', *Indian Journal of Physics*, vol. 93, no. 6, pp. 739–747, Jun. 2019, doi: 10.1007/s12648-018-1355-5.
- [36] J. R. Srour and J. W. Palko, "Displacement damage effects in irradiated semiconductor devices," *IEEE Trans Nucl Sci*, vol. 60, no. 3, pp. 1740–1766, 2013, doi: 10.1109/TNS.2013.2261316.
- [37] A. F. Özdemir *et al.*, "The analysis of hydrostatic pressure dependence of the Au/native oxide layer/n-GaAs/Au-Ge Schottky diode parameters," *The European Physical Journal Applied Physics*, vol. 60, no. 1, p. 10101, Oct. 2012, doi: 10.1051/epjap/2012110483.
- [38] A. Kaymaz, E. Evcin Baydilli, H. Uslu Tecimer, Ş. Altındal, and Y. Azizian-Kalendaragh, "Evaluation of gamma-irradiation effects on the electrical properties of Al/(ZnO-PVA)/p-Si type Schottky diodes using current-voltage measurements," *Radiation Physics and Chemistry*, vol. 183, p. 109430, Jun. 2021, doi: 10.1016/j.radphyschem.2021.109430.
- [39] H. G. Çetinkaya, M. Yıldırım, P. Durmuş, and Ş. Altındal, "Diode-to-diode variation in dielectric parameters of identically prepared metal-ferroelectric-semiconductor structures," *J Alloys Compd*, vol. 728, pp. 896–901, Dec. 2017, doi: 10.1016/j.jallcom.2017.09.030.
- [40] S. Demirezen, H. G. Çetinkaya, and Ş. Altındal, "Doping rate, Interface states and Polarization Effects on Dielectric Properties, Electric Modulus, and AC Conductivity in PCBM/NiO:ZnO/p-Si Structures in Wide Frequency Range," *Silicon*, Jan. 2022, doi: 10.1007/s12633-021-01640-0.
- [41] B. Rong, L. K. Nanver, J. N. Burghartz, A. B. M. Jansman, A. G. R. Evans, and B. S. Rejaei, "C-V characterization of MOS capacitors on high resistivity silicon substrate," in *Electrical Performance of Electrical Packaging (IEEE Cat. No. 03TH8710)*, pp. 489–492, doi: 10.1109/ESSDERC.2003.1256920.
- [42] M. Ulusoy, Ş. Altındal, Y. Azizian-Kalendaragh, S. Özçelik, and Z. Mirzaei-Kalar, "The electrical characteristic of an MIS structure with biocompatible minerals doped (Brushite+Monetite: PVC) interface layer," *Microelectron Eng*, vol. 258, p. 111768, Apr. 2022, doi: 10.1016/j.mee.2022.111768.
- [43] Ş. Altındal and H. Uslu, "The origin of anomalous peak and negative capacitance in the forward bias capacitance-voltage characteristics of Au/PVA/n-Si structures," *J Appl Phys*, vol. 109, no. 7, p. 074503, Apr. 2011, doi: 10.1063/1.3554479.
- [44] Ç. Bilkan and Ş. Altındal, "Investigation of the C-V characteristics that provides linearity in a large reverse bias region and the effects of series resistance, surface states and interlayer in Au/n-Si/Ag diodes," *J Alloys Compd*, vol. 708, pp. 464–469, Jun. 2017, doi: 10.1016/j.jallcom.2017.03.013.
- [45] J. R. Srour, C. J. Marshall, and P. W. Marshall, "Review of displacement damage effects in silicon devices," *IEEE Trans Nucl Sci*, vol. 50, no. 3, pp. 653–670, Jun. 2003, doi: 10.1109/TNS.2003.813197.
- [46] E. H. Nicollian and J. R. Brews, *MOS (Metal Oxide Semiconductor) Physics and Technology*. Hoboken, NJ: Wiley, 2003.
- [47] A. Teffahi *et al.*, "Effect of 60Co  $\gamma$ -ray irradiation on electrical properties of Ti/Au/GaAs1-xNx Schottky diodes," *Current Applied Physics*, vol. 16, no. 8, pp. 850–858, Aug. 2016, doi: 10.1016/j.cap.2016.05.003.
- [48] S. Kaya, A. Aktag, and E. Yilmaz, "Effects of gamma-ray irradiation on interface states and series-resistance characteristics of BiFeO3 MOS capacitors," *Nucl Instrum Methods Phys Res B*, vol. 319, pp. 44–47, Jan. 2014, doi: 10.1016/j.nimb.2013.11.006.
- [49] Ş. Karataş, A. Türüt, and Ş. Altındal, "Irradiation effects on the C-V and G/w-V characteristics of Sn/p-Si (MS) structures," *Radiation Physics and Chemistry*, vol. 78, no. 2, pp. 130–134, Feb. 2009, doi: 10.1016/j.radphyschem.2008.09.006.
- [50] R. Castagné and A. Vapaille, 'Description of the SiO2-Si interface properties by means of very low frequency MOS capacitance measurements', *Surf Sci*, vol. 28, no. 1, pp. 157–193, Nov. 1971, doi: 10.1016/0039-6028(71)90092-6.
- [51] S. Maurya and S. Awasthi, "Effect of zero bias, 2.7 MeV proton irradiation on HfO2," *J Radioanal Nucl Chem*, vol. 318, no. 2, pp. 947–953, Nov. 2018, doi: 10.1007/s10967-018-6229-y.

## BIOGRAPHIES



AHMET KAYMAZ received the B.S. degree in electrical and electronics engineering from Pamukkale University, Denizli, in 2006. He also received his M.S. and Ph.D. in electrical and electronics engineering from Karabuk University, Karabuk, Turkey, in 2015 and 2020, respectively. From

2010 to 2020, he was a Research Assistant at Karabuk University. Since 2020, he has worked as an Assistant Professor at Karabuk University, Engineering Faculty, Department of Mechatronics Engineering.

# Performance Evaluation of Three-Phase Grid Connected Inverter with Various Control Methods

Ekrem Demir, Ozan Gulbudak, Mustafa Gokdag


**Abstract**— Grid-connected inverters, one of the widely used power systems to benefit from renewable energy systems, play an important role. According to the TS EN 50160 standard specified in our country, the total harmonic distortion value of the grid current of the grid-connected inverters must be below 5%. Various filter models are used between the inverter and the grid to suppress the harmonic distortions of the current generated from the inverters and to keep the THD value of the grid current below the specified standard. Among these filter models, L and LCL filter models are widely used. Among these filters, the LCL filter suppresses harmonics more than the L filter. In addition to the THD value of the mains current being below the desired standard, the dynamics of the system should be regular. Various feedback strategies (Control methods) are available to regulate the dynamics of grid-connected systems. Linear controllers, non-linear controllers and predictive controllers play an important role in controlling grid-connected inverter systems. In this study, different control strategies are investigated to analyze the performance of the grid-tied inverter equipped with an LCL filter. Then, simulation studies were carried out by applying traditional Proportional-Integral-Derivative (PID) control, Sliding Mode Control (SMC) and Model Predictive Control (MPC) method to grid-connected LCL filtered inverter. Simulation studies were carried out using MATLAB and theoretical concepts were verified by simulation studies.

**Index Terms**—PID control, Sliding mode control, Model predictive control, grid-tide inverter


## I. INTRODUCTION

RECENTLY, Renewable energy production system(REPS) applications have increased due to the negative effects and costs of fossil fuels(health cost and environmental cost) on the environment in terms of energy production systems [1].


EKREM DEMİR, is with Department of Electrical Engineering University of Karabuk University, Karabuk, Turkey, (e-mail: [edemir@karabuk.edu.tr](mailto:edemir@karabuk.edu.tr)).

 <https://orcid.org/0000-0001-7882-9634>

OZAN GULBUDAK, is with Department of Electrical Engineering University of Karabuk University, Karabuk, Turkey, (e-mail: [ozangulbudak@karabuk.edu.tr](mailto:ozangulbudak@karabuk.edu.tr)).

 <https://orcid.org/0000-0001-9517-3630>

MUSTAFA GOKDAĞ, is with Department of Electrical Engineering University of Karabuk University, Karabuk, Turkey, (e-mail: [mgokdag@karabuk.edu.tr](mailto:mgokdag@karabuk.edu.tr)).

 <https://orcid.org/0000-0001-5589-2278>

Manuscript received Sep 13, 2022; accepted Feb 9, 2023.

DOI: [10.17694/bajece.1174749](https://doi.org/10.17694/bajece.1174749)

Three-phase grid-connected inverter topology is depicted in Fig. 1. [2], [3].

Various filters and control methods are used to suppress the harmonics of the inverter's output current connected to the grid. Among the filters, the L filter is not preferred to be used due to its high cost and slow system dynamic response in high power applications. Furthermore, the use of L filter may suffer from poor harmonic rejection capability. Thus, the LCL filter is usually preferred since third-order attenuation is achieved resulting in improved power quality [4], [5].

In the literature, several control methods have been reported to control the grid-connected system. In traditional control routine, a piece-wise modulator combined with linear controller such as PID controller is used. The traditional strategy offers a reasonable energy conversion operation. However, the dynamic response degraded due to the slow dynamics of the modulator [6], [7]. The other critical aspect of the traditional method, the feedback design is based on the linear relationship between input-output variables (basically pole-zero based transfer function). The controller parameters are tuned such that a decent closed-loop performance is achieved. However, the controller parameters (such as proportional or integral coefficients) are fixed during the operation, thus a deviation from the operating point negatively influences the reference tracking performance. Due to this unpleasant characteristics, nonlinear control strategies are desirable to improve transient performance of the system. Nonlinear control methods overcome stated problems since they have capability to adapt the new operating conditions [8].

This paper presents the performance evaluation of different control strategies for grid-connected inverter. Three feedback methods are considered as case studies: PID controller, SMC and MPC. The performance evaluation is conducted regarding various evaluation metrics. Among aforementioned control methods, MPC strategy is very promising. MPC provides a rapid response to the load perturbations while ensuring the closed-loop stability. Mathematical concepts are verified by the simulation works, and each control method is tested considering real-case test scenarios.

## II. SYSTEM MODEL

The three-phase voltage source inverter (VSI), see Fig. 1, has eight permissible switching combinations. Each discrete semiconductor device can have two discrete values (1 or 0). There are two switching limitations in VSI operation. The



switching devices on the same VSI leg cannot be simultaneously conducted due to dc-bus short circuit. Table I summarize allowable switching positions for VSI [9].

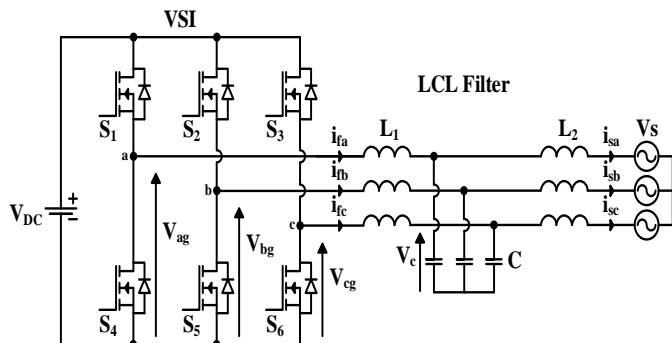


Fig. 1. The grid-connected VSI with LCL-type filter [3]

TABLE I ALLOWABLE SWITCH POSITIONS OF INVERTER LEGS [9]

$S_a$	$S_b$	$S_c$
0	0	0
1	0	0
1	1	0
0	1	0
0	1	1
0	0	1
1	0	1
1	1	1

A. Output Filter Model

Power converters are used to integrate most renewable energy systems with the electrical grid. In the grid-connected systems, an output filter is often used to reduce the harmonics of the grid current generated from power converters. These filters can take different structures such as L, LC, LCL filters [10], [11].

The L filter has a simple structure since it is a first-order filter. However, in order to reduce the harmonics of the mains current, a large inductance value L filter must be used. A filter of this value has disadvantages such as high cost and negative control time response [11], [12].

An LC filter has been proposed as an alternative to the L filter. Because the LC filter is a second order filter, it reduces the filter volume and increases attenuation for high frequencies. However, it has disadvantages such as the has of inrush currents in the output capacitance , a resonant frequency that amplify the mains current harmonics, and the instability caused by the direct connection of the capacitor in parallel to the electrical network [11], [13].

Although the LCL filter has a more difficult design due to having a third order filter compared to the L and LC filters, it offers better harmonic attenuation performance and lower cost to reduce the mains current harmonics [14]. In this work, LCL filter is used, and the design guideline [15] to determine LCL filter parameters is given in Fig. 2 [16]. Based on the algorithm presented in , the selected filter parameters are tabulated in Table 2.

TABLE II LCL FILTER PARAMETERS USED IN SIMULATION STUDY

LCL Filter Parameters		System Parameters	
Inverter side inductor	$L_i = 24.44 \text{ mH}$	One Phase Effective Voltage	$E_n = 220 \text{ V}$
Damping Resistor	$R_f = 1.1772 \Omega$	Active Power	$P = 2700 \text{ W}$
Capacitor Filter	$C_f = 8.88 \mu\text{F}$	DC link Voltage	$V_{DC} = 750 \text{ V}$
Grid side inductor	$L_g = 0.11 \text{ mH}$	Grid Frequency	$f_g = 50 \text{ Hz}$
Resonance angular velocity	$\omega_{res} = 32068 \text{ rad}$	Switching Frequency	$f_{sw} = 12.5 \text{ kHz}$
Resonance Frequency	$f_{res} = 5103 \text{ Hz}$	Attenuation Factor	$k_a = 0.2(\%20)$

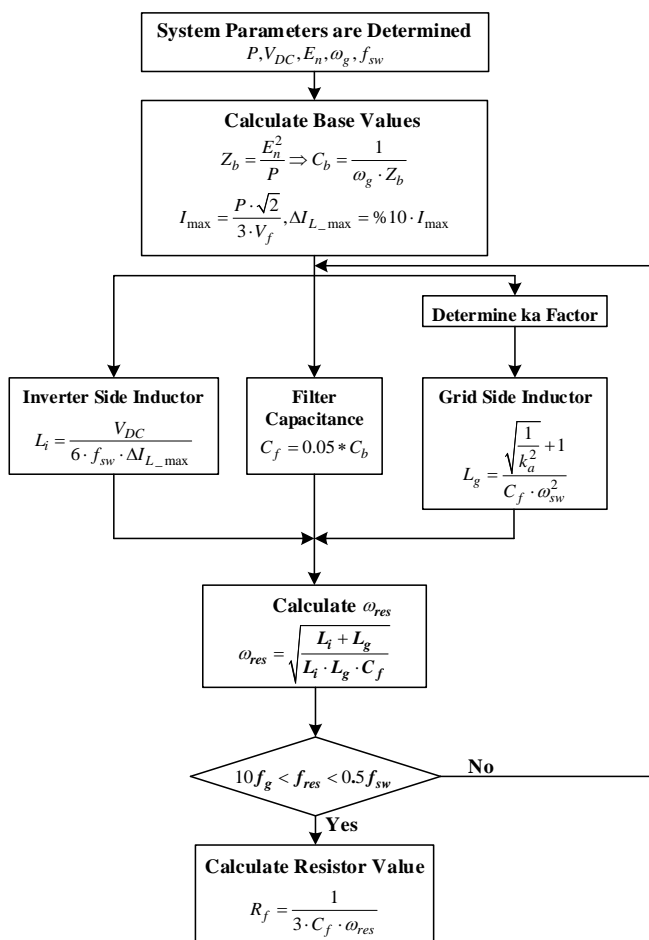


Fig. 2. Algorithm of LCL-filter [16]

III. CONTROL METHOD

This section presents feedback strategies to control the grid-connected VSI with LCL filter. Herein, three control methods are discussed by providing the mathematical models and design steps. Firstly, linear PID controller is discussed. Then, SMC and MPC methods will be explained.



A. Classic PID Control

The control system with feedback classic PID controller is given in Fig. 3. Where  $r$ ,  $e$ ,  $y$  are respectively reference, error and the output of the system that is controlled variable. Also, in the Fig. 3,  $G(s)$  represents the transfer function of the system to be controlled and  $C(s)$  represents the PID controller [17].

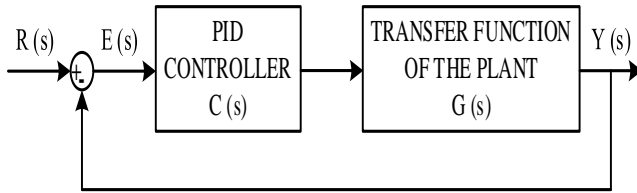


Fig. 3. The PID control block diagram of system [17]

The PID controller is used to reduce or eliminate the steady state error as well as improve the dynamic response [18]. The transfer function of the PID controller is given in the equation which is the below [19]:

$$C(s) = K_p + \frac{K_I}{s} + K_D s \tag{1}$$

Where,  $K_p$ ,  $K_I$ ,  $K_D$  represents the proportional, integral, and derivative gain of the PID controller controlling the system, respectively [19].

In this work, The PID control method compares the inductor current that is near grid with the desired reference current. Then it multiplies this error with the PID coefficients we have determined. Finally, it determines the status of the switches of the inverter system by comparing the obtained value with the carrier signal as shown in Fig. 4.

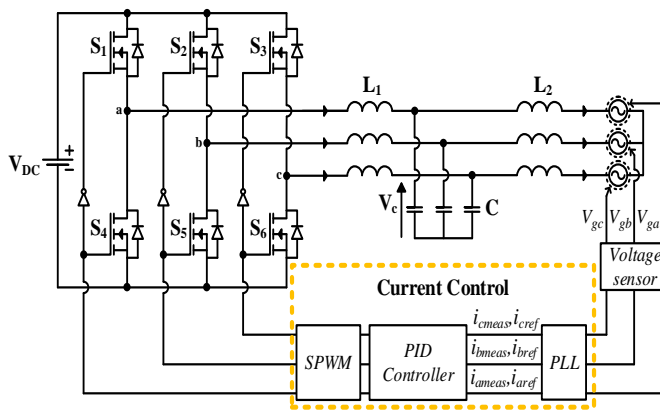


Fig. 4. Classic PID Control scheme for the grid connected VSI

B. Sliding-mode Control Sliding-mode control of grid-connected VSI

The sliding mode control (SMC) is a nonlinear feedback control strategy. SMC is an encouraging control strategy in power electronics applications where the control of multiple control objectives is required. The state variables usually are defined as trajectory error, and the control of the state variables is achieved by rotating the sliding line. Due to the resonance problem of the LCL-type filter, the sliding surface function can

be properly selected [20]. In this work, the sliding surface function is formed by the grid-side current, capacitor voltage, and time-derivative of the capacitor voltage.

The dynamic model of the system is given by

$$L_1 \frac{di_f}{dt} = v_g - v_c \tag{2}$$

$$L_2 \frac{di_s}{dt} = v_c - v_s \tag{3}$$

$$C \frac{dv_c}{dt} = i_f - i_s \tag{4}$$

In (1)-(3),  $v_g = [S_1 v_{dc} \ S_2 v_{dc} \ S_3 v_{dc}]$  with  $S_1, S_2, S_3 \in \{1, 0\}$  and  $S_3 \in \{1, 0\}$ ,  $i_f = [i_{fa} \ i_{fb} \ i_{fc}]$ . The input voltage  $v_g$  depends on the switching positions. The state variables are expressed as

$$x_1 = v_c - v_c^* \tag{5}$$

$$x_2 = \frac{dv_c}{dt} - \frac{dv_c^*}{dt} \tag{6}$$

$$x_3 = i_s - i_s^* \tag{7}$$

Where  $v_c = [v_{ca} \ v_{cb} \ v_{cc}]$ ,  $i_s = [i_{sa} \ i_{sb} \ i_{sc}]$ ,  $v_c^* = [v_{ca}^* \ v_{cb}^* \ v_{cc}^*]$  and  $i_s^* = [i_{sa}^* \ i_{sb}^* \ i_{sc}^*]$ . The vector  $v_c^*$  denotes the capacitor voltage reference and  $i_s^*$  is the grid current reference.

From (4) and (5), the time-derivative of  $x_1$  equals  $x_2$  ( $\dot{x} = x_2$ ).

Conceptually, the SMC aims to control the capacitor voltage and the grid current. By using the state variables defined in (4)-(6), the sliding surface function is defined as

$$S = \lambda x_1 + x_2 + \sigma x_3 \tag{8}$$

In (7),  $\lambda$  and  $\sigma$  are the time-invariant parameters that define the moving speed of the sliding line. The parameter  $\lambda$  is the tuning term of the capacitor voltage control term. Fundamentally, it manages the importance of capacitor voltage control. The parameter  $\sigma$  is the constant gain of the instantaneous grid current error. The grid current control performance can be tuned by adjusting  $\sigma$ . Thus, the selection of  $\lambda$  and  $\sigma$  are quite important since they have a noticeable influence on the closed-loop dynamics. During the sliding mode, the sliding function equals zero ( $S = 0$ ). In this case, the state variable lies on the sliding line, and they move to the origin of the phase-plane. To ensure the asymptotical stability, the SMC stability condition is considered.

$$S \dot{S} < 0 \tag{9}$$

On the authority of (5), the state variable error converges to zero if the condition  $S \dot{S} < 0$  is satisfied. The time-derivative of (4) results

$$\dot{S} = \lambda \dot{x}_1 + \dot{x}_2 + \sigma \dot{x}_3 \quad (10)$$

By managing (1) and (2), the following expressions can be obtained.

$$\frac{di_f}{dt} = \frac{1}{L_1}(v_g - v_c) \quad (11)$$

$$\frac{di_s}{dt} = \frac{1}{L_2}(v_c - v_s) \quad (12)$$

By applying the same procedure, the time-derivative of the capacitor voltage is given by

$$\frac{dv_c}{dt} = \frac{1}{L_2}(i_f - i_s) \quad (13)$$

By substituting (12) into (2),  $x_2$  results as:

$$x_2 = \frac{1}{C}(i_f - i_s) - \frac{dv_c^*}{dt} \quad (14)$$

The time-derivative of  $x_2$  can be determined by taking a derivative of (13). Hence, the derivative term of  $x_2$  is expressed as

$$\dot{x}_2 = \frac{1}{C} \left( \frac{di_f}{dt} - \frac{di_s}{dt} \right) - \frac{d^2v_c^*}{dt^2} \quad (15)$$

Using (10) and (11), the expression (14) becomes as follows:

$$\dot{x}_2 = \frac{1}{L_1 C} v_g - v_c \left( \frac{1}{L_1 C} + \frac{1}{L_2 C} \right) + \frac{1}{L_1 C} v_s - \frac{d^2v_c^*}{dt^2} \quad (16)$$

The time derivative of  $x_3$  is expressed as

$$\dot{x}_3 = \frac{di_s}{dt} - \frac{di_s^*}{dt} \quad (17)$$

To implement the SMC method, a proper control input should be defined. The control input  $u$  is defined as

$$u = -\text{sign}(S) \quad (18)$$

The control input has the value of 1 when  $S > \Psi$ , and it holds the value of -1 when  $S > -\Psi$ . As aforementioned before, S refers to the sliding surface defined in (7). The control input is determined in a hysteresis-based mechanism. In this work, the SMC method is implemented in the discrete-time domain. To derive the sampled model of the system, numerical discretization methods can be applied. In this work, the Forward Euler method is used to derive the discrete-time model of the system. By using the Forward Euler method and (1)-(3), the sampled model of the system can be expressed as

$$i_f(k+1) = i_f(k) + \frac{T_s}{L_1}(v_g(k) - v_c(k)) \quad (19)$$

$$i_s(k+1) = i_s(k) + \frac{T_s}{L_2}(v_c(k) - v_s(k)) \quad (20)$$

$$v_c(k+1) = v_c(k) + \frac{T_s}{C}(i_f(k) - i_s(k)) \quad (21)$$

The working principle of the SMC method for the grid connected VSI is illustrated in Fig. 5.

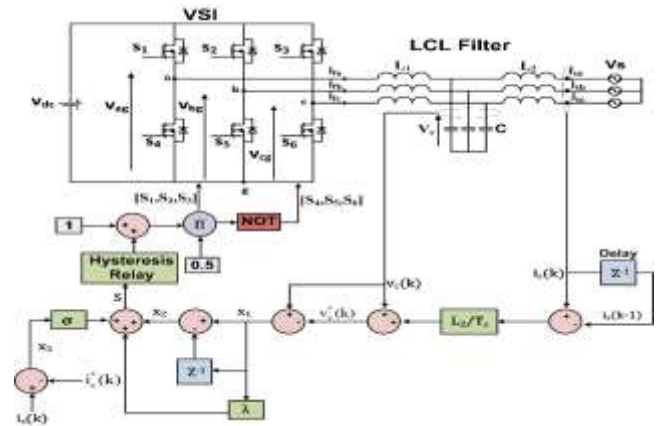


Fig. 5. The SMC scheme for the grid-connected VSI

### C. Model Predictive Control

The MPC is a nonlinear control strategy. This control method has been applied in power electronics applications since 1980. Recently, with the improvement of the performance of microprocessors, the interest in the MPC algorithm has increased even more. The main feature of this algorithm, whose working principle is graphically illustrated in Fig. 6, is to predict the future behavior of predefined control variables on the time horizon with a certain sampling time. It is then to use the estimated variables to obtain the optimal switching state by minimizing the cost function [21]–[24].

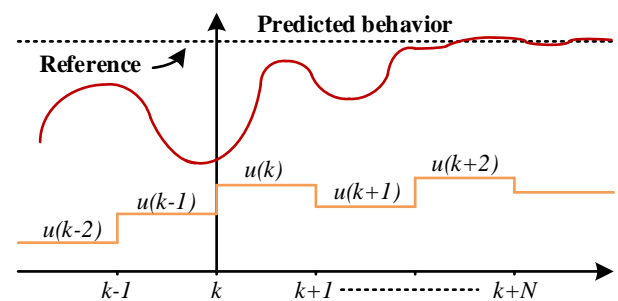


Fig. 6. Working principle of MPC [21]

For power electronics inverters, the MPC can be designed using the following steps [25]:

- 1) Measuring currents and voltages of materials required for modelling.
- 2) Generating all possible switching states and modeling of the power inverter which these states are identifying relation to the input or output voltages or currents.

- 3) Defining a cost function that represents the desired behavior of the system.
- 4) Obtaining discrete-time models that allow one to predict the future behavior of the variables to be controlled.

As a first step in this study, the dynamic model of the system in the  $t$  domain was obtained by applying the ambient current method. The dynamic model of the LCL filter is given as:

$$-V_{in} + L_1 \frac{dI_0}{dt} + I_C R + V_C = 0 \quad (22)$$

$$C \frac{dV_C}{dt} = I_0 - I_g \quad (23)$$

$$-V_C - I_C R + L_2 \frac{dI_g}{dt} + V_g = 0 \quad (24)$$

Then, discrete time models are obtained that allow to predict the behavior of the variables to be controlled for all possible switching states. Numerical methods (such as Forward Euler method or Tustin strategy) can be used to formulate the discrete-time model of the system. The discrete-time model of the dynamical model of the system given above is given as follows:

$$-V_{in}(k) + L_1 \left( \frac{I_0(k+1) - I_0(k)}{T_s} \right) + I_C(k)R + V_C(k) = 0 \quad (25)$$

$$C \left( \frac{V_C(k+1) - V_C(k)}{T_s} \right) = I_0(k+1) - I_g(k) \quad (26)$$

$$-V_C(k+1) - I_C(k)R + L_2 \left( \frac{I_g(k+1) - I_g(k)}{T_s} \right) + V_g(k) = 0 \quad (27)$$

The cost function is calculated for each estimate. Calculated cost functions are compared between them. Finally, the switching state that minimizes this function is chosen among them. The cost function of the system is given as:

$$g = |I_{ref} - I_{pre}|^2 \quad (28)$$

The working principle of the MPC method for the grid connected VSI is illustrated in Fig. 7.

#### IV. SIMULATION RESULTS

This section presents the simulation and comparison results. Performance evaluation is performed regarding steady-state performance, transient characteristics and harmonic suppression capability.

##### A. Steady-Performance

The steady states and the total harmonic distortion of the grid side current and voltage with respectively PID, SMC and MPC control methods applied are given in Fig. 8, Fig. 9 and Fig. 10. When using the respectively PID controller, SMC and MPC, FFT analysis on the grid current yields a THD value of 6.15%, 6.22% and 1.70% as shown in Fig. 8 (b), Fig. 9 (b) and Fig. 10 (b). As a result, it has been observed that if the MPC method is applied to the system, the system suppresses the harmonics of the mains current better and the mains current has a more stable structure compared to other control methods.

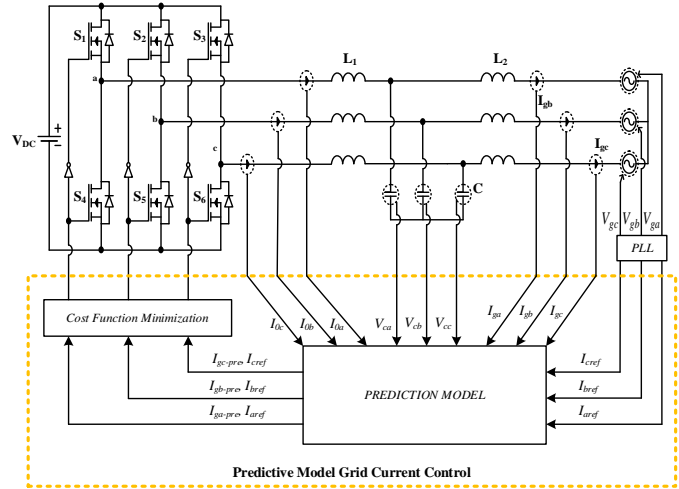


Fig. 7. The MPC scheme for the grid-connected VSI

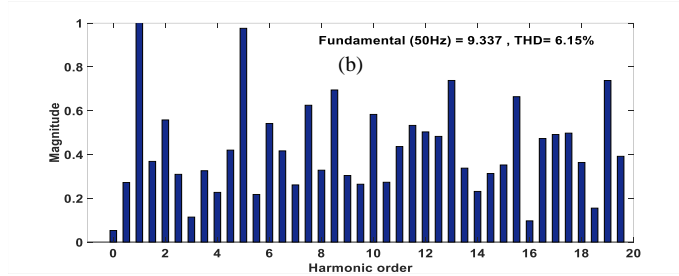
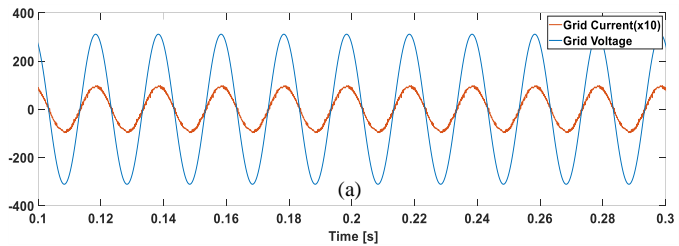


Fig. 8. For PID control method (a) steady-state results of grid currents and voltages and (b) FFT analysis of the grid current

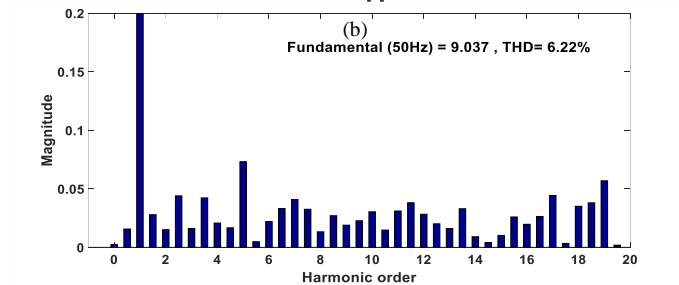
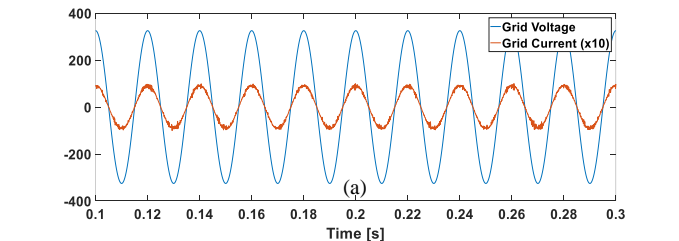


Fig. 9. For SMC control method (a) steady-state results of grid currents and voltages and (b) FFT analysis of the grid current

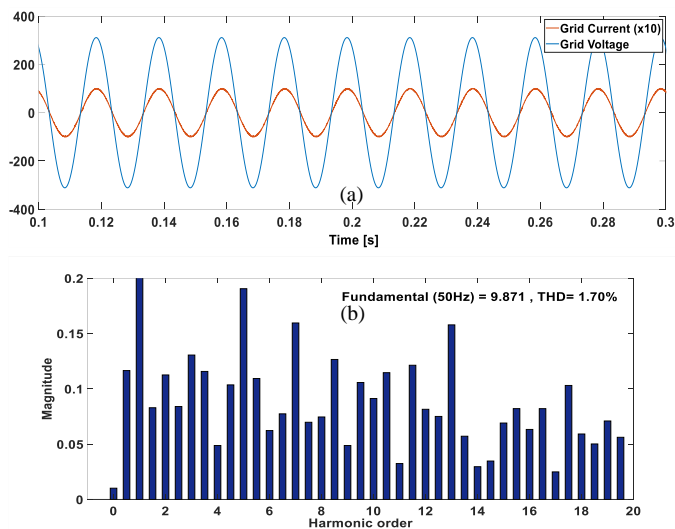


Fig. 10. For MPC control method (a) steady-state results of grid currents and voltages and (b) FFT analysis of the grid current

The steady states of the inverter side current and capacitor voltage with the application of the specified control methods to the system are given in Fig. 11 and Fig. 12. In addition, THD results for mains and inverter side current and capacitor voltage as a result of applying the specified control methods to the system are given in TABLE III in tabular form.

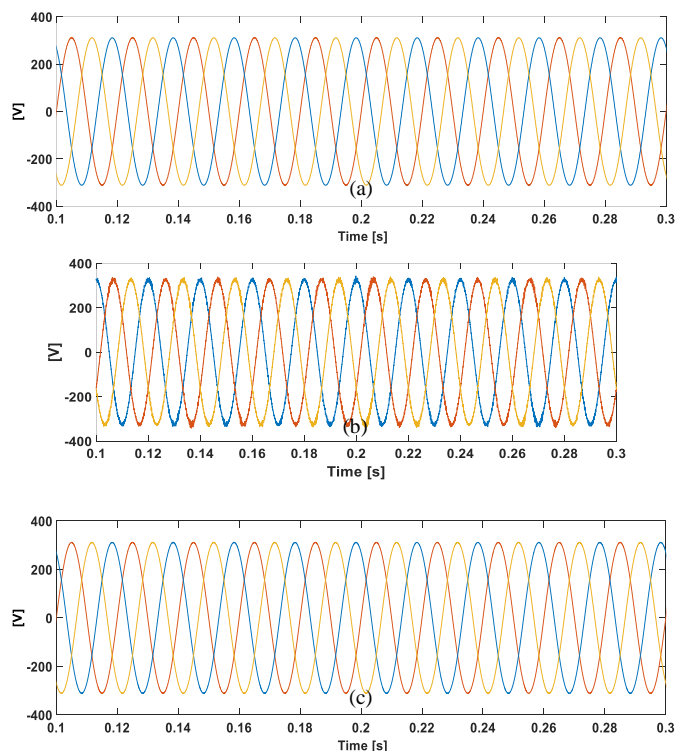


Fig. 11. For (a)PID, (b)SMC and (c) MPC methods steady-state results of capacitor voltages

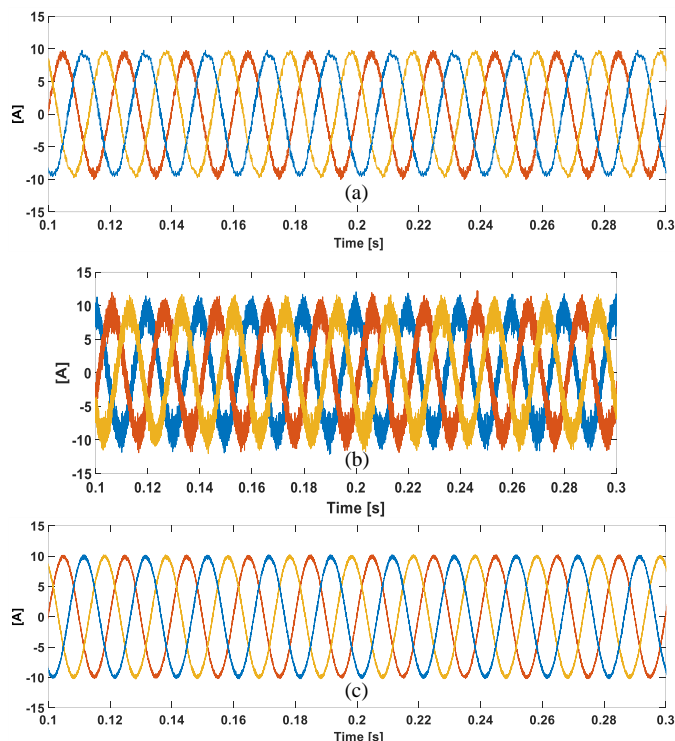


Fig. 12. For (a)PID, (b)SMC and (c) MPC methods steady-state results of inverter currents

TABLE III THD RESULTS FOR GRID SIDE, INVERTER SIDE CURRENT AND CAPACITOR VOLTAGE

Control Methods	THD of Grid Side Current	THD of Capacitor Voltage	THD of Inverter Side Current
PID	6,15 %	0,52 %	5,29 %
SMC	6,22 %	2,04 %	16,06 %
MPC	1,70 %	0,21 %	2,06 %

As seen in Fig. 8, Fig. 9, Fig. 10, Fig. 11, Fig. 12 and TABLE III, when the MPC method is applied to the system, it has been observed that it gives less THD than other methods. Moreover, it has been the inverter and grid current and capacitor voltage have a more stable structure.

**B. Transient-Performance**

During normal conditions, a step change is applied by switching the current mains current reference from 10A to 20A in 0.4 seconds using the PID, SMC and MPC control methods, respectively. Then, the transient performance of the grid current and voltage, capacitor voltage, and current on the inverter side is investigated.

Figure 11 (a), (b) and (c) show the simulation results of the transient response of measured grid current and voltage as a result of the change in reference current using the respective control methods, respectively. If these three methods are applied to the system, it has been observed that the MPC method reaches the desired reference current value in a shorter time compared to the SMC method and the SMC method compared to the PID control method. In other words, temporarily, it has been observed that the MPC method



responds faster to reach the desired reference value compared to other methods.

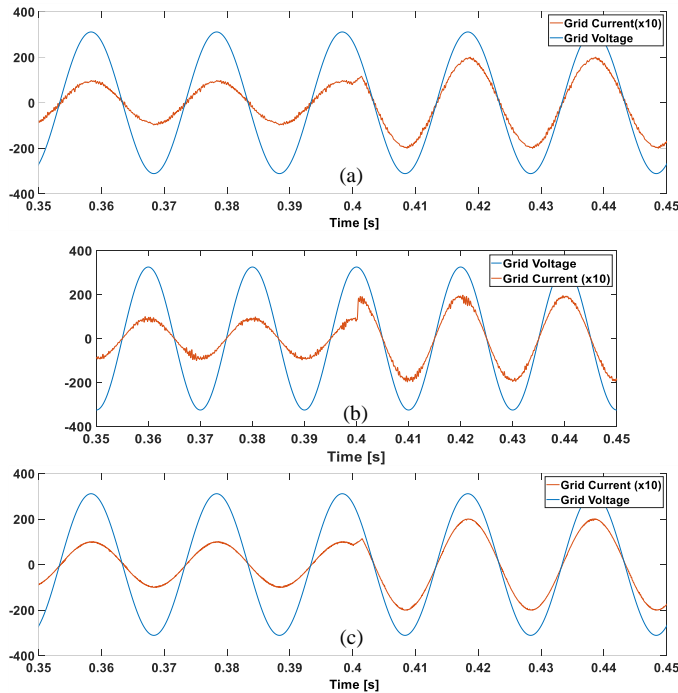


Fig. 13. For (a)PID, (b)SMC and (c) MPC methods transient results of grid currents and voltages

Figure 12 (a), (b) and (c) show the simulation results of the transient response of capacitor voltage as a result of the change in reference current using the respective control methods, respectively. In the case of MPC method is applied, it has been observed that the capacitor voltage is closer to the mains voltage compared to other control methods.

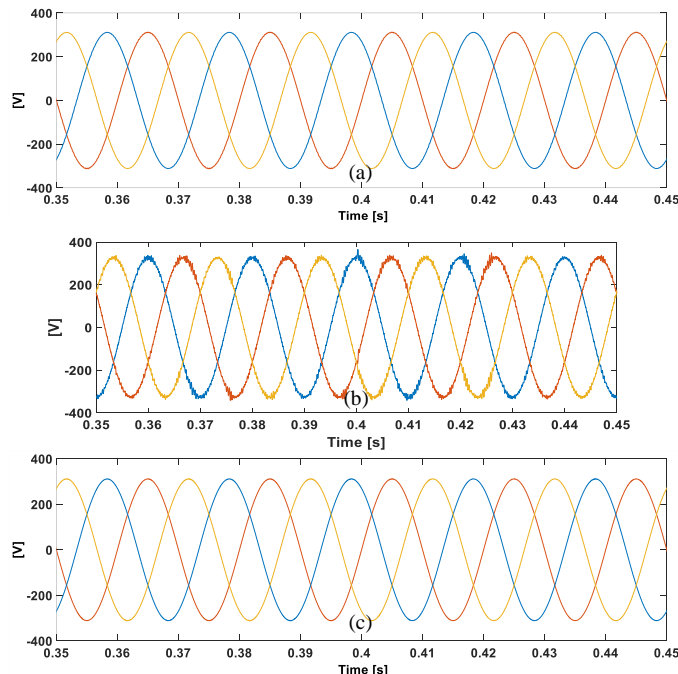


Fig. 14. For (a)PID, (b)SMC and (c) MPC methods transient results of capacitor voltages

Figure 13 (a), (b) and (c) show the simulation results of the transient response of inverter side current as a result of the change in reference current using the respective control methods, respectively. It has been observed that if the MPC method is applied to the system, it responds faster to reach the desired reference value of the current on the inverter side compared to other control methods.

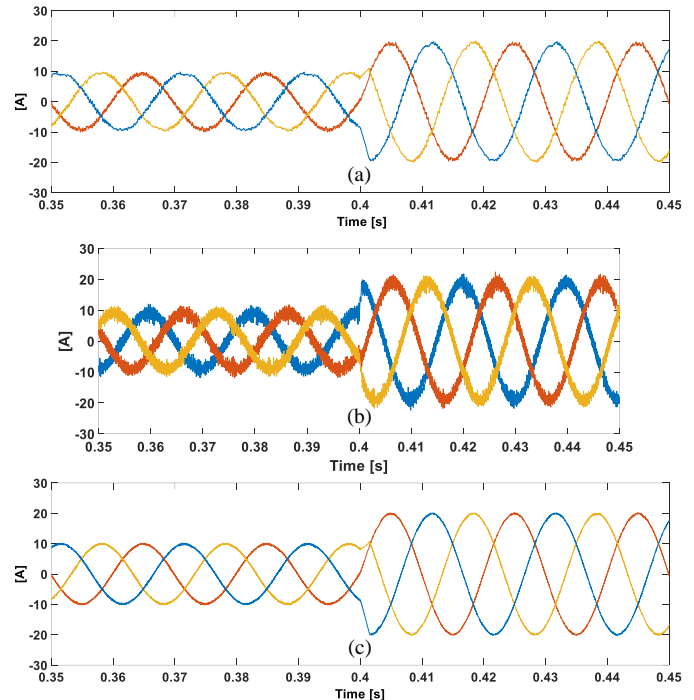


Fig. 15. For (a)PID, (b)SMC and (c) MPC methods transient results of inverter currents

### V. CONCLUSION

In this study, a three-phase grid-connected inverter system is designed. LCL filter is designed so that the mains current of the designed inverter system to be below 5% of THD value. In order for the grid current of the three-phase grid-connected inverter system to reach the desired reference current and the dynamic performance of the system to be good the control of the inverter system with different control methods has been carried out with a simulation study. First of these control methods, the PID control method, which is a linear control method, was applied to the inverter system. The PID coefficients of the PID control method are selected randomly. Secondly, the SMC method, which is a nonlinear control method, was applied to the system. For SMC control, the sliding surface function must be close to zero. Finally, the MPC control method, which is a predictive control method, has been applied to the inverter system. With this control method, the control of the system is achieved by estimating the future value of the measured current.

PID, SMC and MPC methods were applied to the designed LCL filtered grid-tied inverter system, respectively, and a simulation study was carried out. In the simulation study, firstly, steady state analysis was made, and it was seen that the system was stable in the case of applying the specified control

methods to the system. Secondly, FFT analysis of the inverter side, grid side current and capacitor voltage was performed, and it was observed that the MPC method was better than the other control methods in terms of THD value. Finally, transient analysis was performed, and it was observed that the measured current reached from 10A to 20A in a shorter time if the MPC method was applied compared to other control methods.

As a result, it has been seen that the MPC method gives better results than other control methods when applied to the inverter system. In future studies, the MPC method will be examined because it is easy to operate and control functions can be easily added to the cost function.

## REFERENCES

- [1] A. Demiroren and U. Yilmaz, "Analysis of change in electric energy cost with using renewable energy sources in Gökceada, Turkey: An island example," *Renew. Sustain. Energy Rev.*, vol. 14, no. 1, pp. 323–333, 2010, doi: 10.1016/j.rser.2009.06.030.
- [2] N. F. Guerrero-Rodríguez, A. B. Rey-Boué, and E. Reyes-Archundia, "Overview and comparative study of two control strategies used in 3-phase grid-connected inverters for renewable systems," *Renew. Energy Focus*, vol. 19–20, no. June, pp. 75–89, 2017, doi: 10.1016/j.ref.2017.05.007.
- [3] H. Zhang, J. Xian, J. Shi, S. Wu, and Z. Ma, "High Performance Decoupling Current Control by Linear Extended State Observer for Three-Phase Grid-Connected Inverter with an LCL Filter," *IEEE Access*, vol. 8, pp. 13119–13127, 2020, doi: 10.1109/ACCESS.2020.2965650.
- [4] M. Ben Saïd-Romdhane, M. W. Naouar, I. S. Belkhdja, and E. Monmasson, "Simple and systematic LCL filter design for three-phase grid-connected power converters," *Math. Comput. Simul.*, vol. 130, pp. 181–193, 2016, doi: 10.1016/j.matcom.2015.09.011.
- [5] C. Gurrola-Corral, J. Segundo, M. Esparza, and R. Cruz, "Optimal LCL-filter design method for grid-connected renewable energy sources," *Int. J. Electr. Power Energy Syst.*, vol. 120, no. 8, p. 105998, 2020, doi: 10.1016/j.ijepes.2020.105998.
- [6] K. Zeb et al., "A comprehensive review on inverter topologies and control strategies for grid connected photovoltaic system," *Renew. Sustain. Energy Rev.*, vol. 94, no. November 2017, pp. 1120–1141, 2018, doi: 10.1016/j.rser.2018.06.053.
- [7] H. Athari, M. Niroomand, and M. Ataei, "Review and Classification of Control Systems in Grid-tied Inverters," *Renew. Sustain. Energy Rev.*, vol. 72, no. October 2016, pp. 1167–1176, 2017, doi: 10.1016/j.rser.2016.10.030.
- [8] D. Menaga and V. Sankaranarayanan, "Performance comparison for grid connected photovoltaic system using sliding mode control," *J. King Saud Univ. - Eng. Sci.*, vol. 33, no. 4, pp. 276–283, 2021, doi: 10.1016/j.jksues.2020.04.012.
- [9] J. Rodriguez, P. Cortes, R. Kennel, and M. P. Kazmierkowski, "Model predictive control - A simple and powerful method to control power converters," 2009 IEEE 6th Int. Power Electron. Motion Control Conf. IPEMC '09, vol. 56, no. 6, pp. 41–49, 2009, doi: 10.1109/IPEMC.2009.5289335.
- [10] D. M. C. Milbradt, G. V. Hollweg, P. J. D. de Oliveira Ewald, W. B. da Silveira, and H. A. Gründling, "A robust adaptive One Sample Ahead Preview controller for grid-injected currents of a grid-tied power converter with an LCL filter," *Int. J. Electr. Power Energy Syst.*, vol. 142, no. May, 2022, doi: 10.1016/j.ijepes.2022.108286.
- [11] D. Sgrò, S. A. Souza, F. L. Tofoli, R. P. S. Leão, and A. K. R. Sombra, "An integrated design approach of LCL filters based on nonlinear inductors for grid-connected inverter applications," *Electr. Power Syst. Res.*, vol. 186, no. May, p. 106389, 2020, doi: 10.1016/j.epsr.2020.106389.
- [12] X. Q. Guo, W. Y. Wu, and H. R. Gu, "Modeling and simulation of direct output current control for LCL-interfaced grid-connected inverters with parallel passive damping," *Simul. Model. Pract. Theory*, vol. 18, no. 7, pp. 946–956, 2010, doi: 10.1016/j.simpat.2010.02.010.
- [13] C. C. Gomes, A. F. Cupertino, and H. A. Pereira, "Damping techniques for grid-connected voltage source converters based on LCL filter: An overview," *Renew. Sustain. Energy Rev.*, vol. 81, no. 2018, pp. 116–135, 2018, doi: 10.1016/j.rser.2017.07.050.
- [14] C. Gurrola-Corral, J. Segundo, M. Esparza, and R. Cruz, "Optimal LCL-filter design method for grid-connected renewable energy sources," *Int. J. Electr. Power Energy Syst.*, vol. 120, no. 2020, pp. 1–14, 2020, doi: 10.1016/j.ijepes.2020.105998.
- [15] J. Zhao, W. Wu, Z. Shuai, A. Luo, H. S. H. Chung, and F. Blaabjerg, "Robust Control Parameters Design of PBC Controller for LCL-Filtered Grid-Tied Inverter," *IEEE Trans. Power Electron.*, vol. 35, no. 8, pp. 8102–8115, 2020, doi: 10.1109/TPEL.2019.2963200.
- [16] M. Dursun and M. K. Dosoglu, "LCL Filter Design for Grid Connected Three-Phase Inverter," *ISMSIT 2018 - 2nd Int. Symp. Multidiscip. Stud. Innov. Technol. Proc.*, no. 3, pp. 3–6, 2018, doi: 10.1109/ISMSIT.2018.8567054.
- [17] M. I. Solihin, L. F. Tack, and M. L. Kean, "Tuning of PID Controller Using Particle Swarm Optimization (PSO)," *Int. J. Adv. Sci. Eng. Inf. Technol.*, vol. 1, no. 4, p. 458, 2011, doi: 10.18517/ijaseit.1.4.93.
- [18] T. Adel and C. Abdelkader, "A Particle Swarm Optimization approach for optimum design of PID controller for nonlinear systems," in 2013 International Conference on Electrical Engineering and Software Applications, ICEESA 2013, 2013, pp. 1–4, doi: 10.1109/ICEESA.2013.6578478.
- [19] Y. Li, K. H. Ang, and G. C. Y. Chong, "PID Control System Analysis and Design: Problems, Remedies, and Future Directions," *IEEE Control Syst.*, vol. 26, no. 1, pp. 32–41, 2006, doi: 10.1109/MCS.2006.1580152.
- [20] H. Li, W. Wu, M. Huang, H. Shu-Hung Chung, M. Liserre, and F. Blaabjerg, "Design of PWM-SMC Controller Using Linearized Model for Grid-Connected Inverter with LCL Filter," *IEEE Trans. Power Electron.*, vol. 35, no. 12, pp. 12773–12786, 2020, doi: 10.1109/TPEL.2020.2990496.
- [21] M. B. Shadmand, R. S. Balog, and H. Abu-Rub, "Model predictive control of PV sources in a smart DC distribution system: Maximum power point tracking and droop control," *IEEE Trans. Energy Convers.*, vol. 29, no. 4, pp. 913–921, 2014, doi: 10.1109/TEC.2014.2362934.
- [22] A. Abu-Rmieleh and W. Garcia-Gabin, "A gain-scheduling model predictive controller for blood glucose control in type 1 diabetes," *IEEE Trans. Biomed. Eng.*, vol. 57, no. 10 PART 1, pp. 2478–2484, 2010, doi: 10.1109/TBME.2009.2033663.
- [23] M. Shadmand, R. S. Balog, and H. Abu Rub, "Maximum Power Point Tracking using Model Predictive Control of a flyback converter for photovoltaic applications," 2014 Power Energy Conf. Illinois, pp. 1–5, 2014, doi: 10.1109/peci.2014.6804540.
- [24] P. Cortes, A. Wilson, S. Kouro, J. Rodriguez, and H. Abu-Rub, "Model predictive control of multilevel cascaded H-bridge inverters," *IEEE Trans. Ind. Electron.*, vol. 57, no. 8, pp. 2691–2699, 2010, doi: 10.1109/TIE.2010.2041733.
- [25] M. B. Shadmand, M. Mosa, R. S. Balog, and H. A. Rub, "An improved MPPT technique for high gain DC-DC converter using model predictive control for photovoltaic applications," *Conf. Proc. - IEEE Appl. Power Electron. Conf. Expo. - APEC*, pp. 2993–2999, 2014, doi: 10.1109/APEC.2014.6803730.

## BIOGRAPHIES



**EKREM DEMİR** graduated from Sakarya University in Turkey in 2015 in the field of electrical and electronic engineering and received his M.Sc. He graduated from Karabuk University, Department of Electrical and Electronics Engineering in 2020. He has been working as a Research Assistant at Karabuk University, Department of Electrical and Electronics Engineering since 2018. His research interests include inverter topologies, converter topologies, PID control and model predictive control.



**OZAN GULBUDAK** received the B.Sc. and the M.Sc. degree in electrical engineering from Mersin University, Turkey in 2008 and 2010. He received Ph.D. degree from the University of South Carolina, Columbia, USA. Since 2017, he has been with Karabuk University, where is currently Assistant Professor. His research interests include model predictive control, development of control platforms based on FPGA, direct matrix converters, inverter topologies and motor drives.



**MUSTAFA GOKDAG** received the B.Sc. degree with Honor in electrical and electronics engineering from Firat University, Turkey, in 2009, and the M.Sc. and Ph.D. degrees in electrical and electronics engineering from Karabuk University, Turkey, in 2011 and 2016 respectively. From 2009 to 2016, he was a Research Assistant with the department of electrical and electronics engineering in Karabuk University. Since 2016, he has been an Assistant Professor in same department. His research interests include modeling and control of dc-dc power converters and model predictive control of ac-dc, dc-ac, and ac-ac power converters for renewable and electrical drives.

# DALI Compatible Smart LED Driver Controller with Wi-Fi Communication

Nazmi Ekren and Bunyamin Sogut


**Abstract**— DALI (Digital Addressable Lighting Interface) is one of the communication types commonly used in smart LED systems. Energy savings and user comfort can be achieved by making scenario definitions for LED drivers. In this study, the design of the LED driver controller, which is controlled via Wi-Fi communication with the user interface supporting the DALI protocol, will be mentioned. Communication of the developed controller with the user interface will be carried out wirelessly. Wi-Fi has been preferred. The hardware part of this developed system consists of a processor-supported control circuit, a communication unit circuit and DALI hardware circuit parts. The designed smart LED driver controller can fulfill the standard requirements of the DALI protocol. It converts the command information received over Wi-Fi to the DALI protocol and provides control of the LED driver. The control device will be controlled and monitored via smartphone, computer, tablet, and web. In conclusion, with the commands given from the user interface, the LED driver turns on/off the light, increases/decreases the light intensity and similar commands available in DALI standards are controlled.

**Index Terms**— DALI Protocol, LED Driver, Smart Lighting, Energy Saving, Wi-Fi Communication.


## I. INTRODUCTION

**E**NERGY SAVING is using less energy by changing behaviors or habits. Energy efficiency using new technologies without reducing quality and performance, better it is the provision of living conditions. Energy efficiency should be increased to use limited energy with better quality and to provide a more economical structure to enterprises. So, it is necessary to analyze the energy in every aspect. LED lamps consume 90% less energy and are produce lighter,

**NAZMI EKREN** is with Department of Electrical Engineering, Marmara University, Istanbul, Türkiye, (e-mail: nazmiekre@marmara.edu.tr).

 <https://orcid.org/0000-0003-3530-9262>

**BUNYAMIN SOGUT** is with Akim Metal R&D Center, Istanbul, Türkiye, (e-mail: bsogut@akimmetal.com.tr).

 <https://orcid.org/0000-0002-6152-2473>

Manuscript received Feb 23, 2023; accepted Apr 10, 2023.  
DOI: [10.17694/bajece.1254909](https://doi.org/10.17694/bajece.1254909)

compared to light bulbs. In this way, they help to achieve energy savings [1].

Many automation and smart technology solutions are used in the field of energy efficiency and saving. The most effective solution for the development of smart lighting systems is the use of universal protocols. One of these protocols is DALI.

DALI is a concept that stands for a smart lighting management system that provides increased energy savings, easier installation and maintenance, and maximum control and retrofit flexibility in a completely open standard. DALI is not a single product. It is an industry-standard protocol that allows the seamless mixing and matching of DALI-compatible components from different manufacturers (ballasts, control systems, sensors, controllers, switches, etc.) into complete systems [2]. Wireless technology has been identified as a promising wiring and communication alternative for building systems. Low cost and less complexity, as well as increased flexibility in wiring, are the main advantages of wireless-enabled systems over wired counterparts [2].

To control the LED drivers that support the DALI protocol, a master controller is needed, which is the requirement of each communication protocol [3]. Controllers serve to transfer the situations desired by the user to slave devices. Commands to controllers are usually sent via a user interface. Human interaction is also provided by the application tier via graphical user interfaces (GUI) [4]. For commands to be sent to the controllers via the user interface, communication is needed between the computer and the controller. This communication is divided into 2 groups, wired or wireless. In the study, the communication between the user interface and the controller is carried out wirelessly using Wi-Fi communication.

In this study, the product to be presented to the customer who provides remote control of the DALI communication protocol is aimed. The working output is the product, and it is planned to remotely control the LED drivers that support the DALI communication protocol. A DALI protocol controller with Wi-Fi support has been made. Thanks to this device, 64 DALI-supported LED drivers on the line were connected to the DALI controller, which is the output of this study, and the control was made. With these controls, it is possible to remotely control the device by connecting to any Wi-Fi line by making a DALI line connection in the environment where DALI-supported LED drivers are located.

The final output of the study is a product designed with hardware and software. The WEB page has been designed for



testing this product. It is possible to access this WEB page from any platform with an internet and internet browser, such as a computer, tablet mobile phone and it is possible to control the LED lighting from anywhere desired.

## II. RELATED STUDIES IN THE LITERATURE

20% of the consumed electrical energy is spent in industrial enterprises, 30% in stores, and approximately 40% in offices for lighting purposes. The share of lighting in energy consumption and energy expenditure is the largest item after heating and cooling systems. Considering that the electrical energy spent on lighting in buildings created with a modern understanding is about 60%, the importance of energy saving in lighting is better understood. The next step is to check the lighting. Lighting control, which will be carried out using appropriate control techniques and systems, should create lighting that can be suitable for each element working in terms of the amount and quality of light. By automatically controlling the lighting, it is also possible to manage consumption and expenditure more effectively by actively saving energy.

Bellido-Outeirino F. J., Arc. [5] his work focuses on the integration of DALI devices into wireless sensor networks to use energy effectively. Since different manufacturers are usually interested in one aspect of building automation, the building automation system offered to the end user has an integrated building management system and different sub-communication systems. Their main purpose is to provide the end consumer with an economical, fully centralised system in which automation systems are managed by IEEE 802.15.4 based wireless sensor network [5].

In the study conducted by the Moeck M [6] et al., they focused on the development of a prototype in a WSN network (Wireless Sensor Network) that also integrates the DALI protocol. Since DALI is a communication protocol standard that has been used for many years and is highly preferred by manufacturers, it is quite easy to find DALI compatible devices. This is one of the biggest reasons why they prefer [6].

In Bellido-Outeirino, F. J Arc's [7] work, he uses IEEE 802.15.4 networks with WSN to control DALI devices. ZigBee for working directly on the PHY (Physical Layer) and MAC (Media Access Control) layer of IEEE 802.15.4 [7] instead of using it, they decided to implement a WSN based on IEEE 802.15.4. Due to the lack of an interoperable protocol between different manufacturers, they did not prefer to use ZigBee.

In the study of Man-Lin Wu [8] et al., they focused on software development of the DALI master and DALI slave equipment manufacturer, while general lighting manufacturers focused on purchasing commercially available options to reduce individual costs and business development time.

In a study conducted by Delvaeye et al. [9, 10] in Belgium, they stated that the electrical energy savings in the lighting system of a DALI-controlled open-loop system are 46%, based on a one-year measurement.

In the study conducted by George K. Man [11], they have made a low-cost, low-power, efficient DALI LED driver controller based on Raspberry, which is open source. The Pi3

microcontroller was developed as a prototyping platform, control software and Linux kernel.

In the study by Jingyu Liu et al., [12] they used the DALI protocol to communicate the controller with LED luminaires. The simulation results show that an uncontrolled lighting system can provide sufficient illumination. The lighting system has determined wider controllability in order to ensure that the lighting environment operates in the most energy-saving way. The experimental results show that significant lighting energy is obtained by using the designed controller.

In the study conducted by Niko Gentile et al., [13] lighting systems were also used in places where daylight was insufficient, thanks to the increased control capabilities with LED technology. The use of daylight in integrative lighting is currently very limited.

In the study by Zhong Chen et al., [14] they worked on the DALI protocol by adjusting the LED light in busy places.

In the study by Mary Ann George et al., [2] they designed a lighting system with two dependent microcontrollers using a temperature sensor and a motion sensor by creating a photo-sensor interface with wireless technology.

In the work done by Oscar Osvaldo et al., [15] a bridge is created between the DALI bus, providing the necessary timing for the hardware and MCU selection of the DALI protocol, bus bits, Manchester coding and frame formatting.

It was implemented by Francisco Bellido-Outeiriño et al. [16] by integrating the DALI protocol with the advanced control system on the lighting system. Although designed for lighting control, DALI has also been adapted to other applications, such as the following. HVAC, motor, or fan controllers etc., the automation system that allows monitoring and control, which is part of the system, has been used in applications for the end user and energy efficiency.

In the work by Gil-de-Castro A et al., [17] the term smart grid refers to a fully modernized electrical distribution system that monitors, protects and optimizes the operation of its interconnected elements end-to-end. Smart Grid is expected to affect all areas of electric power systems, productions, distributions, end consumers, citizens, electric vehicles, street lightings and other home devices. There is a great potential to renew existing old street lighting and save energy consumption.

In the study by Domingo-Perez F et al., [18] a new remote management system for street lighting is presented. The management system was implemented using a wireless communication system and a lighting control protocol. It focuses on developing a street lighting management system using wireless sensor networks and DALI ballasts, and experimental results obtained from various tests are presented. To test the network and obtain the results, they implemented a JAVA-based SCADA (Supervisory Control and Data Acquisition) interface. The user can send a command to the PAN coordinator using this interface; the coordinator sends the selected command to the selected node.

Nowadays, some smart lighting applications can be made on mobile phones. Samuel Tang et al., [19] developed an algorithm by using the smart lighting system application, the daylight on the smartphone, and enabled the lighting system to be controlled wirelessly.

The system designed by Tullio de Rubeis et al. [20] is based on a mountable smart control unit and lighting control devices. The installation is non-invasive and does not require any modifications. Communication Provides communication between each lamp and the control system via 2.4GHz wireless protocol.

T.W. Kruisselbrink et al., [21] on the other hand, tested using two alternative brightness-based lighting control algorithms. In algorithm 1, the goal is to maintain desktop lighting. If it is algorithm 2, the goal is to maintain the predefined stage lighting.

The study by Ivan Chew et al. [22] focuses on energy-efficient, commercial and advanced smart lighting systems in smart lighting technology. In addition, the review of smart lighting connection options and their potential are discussed.

Kim D. In the study by H et al., [23] the modern lighting control system heralds a radical change since the development of LED lighting and the universalization of the Internet. An advanced lighting system starts to be controlled anywhere at any time without time and space restrictions via the Internet, and the ambient light can be controlled automatically depending on the environment. In addition, lighting controls began to illuminate the room as a single unit, and wireless communication began to be used instead of the wired communication technologies described for individual lighting control. In the study, lighting control system using wireless technology and lighting elements that should be considered by applying ad hoc mode or infrastructure mode of wireless communication technology are summarized. In this study, performance factors for wireless lighting control networks are studied. Some factors, such as latency, packet loss and the number of nodes are also as important as the traditional wireless communication network. But it is not as important as others, such as power saving and mobility. Problems such as improving communication broadcasting remain a challenge that needs to be solved.

In the study by Han Zon et al., [24] a study was conducted with the aim of reducing energy consumption while maintaining the lighting comfort of the building occupants. Using WinLight by existing Wi-Fi infrastructure, a suitable dimming command is calculated for each lamp of a lighting system. For this, a control algorithm has been created. A centralized lighting control system assigns these commands to a regional gateway, and occupancy-oriented lighting control is achieved by locally activating the brightness adjustment.

In the study carried out by Qiu C and his colleagues, he presents a wireless control system for visible light communication (VLC). It is equipped with BLE (Bluetooth Low Energy) SoC (Security Operations Center) to support iBeacon. VLC data/frequency can be easily configured by smartphone. This combined beacon/lighting/VLC function helps to reduce the cost of beacon placement and improve indoor localization accuracy [25]. The underlying communication technology of iBeacon is Bluetooth Low Energy. It transmits a signal with only small bits of data, typically a unique identifier. This allows mobile apps (Applications) to Decouple between beacons and act when necessary.

In the work of Zheng Z. et al., [26] visible light communication (VLC) technology uses light-emitting diodes (LED) as a medium to enable high-speed communication. The information is transmitted in the form of binary data by modulating the intensity of the LED light. As a new type of highly effective location-based technology, it is currently receiving great attention. In these two studies, it was integrated into a single system based on Bluetooth SoC. This compact system provides accurate location inside spaces and provides a flexible configuration in system parameters.

In the study of George M. et al., [2] a photo sensor, temperature sensor and occupancy sensor interface were installed on the Master CC2531 USB Dongle. By sending control signals to two dependent microcontrollers (CC2531 USB Dongles) using these sensor inputs, it has been enabled to control the ballast in two different regions using ZigBee Communication.

Michael Kent et al., [27] for energy efficiency, processed real-time lighting data with sensors that transfer to a light control controller, and controlled whether daylight provides more illumination than required or desired.

A smart LED luminaire was designed by Ivan Chew et al. [28] in this fixture; the LED driver consists of LEDs, ZigBee module, microcontroller and sensors. By creating an interface with the wireless communication module, the ambient light level was controlled.

In the study by Michael Papinutto et al., [29] as a result of current research they mainly focused on energy saving and automation mostly does not allow customization. In this case, users have developed strategies themselves to bypass automation.

In the study by Nima Hafezparast Moadab et al., [30] advanced and integrated lighting technology control, including an internet-based network, can be made for data communication used by lighting systems. Different scenarios have been developed by conducting this light simulation study in Sweden. The result of the study shows that the appropriate use of smart lighting solutions, including optimized sensor applications, has the potential to generate savings. Electric lighting energy consumption compared to non-smart systems, energy savings of more than 50% have been achieved.

L.T. In the study by Doulos et al., [31] the energy efficiency of LED luminaires is much better than others. Although the power factor values of luminaires with T5 fluorescent lamps are lower, they are pale.

When the differences between the other studies in the literature and this study are examined, the studies in the literature are generally suitable for automation systems. It has been seen that multiple sensors are remotely managed systems with wireless communication protocols for large businesses. These large systems are quite costly. In this study, the main purpose is to make DALI communication protocol supported master device. With this study, an interface was developed, and master device control was provided. The simple structure of the interface provides ease of use and low cost for customers.

III. MATERIAL AND METHOD

The modern lighting system is not thought out independently of the controls. It allows for ensuring the regulatory parameters of the light environment with minimal energy costs. Various solutions can be used to control the light current. The protocols used in these systems are analogue 0-10V control, DMX512 (Digital Multiplex) protocol, RDM protocol (Remote Device Management), KNX (Konnex) protocol, Modbus and one of the most common ones is the DALI protocol [32].

A. The DALI Protocol

DALI is a communication protocol developed for lighting systems in accordance with the IEC 62386 technical standard. Devices working with the DALI protocol send messages to each other over the DALI line in a wired way [33]. The DALI protocol is used for communication between the master device and the slave. DALI is compatible with LED drivers provides energy saving in lighting systems with high efficiency. The DALI communication system consists of at least one controls, one DALI-supported LED driver and one power supply to supply the DALI line. The master can send commands and control all the lighting hardware in the DALI line individually or in groups [34].

In this study, commands will be sent to the controller via a user interface. However, in DALI systems, the controls do not have to be a user interface. The intensity of the light falling on the sensor is measured according to the illumination level of the environment. The sensor connected to the DALI line sends commands directly, and the sensor can control a lighting device or a group in a slave state [35].

The address information of the DALI LED driver devices and grouping information are made with the commands that will be sent to the LED drivers via the DALI line. In the DALI communication system, each lighting device has an address between 0 and 63. In other words, a DALI control device can control up to 64 drive devices [36]. In the case of using more LED drivers, controls should be used once for every 64 groups and their controls should be performed separately.

If we look at the general automation system structure in Figure 1, communication is used between the DALI controller and the lighting hardware, while Wi-Fi communication is selected between the control device and the user interface software. Depending on the control device, a different method can also be selected instead of Wi-Fi [8].

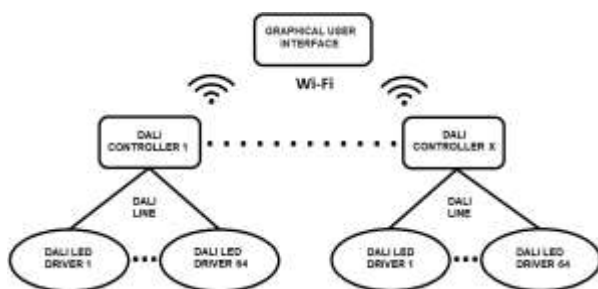


Fig.1. General Automation System Architecture.

Electrical characteristics of the DALI controller There is a double-wired connection between the DALI drives. A bridge

diode is used at the input of the DALI circuit for protection purposes. The purpose of this is a precaution taken even though the team making the installation in the field environment makes the connections in reverse. There are no polarization restrictions due to this bridge diode. There is no positive or negative direction status for the cable that provides data communication [37]. A signal mark above 9.5 V is a sign of a high level. A signal less than 6.5 V is a low-level signal. The main control unit communicates with the DALI-supported LED drivers by setting the level to high or low according to the DALI protocol [34].

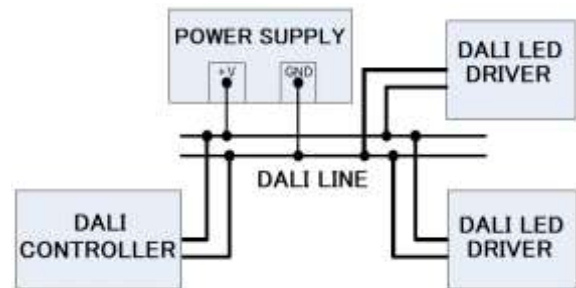


Fig.2. DALI Connection Diagram.

Logic 1 and logic 0 values are used when making DALI communication. For DALI communication to be successful, at least one control, at least one DALI-supported LED driver and power supply are needed on the connection line, as shown in Figure 2. Since the DALI devices do not supply the communication line, the DALI line must be short-circuited to set the voltage level on the line to logic 0. But since a short circuit during switching for communication will damage the DALI hardware, according to DALI standards, the power supply must allow a maximum current of 250 mA. In the DALI communication system, all lighting hardware communicates via the same communication line. The length of the cable line used should be a maximum of 300 meters.

According to DALI standards, each of the DALI devices in the communication system should be designed to consume a maximum current of 2mA. The cable used for the line must be 600V isolated. Communication is provided by the binary number system (0-1), the logic value graph used in DALI is given in Figure 3 [8].

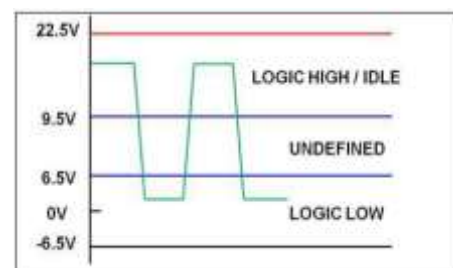


Fig.3. DALI Electrical Characteristics [8, 9].

B. Wireless Communication Protocols and Wi-Fi

Although it does not realize smart lighting systems, the most effective solution is to use universal protocols. Wireless communication protocols are one of the most important issues



for IoT (Internet of Things). Communication protocols allow the devices in the system to communicate with each other.

These communication protocols are LoRa, Wi-Fi, Wi-SUN (Wireless Smart Utility Network), 4G/LTE (Long Term Evolution), LTE-M, Zigbee and Bluetooth [38]. Wi-Fi is the most recognized wireless network technology in the world. It is used to connect phones, computers, and tablets to the Internet. This study will also be used for controls and user interface communication on the computer using Wi-Fi communication [39]. It is compatible with IEEE 802.11 based standard. It communicates on 2.4GHz and 5GHz frequencies. It provides a usage environment for end users due to its advantages of fast and easy accessibility, sensitive security approach, high service quality and convenient usability [40]. In order for us to use Wi-Fi communication, it is necessary to add a Wi-Fi module to the card on which our DALI software is located. The hardware and software block connection diagram that should belong to the Wi-Fi connection area is given in Figure 4.

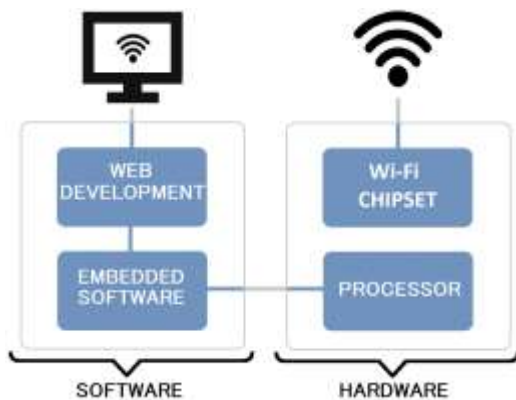


Fig.4. Wi-Fi Hardware and Software Block Diagram.

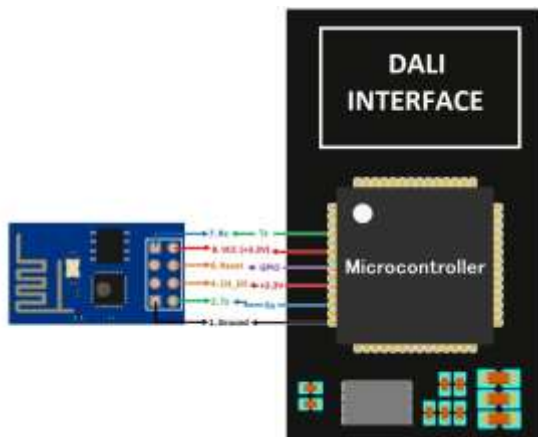


Fig.5. Connection of ESP8266 with Microcontrollers.

The ESP8266 module was also used in our project to work, so that we could only connect to the Internet and get the user's settings via the web-based interface. The ESP8266 is a WiFi chip with microcontroller capability and full TCP/IP (Internet Protocol-Internet Protocol) protocol stack that allows any microcontroller to access the WiFi network [41]. The ESP8266 module can host an application in itself or be

controlled by another application processor [42]. Data exchange is provided via the main processor UART communication protocol with the ESP8266 module. An example illustration of the connection diagram is shown in Figure 5.

IV. HARDWARE AND SOFTWARE OPERATION

A. Hardware

The general hardware stages of our study have a main control unit, ESP8266 wireless communication module connected to the main control unit, DALI hardware circuit that will allow communication with DALI compatible LED drivers. The block diagram of the hardware made within the scope of the study is shown in Figure 6.

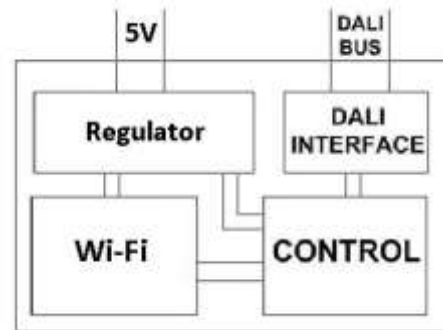


Fig.6. Hardware Block Diagram.

In the main control unit section, the data received via Wi-Fi communication is transferred to the LED drivers via the DALI hardware circuit with the DALI messaging software. The DALI control circuit is connected to our processor in the main control section via 2 GPIO pins. One of the pins is set as signal input (IN) and the other is set as signal output (OUT) pin. The reason we need the DALI hardware circuit is that the processor pins work with 3.3 V. But for the DALI protocol logic 1 signal, we need values between 9.5V and 22.5V, and for the logic 0 signal, between -6.5V and 6.5V. The remaining sections between 6.5V and 9.5V are Decoded as meaningless and are not processed.

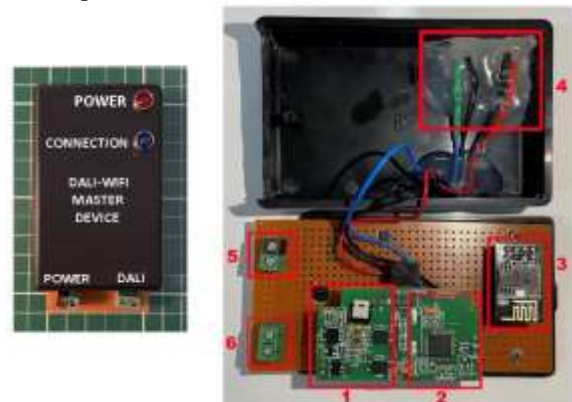


Fig.7. DALI Compatible Smart LED Driver Controller with Wi-Fi Communication.

There is a bridge diode at the place where the DALI hardware circuit is connected to the DALI line. Although DC is a voltage, the bridge diode must be present here for the requirement of the DALI protocol. Many devices can be connected to the DALI line at the same time. There are cable



tangles in large automation systems. Polarization is eliminated in the DALI line thanks to the bridge diode. It is ensured that the cables in the DALI line are connected in 2 directions.

In this study, a device that transmits the data received from the web interface to the DALI control device via Wi-Fi and controls a DALI-compatible LED driver over the DALI line has been designed.

Figure 7 shows a visual of the control device.

As can be seen in Figure 7, the part indicated with 1 is the DALI hardware circuit. It transmits signals to the processor in isolation. The high-level signal between 9.5V and 22.5 V on the DALI line decelerates the signal level of the processor to 3.3 V. The low-level signal between -6.5V and 6.5V decays to the 0V level. In the same way, the signals sent from the processor reach the level of DALI standards. The part indicated with 2 is the hardware unit belonging to the processor and peripherals. The preparation of DALI messages with the analysis of data from Wi-Fi is carried out in this unit. the part indicated with 3 is the ESP8266 Wi-Fi module. The user interface data is received thanks to this module and transferred to the processor via UART. the part indicated with 4 has warning LEDs. One of these LEDs, the power LED, lights up if there is energy in the device, and the other is the LED that turns off if the connection LED is in communication with the user interface. The part specified with 5 is the power terminal. The part specified with 6 is the terminal used for DALI communication.

*B. Software Structure*

When the device made within the scope of the study is energized, the systemically necessary initial adjustments are made first. These are setting the processor frequency, setting the input-output pins used, the communication settings, and starting the timers. After these adjustments are made, the initial settings of the wireless communication unit are made first on our processor. Later Communication settings for the DALI protocol are made and the device is made ready. After the initial adjustments are completed, Wi-Fi messages are checked every second. The values taken from the interface are compared with the old values. In the beginning, the received message is checked. If there are no changes in the received parameters, the control is performed from the beginning. The DALI message is not created. If there are changes in the received values, the message content is assigned to the relevant variables in a meaningful way and the DALI message starts to be created. In Figure 8, the general software code flow structure is shared.

DALI uses Manchester encoding to send the start bit and information bits. The information rate is 1200 bps with a gap of  $\pm 10\%$ . The duration of one bit is 833.33  $\mu$ s, as shown in figure 9. The largest valence bit (MSB) is sent first. As shown in Figure 9, the 833.33us bit duration can be between 749.99  $\mu$ s and 916.66  $\mu$ s with a 10% margin of error. Likewise, 416.66  $\mu$ s with a half-bit duration can be between 374.99  $\mu$ s and 458.33  $\mu$ s with a 10% margin of error.

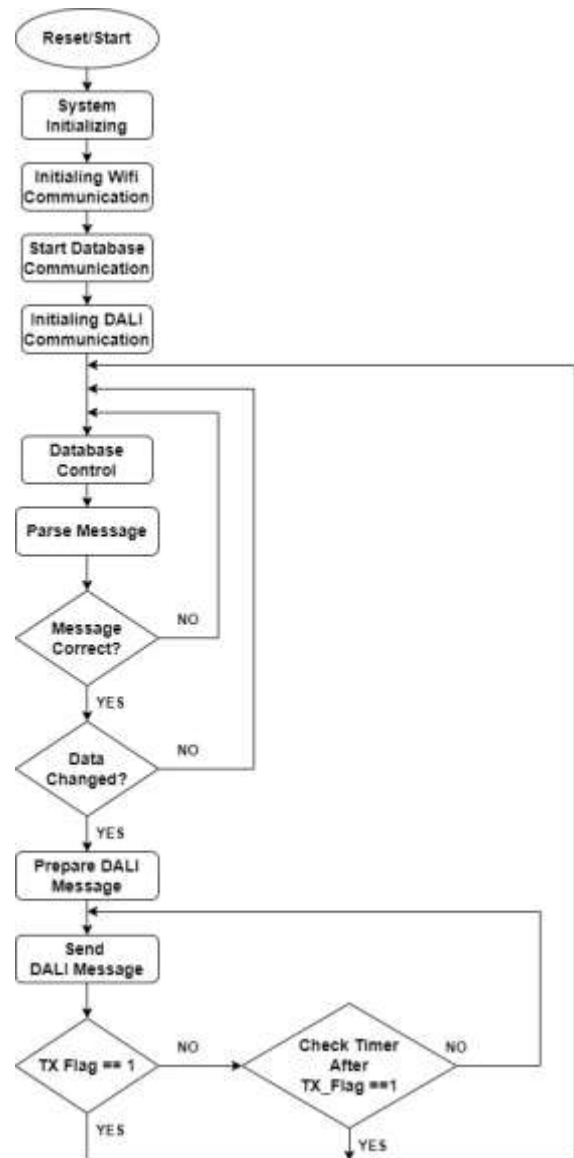


Fig.8. General Code Flow Chart.

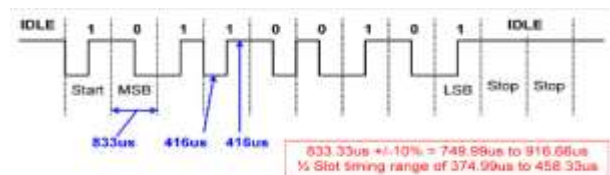


Fig.9. DALI Communication [8, 9].

In the forward direction, the message is the packet sent to the LED driver by the controller. The message in the reverse direction is the response packet sent back to the controller by the LED driver. It consists of a start bit, eight data bits and two stop bits.

The timing requirements for messages sent consecutively, as shown in Figure 10, are given below [43];

- The time Deciphered between two consecutive message data sent must be at least 9.17ms.
- The transition time between the message data received in the reverse direction and the message data sent in the

forward direction should be in the range of 2.97ms to 9.17ms.

- The control unit sends the message data in the forward direction and waits for 9.17ms. If the message data has not been sent in the reverse direction after 9.17ms has passed, the LED driver interprets this status as “no response has been received”.
- There should be at least 9.17ms time gap between the two-message data in the backward and forward directions.

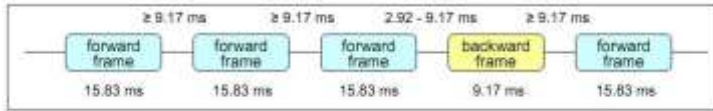


Fig.10. Message Data Sent Back to Back Duration Display [34] [39]

Manchester coding, in most cases, plays a critical role in binary data transmission, especially in analogue, radio frequency, optical, high-speed digital communication or long-distance digital communication. The package sent between the controller and the LED driver is a two-phase manchester package. Manchester coding is performed before the package is sent from the controller. Then the package is received by the LED driver, decoded, and the address and messages are processed accordingly.

The sample encoding in which a message is sent to the DALI line is shared in Figure 11. As can be understood from the visual, some commands are sent to the LED driver located at address 1 according to the Set\_DALI\_Level. If the level to be sent is 0, the OFF signal, if the minimum level is equal to 1, the minimum level message, if the maximum level is equal to 100, the maximum level message has been sent. If there is an intermediate value LED brightness level other than these levels, that level is printed directly on the line with SET\_Decal\_level.

```

259 if (Flag_Changed_DALI_Level == TRUE)
260 {
261     Flag_Changed_DALI_Level = FALSE;
262     if (Set_DALI_Level == 0)
263     {
264         DALI_Send_Cmd(ADDRESS01, OFF, SHORT_ADDRESS, FOLLOWING_FORWARD);
265     }
266     else if (Set_DALI_Level == 1)
267     {
268         DALI_Send_Cmd(ADDRESS01, RECALL_MIN_LEVEL, SHORT_ADDRESS, FOLLOWING_FORWARD);
269     }
270     else if (Set_DALI_Level == 100)
271     {
272         DALI_Send_Cmd(ADDRESS01, RECALL_MAX_LEVEL, SHORT_ADDRESS, FOLLOWING_FORWARD);
273     }
274     else
275     {
276         DALI_Send_Cmd(ADDRESS01, Set_DALI_Level, SHORT_ADDRESS, FOLLOWING_DIRECT_ARC_POWER_LVL);
277     }
278 }

```

Fig.11. Sending a DALI Message Flow.

The DALI message to be sent in the DALI\_Send\_Cmd function is being prepared. As shown in Figure 12, the required address information for the message to be sent is set first. After that, our existing data is encoded in manchester, and the buffer encoded in manchester as dali\_array\_cmd is created. After that, the Timer\_Start function is called and the manchester encoded data is sent to the processor pins here and DALI messaging starts.

```

330 unsigned char DALI_Send_Cmd(unsigned char ballastAddr, unsigned char cmd,
331                             unsigned char typeOfCmd, unsigned char followingType)
332 {
333     unsigned char data_array[2];
334     unsigned char i;
335     //set output pin to 0
336     _OUT_LINE(1);
337
338     tick_count = 0;
339     bit_count = 0;
340     //set DALI state to send data
341     dali_state = SENDING_DATA;
342     //fetch ballast address and command
343     data_array[0] = (char)ballastAddr;
344     data_array[1] = (char)cmd;
345
346     //reset dali_array_cmd values
347     for (i = 0; i < 17; i++)
348         dali_array_cmd[i] = 0;
349
350     //önderilecek IFD sorusu bilileri sirilim
351     PrepareAddressByte(data_array, typeOfCmd, 0, followingType);
352
353     //encode data - Manchester encoding
354     PrepareDataToSend(data_array, dali_array_cmd, 2);
355
356     Timer_Start();
357
358     return TRUE;
359 }

```

Fig.12. DALI Message Sending Function Software.

```

370
371 void PrepareDataToSend(unsigned char *commandArray, unsigned char *tx_array,
372                       unsigned char bytesInCmd)
373 {
374     //set default value for the mask
375     unsigned char mask = 0x80;
376     //variable which hold one byte value - one element from commandArray
377     unsigned char dummy;
378     //number of bytes in command
379     unsigned char bytes_counter;
380     unsigned char i;
381     //number of active bit
382     unsigned char bitCounter;
383     //set default value
384     bitCounter = 8;
385     for (i = 0; i < 9; i++)
386     {
387         tx_array[i] = 0;
388     }
389     //loop through all bytes in commandArray
390     for (bytes_counter = 0; bytes_counter < bytesInCmd; bytes_counter++)
391     {
392         //assign byte for use
393         dummy = commandArray[bytes_counter];
394         //set mask to default value
395         mask = 0x80; //0b10000000
396         //increment number of active bit
397         bitCounter++;
398         //check if active bit is the first one
399         if (bitCounter == 1)
400         {
401             //start bit is always 1 - in manchester that is END_BIT_PULSE
402             tx_array[0] = DALI_END_BIT_PULSE;
403         }
404         //byte command
405         //go through all bytes and use Manchester
406         for (i = 1; i < 8; i++) //1 & 9
407         {
408             //check if bit is one
409             if (dummy & mask)
410             {
411                 //assign pulse value - manchester
412                 tx_array[i + (8 * bytes_counter)] = DALI_END_BIT_PULSE;
413             }
414             else
415             {
416                 //assign pulse value - manchester
417                 tx_array[i + (8 * bytes_counter)] = DALI_START_BIT_PULSE;
418             }
419             //check mask value
420             if (mask == 0x01)
421                 mask <<= 7; //shift mask bit to MSB
422             else
423                 mask >>= 1; //shift mask bit to 1 right
424         }
425     }
426 }
427
428 //*****

```

Fig.13. Manchester Coding of the Data.

The prepared hardware and software have been tested. The image taken at the DALI line exit is given in Figure 14. When the oscilloscope images were examined, the accuracy of the results obtained was seen in both communication signals.

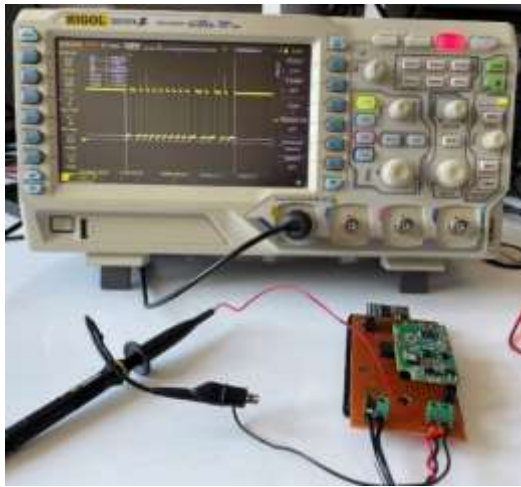


Fig.14. DALI Hardware Circuit Output Even the DALI Message Sent.

Tests were carried out with a Tridonic brand LED driver that has passed DALI standards tests and has a DALI certificate. Brightness reduction, brightness increase, minimum and maximum levels have been adjusted via the web interface. It was observed that the study fulfilled the required standards of DALI with the tests performed.



Fig.15. Experimental Setup.

Figure 15 shows the image of the experiments with the Tridonic brand LED driver. In the tests carried out, Tridonic brand power supply was used to supply the DALI line. As a result of the tests, it has been understood that the designed control device will be used safely in practical work due to the low cost of the materials used, easy to supply and the stability of the system.

It has been observed that the data entered via the user interface is transferred from the module to the processor via the UART protocol. The data were observed with the oscilloscope, and it was seen that the communication speed was within the tolerance gap determined. Live data tracking

was performed via debug (debugging) via the processor. The data were examined, and the accuracy was observed.

With the Data assignment, it is known which command the user sent. The DALI command message is created. It was seen by debugging that the DALI message was created and sent after manchester encoding was performed. The DALI signals sent were examined with the help of an oscilloscope. The communication speed of the studied DALI signals is stated in the DALI technical document [5]. It was observed that it was in the specified gap. Peak signals at the highest and lowest levels also have electrical properties [9] it was seen that he was in it. After the accuracy of the tests was observed, it was observed that it communicated with the Tridonic brand LED driver. The desired LED brightness level has been checked.

As shown in Figure 16, there is a DALI signal at the output of our processor, the current high level of which is 3.24V, the low level of which is measured as 200mV. This signal is measured directly from the processor output. In the continuation of the circuit, this signal is transferred to the DALI hardware circuit. The signal level of the signal coming out of the processor will be printed on the DALI line so that the high level, which is the DALI standard, is between 9.5V and 22.5V, and the low level is between -6.5V and 6.5V.

In Figure 16, the same DALI signal at the processor output is zoomed in and the time of  $\frac{1}{2}$  bit of the signal is measured. This value, which is seen as the BX-AX (Cursor B, Axis X - Cursor A, Axis X) difference in the oscilloscope image, is seen as 420us. As mentioned earlier, there is a margin of error of 10%. Under normal conditions, this level should be 416us with a  $\pm 10$  difference between 374.99us and 458.33us, which is sufficient for communication.

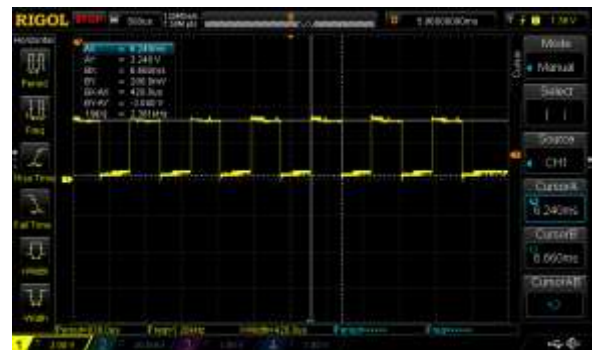


Fig.16. Measurement of Processor Output DALI Data Bit Time.

The 0V-3.3V signal at the processor output is sent to the line by passing through the DALI hardware circuit while pressing the DALI line. The reason for this is that we can print a signal even at the DALI signal level. If this circuit is not used, our high signal, which is 3.3V, will remain between -6.5 V and 6.5 V at the low level according to DALI standards. Therefore, it will be a meaningless message for other devices on the DALI line.

Figure 17 and figure 18 show the signal passing through the DALI hardware circuit. The maximum point of the signal AY (Cursor A, Axis Y) was measured at 17.40V. The high signal level, which is a requirement of the DALI standard, is between 9.5V and 22.5V. In the same way, the low signal level



measured BY (Cursor B, Axis Y) 1.3V is between -6.5V and 6.5V, which is a requirement of the DALI standard.



Fig.17. Observing Peaks at a High Level of the DALI Signal.

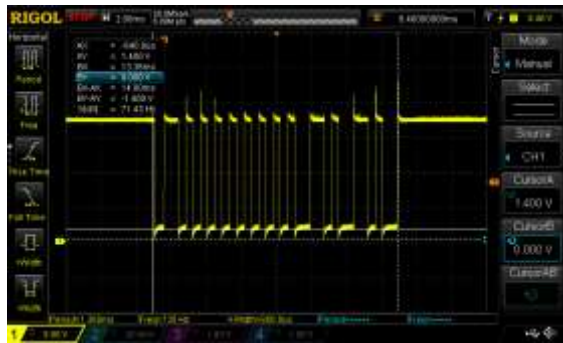


Fig.18. Observing Peaks at a Low Level of the DALI Signal.

Figure 17 shows the peak points in the transitions from 0 to 1 signal level due to the nature of communication signals at a high signal level. It is observed that the maximum point of this level is 21.90V, which is indicated by the AY. Since it is below 22.5V and is an instant value, it does not have a negative impact on our messaging. The same situation is shown in figure 18 for the low level. Here, the peak points in the transitions from 1 to 0 signal level are seen. The lowest signal level was measured as 0V shown in the BY. This situation is not a negative situation for our messaging.

```

void Uart_Initialize(void)
{
    USART_InitTypeDef USART_InitStructure;
    NVIC_InitTypeDef NVIC_InitStructure;

    // USART1 enable (Clock enable)
    RCC_APB2PeriphClockCmd(RCC_APB2Periph_USART1, ENABLE);

    USART_InitStructure.USART_BaudRate = 115200; //Baudrate ayari
    USART_InitStructure.USART_HardwareFlowControl = USART_HardwareFlowControl_None;
    //USART Full-Duplex calismasi TX ve RX modu aktif edilir
    USART_InitStructure.USART_Mode = USART_Mode_Tx | USART_Mode_Rx;
    USART_InitStructure.USART_Parity = USART_Parity_No; //Parity kullanilmiyoruz
    USART_InitStructure.USART_StopBits = USART_StopBits_1; //Stop bit 1 ayarlaniyor
    USART_InitStructure.USART_WordLength = USART_WordLength_8b; //Data bit uzunlugumuz 8
    USART_Init(USART1, &USART_InitStructure);

    // USART1 ka interrupt aktif ediliyor. USART'dan herhangi bir data geldigide
    // USART1_IRQOndir() adıyla islemlendirildi: fonksiyona gider
    USART_ITConfig(USART1, USART_IT_RXNE, ENABLE); // USART1 ka interrupt aktif ediliyor
}

NVIC_InitStructure.NVIC_IRQChannel = USART1_IRQn;
NVIC_InitStructure.NVIC_IRQChannelPriority = 8; //8 yuzde an onemlilik kaynag yanismasi
NVIC_InitStructure.NVIC_IRQChannelCmd = ENABLE; //USART1 interrupt kanali aktif edilir.
NVIC_Init(&NVIC_InitStructure);

USART_Cmd(USART1, ENABLE); // USART1 aktif edilir.
}
    
```

Fig.19. Making UART Settings

The ESP8266 module is connected via UART with the processor. It is necessary to make software settings for the processor to recognize the ESP8266 module. The ESP8266 module is connected to the processor via GPIO pins PA9 (TX) and PA10 (RX). It is software-configured that the UART connections of the PA9 and PA10 pins will be used. After the pin settings are made, the UART settings of the ESP8266 module are set via the processor as shown in Figure 19. After these adjustments are completed, the module is ready for communication.

After the necessary adjustments have been made to recognize the ESP8266 module by the processor, some commands are available to communicate with the module. These commands are referred to as AT commands. For the adjustment of the ESP8266 module given in Figure 20, the settings written in the technical document are encoded and transferred to the module via UART communication. After each message is sent, a check is made to see if the “OK” response has been received. If “OK” has been received, it is understood that the message has successfully reached the module and the settings we have sent have been applied.

```

void ESP_Ready(void)
{
    switch(ESPInitCase)
    {
        case 0:
            USART_puts(USART1, "AT+RESTORE");
            Delay(5000);
            ESPInitCase = 1;
            break;
        case 1:
            if (strstr(g_arduinoSerialData, "OK") != NULL)
            {
                //Clear the buffer
                Clear_ESPBuffer();
                ESPInitCase = 2;
            }
            else
            {
                Clear_ESPBuffer();
                ESPInitCase = 0;
            }
            break;
        case 2:
            USART_puts(USART1, "AT+SD=0");
            Delay(5000);
            ESPInitCase = 3;
            break;
        case 3:
            if (strstr(g_arduinoSerialData, "OK") != NULL)
            {
                Clear_ESPBuffer();
                ESPInitCase = 4;
            }
            else
            {
                Clear_ESPBuffer();
                ESPInitCase = 0;
            }
            break;
        case 4:
            USART_puts(USART1, "AT+SD=1");
            Delay(5000);
            ESPInitCase = 5;
            break;
        case 5:
            if (strstr(g_arduinoSerialData, "OK") != NULL)
            {
                Clear_ESPBuffer();
                ESPInitCase = 6;
            }
            else
            {
                Clear_ESPBuffer();
                ESPInitCase = 0;
            }
            break;
        case 6:
            USART_puts(USART1, "AT+SD=2");
            Delay(5000);
            ESPInitCase = 7;
            break;
        case 7:
            if (strstr(g_arduinoSerialData, "OK") != NULL)
            {
                Clear_ESPBuffer();
                ESPInitCase = 8;
            }
            else
            {
                Clear_ESPBuffer();
                ESPInitCase = 0;
            }
            break;
        case 8:
            USART_puts(USART1, "AT+SD=3");
            Delay(5000);
            ESPInitCase = 9;
            break;
        case 9:
            if (strstr(g_arduinoSerialData, "OK") != NULL)
            {
                Clear_ESPBuffer();
                ESPInitCase = 10;
            }
            else
            {
                Clear_ESPBuffer();
                ESPInitCase = 0;
            }
            break;
        case 10:
            USART_puts(USART1, "AT+SD=4");
            Delay(5000);
            ESPInitCase = 11;
            break;
        case 11:
            if (strstr(g_arduinoSerialData, "OK") != NULL)
            {
                Clear_ESPBuffer();
                ESPInitCase = 12;
            }
            else
            {
                Clear_ESPBuffer();
                ESPInitCase = 0;
            }
            break;
        case 12:
            USART_puts(USART1, "AT+SD=5");
            Delay(5000);
            ESPInitCase = 13;
            break;
        case 13:
            if (strstr(g_arduinoSerialData, "OK") != NULL)
            {
                Clear_ESPBuffer();
                ESPInitCase = 14;
            }
            else
            {
                Clear_ESPBuffer();
                ESPInitCase = 0;
            }
            break;
    }
}
    
```

Fig.20. Setting Up the ESP8266 Module

With the help of the user interface page, users can control the brightness of Decelerated lighting system. The ESP8266 module checks the web service API, where the user interface stores data at intervals to check for changes. If there is a change in the received brightness value, the message content is assigned to the relevant variables and the DALI message starts to be created.

As can be seen in the image in Figure 21, with the AT+CIPSTART command, we first go to our site. We are establishing a TCP connection. If we get the answer “OK“, the site connection is provided, if the answer ”ALREADY“ comes, it means that we are already connected to the site. In both cases, the next step is taken. We send length information before our query message with AT+CIPSEND command “>” when the answer comes, we query our brightness data to the site with “GET”.



```

204 case 12:
205 USART_puts(USART1, "AT+CIPSTART=0,\"TCP\",1,\"banyanoguz@iitb.ac.in:8080\",8080);
206 Delay(Connect(0xFFFF));
207 ESPInitCase = 13;
208 break;
209 case 13:
210 if ((strstr(g_arduinoESP8266Buf, "0") != NULL) || (strstr(g_arduinoESP8266Buf, "ALREADY") != NULL))
211 {
212     Clear_ESPBuffer();
213     ESPInitCase = 14;
214 }
215 }
216 else
217 {
218     // Device go to Sleep Under Mode=
219     Clear_ESPBuffer();
220     ESPInitCase = 12;
221 }
222 break;
223 case 14:
224 USART_puts(USART1, "AT+CIPSEND=6,8080\r\n");
225 Delay(Connect(0xFFFF));
226 SPDS_SendData(SPD08, SPD0_Min_0);
227 ESPInitCase = 15;
228 break;
229 case 15:
230 if ((strstr(g_arduinoESP8266Buf, "\r") != NULL))
231 {
232     Clear_ESPBuffer();
233     ESPInitCase = 16;
234 }
235 else
236 {
237     Clear_ESPBuffer();
238     ESPInitCase = 12;
239 }
240 break;
241 case 16:
242 USART_puts(USART1, "GET /getdata HTTP/1.0\r\nHost: banyanoguz@iitb.ac.in:8080\r\n\r\n");
243 Delay(Connect(0xFFFF));
244 ESPInitCase = 17;
245 break;

```

Fig.21. Providing a Connection to the Site by Establishing a TCP Connection with ESP8266.

After the query message is sent, a long message with brightness data is received via the site. For 50% brightness on the interface web service, the brightness data is kept as Wi-Fi data:050, which will be on the Wi-Fi at the beginning. As shown in Figure 22, the Wi-Fi data address is taken for the incoming message using the strstr function. Since the incoming data is ASCII (American Standard Code for Information Interchange), it is necessary to perform the decimal conversion. The conversion is performed with the Convert\_ASCII\_Buf\_to\_Dec function. Since Wi-Fi data's address was taken during the conversion, 8 is added to the address of Wi-Fi data to reach our main data, it reaches the address of the main data and transactions are made through it. The reason for adding 8 is that Wi-Fi data takes up 8 bytes of space in ASCII.

```

250 case 17:
251 if ((strstr(g_arduinoESP8266Buf, "wifiData:") != NULL))
252 {
253     Start_DALI_Level_Address = strstr(g_arduinoESP8266Buf, "wifiData:");
254     Set_DALI_Level = Convert_ASCII_Buf_to_Dec(Start_DALI_Level_Address);
255     SPDS_ResetData(SPD08, SPD0_Min_0);
256     if (Previous_DALI_Level != Set_DALI_Level)
257     {
258         Previous_DALI_Level = Set_DALI_Level;
259         Flag_Changed_DALI_Level = TRUE;
260     }
261     if (Flag_Changed_DALI_Level == TRUE)
262     {
263         Flag_Changed_DALI_Level = FALSE;
264         if (Set_DALI_Level == 0)
265         {
266             DALI_Send_Cmd(ADDRESS081, OFF, SHORT_ADDRESS, FOLLOWING_COMMAND);
267         }
268         else if (Set_DALI_Level == 1)
269         {
270             DALI_Send_Cmd(ADDRESS081, RECALL_MIN_LEVEL, SHORT_ADDRESS, FOLLOWING_COMMAND);
271         }
272         else if (Set_DALI_Level == 100)
273         {
274             DALI_Send_Cmd(ADDRESS081, RECALL_MAX_LEVEL, SHORT_ADDRESS, FOLLOWING_COMMAND);
275         }
276         else
277         {
278             DALI_Send_Cmd(ADDRESS081, Set_DALI_Level, SHORT_ADDRESS, FOLLOWING_DIRECT_ARG_POWER_LEVEL);
279         }
280     }
281     Clear_ESPBuffer();
282     ESPInitCase = 12;
283 }
284 else
285 {
286     Clear_ESPBuffer();
287     ESPInitCase = 12;
288 }
289 break;

```

Fig.22. Getting the Brightness Data Starting the DALI Query.

254, seen in Figure 22. Whether the value read in the line is different or the same from the previous value is checked. If the value is different, a DALI message is generated according to the incoming value. If the incoming brightness level is 0, an OFF message is sent to our LED driver. If the brightness level is 1, the minimum level, and if the brightness level is 100, the maximum level message is sent. If a different value other than

these values is received, the brightness data is sent directly to the LED driver.

The Web page developed within the scope of the project is shown in Figure 23. With the help of this interface, users are able to control the brightness of the selected lighting system [44]. The brightness can be increased or decreased at the desired level with the buttons on the page.



Fig.23. DALI Control Unit User Interface

The web application is formed with Asp.NET MVC (Model View Controller). HTML, CSS and Javascript languages were used on the front. On the server side, the C# programming language is used. When clicking on the buttons from the front, HTTP POST (Power on Self Testing) data is sent to the Controller class using the method. Then these data are recorded in the database. In the MVC project prepared in layered architecture, EntityFramework library was used for database operations. MSSQL as a database (Microsoft SQL Server) The server has been selected. The created tables and columns are shown in Figure 24.

EntityInfos			
	Column Name	Data Type	Allow Nulls
?	Id	int	<input type="checkbox"/>
	Brightness	int	<input type="checkbox"/>
	DaliNo	int	<input type="checkbox"/>
	MaxLevel	int	<input type="checkbox"/>
	MinLevel	int	<input type="checkbox"/>
			<input type="checkbox"/>

Fig.24. Database Table

Within the scope of the project, the current brightness of the DALI system of the embedded system, except for the website the Web service has been written so that it can read the data. For the service designed with REST architecture Asp.NET API is used. Thanks to this service, devices are prevented from connecting to the database and it is ensured that they can receive only the necessary data via the HTTP protocol. The data is sent in string type for easy reading by the embedded system. The C# method, which retrieves the current brightness value from the database and works with HTTP GET, is given in Figure 25.

```
[HttpGet]
public IActionResult GetBrightness()
{
    Repository repository = new();
    var entity = repository.Get();
    var value = $"{entity?.Brightness:D3}";
    return Ok(value);
}
```

Fig.25. Reading the Brightness Data

## V. CONCLUSION

In this study, the construction of a smart LED driver control is presented. In the details of the study, the hardware features of the circuit made, the working principles were mentioned, the flow chart of the software and needs to work in the hardware for the system to work, the software details were mentioned. The DALI protocol, which is one of the most preferred communication protocols in lighting systems, has been preferred. In the communication via the interface, the most preferred Wi-Fi communication is used wirelessly. ESP8266 was preferred because it can be found quickly in the market for Wi-Fi communication and is inexpensive in cost.

When other studies in the literature are examined, it has been seen that more than one sensor for automation systems are generally large systems that require cost and are managed remotely with wireless communication protocols. In this study, the end product to be presented to the customer, which provides remote control of the DALI communication protocol, has been revealed. It provides a significant advantage to customers compared to other products in terms of cost. A DALI protocol controller with Wi-Fi support has been made. With this controller, it is possible to remotely control the device by connecting to any Wi-Fi line by making a communication line connection in the environment where DALI supported LED drivers are located. For control, use any device with an Internet connection (computer, tablet, mobile phone, etc.). The interface is accessible and LED lighting can be controlled from anywhere desired.

After the theoretical studies of the circuit were carried out, experimental studies were carried out, the oscilloscope images of the communication data of the results were examined and described in detail in the previous sections. The thesis study was verified by conducting tests with a Tridonic brand LED driver that has a DALI certificate.

## ACKNOWLEDGMENT

This study was produced from the master thesis named 'DALI compatible smart LED driver controller with WiFi communication'.

## REFERENCES

- [1] B. Söğüt, B. Fulin, and F. Parlak, "DALI Protokolü ile Kontrol Edilebilen Enerji Tasarruflu LED Sürücü," in *Elektrik Elektronik Mühendisliği Kongresi (EEMKON)*, Istanbul, TURKEY, 2017, p. 84.
- [2] M. A. George, S. Choudhary, D. Sahay, T. Yerra, and C. P. Kurian, "Digitally Addressable Wireless Interface for Lighting Control System," in *2013 Texas Instruments India Educators' Conference*, 4-6 April 2013 2013, pp. 222-229, doi: 10.1109/TIIEC.2013.46.
- [3] K. Lohia, Y. Jain, C. Patel, and N. Doshi, "Open Communication Protocols for Building Automation Systems," *Procedia Computer Science*, vol. 160, pp. 723-727, 01/01 2019, doi: 10.1016/j.procs.2019.11.020.
- [4] M. K. Manyake and T. N. D. Mathaba, "An Internet of Things Framework for Control and Monitoring of Smart Public Lighting Systems: A Review," in *2022 International Conference on Artificial Intelligence, Big Data, Computing and Data Communication Systems (icABCD)*, 4-5 Aug. 2022 2022, pp. 1-9, doi: 10.1109/icABCD54961.2022.9856268.
- [5] F. J. Bellido-Outeirino, J. M. Flores-Arias, F. Domingo-Perez, A. Gil-de-Castro, and A. Moreno-Munoz, "Building lighting automation through the integration of DALI with wireless sensor networks," *IEEE Transactions on Consumer Electronics*, vol. 58, no. 1, pp. 47-52, 2012, doi: 10.1109/TCE.2012.6170054.
- [6] M. Moeck, "Developments in Digital Addressable Lighting Control," *Journal of Light & Visual Environment*, vol. 28, pp. 104-106, 09/01 2004, doi: 10.2150/jlve.28.104.
- [7] F. J. B. Outeiriño, F. Domingo-Perez, A. d. R. Gil-de-Castro, J. F. Arias, and A. Moreno-Munoz, "In-building lighting management system with wireless communications," in *2012 IEEE International Conference on Consumer Electronics (ICCE)*, 13-16 Jan. 2012 2012, pp. 83-85, doi: 10.1109/ICCE.2012.6161751.
- [8] M. L. Wu, C. M. Kung, and Y. N. Lin, "DALI-2 Intelligent Lighting Control System," in *2020 International Symposium on Computer, Consumer and Control (IS3C)*, 13-16 Nov. 2020 2020, pp. 158-161, doi: 10.1109/IS3C50286.2020.00048.
- [9] R. Delvaeye, W. Ryckaert, L. Stroobant, P. Hanselaer, R. Klein, and H. Breesch, "Analysis of energy savings of three daylight control systems in a school building by means of monitoring," *Energy and Buildings*, vol. 127, 06/01 2016, doi: 10.1016/j.enbuild.2016.06.033.
- [10] S. Babu *et al.*, "Investigation of an integrated automated blinds and dimmable lighting system for tropical climate in a rotatable testbed facility," *Energy and Buildings*, vol. 183, pp. 356-376, 2019/01/15/ 2019, doi: <https://doi.org/10.1016/j.enbuild.2018.11.007>.
- [11] G. Adam, "DALI LED Driver Control System for Lighting Operations Based on Raspberry Pi and Kernel Modules," *Electronics*, vol. 8, p. 1021, 09/12 2019, doi: 10.3390/electronics8091021.
- [12] J. Liu, W. Zhang, X. Chu, and Y. Liu, "Fuzzy Logic Controller for Energy Savings in a Smart LED Lighting System Considering Lighting Comfort and Daylight," *Energy and Buildings*, vol. 127, 05/01 2016, doi: 10.1016/j.enbuild.2016.05.066.
- [13] N. Gentile *et al.*, "Evaluation of integrated daylighting and electric lighting design projects: Lessons learned from international case studies," *Energy and Buildings*, vol. 268, p. 112191, 2022/08/01/ 2022, doi: <https://doi.org/10.1016/j.enbuild.2022.112191>.
- [14] Z. Chen, C. B. Sivaparthipan, and B. Muthu, "IoT based smart and intelligent smart city energy optimization," *Sustainable Energy Technologies and Assessments*, vol. 49, p. 101724, 2022/02/01/ 2022, doi: <https://doi.org/10.1016/j.seta.2021.101724>.
- [15] O. O. Ordaz-García, M. Ortiz-López, F. J. Quiles-Latorre, J. G. Arceo-Olague, R. Solís-Robles, and F. J. Bellido-Outeiriño, "DALI Bridge FPGA-Based Implementation in a Wireless Sensor Node for IoT Street Lighting Applications," *Electronics*, vol. 9, no. 11, doi: 10.3390/electronics9111803.
- [16] F. J. Bellido-outeirino, J. M. Flores-arias, M. Linan-Reyes, E. J. Palacios-garcia, and J. J. Luna-rodriguez, "Wireless sensor network and stochastic models for household power management," *IEEE Transactions on Consumer Electronics*, vol. 59, no. 3, pp. 483-491, 2013, doi: 10.1109/TCE.2013.6626228.
- [17] A. Gil-de-Castro, A. Moreno-Munoz, and J. J. de la Rosa, *Characterizing the harmonic attenuation effect of high-pressure sodium lamps*. 2010, pp. 1-6.
- [18] F. Domingo-Perez, A. Gil-de-Castro, J. M. Flores-Arias, F. J. Bellido-Outeirino, and A. Moreno-Munoz, "Lighting control system based on DALI and wireless sensor networks," in *2012 IEEE PES Innovative Smart Grid Technologies (ISGT)*, 16-20 Jan. 2012 2012, pp. 1-6, doi: 10.1109/ISGT.2012.6175666.
- [19] S. Tang, V. Kalavally, K. Y. Ng, and J. Parkkinen, "Development of a prototype smart home intelligent lighting control architecture using sensors onboard a mobile computing system," *Energy and Buildings*, vol. 138, pp. 368-376, 2017/03/01/ 2017, doi: <https://doi.org/10.1016/j.enbuild.2016.12.069>.
- [20] T. de Rubeis *et al.*, "A first approach to universal daylight and occupancy control system for any lamps: Simulated case in an academic classroom," *Energy and Buildings*, vol. 152, pp. 24-39, 2017/10/01/ 2017, doi: <https://doi.org/10.1016/j.enbuild.2017.07.025>.
- [21] T. W. Kruisselbrink, R. Dangol, and E. J. van Loenen, "A comparative study between two algorithms for luminance-based lighting control,"

- Energy and Buildings*, vol. 228, p. 110429, 2020/12/01/ 2020, doi: <https://doi.org/10.1016/j.enbuild.2020.110429>.
- [22] I. Chew, D. Karunatilaka, C. P. Tan, and V. Kalavally, "Smart lighting: The way forward? Reviewing the past to shape the future," *Energy and Buildings*, vol. 149, pp. 180-191, 2017/08/15/ 2017, doi: <https://doi.org/10.1016/j.enbuild.2017.04.083>.
- [23] D. H. Kim, J. S. Sung, S. Park, and T. G. Kang, "A study on the performance factors for wireless lighting control networks," in *2016 International Conference on Information and Communication Technology Convergence (ICTC)*, 19-21 Oct. 2016 2016, pp. 906-908, doi: 10.1109/ICTC.2016.7763326.
- [24] H. Zou, Y. Zhou, H. Jiang, S.-C. Chien, L. Xie, and C. J. Spanos, "WinLight: A WiFi-based occupancy-driven lighting control system for smart building," *Energy and Buildings*, vol. 158, pp. 924-938, 2018/01/01/ 2018, doi: <https://doi.org/10.1016/j.enbuild.2017.09.001>.
- [25] C. Qiu, B. Hussain, and C. P. Yue, "Bluetooth Based Wireless Control for iBeacon and VLC Enabled Lighting," in *2019 IEEE 8th Global Conference on Consumer Electronics (GCCE)*, 15-18 Oct. 2019 2019, pp. 614-615, doi: 10.1109/GCCE46687.2019.9015330.
- [26] Z. Zheng, L. Liu, and W. Hu, "Accuracy of Ranging Based on DMT Visible Light Communication for Indoor Positioning," *IEEE Photonics Technology Letters*, vol. 29, no. 8, pp. 679-682, 2017, doi: 10.1109/LPT.2017.2677424.
- [27] M. Kent, N. K. Huynh, S. Schiavon, and S. Selkowitz, "Using support vector machine to detect desk illuminance sensor blockage for closed-loop daylight harvesting," *Energy and Buildings*, vol. 274, p. 112443, 2022/11/01/ 2022, doi: <https://doi.org/10.1016/j.enbuild.2022.112443>.
- [28] I. Chew, V. Kalavally, N. W. Oo, and J. Parkkinen, "Design of an energy-saving controller for an intelligent LED lighting system," *Energy and Buildings*, vol. 120, pp. 1-9, 2016/05/15/ 2016, doi: <https://doi.org/10.1016/j.enbuild.2016.03.041>.
- [29] M. Papinutto *et al.*, "Saving energy by maximising daylight and minimising the impact on occupants: An automatic lighting system approach," *Energy and Buildings*, vol. 268, p. 112176, 2022/08/01/ 2022, doi: <https://doi.org/10.1016/j.enbuild.2022.112176>.
- [30] N. Hafezparast Moadab, T. Olsson, G. Fischl, and M. Aries, "Smart versus conventional lighting in apartments - Electric lighting energy consumption simulation for three different households," *Energy and Buildings*, vol. 244, p. 111009, 2021/08/01/ 2021, doi: <https://doi.org/10.1016/j.enbuild.2021.111009>.
- [31] L. T. Doulos, A. Kontadakis, E. N. Madias, M. Sinou, and A. Tsangrassoulis, "Minimizing energy consumption for artificial lighting in a typical classroom of a Hellenic public school aiming for near Zero Energy Building using LED DC luminaires and daylight harvesting systems," *Energy and Buildings*, vol. 194, pp. 201-217, 2019/07/01/ 2019, doi: <https://doi.org/10.1016/j.enbuild.2019.04.033>.
- [32] A. V. Kudryashov, E. S. Galishheva, and A. S. Kalinina, "Lighting Control Using DALI Interface," in *2018 International Conference on Industrial Engineering, Applications and Manufacturing (ICIEAM)*, 15-18 May 2018 2018, pp. 1-5, doi: 10.1109/ICIEAM.2018.8728728.
- [33] S. G. Varghese, C. P. Kurian, and V. I. George, "A study of communication protocols and wireless networking systems for lighting control application," in *2015 International Conference on Renewable Energy Research and Applications (ICRERA)*, 22-25 Nov. 2015 2015, pp. 1301-1306, doi: 10.1109/ICRERA.2015.7418618.
- [34] Z. Yuejun, Z. Ping, and W. Mingguang, "Research on DALI and Development of Master-Slave module," in *2006 IEEE International Conference on Networking, Sensing and Control*, 23-25 April 2006 2006, pp. 1106-1110, doi: 10.1109/ICNSC.2006.1673307.
- [35] A. Kudryashov, "Lighting Control System for Premises with Display Screen Equipment," *IOP Conference Series: Materials Science and Engineering*, vol. 262, p. 012091, 11/01 2017, doi: 10.1088/1757-899X/262/1/012091.
- [36] R. Sahu, "DALI Protocol and Interface with DALI Devices from External Master Controller," 07/25 2019.
- [37] M. M. Rahman, E. J. Noor, M. O. Islam, and M. S. Salakin, "Arduino and GSM based smart energy meter for advanced metering and billing system," in *2015 International Conference on Electrical Engineering and Information Communication Technology (ICEEICT)*, 21-23 May 2015 2015, pp. 1-6, doi: 10.1109/ICEEICT.2015.7307498.
- [38] G. Gu and G. Peng, "The survey of GSM wireless communication system," in *2010 International Conference on Computer and Information Application*, 3-5 Dec. 2010 2010, pp. 121-124, doi: 10.1109/ICCIA.2010.6141552.
- [39] Yoppy, R. H. Arjadi, H. Candra, H. D. Prananto, and T. A. W. Wijanarko, "RSSI Comparison of ESP8266 Modules," in *2018 Electrical Power, Electronics, Communications, Controls and Informatics Seminar (EECCIS)*, 9-11 Oct. 2018 2018, pp. 150-153, doi: 10.1109/EECCIS.2018.8692892.
- [40] H. K. Lee, Y. Kim, and T. J. Lee, "Wi-fi boost protocol in a heterogeneous network with Wi-Fi and RFID," in *2016 Fifth International Conference on Future Generation Communication Technologies (FGCT)*, 17-19 Aug. 2016 2016, pp. 32-35, doi: 10.1109/FGCT.2016.7605064.
- [41] S. Üstün Ercan and M. Mohammed, "IoT and XBee Based Central Car Parking Management System," *Balkan Journal of Electrical and Computer Engineering*, 01/30 2023, doi: 10.17694/bajece.1160300.
- [42] A. R. Barai, M. R. K. Badhon, F. Zhora, and M. R. Rahman, "Comparison between Noninvasive Heart Rate Monitoring Systems using GSM Module and ESP8266 Wi-Fi Module," in *2019 3rd International Conference on Electrical, Computer & Telecommunication Engineering (ICECTE)*, 26-28 Dec. 2019 2019, pp. 45-48, doi: 10.1109/ICECTE48615.2019.9303572.
- [43] B. Güngör, "DALI Arabirimi Üzerinden Bir Acil Aydınlatma ve Yönlendirme Sistemi Yönetimi ve Uygulamasını," Yüksek Lisans Tezi, Okan Üniversitesi, 2011.
- [44] M. Şensoy, "Akıllı binalarda web teknolojilerinin kullanımı," Yüksek Lisans Tezi, Fen Bilimleri Enstitüsü, Marmara Üniversitesi, 2022.

## BIOGRAPHIES

**NAZMI EKREN** Esenler, Istanbul, in 1966. He received the B.S. and M.S. degrees in electrical engineering from the Yıldız Technical University, Istanbul, in 1983 and from Marmara University, Istanbul, in 1992. He received a Ph.D. degree from Istanbul University, Istanbul, Türkiye, in 1996.



He has been an Associate Professor with the Electrical and Electronics Engineering Department, Faculty of Technology at Marmara University. He is the author of more than 70 articles, and almost 100 proceedings. His research interests include electrical energy, lighting technology, renewable energy, biomaterials, and nanomaterials.

**BUNYAMIN SOGUT** Altındag, Ankara, in 1992. He received the B.S. degrees in electronic engineering from the Gebze Technical University, Kocaeli, in 2010 and the M.S. degrees in electric electronic engineering from Marmara University, Istanbul, in 2020.





# An Approach for DC Motor Speed Control with Off-Policy Reinforcement Learning Method

Sevilay Tufenkci, Gurkan Kavuran, Celaleddin Yeroglu

**Abstract**—Integration of self-learning mechanisms with control systems is frequently encountered in the literature due to the development of autonomous systems. This paper proposes a tuning method of PI controllers using a deep reinforcement learning algorithm, which is known as self-learning structure. The coefficients of the PI controller, which is used to control a DC motors, are determined. The proposed method aims to adjust the voltage value applied to the input of the DC motor to reach the desired speed with the tuned PI controller using the twin-delayed deep deterministic policy gradient (TD3) reinforcement learning algorithm. The  $K_p$  and  $K_i$  coefficients of the PI controller are taken as the absolute values of the neural network weights, which are driven by Gradient descent optimization to positive values with a fully connected layer. The proposed tuning method has been shown to provide a higher gain margin and a more optimal solution.

**Index Terms**— Deep reinforcement learning, DC motor, PI controller, Twin-delayed deep deterministic policy gradient

## I. INTRODUCTION

IN RECENT YEARS, the interest in artificial intelligence and machine learning issues has increased with remarkable developments. Many thanks to the modern control techniques, which is one of the application areas of these studies, the system has revealed what is expected from it without any external influence [1, 2].

Reinforcement learning uses an agent that perceives its environment and acquires information as a result of its

interaction with its environment and can act in line with this information. This agent helps the system choose the most appropriate action to achieve its purpose. [2] It is a method that enables learning using a series of reward and punishment systems in its background. The aim of the agent is to realize learning by trying to increase the reward value.

Reinforcement learning, a method derived from the science of psychology, is based on the famous psychologist Skinner's (1938) saying, "behaviors are affected by consequences".


Reinforcement learning is a method used to match actions and situations [3]. There are many studies in the literature using reinforcement learning. Some of them are used in many different areas, such as motor control [4, 5, 6], mobile robots [7, 8], and video games [9].

The Q-Learning method is a special type of reinforcement learning approach and is the most well-known among others [10, 11]. This method was first named in 1989 by using the letter Q for the Watkins value function. This method is based on the Markov theory of decision processes. The environment in which the agent is located is modelled as a probabilistic process with the Markov feature and while the present state is in the present state, future situations are evaluated independently from past situations. With the Q-learning algorithm, the agent can find the action that can get the greatest reward for the defined situations in the environment with the q-table.


The reinforcement learning method may find it difficult to find solutions in continuous action areas, high dimensional inputs, or complex actions [12, 13, 14]. Deep Q-Network algorithms have emerged to overcome this problem [15]. However, in these algorithms, the action that maximizes the action value is due to an outcome and is not sufficient in continuous domains.

Deterministic Policy Gradient (DPG) algorithms have emerged to solve the problem that arises with high dimensional and continuous domains [16]. This method, which uses a non-political actor-critic structure and performs deterministic learning, has performed well. Then, Deep Deterministic Policy Gradient (DDPG), which gives better results in large size and continuous actions, was developed based on the DPG algorithm [17]. With the advances made in this area, a new algorithm called Twin Delay Deep


**SEVILAY TUFENKCI**, is with Department of Computer Technology Department, Malatya Turgut Ozal University, Malatya, Turkey (e-mail: [sevilay.tufenkci@gmail.com](mailto:sevilay.tufenkci@gmail.com))

 <https://orcid.org/0000-0001-9815-7724>

**GURKAN KAVURAN**, is with Department of Electrical-Electronics Engineering, Malatya Turgut Ozal University, Malatya, Turkey (e-mail: [gurkan.kavuran@ozal.edu.tr](mailto:gurkan.kavuran@ozal.edu.tr)).

 <https://orcid.org/0000-0003-2651-5005>

**CELALEDDIN YEROGLU**, is with Department of Computer Engineering, Inonu University, Malatya, Turkey (e-mail: [c.yeroglu@inonu.edu.tr](mailto:c.yeroglu@inonu.edu.tr)).

 <https://orcid.org/0000-0002-6106-2374>

Manuscript received May 10, 2022; accepted Aug 3, 2022.

DOI: [10.17694/bajece.1114868](https://doi.org/10.17694/bajece.1114868)



Deterministic Policy Gradient (TD3) has been produced in a recent period [18]. It has been the best among the previously developed models with its performance in high dimension and continuous areas using a non-policy learning method.

DC motors are ubiquitous in terms of their simplicity and ease of use. They are encountered in various industrial applications as well as small household appliances. However, it needs a control structure to operate as desired. The purpose of this control structure is to keep the output of the system, i.e. its speed, at a predetermined reference value for the system. There have been many studies on DC motor applications for decades [19, 20].

The motivation and novelty of the paper can be explained as follows;

- The training of the RL-based controller tuning approach benefits greatly from experience-based learning in a realistically structured simulation environment.
- The simulation environment may be used to train controller tuning algorithms in order to get the optimum practical performance against uncertainty, noise, and external disturbances.
- According to simulation environment results, RL approaches are intrinsically ideal for experience-based learning and performance improvement, which was a major motivator for the authors of the current work.
- We concentrated on creating an appropriate simulation environment for successful RL-based controller tuning.
- The Kp and Ki coefficients are the absolute values of the neural network weights, which are pushed to positive values using Gradient Descent Optimization with a fully connected layer.

Within the scope of this study, the TD3 method was used to achieve the desired operating speed for a DC motor and to maintain it at this speed. In order for the system to be at the desired speed, it is aimed to perform the desired behavior within the reward and penalty structure, and in line with this purpose, the voltage input value of the system that will provide this speed is adjusted as a result of learning.

## II. MATERIALS AND METHODS

### A. Reinforcement Learning

Reinforced learning is a learning method that enables an agent who can perceive the environment and act in his environment to choose the most appropriate actions to achieve his goal [2]. When the agent performs an action in the environment, the reward or punishment structure is used to show the suitability of this action for the system. With this structure, the agent performs the best action among the situations while trying to reach the highest reward value [21, 22].

This method, which is developed on the basis of behavioral psychology, interacts with its environment in this problem environment to provide a solution to a problem. It tries to find

the most appropriate solution by trying different ways in the environment to reach a solution. Unlike consultancy and non-consultancy learning methods, it realizes learning without using any data set. The learning process is entirely dependent on the interaction with the environment.

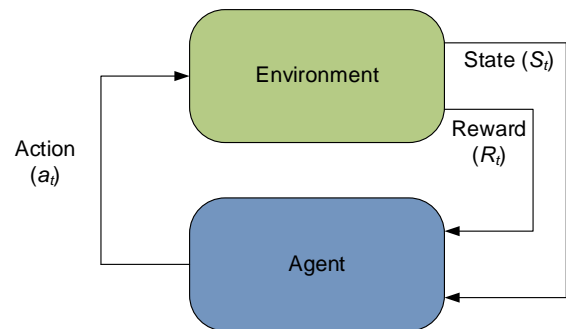


Fig.1. Block Diagram of Reinforced Learning System

Figure 1 presents the structure of the reinforcement learning system. Its essential components are action ( $A_t$ ), agent, environment, reward ( $R_t$ ), principle, and state function ( $S_t$ ). Within this structure, the agent is the decision maker that performs the learning process. On the other hand, an agent takes actions in the environment and constantly interacts. The principle refers to the possibility of choosing each action that can be selected in its environment. The total reward to be obtained from the situation of the agent and other conditions that will occur accordingly is expressed as a state function [3].

### B. Markov Decision Process

In the reinforcement learning method, the environment is modeled as a probabilistic process, and the future situations occur independently from the past situations.

In Figure 1,  $S_t$  and  $R_t$  represent the results after an action is performed and they are random variables. The general form of the probability density function including  $S_t$  and  $R_t$ .

$$p(s', r | s, a) = P[S_t = s', R_t = r | S_{t-1} = s, A_{t-1} = a] \quad (1)$$

where  $s, s' \in S, r \in R$  and  $a \in A$ .

Equation (1) expresses the basis of the working structure of the Markov process. When this equation is examined, it is revealed that the state and the form of the reward at time  $t$  depend only on the situation and action found a step earlier. Transition possibilities depend on these;

$$p(s' | s, a) = P[S_t = s' | S_{t-1} = s, A_{t-1} = a] = \sum_{r \in R} p(s', r | s, a) \quad (2)$$

$$r(s, a) = E[R_t | S_{t-1} = s, A_{t-1} = a] = \sum_{r \in R} r \sum_{s' \in S} p(s', r | s, a) \quad (3)$$

Equation (3) uses the marginal distribution of  $R_t$  to obtain the expected reward.

### C. Twin Delayed Deep Deterministic Policy Gradient Algorithm (TD3)

TD3 algorithm was built on the basis of the Deep Determinative Policy Gradient algorithm that emerged in 2015 [17]. This method, aims to increase the stability and

performance of the system by taking into account the approach error in the DDPG algorithm [18]. For this, it is based on the method applied to reduce over prediction in the Double-DQN algorithm [18] and is essentially a combination of three deep reinforcement learning techniques named Actor-Critic [23], Policy Gradient [16], and Double Deep Q-Learning [24].

The first technique applied in the TD3 algorithm is clipped double-Q learning. This technique consists of two Bellman equations, two-actor networks, and two critical network structures. Another applied technique is that it performs policy updates less frequently, unlike learning Q. It makes the process of updating the policy depending on the update of the value function of the model. This leads to a value estimation with a lower variance while providing a good policy that ensures the system's stability and reduces errors.

It realizes learning by adding noise to the policy with its Target Policy Smoothing. In order to obtain a satisfactory study result, it learns to evaluate all kinds of situations that may occur in terms of the system and its actions in a wide variety of environments. TD3 adds random noise to the target action and averaging over mini-batches.

$$y \equiv r + \gamma Q_w(s', \mu_\theta(s') + \varepsilon) \quad (4)$$

$$\varepsilon \approx \text{clip}(N(0, \sigma), -c, c) \quad (5)$$

where  $r$  is the reward value and  $\gamma$  is a discount factor expressing the effect of the reward value on reinforcement learning agents in the future, and this factor takes a value between 0 and 1 [25]. Since TD3 has two critical models that determine the loss function, it is expressed as  $MSELoss(Q_1(s, a'), Q_t) + MSELoss(Q_2(s, a'), Q_t)$ .

The critical loss is posted back, and the values are adjusted to determine the parameter values. As a result of these, the parameter of the actor model can be defined as;

$$\theta_i \leftarrow \min_{\theta_i} N^{-1} \sum_{i=1}^N (y - Q_{\theta_i}(s, a))^2 \quad (6)$$

$$\nabla_{\varphi} J(\varphi) = N^{-1} \sum \nabla_a Q_{\theta_i}(s, a) \Big|_{a=\pi_{\varphi}(s)} \nabla_{\varphi} \pi_{\varphi}(s) \quad (7)$$

where  $N$  is from the repeat buffer  $[s_t, a_t, r_t, s_{t+1}]$ . We are updating  $\varphi_i$ , where  $\varphi_i$  and  $\theta$  are the parameter actor and critic weights, respectively.

$$\theta'_i \leftarrow \tau \theta_i + (1 - \tau) \theta'_i \quad (8)$$

$$\varphi'_i \leftarrow \tau \varphi_i + (1 - \tau) \varphi'_i \quad (9)$$

Finally, we update the target networks as in Equations (8) and (9).

#### D. Brushed DC motor

Nowadays, the design and control of DC motors, which have a place in robotic applications, the military, and many other industrial areas, are among the subjects of interest. Among the many types of DC motors, brushed DC motors are

widely used. The speed of brushed DC motors can be changed by varying the input voltage or the magnetic field. Depending on the field's connections to the power source, the speed and torque characteristics of a brushed motor can be varied to provide constant speed. The electrical circuit of the armature part has been shown with rotor structure in Figure 2.

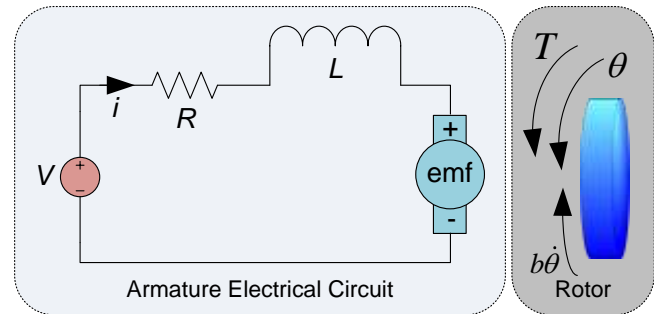


Fig.2. Equivalent Circuit for DC Motor

For the given model, it is assumed that the input of the system is the voltage source applied to the motor's armature and the rotation speed of the shaft  $\theta$  at its output. Among the parameters presented in the model,  $J$  is the moment of inertia of the rotor,  $R$  is the electrical resistance,  $L$  is the electrical inductance,  $b$  is the motor viscous friction constant,  $K_e$  is the electromotive force constant, and  $K_t$  is the motor torque constant [26]. The general form of the motor torque equation for an armature controlled motor;

$$T = K_t i \quad (10)$$

The back emf,  $e$ , is proportional to the angular velocity of the shaft multiplied by a constant factor  $K_e$ .

$$e = K_e \dot{\theta} \quad (11)$$

Rate of change integrals are taken for the rotational acceleration and the armature current. Then, by applying Newton's law and Kirchoff's law to the system, the equations are obtained.

$$J \frac{d^2 \theta}{dt^2} = T - b \frac{d\theta}{dt} \Rightarrow \frac{d^2 \theta}{dt^2} = \frac{1}{J} \left( K_t i - b \frac{d\theta}{dt} \right) \quad (12)$$

$$L \frac{di}{dt} = -Ri + V - e \Rightarrow \frac{di}{dt} = \frac{1}{L} \left( -Ri + V - K_e \frac{d\theta}{dt} \right) \quad (13)$$

The transfer function is used to express the relationship between the input and output of the system. The Laplace transform is applied to obtain the transfer function of the system and the system is expressed in the  $s$  domain.

$$s(Js + b)\theta(s) = KI(s) \quad (14)$$

$$(Ls + R)I(s) = V(s) - K_s \theta(s) \quad (15)$$

The open-loop transfer function of the system obtained via Equation (16) by using the above two equations;

$$P(s) = \frac{\theta(s)}{V(s)} = \frac{K}{(Js+b)(Ls+R)+K^2} \left| \frac{\text{rad/sec}}{V} \right| \quad (16)$$

### III. DESIGN OF TD3 BASED PI CONTROLLER

In this study, TD3 algorithm, which is one of the reinforcement learning methods, is used in the provision of speed control of a DC motor system. With this algorithm, a controller is used to perform the speed control of the DC motor, and the controller coefficients are adjusted. The open-loop transfer function form of the DC motor system to be controlled here;

$$P(s) = \frac{1.25}{(0.5s+0.01)(0.05s+0.4)+1.25^2} \left| \frac{\text{rad/sec}}{V} \right| \quad (17)$$

The general form of the transfer function of the PI control system used in the study;

$$C(s) = k_p + \frac{k_i}{s} \quad (18)$$

An agent is used in the reinforcement learning environment to adjust the PI coefficients required for speed control. The environment required for the agent to provide control is designed using Matlab Simulink. To simulate the controller in this model, the simulation time is set as  $T_f = 40$  and the controller sampling time  $T_s = 1$  seconds.

In the model, a reference signal consists of the observation vector for observing the results that will arise due to this signal, and the reward structure that forms the reward and punishment structure of the system in line with the action taken and the output signal. The observation vector used for this learning environment;

$$\left[ \int edt e \right]^T \quad (19)$$

$$e = r - s \quad (20)$$

where  $s$  refers to the speed of the DC motor, and  $r$  represents a randomly determined reference speed between 0 and 155 as the input. Negative defined reward function that maximizes the reward that will guide the reinforcement learning agent to achieve the goal;

$$\text{Reward} = -((ref - s)^2(t) + 0.01u^2(t)) \quad (21)$$

In order to decide which, action the TD3 agent will perform as an actor in line with the observations, a deep neural network structure is used as shown in Figure 3, which consists of an input and output based on observations.

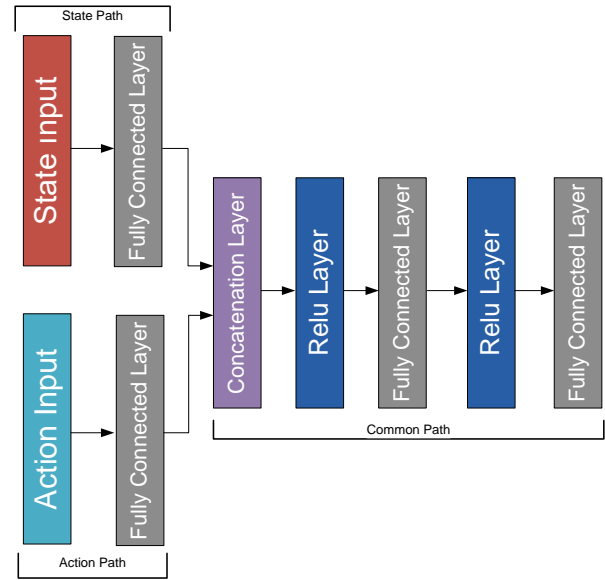


Fig.3. The critic network configuration

Figure 3 above, it refers to the fully connected layer with  $fc$ . The weights in the fully connected layer can take a negative value, and in this study, the  $abs(weights) * X$  change in this layer ensures that the weights are only positive. Thus, the PI controller used within the scope of the study is expressed as a single layer fully connected neural network model consisting of error and integral of the error.

$$u = \left[ \int edt e \right] * [K_i K_p]^T \quad (22)$$

The output of the neural network  $u$  expressed here, the controller coefficients  $K_p$  and  $K_i$  represent the absolute value of the neural network weights.

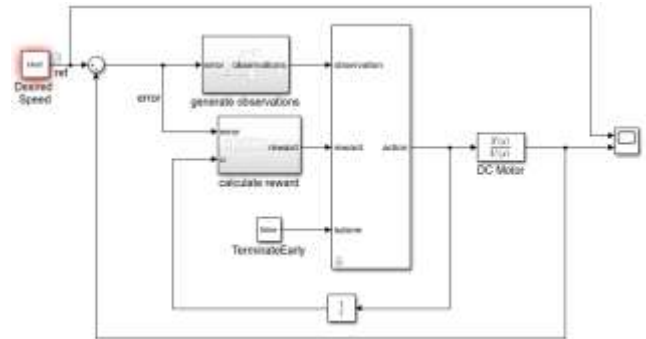


Fig.4. Simulink diagram of the proposed structure.

### IV. SIMULATION RESULTS

This study carried out training to provide speed control of a DC motor system using the Twin Delay DDPG algorithm. The training-dependent learning process and learning process results are presented in Figure 5 and Table 1, respectively.

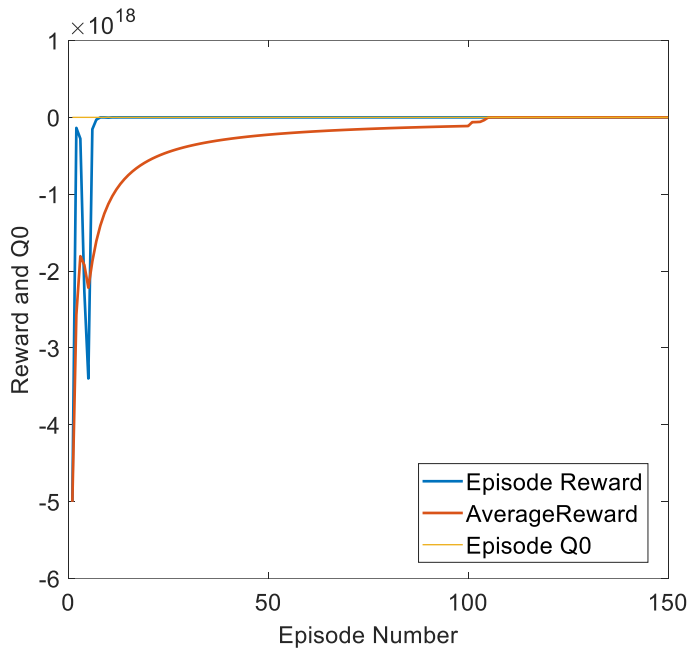


Fig.5. The representation of the learning process performance.

TABLE I  
VARIABLES OF TRAINING PROCESS

Maximum Number of Episodes	150
Maximum Steps per Episodes	40
Score Averaging Window Length	100
Training Stopped at Value	-355
Actor Learn Rate	1.00E-03

The reference input was chosen as a set of random values in the range of 0-150 rad/sec to train the system robustly and keep track of the desired reference input in a wide range of structurally acceptable. The following values for the controller coefficients were obtained for the system to perform the desired behavior at the end of 150 iterations.

$$C(s) = 0.1839 + \frac{0.4508}{s} \quad (23)$$

We obtained the system response when the variable speed value is given as the desired input according to time is shown in Figure 6. As can be seen in this figure, it is seen that the system has reached the desired output value for any value entered in a specific range. Figure 6. shows that the system follows the variable step input with high performance.

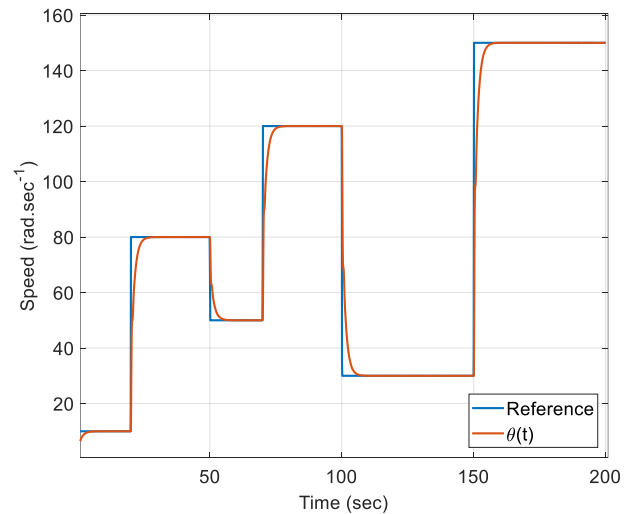


Fig.6. The step response of the DC motor system obtained with the TD3 algorithm

## V. CONCLUSIONS

The speed control of DC motors, used in many areas, is carried out using the TD3 algorithm, one of the reinforcement learning algorithms. The learning process is carried out according to a randomly generated reference input in this predetermined value for the system to work in the desired range. As a result of the learning, it has been shown with the simulation results that the system reaches the desired output value. In this study, unlike other learning methods, the effectiveness of the reinforcement learning method, which does not require any prior data, is presented in the speed control of the DC motor.

## References

- [1] R.S. Sutton, "Reinforcement Learning: Past, Present and Future", Lect. Notes Comput. Sci. (including Subser. Lect. Notes Artif. Intell. Lect. Notes Bioinformatics), Vol. 1585, 1998, 195–197.
- [2] L.P. Kaelbling, M.L. Littman, A.W. Moore, "Reinforcement Learning: A Survey", J. Artif. Intell. Res., Vol. 4, 1996, pp. 237–285.
- [3] R.S. Sutton, A.G. Barto, "Reinforcement Learning: An Introduction", 1998.
- [4] J. Xue, Q. Gao, W. Ju, "Reinforcement learning for engine idle speed control", 2010 Int. Conf. Meas. Technol. Mechatronics Autom. ICMTMA 2010, Vol. 2, 2010, pp. 1008–1011.
- [5] A. Traue, G. Book, W. Kirchgässner, O. Wallscheid, "Toward a reinforcement learning environment toolbox for intelligent electric motor control", IEEE Transactions on Neural Networks and Learning Systems, 2020.
- [6] Z. Song, J. Yang, X. Mei, T. Tao, M. Xu, "Deep reinforcement learning for permanent magnet synchronous motor speed control systems", Neural Computing and Applications, Vol. 33, 10, 2021, pp. 5409–5418.
- [7] E. Uchibe, M. Asada, K. Hosoda, "Behavior coordination for a mobile robot using modular reinforcement learning", IEEE Int. Conf. Intell. Robot. Syst., Vol. 3, 1996, pp. 1329–1336.
- [8] Z. Linan, Y. Peng, C. Lingling, Z. Xueping, T. Yantao, "Obstacle avoidance of multi mobile robots based on behavior decomposition reinforcement learning", 2007 IEEE Int. Conf. Robot. Biomimetics, ROBIO, 2007, pp. 1018–1023.
- [9] N.J. Van Eck, M. Van Wezel, "Application of reinforcement learning to the game of Othello", Comput. Oper. Res., Vol. 35, 2008, pp. 1999–2017.
- [10] C.J.C.H. Watkins, "Learning from delayed rewards", 1989.
- [11] C.J.C.H. Watkins, P. Dayan, "Q-learning", Mach. Learn. 1992, Vol. 83, 8, 1992, pp. 279–292.



- [12] Y. Liu, H. Wang, T. Wu, Y. Lun, J. Fan, J. Wu, "Attitude control for hypersonic reentry vehicles: An efficient deep reinforcement learning method", *Applied Soft Computing*, Vol. 123, 2022, 108865.
- [13] S. Zhang, Y. Li, Q. Dong, "Autonomous navigation of UAV in multi-obstacle environments based on a Deep Reinforcement Learning approach", *Applied Soft Computing*, Vol. 115, 2022, 108194.
- [14] K. M. Zielinski, L. V. Hedges, J. B. Florindo, Y. K. Lopes, R. Ribeiro, M. Teixeira, D. Casanova, "Flexible control of Discrete Event Systems using environment simulation and Reinforcement Learning", *Applied Soft Computing*, Vol. 111, 2021, 107714.
- [15] V. Mnih, K. Kavukcuoglu, D. Silver, A. Graves, I. Antonoglou, D. Wierstra, M. Riedmiller, "Playing Atari with Deep Reinforcement Learning", 2013.
- [16] D. Silver, G. Lever, N. Heess, T. Degris, D. Wierstra, M. Riedmiller, "Deterministic Policy Gradient Algorithms".
- [17] T.P. Lillicrap, J.J. Hunt, A. Pritzel, N. Heess, T. Erez, Y. Tassa, D. Silver, D. Wierstra, "Continuous control with deep reinforcement learning", 4th Int. Conf. Learn. Represent. ICLR 2016 - Conf. Track Proc., 2015.
- [18] S. Fujimoto, H. Hoof, D. Meger, "Addressing Function Approximation Error in Actor-Critic Methods", <http://proceedings.mlr.press/v80/fujimoto18a.html>, 2018.
- [19] F. Harashima, S. Kondo, "Design Method For Digital Speed Control System Of Motor Drives", *PESC Rec. - IEEE Annu. Power Electron. Spec. Conf.*, 1982, pp. 289–297.
- [20] D. Germanton, M. Lehr, "Variable speed DC motor controller apparatus particularly adapted for control of portable-power tools", 1989.
- [21] Y. Hoshino, "A proposal of Reinforcement Learning System to Use Knowledge effectively", 2003, pp. 1582–1585.
- [22] S.J. Russell, P. Norvig, "Artificial Intelligence A Modern Approach", 2003.
- [23] R.S. Sutton, D. Mcallester, S. Singh, Y. Mansour, "Policy gradient methods for reinforcement learning with function approximation", *Adv. NEURAL Inf. Process. Syst.* 12, Vol. 12, 2000, pp. 1057--1063.
- [24] H. van Hasselt, A. Guez, D. Silver, "Deep Reinforcement Learning with Double Q-Learning", *Proc. AAAI Conf. Artif. Intell.* 30, 2016.
- [25] W.B. Knox, P. Stone, "Reinforcement learning from human reward: Discounting in episodic tasks", *Proc. - IEEE Int. Work. Robot Hum. Interact. Commun.*, 2012, pp. 878–885.
- [26] University of Michigan: Control Tutorials for MATLAB and Simulink - Motor Speed: System Modeling, <https://ctms.engin.umich.edu/CTMS/index.php?example=MotorSpeed&section=SystemModeling>.



**CELALEDDIN YEROĞLU**, received the BSc degree in electronics engineering from Hacettepe University, in 1991, and the Master and PhD degree from the Department of Computer Engineering, Trakya University, in 2000. He received second PhD degree in 2011 from the Department of Electrical and Electronics Engineering, Inonu University. Since 2009, he has been working with the Computer Engineering Department, Inonu University. His research interests include intelligent systems, control theory and applications, simulation and modeling of networks.

## BIOGRAPHIES



**SEVILAY TUFENKCI** graduated from Selçuk University Computer Engineering Department in 2017. She graduated her MSc program in Inonu University, department of Computer Engineering in 2019 and is continuing her PhD program in the Computer Engineering Department of Inonu University. Her research interests are control systems,

metaheuristic optimization and reinforcement learning methods.



**GURKAN KAVURAN** received his B.Sc. degree in Electrical and Electronics Engineering from Firat University in 2008. He received PhD degree in Electrical and Electronics Engineering from Firat University in 2017. His research interests include robotics, fractional calculus, control theory and applications, modeling and simulation, signal processing.

# Sensor and Actuator Fault Tolerant Control of Grid-Tied Microgrid

Heybet Kilic, Musa Yilmaz

**Abstract**—The rising penetration of the deployed renewable energy resources (DERs) in the electrical grid introduces new challenges in terms of grid's reliable operation. DERs are bonded to the backbone system at a Point of Common Coupling (PCC) at the distribution level, possibly via a micro grid. Micro grids generally operates in grid-tied and islanded modes. In islanded mode, the reactive and active power ought to reach balance with the load demand., while in the grid-tied mode, the active and active powers must be desired criteria defined by the distribution system operator. Therefore, in both cases, proper control is vital to the microgrid's operation and its DERs. In this article, a fault tolerant control (FTC) method bottomed on  $H_\infty$  observer is advised for a DER supplying a grid-tied microgrid to make it resilient against sensor and actuator faults and guarantee its reliable operation.

**Index Terms**—Distributed energy resources, fault tolerant control, microgrid, sensor and actuator faults.

## I. INTRODUCTION

Traditional power generation in electrical grids is dependent on fossil fuels, which are known to release carbon dioxide. Because of the increasing demand for power, electrical networks must contend with a substantial amount of power loss, voltage fluctuation, and feeder blockage. Integration of effective power electronic converters with distributed energy sources (DERs) [1]- [2] through the use of microgrids in the distribution grid is a potential approach that may be taken to solve the problem. DERs are distributed energy resources that are typically based on renewable energy sources (such as fuel cells, solar, or wind) and are put in close proximity to areas where customers obtain their electricity. When a DER is deployed, load dependability is improved, and in the event that there is an interruption in power supply, the load demand can be satisfied by operating DERs in an isolated mode. However, the main drawbacks of distributed energy resources (DERs) include the unpredictability of their power output as well as the inherent intermittent nature of renewable energy sources [3]. The solution is controllers for the power electronic interfaces of DERs that are resistant to the failure of sensors and actuators and can regulate DER output power

to the desired level. It has been determined that this resolution is effective.

Conventional power generation in electrical grids relies on the fossil fuels emitting CO<sub>2</sub>. Also, electrical grids have to deal with the considerable power loss, voltage fluctuation, and feeder blockage because of rising load requisition. Combining DERs with high-performance power electronic converters is a realistic solution. [1]- [2] through the microgrid in the distribution grid. DERs are primarily based on renewable energie sources (such as fuel cell , solar, wind) and are installed near electricity consumers. Deploying a DER also improve load dependable in case of the power interruption, the load demand can be met by operating of DERs in islanded mode. However, uncertainty of power output and inherent intermittency of renewable energy sources are often seen as DERs' most significant drawbacks. [3]. The problem can be fixed by using DER power electrical interface controllers, which are resilient in the face of malfunctioning sensors and actuators that regulate the DER's power output.

Although the researchers have been studied the microgrid and distribution network fault detection and protection, studies on the sensor or actuator fault tolerant control(FTC) of microgrid is restricted. There are several approaches to detection sensor fault in power systems [4]–[11]: in [4], two observer-basis sensor failure perception approaches are proposed because of control loops of power system load frequency ; in [5], [6], an obscure input observer-established sensor failure determined method purpose of load frequency control loop of interdependent power system is discussed; Kalman filter and chi-squared test used in [7] to define failures or cyber offensive on the phasors-measurement unit (PMU); in [8], an observer-based FTC approach for the grid-tied microgrid is investigated; a virtual actuator based FTC approach for the power systems is proposed in [9]; in [12], For a wind energy system with a doubly fed induction generator (DFIG) coupled to a microgrid, a new FTC approach is proposed to enable ride through in any voltage sag scenarios, even deep sags. In spite of the researches done so far, there is a lack of sufficient studies on fault tolerant control of the voltage source converter (VSC) coupled DERs in microgrid. Moreover, there is no studies to address the simultaneous sensor and actuator FTC. In addition, researchers and scientists from a wide range of disciplines are interested in studying FTC strategies for sensor and actuator faults [10], [11], [13]–[15].

In this research, an observed-based FTC for the VSC-coupled DER with sensor or/and actuator failures is suggested. The motivation for this paper comes from the aforementioned issues for the reliable operation of microgrids, as well as the

Heybet Kilic is with the Department of Electric Power and Energy System , Dicle University, Diyarbakir, 21280 TURKEY e-mail: heybet.kilic@dicle.edu.tr

Musa Yilmaz is with the Department of Electrical and Electronics, Batman University, Batman, 72000 TURKEY e-mail: musa.yilmaz@batman.edu.tr

This project was supported by the scientific research projects coordinatorship of batman university with the project number of BTU BAP-2019-MMF-03.

Manuscript received January 30, 2023; revised April 12, 2023.  
DOI: 10.17694/bajece.1244981

paucity of studies on FTC for sensor and actuator faults. In contrast to the study that came before it, the observer that is being offered in this paper is intended to give simultaneous estimation of the system state, flaws in the sensor or actuator, and it consists of the two processes that are outlined below. The accuracy of the observations is improved by first implementing a virtual observer, and then, because the virtual observer takes into account quantities that cannot be measured directly, a real observer is constructed with the assistance of the virtual observer. An observer-based FTC is designed to be implemented in the second step of the process in order to remove the impact that failures and discomforts have on the performance of the DER that is linked to the grid-tied microgrid.

This article is structured as : The Section II, presents the state-space model of microgrid ; The Section III, displays an observer for evaluating controller feedback amplification as well as system states and faults; the proposed FTC is applied to the mesh microgrid in the Section IV, and its performance is evaluated using several simulated events; and finally, the article end is in the Section VI.

## II. GRID-TIED MICROGRID MODEL

We consider the microgrid as a linear time invariant (LTI) system which is modeled as follows:

$$\Sigma : \begin{cases} \dot{x}(t) = Ax(t) + Bu(t) + D\epsilon(t) \\ y(t) = Cx(t), \end{cases} \quad (1)$$

where  $x(t) = (x_1, x_2, x_3, \dots, x_n)^T \in \mathbb{R}^n$  is the state vector of the system,  $u(t) = (u_1, u_2, u_3, \dots, u_m)^T \in \mathbb{R}^m$  is the control vector,  $y(t) = (y_1, y_2, y_3, \dots, y_q)^T \in \mathbb{R}^q$  is the output vector of the system, and  $\epsilon(t) = (\epsilon_1, \epsilon_2, \epsilon_3, \dots, \epsilon_p)^T \in \mathbb{R}^p$  is the external disturbance. Also,  $A \in \mathbb{R}^{n \times n}$ ,  $B \in \mathbb{R}^{n \times m}$ ,  $C \in \mathbb{R}^{q \times n}$ , and  $D \in \mathbb{R}^{n \times p}$  are the known system matrices. The following set of equations is used to obtain the state space model of a DER in a grid-tied microgrid.

$$\begin{aligned} \dot{i}_{1d} &= -\frac{R_1}{L_1}i_{1d} + \omega i_{1q} - \frac{v_{cfd}}{L_1} + \frac{v_{dc}}{2L_1}m_d \\ \dot{i}_{1q} &= -\omega i_{1d} - \frac{R_1}{L_1}i_{1q} - \frac{v_{cfq}}{L_1} + \frac{v_{dc}}{2L_1}m_q \\ \dot{i}_{2d} &= \frac{1}{L_2}(v_{cfd} - v_{sd}) + \omega i_{2q} \\ \dot{i}_{2q} &= \frac{1}{L_2}(v_{cfq} - v_{sq}) - \omega i_{2d} \\ \dot{v}_{cfd} &= \frac{1}{C_f}(i_{1d} - i_{2d}) + \omega v_{cfq} \\ \dot{v}_{cfq} &= \frac{1}{C_f}(i_{1q} - i_{2q}) - \omega v_{cfd}, \end{aligned} \quad (2)$$

$v$  means the voltage and  $i$  means current,  $d$ ,  $q$  denote the  $dq$  components,  $t$  and  $f$  show the DER's terminal and filter parameters,  $R_1$  is the DER-side resistance, and  $C_f$  is the capacitor and  $L_1$  is the inductance of DER-side of the LCL filter. The angular frequency is  $\omega = 2\pi f$ , the grid frequency is  $f$ .  $m_d$  and  $m_q$  shows, modulation indexes and they regulate the DER's output voltage as follows:

$$v_{td} = m_d \frac{v_{dc}}{2}, \quad v_{tq} = m_q \frac{v_{dc}}{2}. \quad (3)$$

According to (2) and (3), the state, input, and disturbance vectors in (1) are obtained as follows: the state vector is  $x = [i_{1q} \ i_{1d} \ i_{2d} \ i_{2q} \ v_{cfd} \ v_{cfq}]^T \in \mathbb{R}^{n=6}$ ; the input vector is  $u = [m_d \ m_q]^T \in \mathbb{R}^{m=2}$ ; and  $\epsilon = [v_{sd} \ v_{sq}]^T \in \mathbb{R}^{p=2}$  is known as disturbance vector. The matrices of the DER state space model (1) are as follow:

$$A = \begin{bmatrix} -\frac{R}{L_1} & \omega & 0 & 0 & -\frac{1}{L_1} & 0 \\ -\omega & -\frac{R}{L_1} & 0 & 0 & 0 & -\frac{1}{L_1} \\ 0 & 0 & -\frac{R}{L_2} & \omega & -\frac{1}{L_2} & 0 \\ 0 & 0 & \omega & -\frac{R}{L_2} & 0 & -\frac{1}{L_2} \\ \frac{1}{C_f} & 0 & -\frac{1}{C_f} & 0 & 0 & \omega \\ 0 & \frac{1}{C_f} & 0 & -\frac{1}{C_f} & -\omega & 0 \end{bmatrix}$$

$$B = \frac{V_{dc}}{2} \begin{bmatrix} \frac{1}{L_1} & 0 \\ 0 & \frac{1}{L_1} \\ 0 & 0 \\ 0 & 0 \\ 0 & 0 \\ 0 & 0 \end{bmatrix}, \quad D = \begin{bmatrix} 0 & 0 \\ 0 & 0 \\ -\frac{1}{L_2} & 0 \\ 0 & 0 \\ 0 & 0 \\ 0 & 0 \end{bmatrix}$$

$$C = \begin{bmatrix} 0 & 0 & 1 & 0 & 0 & 0 \\ 0 & 0 & 0 & 1 & 0 & 0 \end{bmatrix}.$$

The active and reactive powers delivered to the grid by DER at the point of common coupling (PCC) are obtained by:

$$\begin{aligned} P_s &= \frac{3}{2}(v_{sd}i_{2d} + v_{sq}i_{2q}) \\ Q_s &= \frac{3}{2}(-v_{sd}i_{2q} + v_{sq}i_{2d}). \end{aligned} \quad (4)$$

As the phase locked loop (PLL) provides that  $v_{sd} = |V_s|$  and  $v_{sq} = 0$ , where  $|V_s|$  is the voltage magnitude, we can write:

$$\begin{aligned} P_s &= \frac{3}{2}|V_s|i_{2d} \\ Q_s &= -\frac{3}{2}|V_s|i_{2q}. \end{aligned} \quad (5)$$

The objective of the DER's controller is to generate the PWM signals so that  $i_{2d}$  and  $i_{2q}$  track their corresponding reference values obtained by the desired active ( $P_{sref}$ ) and reactive powers ( $Q_{sref}$ ) as the following [16].

$$\begin{aligned} P_{sref} &= \frac{3}{2}|V_s|i_{2dref} \\ Q_{sref} &= -\frac{3}{2}|V_s|i_{2qref}. \end{aligned} \quad (6)$$

## III. FAULT-TOLERANT CONTROL DESIGN

In the content of this article, we contemplate sensors and actuators failures. whenever sensors failure happens, the actual reading of the system output described as

$$y^F(t) = Cx(t) + f_s(t), \quad (7)$$

where  $f_s \in \mathbb{R}^q$  is the sensor failure. Additionally, whenever an actuators failure happen, the control input described as

$$u(t) = u_F(t) + f_a(t), \quad (8)$$

where  $f_a \in \mathbb{R}^m$  is the actuator failure, and  $u_F(t)$  is the control signal.

To derive the observer and control law, the following assumptions and definition must be considered.

*Assumption 1:*  $A$  and  $B$  matrices are controllable,  $A$  and  $C$  are observable.

*Assumption 2:*  $f_a$  is the element of  $\mathcal{L}_2[0, \infty)$

*Definition 1:* A stable system with  $\mathcal{H}_\infty$  performance must satisfy the following conditions:

- 1) The system must be stable with zero disturbance.
- 2) For an arbitrary positive constant  $\gamma$  with zero initial condition, the following condition must be hold:

$$\int_0^\infty x^T(t)x(t)dt < \gamma^2 \int_0^\infty \epsilon^T(t)\epsilon(t)dt.$$

Three failure scenarios are considered, sensor failure, actuator failure, and simultaneous actuators and sensors failures. All scenarios proceed as follows. Initial, an observer is offered to evaluate system states (1) and the faults. Later, an observer-based controller was developed.

#### A. Sensor Fault

We contrived the below observer for the system (1) with sensor failure (7):

$$\begin{cases} \dot{\psi}(t) = \mathcal{A}\psi(t) + \mathcal{B}u(t) + \mathcal{L}y^F(t) \\ r_F(t) = \psi(t) + \mathcal{C}y^F(t), \end{cases} \quad (9)$$

where  $\psi(t)$  is an ancillary variant, matrixes  $\mathcal{A}$ ,  $\mathcal{B}$ ,  $\mathcal{C}$ , and  $\mathcal{L}$  are parameters of observer,  $r_F(t)$  is the prediction for  $x(t)$  and  $f_s(t)$ .

To contrive the observer for both system,  $x(t)$ , sensor failure,  $f_s(t)$ , system (1) with sensor failure (7) reobtained as ;

$$\begin{cases} F_1\dot{r}(t) = A_0r(t) + Bu(t) + D(t) \\ y_F(t) = F_2r(t), \end{cases} \quad (10)$$

where  $r(t) = \begin{bmatrix} x(t) \\ f_s(t) \end{bmatrix}$ ,  $A_0 = [A \quad 0_{n \times q}]$ ,  $F_1 = [I_n \quad 0_{n \times q}]$ ,  $F_2 = [C \quad I_q]$ . It is clear that  $rank \left( \begin{bmatrix} F_1 \\ F_2 \end{bmatrix} \right) = n + q$ , which means it is full rank and its inverse exists.

Let  $E_1 = \begin{bmatrix} I_n \\ -C \end{bmatrix}$  and  $E_2 = \begin{bmatrix} 0_{n \times q} \\ I_q \end{bmatrix}$ , following calculate can be done easily:

$$\begin{cases} \begin{bmatrix} F_1 \\ F_2 \end{bmatrix} [E_1 \quad E_2] = I_{n+q} \\ [E_1 \quad E_2] \begin{bmatrix} F_1 \\ F_2 \end{bmatrix} = I_{n+q}, \end{cases} \quad (11)$$

which means  $\begin{bmatrix} F_1 \\ F_2 \end{bmatrix}^{-1} = [E_1 \quad E_2]$ . Multiplying  $E_1$  by the both sides of (10) yields:

$$E_1 F_1 \dot{r}(t) = E_1 A_0 r(t) + E_1 B u(t) + E_1 D \epsilon(t), \quad (12)$$

and using (11), i.e.,  $E_1 F_1 + E_2 F_2 = I_{n+q}$ , we have:

$$\dot{r}(t) = E_1 A_0 r(t) + E_1 B u(t) + E_1 D \epsilon(t) + E_2 F_2 \dot{r}_F(t). \quad (13)$$

Now, think of the below conjectural observer:

$$\begin{aligned} \dot{r}_F(t) = & E_1 A_0 r_F(t) + E_1 B u(t) + E_1 D \epsilon(t) + E_2 F_2 \dot{r}_F(t) \\ & + L(y^F(t) - F_2 r_F(t)), \end{aligned} \quad (14)$$

An observer gain matrix denoted by  $L$ . Error dynamics are achieved by defining the estimating error as  $\eta(t) = r(t) - r_F(t)$ .

$$\dot{\eta}(t) = (E_1 A_0 - L F_2) \eta(t) + E_1 D \epsilon(t). \quad (15)$$

For an arbitrary positive stable  $\delta$ , fault (15) will be asymptotically constant with the inconvenience emaciation level  $\delta$ , if a positive matrix  $P \in \mathbb{R}^{(n+q) \times (n+q)}$  exists, any matrix  $H \in \mathbb{R}^{(n+q) \times q}$  satisfies the below linear matrix inequality (LMI):

$$\Pi = \begin{bmatrix} \Delta & P E_1 D \\ * & -\delta^2 I \end{bmatrix} < 0, \quad (16)$$

where  $\Delta = P E_1 A_0 + A_0^T E_1^T P - H F_2 - F_2^T H^T + I$ . The parameters of observer (9) are obtained as follows.

$$\begin{aligned} \mathcal{A} = & E_1 A_0 - L F_2, \quad \mathcal{B} = E_1 B, \quad \mathcal{C} = E_2 \\ \mathcal{L} = & L - (E_1 A_0 - L F_2) E_2, \quad L = P^{-1} H. \end{aligned} \quad (17)$$

Contrived an  $H_\infty$  observer for system (1), acquired  $r_F(t)$  as the conjectural value for  $x(t)$  and  $f_s(t)$ . Acquired the observer controller is ready.  $u(t) = K F_1 r_F(t)$ , The observer-based control input is of the form, where  $K$  is the control gain. This results in a rewrite of the system (1) as:

$$\begin{aligned} \dot{x}(t) = & A x(t) + B K F_1 r_F(t) + D \epsilon(t) \\ = & (A + B K) x(t) - B K F_1 \eta(t) + D \epsilon(t) \\ = & (A + B K) x(t) - B d(t) + D \epsilon(t), \end{aligned} \quad (18)$$

where  $d(t) = K F_1 \eta(t)$ .

For an arbitrary positive stable  $\alpha$ , designed observer (9) with parameters (17) with sensor fault (7) will be asymptotically constant with the inconvenience emaciation level  $\gamma$ , if a positive matrix  $S \in \mathbb{R}^{n \times n}$  and any matrix  $G \in \mathbb{R}^{m \times n}$  fulfil the below LMI:

$$\begin{bmatrix} \bar{\Delta} & S & -B & D \\ * & -I & 0 & 0 \\ * & * - \alpha I & 0 & \\ * & * & * & \delta^2 I \end{bmatrix} < 0, \quad (19)$$

where  $\bar{\Delta} = A S + S A^T + B G + G^T B^T$ . The control gain  $K$  and disturbance attenuation level  $\gamma$  can be calculated as follow:

$$\begin{aligned} K = & G S^{-1} \\ \gamma = & \sqrt{(\alpha \lambda_{max}(K^T K) + 1) \delta^2}. \end{aligned}$$

#### B. Actuator Fault

To get an idea of the state of the system (1),  $x(t)$ , actuator fault,  $f_a(t)$ , Planned below observer:

$$\begin{cases} \dot{\bar{\psi}}(t) = \bar{\mathcal{A}}\bar{\psi}(t) + \bar{\mathcal{B}}u_F(t) + \bar{\mathcal{L}}y(t) \\ \bar{r}_F(t) = \bar{\psi}(t) + \bar{\mathcal{C}}y(t), \end{cases} \quad (20)$$

where  $\bar{\psi}(t)$  is an ancillary variant, matrixes  $\bar{\mathcal{A}}$ ,  $\bar{\mathcal{B}}$ ,  $\bar{\mathcal{C}}$ , and  $\bar{\mathcal{L}}$  are the observer parameters,  $\bar{r}_F(t)$  is the prediction of  $x(t)$ ,  $f_a(t)$ .



Whenever an actuator failure happen, system (1) reformulated :

$$\begin{cases} \bar{E}_1 \dot{\bar{r}}(t) = A_1 r(t) + B u_F(t) + D \epsilon(t) \\ y(t) = \bar{E}_3 r(t), \end{cases} \quad (21)$$

where  $\bar{r}(t) = \begin{bmatrix} x(t) \\ f_a(t) \end{bmatrix}$ ,  $A_1 = [A \ B]$ ,  $\bar{E}_1 = [I_n \ 0_{n \times m}]$ ,  $\bar{E}_3 = [C \ 0_{q \times m}]$ . Defining  $\bar{E}_2 = [B_1 C \ I_m]$  where  $B_1 \in \mathbb{R}^{m \times q}$  is a full column rank (if  $m > q$ ) or row rank (if  $m < q$ ) matrix, it is clear that  $\text{rank} \begin{pmatrix} \bar{E}_1 \\ \bar{E}_2 \end{pmatrix} = n + m$  that means it is full rank, therefore its reverse consists.

Let  $\bar{F}_1 = \begin{bmatrix} I_n \\ -B_1 C \end{bmatrix}$  and  $\bar{F}_2 = \begin{bmatrix} 0_{n \times m} \\ I_m \end{bmatrix}$ , following calculate can be done easily:

$$\begin{cases} \begin{bmatrix} \bar{E}_1 \\ \bar{E}_2 \end{bmatrix} [\bar{F}_1 \ \bar{F}_2] = I_{n+m} \\ [\bar{F}_1 \ \bar{F}_2] \begin{bmatrix} \bar{E}_1 \\ \bar{E}_2 \end{bmatrix} = I_{n+m}, \end{cases} \quad (22)$$

which means  $\begin{bmatrix} \bar{E}_1 \\ \bar{E}_2 \end{bmatrix}^{-1} = [\bar{F}_1 \ \bar{F}_2]$ . Multiplying  $\bar{F}_1$  by the both sides of (21) and using (22) yields:

$$\dot{\bar{r}}(t) = \bar{F}_1 A_1 \bar{r}(t) + \bar{F}_1 B u_F(t) + \bar{F}_1 D \epsilon(t) + \bar{F}_2 \bar{E}_2 \dot{\bar{r}}(t). \quad (23)$$

Now, consider the following virtual observer:

$$\begin{aligned} \dot{\bar{r}}_F(t) &= \bar{F}_1 A_1 \bar{r}_F(t) + \bar{F}_1 B u_F(t) + \bar{F}_1 D \epsilon(t) + \bar{F}_2 \bar{E}_2 \dot{\bar{r}}(t) \\ &\quad + \bar{L}(y^F(t) - \bar{E}_3 \bar{r}_F(t)), \end{aligned} \quad (24)$$

An observer gain matrix denoted by  $L$ . Error dynamics are achieved by defining the estimating error as  $\eta(t) = r(t) - r_F(t)$ .

$$\dot{\eta}(t) = (\bar{F}_1 A_1 - \bar{L} \bar{E}_3) \eta(t) + \bar{F}_1 D \epsilon(t), \quad (25)$$

where  $\bar{\epsilon}(t) = \begin{bmatrix} \epsilon(t) \\ f_a(t) \end{bmatrix}$ ,  $\bar{F}_D = [\bar{F}_1 D \ \bar{F}_2]$ .

For an optional positive stable  $\bar{\delta}$ , fault (25) will be asymptotically constant with inconvenience emaciation level  $\delta$ , if a positive matrix  $\bar{P} \in \mathbb{R}^{(n+q) \times (n+q)}$  exists and any matrix  $\bar{H} \in \mathbb{R}^{(n+q) \times q}$  below LMI:

$$\bar{\Pi} = \begin{bmatrix} \$ & \bar{P} \bar{F}_D \\ * & -\bar{\delta}^2 I \end{bmatrix} < 0, \quad (26)$$

where  $\$ = \bar{P} \bar{F}_1 A_1 + A_1^T \bar{F}_1^T \bar{P} - \bar{H} \bar{E}_3 - \bar{H}_3^T \bar{H}^T + I$ . The parameters of observer (20) are as follows.

$$\begin{aligned} \bar{A} &= \bar{F}_1 A_1 - \bar{L} \bar{E}_2, & \bar{B} &= \bar{F}_1 B, & \bar{C} &= B_1 \bar{F}_2 \\ \bar{L} &= \bar{L} - (\bar{F}_1 A_1 - \bar{L} \bar{E}_3) \bar{F}_2 B_1, & \bar{L} &= \bar{P}^{-1} \bar{H}. \end{aligned} \quad (27)$$

Now, we can reproduce the observer-based controller utilization by  $r_F(t)$ , which is acquired from the created  $H_\infty$  observer (20) with parameters (27) convincing LMI (26) and inconvenience emaciation level  $\bar{\delta}$ .

The following form is the input for the observer-based controller.

$$u_F(t) = (\bar{K} \bar{E}_1 - \bar{E}_4) \bar{r}_F(t), \quad (28)$$

where  $\bar{E}_4 = [0_{m \times n} \ I_m]$ , and  $\bar{K}$  means the control gain. Then we can obtain system (1) with actuator fault (8) as below.

$$\begin{aligned} \dot{x}(t) &= A x(t) + B((\bar{K} \bar{E}_1 - \bar{E}_4) \bar{r}_F(t) + f_a(t)) + D \epsilon(t) \\ &= (A + B \bar{K}) x(t) - B(\bar{K} \bar{E}_1 + \bar{E}_4) \bar{\eta}(t) + D \epsilon(t) \\ &= (A + B \bar{K}) x(t) - B \bar{d}_1(t) + B \bar{d}_2(t) + \bar{D} \bar{\epsilon}(t), \end{aligned} \quad (29)$$

where  $\bar{D} = [D \ 0]$ ,  $\bar{d}_1(t) = \bar{K} \bar{E}_1 \bar{\eta}(t)$ , and  $\bar{d}_2(t) = \bar{E}_4 \bar{\eta}(t)$ .

For an arbitrary positive stable  $\bar{\alpha}$  and  $\bar{\beta}$  created observer (19) with parameters (27) compensate LMI (26). The system (1) with actuator fault (8) will be asymptotically constant with inconvenience emaciation level  $\bar{\gamma}$ , if a positive matrix  $\bar{S} \in \mathbb{R}^{n \times n}$  and any matrix  $\bar{G} \in \mathbb{R}^{m \times n}$  compensates the below LMI:

$$\begin{bmatrix} \bar{\$} & \bar{S} & -B & B & D \\ * & -I & 0 & 0 & 0 \\ * & * & -\bar{\alpha} I & 0 & 0 \\ * & * & * & -\bar{\beta} I & 0 \\ * & * & * & * & -\bar{\delta}^2 \end{bmatrix} < 0, \quad (30)$$

where  $\bar{\$} = \bar{A} \bar{S} + \bar{S} \bar{A}^T + B \bar{G} + \bar{G}^T B^T$ . The control gain  $K$  and disturbance attenuation level  $\gamma$  can be calculated as follows:

$$\begin{aligned} \bar{K} &= \bar{G} \bar{S}^{-1} \\ \bar{\gamma} &= \sqrt{(\bar{\alpha} \lambda_{\max}(\bar{K}^T \bar{K}) + 1) \bar{\delta}^2}. \end{aligned}$$

### C. Sensor and Actuator Faults

Content of this subsection ; sensors and actuators failures are contemplated. For that purpose initial contemplate the below observer by us :

$$\begin{cases} \dot{\hat{\psi}}(t) = \hat{A} \hat{\psi}(t) + \hat{B} u_F(t) + \hat{L} y^F(t) \\ \hat{r}_F(t) = \hat{\psi}(t) + \hat{C} y^F(t), \end{cases} \quad (31)$$

where  $\hat{\psi}(t)$  is an ancillary variant, matrixes  $\hat{A}$ ,  $\hat{B}$ ,  $\hat{C}$ , and  $\hat{L}$  are the observer parameters, and  $\hat{r}_F(t)$  is the estimation of  $x(t)$ ,  $f_s(t)$ ,  $f_a(t)$ .

Considering the similar process of the preceding subsections, system (1) with sensors failure (7) and actuators failure (8) presented as follow:

$$\begin{cases} \dot{\hat{r}}(t) = \hat{F}_1 A_2 \hat{r}(t) + \hat{F}_1 B u_F(t) + \hat{F}_1 D \epsilon(t) \\ \quad + (\hat{F}_2 \hat{E}_2 + \hat{F}_3 \hat{E}_3) \hat{r}(t) \\ y^F(t) = \hat{E}_2 \hat{r}(t), \end{cases} \quad (32)$$

where  $\hat{r} = [x^T(t) \ f_s^T(t) \ f_a^T(t)]^T$ ,  $A_2 = [A \ 0_{n \times q} \ B]$ , and

$$\hat{E} = \begin{bmatrix} \hat{E}_1 \\ \hat{E}_2 \\ \hat{E}_3 \end{bmatrix} = \begin{bmatrix} I_n & 0_{n \times q} & 0_{m \times q} \\ C & I_q & 0_{q \times m} \\ B_1 C & B_1 & I_m \end{bmatrix}$$

$$\hat{F} = \left[ \hat{F}_1 \mid \hat{F}_2 \mid \hat{F}_3 \right] = \begin{bmatrix} I_n & 0_{n \times q} & 0_{n \times m} \\ -C & I_q & 0_{q \times m} \\ 0_{m \times n} & -B_1 & I_m \end{bmatrix}$$

where  $\hat{E}$  is a full rank matrix with an inverse matrix is  $\hat{E}^{-1} = \hat{F}$ . Then, virtual observer design as follow:

$$\begin{aligned} \hat{r}_F(t) = & \hat{F}_1 A_2 \hat{r}_F(t) + \hat{F}_1 B u_F(t) + \\ & (\hat{F}_2 D \epsilon(t) + \hat{F}_3 B_1) \hat{E}_2 \hat{r}(t) + \hat{L}(y^F(t) - \hat{E}_2 \hat{r}_F(t)), \end{aligned} \quad (33)$$

An observer gain matrix denoted by  $L$ . Error dynamics are achieved by defining the estimating error as  $\eta(t) = r(t) - r_F(t)$ .

$$\dot{\eta}(t) = (\hat{F}_1 A_2 - \hat{L} \hat{E}_2) \eta(t) + \hat{D} \hat{\epsilon}(t), \quad (34)$$

where  $\hat{\epsilon}(t) = \begin{bmatrix} \epsilon(t) \\ f_a(t) \end{bmatrix}$ , and  $\hat{D} = \begin{bmatrix} -D \\ -C D \end{bmatrix}$ .

For an arbitrary positive constant  $\hat{\delta}$ , error (34) will be asymptotically constant with inconvenience emaciation level  $\hat{\delta}$ , if a positive matrix  $\hat{P} \in \mathbb{R}^{(n+m+q) \times (n+m+q)}$  exists, any matrix  $\hat{H} \in \mathbb{R}^{(n+m+q) \times q}$  satisfies below LMI:

$$\hat{\Pi} = \begin{bmatrix} \Xi & \hat{P} \hat{D} \\ * & -\hat{\delta}^2 I \end{bmatrix} < 0, \quad (35)$$

where  $\Xi = \hat{P} \hat{F}_1 A_2 + A_2^T \hat{F}_1^T \hat{P} - \hat{H} \hat{E}_2 - \hat{E}_2^T \hat{H}^T + I$ . The parameters of observer (31) are as follows.

$$\begin{aligned} \hat{A} &= \hat{F}_1 A_2 - \hat{L} \hat{E}_2 & \hat{B} &= \hat{F}_1 B & \hat{C} &= \hat{F}_4 & \hat{L} &= \hat{P}^{-1} \hat{H} \\ \hat{L} &= \hat{L} - (\hat{F}_1 A_2 - \hat{L} \hat{E}_2) \hat{F}_4 B_1 & \hat{F}_4 &= \begin{bmatrix} 0_{n \times q} \\ I_q \\ 0_{m \times q} \end{bmatrix}. \end{aligned} \quad (36)$$

The observer-based control input ;

$$u_F(t) = (\hat{K} \hat{E}_1 - \hat{E}_4) r_F(t), \quad (37)$$

where  $\hat{E}_4 = [0_{m \times n} \quad 0_{m \times q} \quad I_m]$ , and  $\hat{K}$  is the control gain. System (1) with both sensor failure (7) and actuator failure (8) happen

$$\begin{aligned} \dot{x}(t) &= A x(t) + B((\hat{K} \hat{E}_1 - \hat{E}_4) \hat{r}_F(t) + f_a(t)) + D \epsilon(t) \\ &= (A + B \hat{K}) x(t) - B(\hat{K} \hat{E}_1 + \hat{E}_4) \hat{\eta}(t) + D \epsilon(t) \\ &= (A + B \hat{K}) x(t) - B \hat{d}_1(t) + B \hat{d}_2(t) + \bar{D} \bar{\epsilon}(t), \end{aligned} \quad (38)$$

Where  $\hat{d}_1(t) = \hat{K} \hat{E}_1 \hat{\eta}(t)$ ,  $\hat{d}_2(t) = \hat{E}_4 \hat{\eta}(t)$ ,  $\bar{D}$  is defined (33).

For an arbitrary positive stable  $\hat{\alpha}$  and  $\hat{\beta}$  designed observer (31) with parameters (36) satisfy LMI (35). The system (1) with sensor failure (7), with actuator failure (8) is asymptotically constant with inconvenience emaciation level  $\hat{\gamma}$ , if a positive matrix  $\hat{S} \in \mathbb{R}^{n \times n}$ , any matrix  $\hat{G} \in \mathbb{R}^{m \times n}$  satisfies following LMI:

$$\begin{bmatrix} \hat{\Xi} & \hat{S} & -B & B & \bar{D} \\ * & -I & 0 & 0 & 0 \\ * & * & -\hat{\alpha} I & 0 & 0 \\ * & * & * & -\hat{\beta} I & 0 \\ * & * & * & * & -\hat{\delta}^2 \end{bmatrix} < 0, \quad (39)$$

where  $\hat{\Xi} = A \hat{S} + \hat{S} A^T + B \hat{G} + \hat{G}^T B^T$ . The control gain  $K$  and disturbance attenuation level  $\hat{\gamma}$  can be calculated as follow:

$$\begin{aligned} \hat{K} &= \hat{G} \hat{S}^{-1} \\ \hat{\gamma} &= \sqrt{(\hat{\alpha} \lambda_{max}(\hat{K}^T \hat{K}) + 1) \hat{\delta}^2}. \end{aligned}$$

## IV. NUMERICAL SIMULATION

As discussed, the main objective of the FTC method is to make the grid-tied microgrid resilient against the impact of failures and inconveniences. The cases considered for the simulation are sensor failure, actuator failure and simultaneous sensor and actuator failuress. The simulated microgrid, which is related to the distribution grid, in Fig. 1. The DER connected to the microgrid is controlled by the designed observer-based FTC which its diagram is shown in Fig. 2

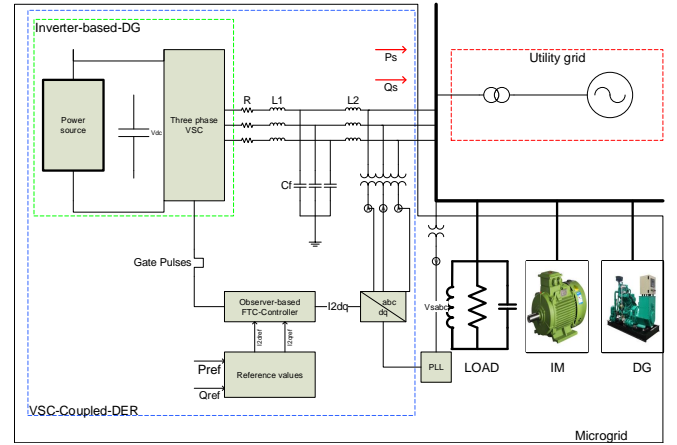


Fig. 1. The simulated grid-tied microgrid.

The simulated distribution grid symbolizes a part of the Canadian reference dispersion system [17]. The microgrid consists of an inverter-based DER, a diesel-based synchronous dispersion generator (DG), an induction motor load, and an RLC load. A diesel engine regulator and an IEEE ST1A excitation system are combined to construct the synchronous DG unit. The inverter-based DER, which is related to the distribution grid at PCC through an LCL filter, consists of a three-phase VSC based on IGBT controlled by space-vector PWM. The data of the excitation system, the synchronous DG unit, the diesel engine regulator and the parameters of the induction motor are taken from [17]. The parameters of the

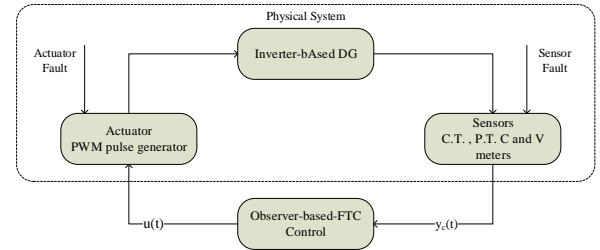


Fig. 2. FTC diagram of the VSC-coupled DER.

simulated microgrid are as follows:  $L = 100$  H;  $R = 0.75$   $\Omega$ ; the line to line rms voltage 480 V; the AC system frequency  $\omega = 377$  rad/s.

To assess the efficiency of the intended FTC, the following events are executed in the microgrid: at  $t = 0.2$  s,  $P_{s_{ref}} = 0$  and  $Q_{s_{ref}} = 0$  where  $P_{s_{ref}}$  and  $Q_{s_{ref}}$  are the reference reactive and active powers; at  $t = 0.25$  s,  $P_{s_{ref}}$  is subjected to

a step change from 0.0 MW to 3.0 MW; at  $t = 0.40$  s,  $P_{sref}$  has a step change from 2.3 MW to  $-3.3$  MW; and finally, at  $t= 0.4$  s,  $Q_{sref}$  has a step change from 0.0 MVar to 1.5 MVar.

The sensor and fault estimation is investigated by LMI which is achieved through two step. The first stage involves using a virtual observer to increase the precision of the observations. As the virtual observer does not include any quantifiable values, the real observer design is also included at this stage. In the second step, based on the real observer, FTC is constructed. The obtained results are based on the current on the q-frame. Fig.3, Fig. 4 and Fig. 5 show actuator, sensor and simultaneous fault cases, respectively.

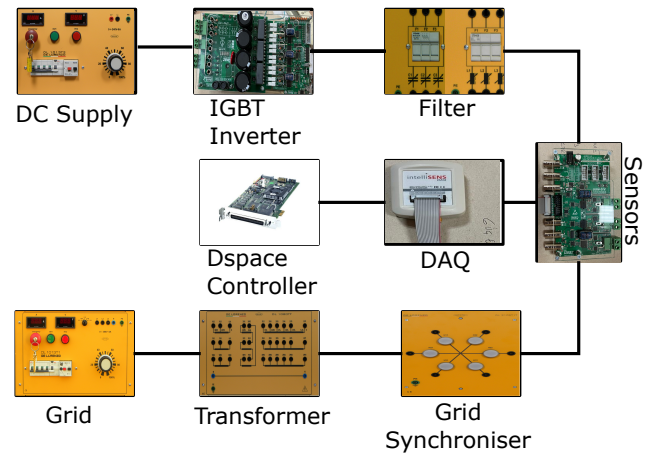


Fig. 6. Experimental Setup.

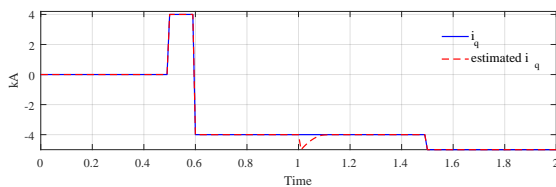


Fig. 3. FTC response for actuator fault on q-frame current.

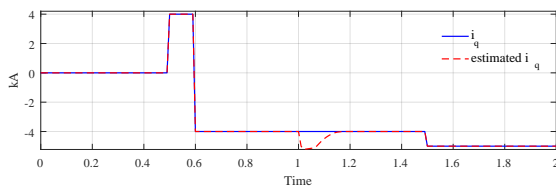


Fig. 4. FTC response for sensor faults on q-frame current.

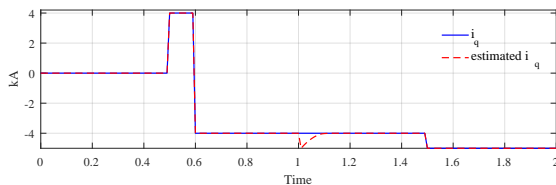


Fig. 5. FTC response for Sensor and actuator faults on q-frame current.

V. EXPERIMENTAL VERIFICATION

The fault-tolerant control algorithm proposed in this study has been experimentally validated for a grid-connected DER. The experimental setup is shown in Figure 6. The dSpace 1103 card was used as the control card in the experiment. Other components used in the experimental setup are shown in Figure 6 with their connections. The DER unit is represented as a DC source as shown in figure 6 and is connected to the mains via a transformer through an LC filter.

Figure 7 and figure 8 show actuator fault without FTC and actuator fault with FTC, respectively. As shown in Figure 8, the proposed fault tolerance algorithm accurately detects and tolerates actuator faults and sets it to the reference value.

On the other hand, sensor faults without FTC and sensor faults with FTC are shown in Figure 9 and Figure 10, respectively. As shown in Figure 10, the proposed fault tolerance

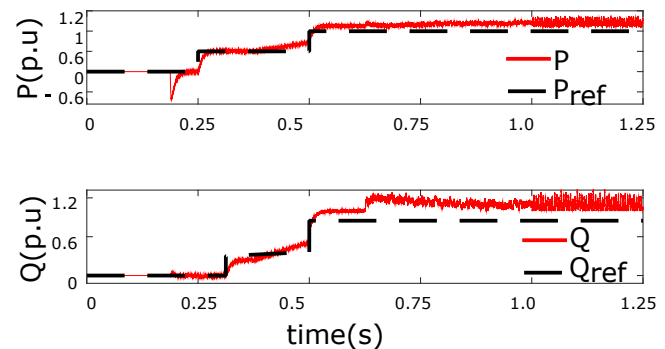


Fig. 7. Actuator faults without FTC.

algorithm accurately detects and tolerates sensor faults and sets it to the reference value.

VI. CONCLUSION

An observer-based FTC was created for a VSC-coupled DER in this article. The VSC-coupled DER is connected to the distribution grid through a microgrid. The proposed FTC design was accomplished through the following two steps: first, a  $H_\infty$  observer was designed to estimate the system state and sensor/actuator fault; second, the estimated fault

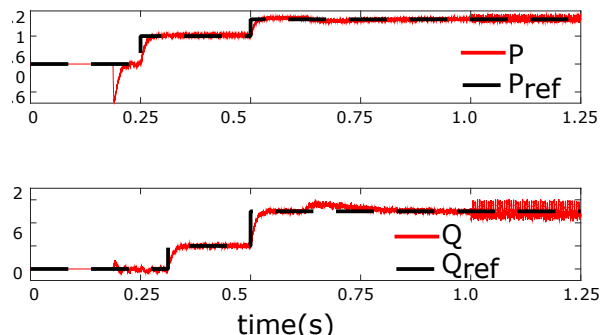


Fig. 8. Actuator faults with FTC.

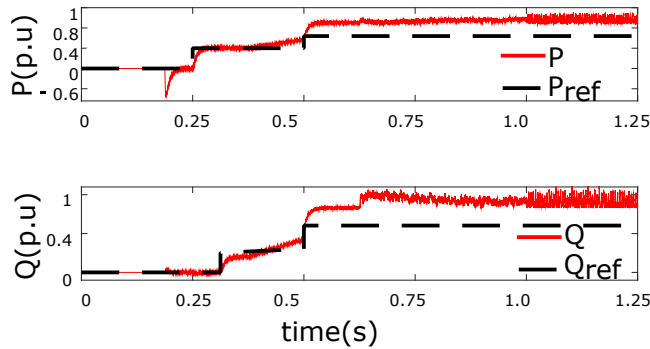


Fig. 9. Sensor faults without FTC.

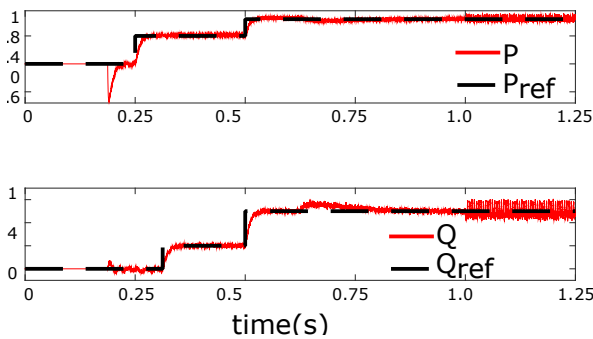


Fig. 10. Sensor faults with FTC.

obtained by the observer was used to calculate the feedback control gain in a manner that satisfies the defined LMI and the disturbance attenuation level; and third, the proposed FTC design was implemented. Both theoretical modeling and actual experimentation have been used to validate the functionality of the proposed FTC. The suggested FTC was able to manage the DER in such a way that its output powers followed the values that were required by carrying out many step adjustments in the reference active and reactive powers when there was a failure in either the sensor or the actuator.

#### ACKNOWLEDGMENT

This project was supported by the scientific research projects coordinator-ship of batman university with the project number of BTU BAP-2019-MMF-03.

#### REFERENCES

- [1] D. E. Olivares, A. Mehrizi-Sani, A. H. Etemadi, C. A. Cañizares, R. Iravani, M. Kazerani, A. H. Hajimiragha, O. Gomis-Bellmunt, M. Saeedifard, R. Palma-Behnke, and G. A. Jimenez-Estevéz, "Trends in microgrid control," *IEEE Transactions on Smart Grid*, vol. 5, no. 4, pp. 1905–1919, 2014.
- [2] S. M. Kaviri, M. Pahlevani, P. Jain, and A. Bakhshai, "A review of ac microgrid control methods," in *IEEE 8th International Symposium on Power Electronics for Distributed Generation Systems (PEDG)*, 2017, pp. 1–8.
- [3] Y. Yoldas, A. Onen, S. M. Mueeen, A. V. Vasilakos, and I. Alan, "Enhancing smart grid with microgrids: Challenges and opportunities," *Renewable and Sustainable Energy Reviews*, vol. 72, no. , pp. 205–214, 2015.
- [4] F. Caliskan and I. Genc, "A robust fault detection and isolation method in load frequency control loops," *IEEE Transactions on Power Systems*, vol. 23, no. 4, pp. 1756–1767, 2009.
- [5] R. L. de Araujo Ribeiro, C. B. Jacobina, E. R. C. da Silva, and A. M. N. Lima, "Fault detection of open-switch damage in voltage-fed pwm motor drive systems," *IEEE Transactions on Power Electronics*, vol. 18, no. 2, pp. 587–593, 2003.

- [6] T. A. Najafabadi, F. R. Salmasi, and P. Jabejdar-Maralani, "Detection and isolation of speed-, dc-link voltage-, and current-sensor faults based on an adaptive observer in induction-motor drives," *IEEE Transactions on Industrial Electronics*, vol. 58, no. 2, pp. 1662–1672, 2011.
- [7] S. Gholami and M. Aldeen, "Control of distributed energy resources under switching transient between grid-connected and islanded operation modes," in *IEEE Power & Energy Society General Meeting*, 2017, pp. 1–5.
- [8] S. Gholami, S. Saha, and M. Aldeen, "Fault tolerant control of electronically coupled distributed energy resources in microgrid systems," *International Journal of Electrical Power & Energy Systems*, vol. 95, pp. 327–340, 2018.
- [9] M. E. Raoufat, K. Tomsovic, and S. M. Djouadi, "Virtual actuators for wide-area damping control of power systems," *IEEE Transactions on Power Systems*, vol. 31, no. 6, pp. 4703–4711, 2016.
- [10] S. Misra, P. V. Krishna, V. Saritha, H. Agarwal, A. V. Vasilakos, and M. S. Obaidat, "Learning automata-based fault-tolerant system for dynamic autonomous unmanned vehicular networks," *IEEE Systems Journal*, vol. 11, no. 4, pp. 2929–2938, 2017.
- [11] S. Akhlaghi and N. Zhou, "Adaptive multi-step prediction based ekf to power system dynamic state estimation," in *IEEE Power and Energy Conference at Illinois*, 2017, pp. 1–8.
- [12] M. Blanke, M. Kinnaert, J. Lunze, M. Staroswiecki, and J. Schroder, *Diagnosis and Fault-Tolerant Control*. Berlin, Germany: Springer-Verlag, 2006.
- [13] D. Krokavec, A. Filasová, and P. Liščinský, "On fault tolerant control structures incorporating fault estimation," *Archives of Control Sciences*, no. No 4, 2016. [Online]. Available: <http://journals.pan.pl/Content/104506/PDF/acsc-2016-0025.pdf>
- [14] Dziekan, M. Witczak, and J. Korbicz, "Active fault-tolerant control design for takagi-sugeno fuzzy systems," *Bulletin of the Polish Academy of Sciences: Technical Sciences*, vol. 59, no. No 1, pp. 93–102, 2011. [Online]. Available: [http://journals.pan.pl/Content/83281/PDF/13\\_paper.pdf](http://journals.pan.pl/Content/83281/PDF/13_paper.pdf)
- [15] B. Zhang, S. Ping, Y. Long, Y. Jiao, and B. Wu, "Research on topology of a novel three-phase four-leg fault-tolerant npc inverter," *Archives of Electrical Engineering*, vol. vol. 71, no. No 2, pp. 489–506, 2022. [Online]. Available: [http://journals.pan.pl/Content/123218/PDF/art14\\_internet.pdf](http://journals.pan.pl/Content/123218/PDF/art14_internet.pdf)
- [16] B. Khaki, H. Kiliç, M. Yilmaz, M. Shafie-Khah, M. Lotfi, and J. P. Catalão, "Active fault tolerant control of grid-connected der: Diagnosis and reconfiguration," in *IECON 2019 - 45th Annual Conference of the IEEE Industrial Electronics Society*, vol. 1, 2019, pp. 4127–4132.
- [17] A. H. K. Alaboudy, H. H. Zeineldin, and J. Kirtley, "Microgrid stability characterization subsequent to fault-triggered islanding incidents," *IEEE Transactions on Power Delivery*, vol. 27, no. 2, pp. 658–669, 2012.



**Heybet kilic** received the B.S. degree in electrical electronics engineering, from Gaziantep University, Gaziantep, Turkey in 2009, the M.S. degree in renewable energy, and the Ph.D. degree in power systems from Dicle University, Diyarbakır, Turkey, in 2016 and 2021, respectively. He is an Assistant Professor with Dicle University, Department of electrical power and energy, where he teaches courses on power system, power electronics, and renewable energy systems since 2015. He is also PhD researcher in Faculty of Electrical Engineering, Mathematics and Computer Science, Electrical Sustainable Energy Department, TU Delft for 3 years. He is also IEEE sensor Member. His research interests include photovoltaics, wind energy conversion, power systems, microgrids, cyber physical-energy systems and data science.





**Musa Yilmaz** received the M.Sc. degree in Electrical Education from the Marmara University, Istanbul, Turkey, in 2004 and a Ph.D. degree in Electrical Education from the Marmara University, Istanbul, Turkey, in 2013. He currently works as an assistant professor at the Electrical and Electronics Engineering, Energy Engineering, Batman University. He joined Smart Grid Research Center (SMERC), University of California Los Angeles (UCLA) in 2015 to 2016 as visiting scholar. Dr. Yilmaz's principal research interest is smart grid and renewable energy.

He has worked extensively in the areas of smart grid and solar energy, and he (with Biosys LLC), is the inventor of a class of ventilator known as "Biyovent". He has served as an editor-in -chief the Balkan Journal Electrical and Computer Engineering (BAJECE) and European Journal of Technique (EJT). He is also a cofounder of INESEG (Publishing organisation). He has published more than 50 research articles. He has published several books chapter and frequently gives invited keynote lectures at international conferences. He has been Principal Investigator of her research team in several European projects.

# Design and Analysis of a High-Efficiency Resonant Converter for EV Battery Charger

Birand Erdogan\*, Adnan Tan, Murat Mustafa Savrun, Mehmet Ugras Cuma and Mehmet Tumay

**Abstract**— The interest in electric vehicle (EVs) components such as battery, battery chargers, and battery management systems is increasing in parallel with the spread of electric vehicles. One of the most critical of these components is battery chargers. Battery chargers are equipped with DC-DC converters with high efficiency, low cost, and wide output voltage range. In order to provide reliable operation of the battery charger, it is of great importance that the DC-DC converters are operated with a robust and stable controller as well as designed optimally. In this paper, a design method for a CLLC resonant converter-based bidirectional dc-dc converter (BiDC) is presented for a battery charger. The resonant converter, whose design details are presented, suggests a resonant system to be used in battery chargers with fewer components than the CLLC converter, and similar voltage gain characteristics for bidirectional power flow operations compared to the LLC converter. The design procedure highlights performing the soft switching operation and determining the resonant tank parameters. In addition, the forward mode and reverse mode gain equations required for the system to operate in the desired output voltage range have been presented. The design procedures have been validated with a CLLC BiDC model with ratings of 1 kW, 400 V input / 300-450 V output in the PSIM environment. The performance results reveal that the zero voltage switching (ZVS) has been performed for primary-side MOSFETs under a wide load range.

**Index Terms**— Battery chargers, CLLC resonant converter, high efficiency, DC-DC converter

## I. INTRODUCTION

WITH INCREASING electrical power demands, battery systems in electric vehicles, which are becoming

**BIRAND ERDOGAN**, is with Department of the Electrical and Electronics Engineering of Adana Alparslan Türkeş Science and Technology University, Adana, Turkey, (e-mail: [berdogan@atu.edu.tr](mailto:berdogan@atu.edu.tr)).

<https://orcid.org/0000-0003-0784-7776>

**ADNAN TAN**, is with Department of the Electrical and Electronics Engineering of Çukurova University, Adana, Turkey, (e-mail: [atan@cu.edu.tr](mailto:atan@cu.edu.tr)).

<https://orcid.org/0000-0002-5227-2556>

**MURAT MUSTAFA SAVRUN**, is with Department of the Electrical and Electronics Engineering of Adana Alparslan Türkeş Science and Technology University, Adana, Turkey, (e-mail: [msavrun@atu.edu.tr](mailto:msavrun@atu.edu.tr)).

<https://orcid.org/0000-0001-5847-5082>

**MEHMET UGRAS CUMA**, is with Department of the Electrical and Electronics Engineering of Çukurova University, Adana, Turkey, (e-mail: [mcuma@cu.edu.tr](mailto:mcuma@cu.edu.tr)).

<https://orcid.org/0000-0001-6040-0362>

**MEHMET TUMAY**, is with Department of the Electrical and Electronics Engineering of Çukurova University, Adana, Turkey, (e-mail: [mtumay@cu.edu.tr](mailto:mtumay@cu.edu.tr)).

<https://orcid.org/0000-0003-2938-8005>

Manuscript received October 23, 2021; accepted December 22, 2022.

DOI: [10.17694/bajece.1013720](https://doi.org/10.17694/bajece.1013720)

increasingly common, can also be used as energy storage and auxiliary services. Grid-integrated electric vehicles are promising technologies for smart grids and reducing the environmental impact of vehicles. This technology is named as vehicle-to-grid concept (V2G) [1-3]. With the V2G concept, which emerged with the spread of distributed generation, EV batteries can transfer power to home loads or to the grid. Considering that EVs are parked for an average of 8 hours a day, in the event of a grid outage and high electricity prices, EVs can be used as a resource, reducing outages and the cost of electricity usage. Thus, bidirectional battery chargers (BCs) are frequently used instead of unidirectional BCs in such applications. The general structure of BC is shown in Fig. 1. BiDCs are used to provide transmission between high voltage buses and low voltage buses. Unlike resonant [4]–[6] or PWM [7]–[9] model unidirectional converters, BiDCs are designed by replacing output rectifiers with MOSFET switches. There are several studies on BiDCs that have soft-switching capability (SSC) with a focus on eliminating the switching loss. The related studies emphasize that BiDCs can be operated at high frequency-high power density without sacrificing efficiency [10-15]. BiDC topologies are divided into isolated and non-isolated, and isolated topologies stand out due to their safety [16] and flexible voltage range. Isolated topologies are divided into two as phase shift method and frequency control methods in resonant structure. The phase shift control method can be used for isolated BiDCs but the gain of the system for this method is limited. In addition, SSC is a problem when the system is operating with a wide load range [17]. The resonant tank, which is frequently used in isolated BiDCs, achieves high gain values as well as performing soft switching in a wide load range. LLC resonant converter is an isolated dc-dc converter that has SSC for a wide load range at the secondary side [18-22]. However, the drawback of the LLC resonant converter is that the voltage gain characteristics it provides in the forward direction cannot be provided in the reverse direction. While the LLC resonant converter's normalized gain is 1 in forward power flow, the converter's normalized gain is lower than 1 in reverse power flow. This drawback has been able to eliminate by using a symmetric resonant tank structure such as CLLC [23-26]. The restriction of the CLLC resonant converter is that there are too many components which is a problem in designing/analyzing the converter and it is also not cost-effective. In order to have a symmetric tank structure and fewer components than CLLC, CLLC resonant converter is proposed in the literature [17, 27]. One of the advantages of

CLLC topology is that the resonant inductor on the secondary side of the CLLC converter is removed and that makes the circuit easier to design. Another advantage is that similar voltage gain characteristics are observed in both directions in CLLC topology which is not seen in LLC resonant converter. The different types of resonant converter topologies used in literature are illustrated in Fig. 2.

In this paper, the high-efficiency resonant converter is presented for BCAs. The contribution of the paper is that the design procedure is improved by considering the reverse side initially so the complexity of designing the system is reduced in comparison with the literature. In addition, CC-CV charging control algorithms are implemented to verify the performance of the battery charger with bidirectional power flow capability which is significant for V2G concept, and these control methods are expressed mathematically. This paper is divided into five sections. In the first section, literature studies on resonant converter topologies are presented. In the second section, resonant converter topology is explained. In the third section, the design procedure and control algorithm is presented. In section 4, simulation results are given for both modes. The last section presents the concluding remarks of the paper.

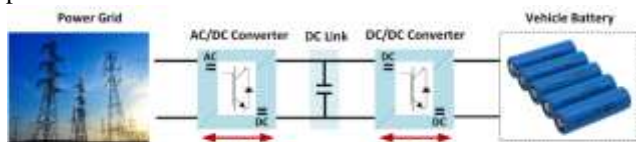


Fig.1. General Structure of BC

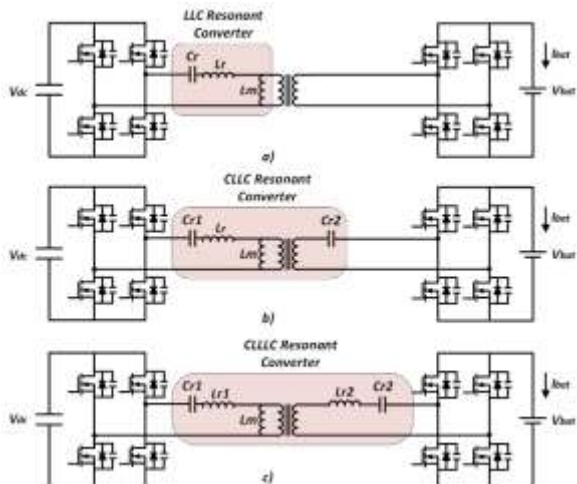


Fig.2. Resonant Converter Topologies a) LLC resonant converter b) CLLC resonant converter c) CLLC resonant converter

II. CLLC RESONANT CONVERTER

In this study, a full-bridge resonant CLLC converter topology, which is illustrated in Fig. 3, is used for BiDC due to high power ratings, similar voltage gain characteristics, and less volume.  $V_{in}$  stands for the input voltage of the proposed system.  $M_1 - M_4$  are the primary MOSFETs.  $L_r$ ,  $C_{r1}$  and  $L_m$ , that are the resonant inductor, primary side resonant capacitor, and the magnetizing inductor, respectively, are the crucial resonant tank elements of the primary side. Additionally,  $C_{r2}$

stands, that is the secondary side resonant capacitor, is the fundamental resonant tank element of the secondary side. Turn ratio of the transformer is denoted as  $n$ .  $R_{o1}$  and  $R_{o2}$  are the load resistors of forward and reverse modes, respectively.  $M_5-M_8$  are secondary side MOSFETs.  $C_1$  and  $C_2$  are the capacitors of input and output parts. First of all, first harmonic approximation method is applied to investigate the working principle of the converter, and determine the transfer function of the resonant tank gain by using the AC equivalent circuit of the system. The AC equivalent circuits of the forward and reverse modes are depicted in Fig. 4.  $R_{ac\_f}$  is the equivalent of the reflected load resistance represented in Eq-1 for forward mode. Addition to that,  $R_{ac\_r}$  (the equivalent of the reflected load resistance) is also determined by virtue of reverse mode and outlined in Eq.2. To better understand, all aforementioned circuit parameters are tabulated in Table-1.

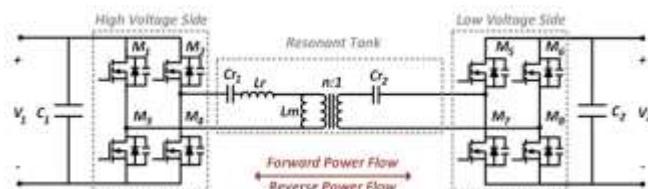


Fig.3. Bidirectional CLLC resonant converter topology

$$R_{ac\_f} = \frac{8n^2 R_{o1}}{\pi^2} \tag{1}$$

$$R_{ac\_r} = \frac{8R_{o2}}{\pi^2} \tag{2}$$

TABLE I  
THE DEFINITIONS OF CIRCUIT PARAMETERS

Parameter	Expression	Meaning
$Q_1$	$\frac{\sqrt{L_r/C_{r1}}}{R_{ac\_f}}$	Quality factor of the forward mode
$Q_2$	$\frac{\sqrt{L_r/C_{r2n}}}{R_{ac\_r}}$	Quality factor of the reverse mode
$C_x$	$\frac{C_{r2n}}{C_{r1}}$	Ratio of resonant capacitors
$L_x$	$\frac{L_m}{L_r}$	Ratio of resonant inductors
$C_{r2n}$	$\frac{C_{r2}}{n^2}$	Normalized Capacitor of $C_{r2}$
$F_x$	$\frac{1}{2\pi\sqrt{L_r C_{r1}}}$	Basic Frequency
$F_n$	$\frac{F_s}{F_x}$	Normalized Frequency

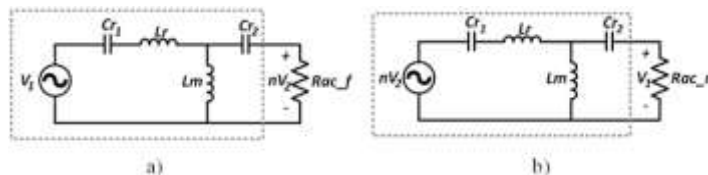


Fig.4. Equivalent Resonant Circuits a) Forward Mode b) Reverse Mode

Based on first harmonic approximation method transfer function of the resonant tank gain for both directions are shown below [17].

$$|G_f| = \left| \frac{nV_2}{V_1} \right| = \frac{1}{\sqrt{\left(\frac{L_x f^2 - 1 + f^2}{L_x f^2}\right)^2 + \left(\frac{Q_1 [C_x L_x f^4 - (C_x L_x + L_x + 1) f^2 + 1]}{C_x L_x f^3}\right)^2}} \quad (3)$$

$$|G_r| = \left| \frac{V_1}{nV_2} \right| = \frac{1}{\sqrt{\left(\frac{C_x L_x f^2 - 1}{C_x L_x f^2}\right)^2 + \left(\frac{Q_2 [C_x L_x f^4 - (C_x L_x + L_x + 1) f^2 + 1]}{L_x f^3 \sqrt{C_x}}\right)^2}} \quad (4)$$

As it is seen from above equations, dc gain of the BiDC depends on  $Q_1$ ,  $Q_2$ ,  $C_n$ ,  $L_n$  and  $f$ . In section 3, design procedure of these parameters are clarified in detail. The crucial parameters namely SSC plays a vital role to improve the efficiency of the any desired systems. Due to the challenging design of SSCs, several restriction criteria should be considered during the analysis and design procedure. In the rest of this section, zero voltage switching (ZVS) boundaries, which take part in primary-side MOSFETs, are explained to minimize the energy losses. ZVS occurs when parasitic capacitors (PrCrS) are fully charged/discharged within desired duration namely dead-time.

The fundamental abbreviations of ZVS condition is outlined in Table 2. Determining the initial primary side current is required for SSC. According to the first harmonic approximation method for forward mode, the current is depicted in equation 5.

$$I_{\text{dead}_f} = \frac{1}{2} \int_0^{t_1} n \frac{v_2 - u_{cr2}}{L_m} dt, u_{cr2} = U_{cr2} \cos(2\pi f_s t + \theta) \quad (5)$$

For the secondary side, initial current is zero (see eq. 6).

$$i_{cr2} = C_{r2} \frac{du_{cr2}}{dt}, i_{cr2}(0) = 0 \quad (6)$$

From these two equations, current within dead-time in forward mode can be expressed as follows [17, 28-32].

$$I_{\text{dead}_f} = \frac{nV_2 t_1}{2L_m} \approx \frac{nV_2}{4f_s L_m} \quad (7)$$

To satisfy the ZVS condition for forward mode, Equation 8 is presented [17, 28-32].

$$\frac{I_{\text{dead}_f} t_{\text{dead}}}{C_{eq_f}} > \Delta u_{AB} = 2V_1 \quad (8)$$

Similar analysis can be done for the opposite direction. According to the first harmonic approximation method for reverse mode,  $I_{\text{dead}_r}$  is shown in equation 9.

$$I_{\text{dead}_r} = \frac{1}{2} \int_0^{t_1} \frac{v_1 - u_{cr1} - u_{Lr}}{L_m} dt, u_{cr1} = U_{cr1} \cos(2\pi f_s t + \theta) \quad (9)$$

Similar to the forward mode, initial secondary side current is zero (see eq. 10).

$$i_{Lr} = C_{r1} \frac{du_{cr1}}{dt}, u_{Lr} = L_r \frac{di_{Lr}}{dt}, \quad (10)$$

$$i_{Lr}(0) = 0$$

From these two equations, current within dead-time in reverse mode can be expressed as follows [17, 28-32].

$$I_{\text{dead}_r} = \frac{V_1 t_1}{2L_m} \approx \frac{V_1}{4f_s L_m} \quad (11)$$

To satisfy the ZVS condition for reverse mode, Equation 12 is presented [17, 28-32].

$$\frac{I_{\text{dead}_r} t_{\text{dead}}}{C_{eq_r}} > \Delta u_{CD} = 2nV_2 \quad (12)$$

TABLE II  
THE ABBREVIATIONS OF CIRCUIT PARAMETERS FOR ZVS  
CONDITION

Parameter	Expression	Meaning
$C_1, C_2, C_3, C_4$	$C_{oss1}$	Parasitic capacitance of primary side MOSFETs
$C_5, C_6, C_7, C_8$	$C_{oss2}$	Parasitic capacitance of secondary side MOSFETs
$C_{eq_f}$	$C_{oss1} + \frac{C_{oss2}}{n^2}$	Equivalent capacitance of primary side in forward mode
$C_{eq_r}$	$C_{oss1} + \frac{C_{oss2}}{n^2}$	Equivalent capacitance of secondary side in reverse mode
$I_{\text{dead}_f}$	$\frac{nV_2}{4f_s L_m}$	Constant current for primary side in dead-time (forward mode)
$I_{\text{dead}_r}$	$\frac{V_1}{4f_s L_m}$	Constant current for secondary side in dead-time (reverse mode)
$u_{cr2}$	$U_{cr2} \cos(2\pi f_s t + \theta)$	Peak voltage on $C_{r2}$

### III. DESIGN PROCEDURE, OPERATING PRINCIPLES AND CONTROL SCHEME

#### A. Design Procedure

In this paper, the novel design method is presented for BCAs. The design parameters based on the battery charger rating are outlined in Table 3. The proposed design procedure is expressed by a flowchart given in Fig. 5. The rating parameters of the CLLC circuit are initially determined before analyzing the proposed method.

TABLE III  
DESIGN SPECIFICATIONS

Power Flow Direction	Max. Power	Primary side V1(V)	Secondary Side V2(V)	Switching Frequency Range
Forward	1kW	400	300-450	180-310 kHz
Reverse	1kW	300-450	400	170-260 kHz



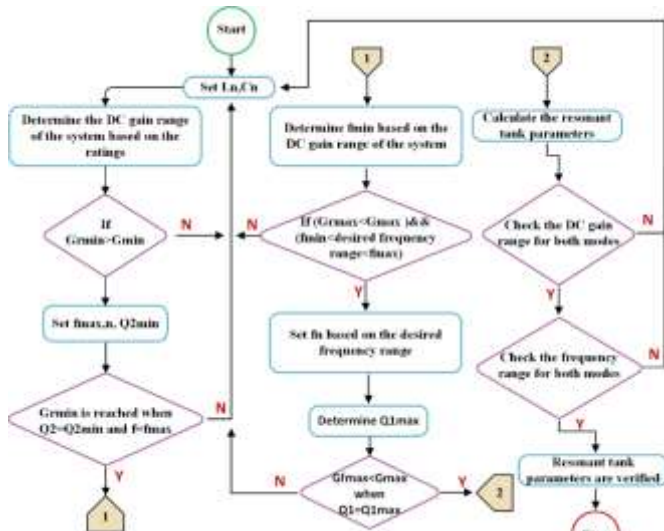


Fig.5. Flowchart of the design procedure

The design procedure initiates with the selecting  $L_n$  and  $C_n$  values. Following that, the fundamental performance parameters, which are maximum ( $G_{max}$ )/minimum ( $G_{min}$ ) DC voltage gain, forward/reverse mode gain range of the system, are determined according to the battery charger ratings. Since the design accuracy performed by considering the reverse mode is higher than the forward mode, the forward mode design is performed following the reverse mode design and the proposed method is started by checking if the minimum reverse mode gain is greater than  $G_{min}$  or not. Maximum normalized frequency, and the minimum quality factor are selected based on the  $G_{min}$  in reverse mode. When  $Q_2$  reaches its designed minimum  $Q_{2min}$  and  $f=f_{max}$ ,  $G_{min}$  is obtained. After determining  $f_{max}$ ,  $f_{min}$  is obtained from DC gain range of the system. If  $f_{min}$  and  $f_{max}$  satisfy the desired DC gain range, normalized frequency is set based on the desired frequency range which is 150-350 kHz. Determining the  $Q_{1max}$  is important because of satisfying the condition for forward mode ( $G_{fmax} < G_{max}$ ). After verifying all the conditions, the resonant tank parameters are able to be computed based on the ZVS equations which are shown in Eq. 8 and Eq. 12. Finally, the DC gain range for both modes and frequency range for both modes are checked before validating the resonant tank parameters. If any problem occurs during the design procedure, the parameters  $L_n$  and  $C_n$  are changed to meet the design requirements of the system, and the design procedure is restarted from the beginning. Fig. 6 shows the forward and reverse DC gain curve of the system with the initial guess of  $L_n=3$  and  $C_n=1.3$ .

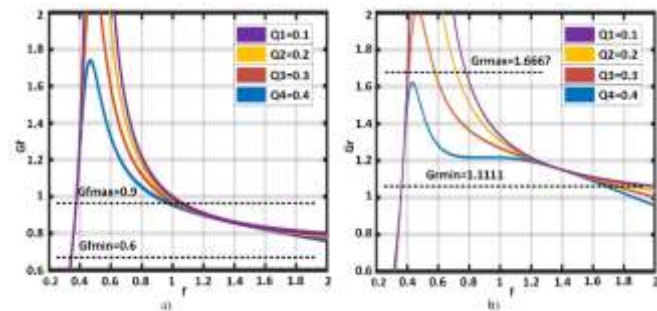


Fig.6. DC gain curves with different Quality Factors a) Forward mode b) Reverse mode

### B. Operating Principles

The operating stages of the circuit is shown in Fig. 7. As illustrated in the figure, the converter has six operating stages during one switching cycle. While stages 1, 2, and 3 are performed in the first half cycle, stages 4, 5, and 6 are performed in the second half cycle. The converter operates within dead-time periods at stage 1 and 4. Stage 2 and 5 corresponds to resonant stages named power transfer stages. The converter operates out of resonance at stages 3 and 6. When the power transfer occurs, primary switches are triggered in inverting mode and the secondary side switches are disabled. Definitions of the converter stages are summarized in Table 4.

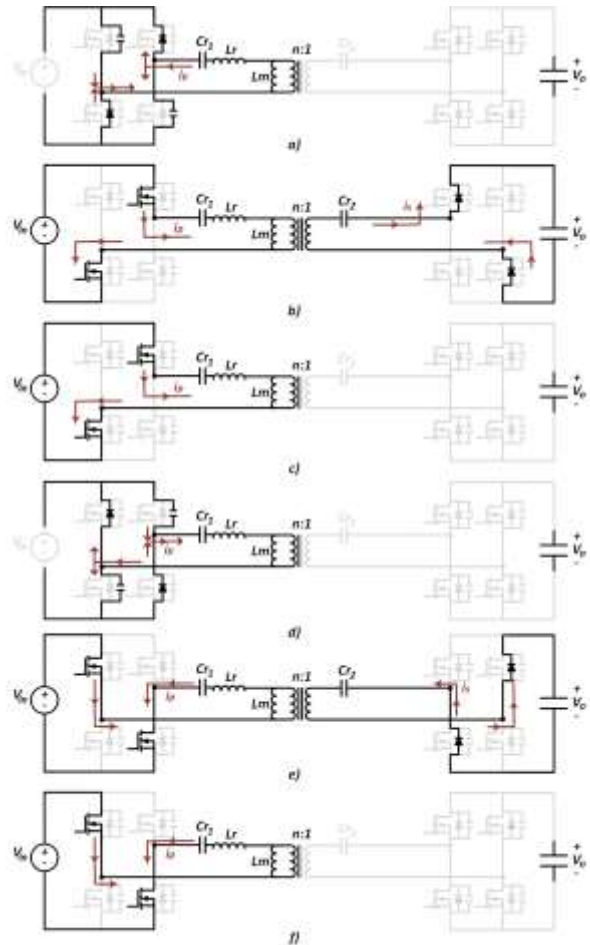


Fig.7. Operating Stages of the Resonant Converter a) Stage 1, b) Stage 2, c) Stage 3, d) Stage 4, e) Stage 5, and f) Stage 6.

TABLE IV  
THE OPERATING PRINCIPLES OF THE CONVERTER

Stages	Explanation
Stage 1	Dead-time duration
Stage 2	Power is transferred to the secondary side
Stage 3	Out of resonance, power transfer is stopped
Stage 4	Dead-time duration
Stage 5	Power is transferred to the secondary side
Stage 6	Out of resonance, power transfer is stopped

### C. Control Scheme

The cascade loop control scheme, designed for CC-CV charging algorithms for battery chargers, consists of the inner

current control loop and the outer voltage control loop as represented in Fig. 8. Pulse frequency modulation is used for controlling the system.

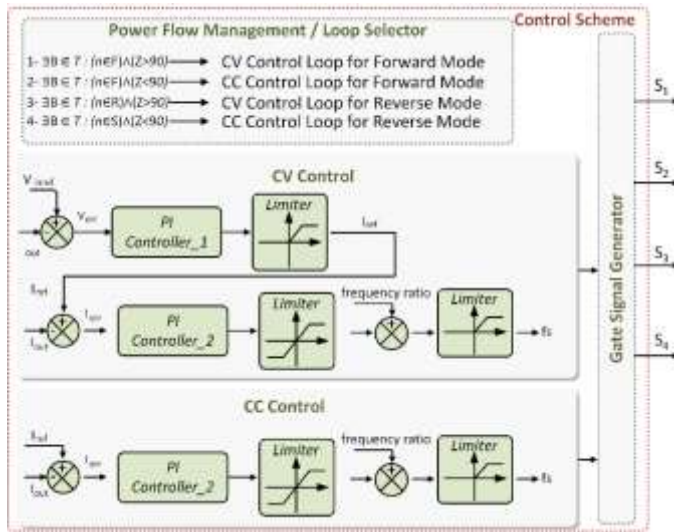


Fig.8. Block diagram of the CLLC resonant converter control system

Mathematical expressions are also shown in Fig. 8. As seen from Fig. 8, a power transfer process is defined by T. Bidirectional power flow capability  $B = F \times S$  formed by forward mode and reverse mode. The measured SOC value is denoted as Z. As expressed in the figure, state 1 indicates that the CLLC converter operates in forward mode and the SOC level of the battery pack is more than 90 so CV control loop is selected by the control unit. Similarly, if the CLLC converter operates in forward mode but the SOC level of the battery pack is less than 90, the CC control loop is selected (state 2). SOC level in the battery pack that is more than 90 in state 3. The difference between state 1 and state 3 is that the converter operates in reverse mode at state 3, a CV control loop. Similar to state 3, the converter operates in reverse mode at state 4. However, the SOC level of the battery pack is less than 90 at state 4 so the CC control loop is selected by the control unit. CC charging is activated when the SOC is smaller than 90 percent. Similarly, CV charging is activated when the SOC is greater than 90 percent. For calculating the SOC value, SOC estimation methods can be used for real BCAs. However, in the simulation model, SOC value is directly measured from batteries so the SOC estimation method is not used in this paper. SOC value is taken and the control unit of the system decides whether CC or CV charge is required. Thus, the necessary signal is transmitted to the switch block. The reference voltage and reference current are denoted as  $V_{ref}$  and  $I_{ref}$ , respectively. In CC charging process, the difference between  $I_{ref}$  and the  $I_o$  generates a signal and enters the PI\_2 controller for generating a duty cycle D when the Switch is OFF. The signal from the PI\_2 controller is extracted from the calculated constant value and enters the limiter block that has upper/lower limits to generate the required switching frequency. The switching signals of MOSFEETs are produced by a gate signal generator considering the computed switching frequency. In the CV charging process (the switch is ON), the difference between  $V_{ref}$  and output voltage generates a signal and enters the PI\_1

controller to be used in the inner loop. The remaining process is the same as in CC.

To summarize the control part, if the SOC value in the battery is below 90 percent while power is transferred from one side to another, the CC charging algorithm is used. CC control loop produces a frequency signal by comparing the measured battery charging current and reference current values and applying the error value to the PI controller. However, if the SOC value in the battery is above 90 percent, the CV charging algorithm is used. The CV control loop produces a reference signal by comparing the measured battery voltage with the reference voltage values and applying the error value to the PI controller. Similarly, this reference signal is compared with the battery current and the error value is applied to another PI controller to output a frequency signal. While CC and CV charging algorithms are used in the resonant converter, frequency control is performed and PI controllers, frequency ratio block and limiters are used to obtain necessary frequencies. The obtained frequency values are converted into switching signals by gate signal generator block.

#### IV. SIMULATION RESULTS

This section presents the performance review of the proposed system. A 1 kW battery charger model was developed using the PSIM simulation program. To examine the performance of the system, analyzes were carried out in all power flow directions and the functionality and applicability of the proposed battery charger were verified. Resonant tank design component values are shown in Table 5.

TABLE V  
THE PARAMETERS OF SIMULATION MODEL

Parameter	Symbol	Value
Primary side Resonant Capacitor	Cr1	25 nF
Resonant Inductor	Lr	37.84 μH
Magnetic Inductor	Lm	57 μH
Secondary side Resonant Capacitor	Cr2	40 nF
Transformer Turn Ratio	n	8/10

All the design parameters are calculated based on the proposed design methodology discussed in sections 2 and 3. Simulation results show that the switching frequency range is between 180 kHz and 310 kHz which is the desired value for this system in forward mode (see Fig. 9). Similarly, the switching frequency range is between 170 kHz and 260 kHz in the reverse mode (see Fig. 10).

In forward mode, ZVS waveforms for maximum and minimum switching frequency are shown in Fig. 8. As seen from the zoom-in view in the figure, the drain-to-source voltage of MOSFET is zero before the gate signal is equal to 1. Therefore, when the switch is turned on, the switching loss is zero. Similar to the Fig. 9, ZVS waveforms for maximum and minimum switching frequency are shown in Fig. 10 for reverse mode and ZVS is also seen from the zoom-in view in Fig. 10. Since zero voltage switching occurs, the switching losses are reduced, and the system's efficiency has increased compared to the traditional converters. The operating ranges of the system in both modes are highlighted in Fig. 9 and 10 by measuring the one period of the cycle.



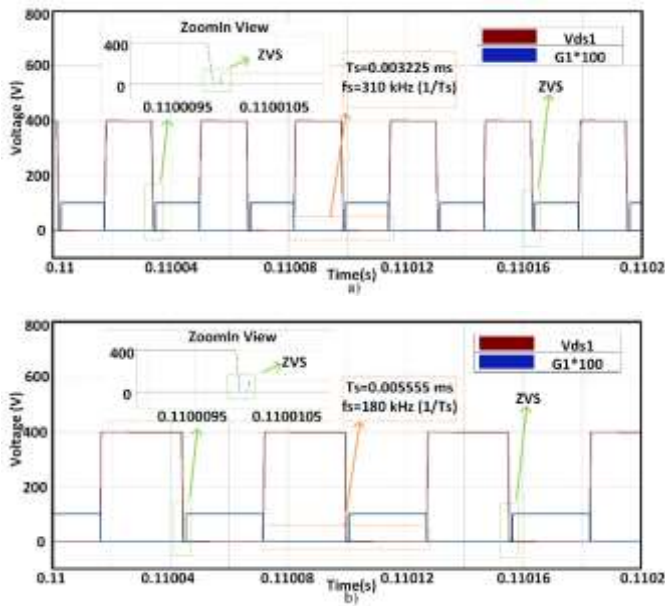


Fig. 9. ZVS waveforms for forward mode a) Maximum switching frequency b) Minimum switching frequency

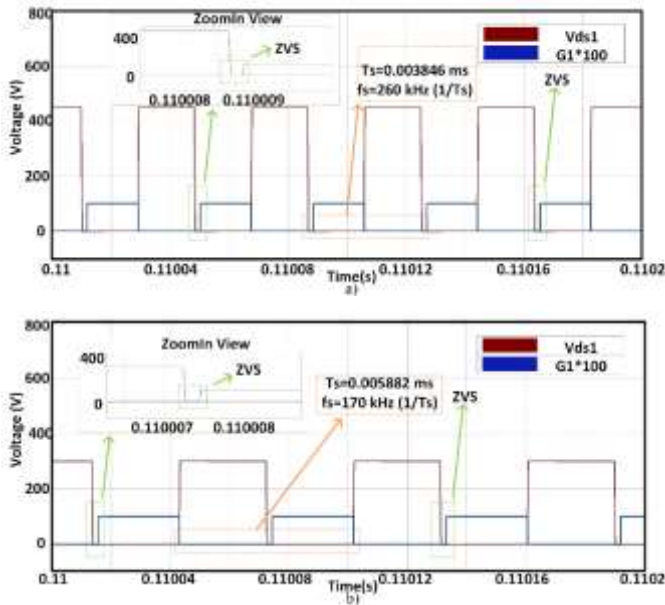


Fig.10. ZVS waveforms for reverse mode a) Maximum switching frequency b) Minimum switching frequency

As can be seen in Fig. 11, during the forward mode operation, the recommended frequency control is performed at 400 V input voltage, and an output voltage range of 300-450 V is obtained. While the output voltage is 450 V at the minimum operating frequency of 180 kHz, it reaches 300 V at the maximum operating frequency of 310 kHz. Similarly, when the system is operating in reverse mode (see Fig. 12), the desired 300-450 V output voltage range can be obtained by the PFM control method (for 400 V input). While the desired output voltage is obtained in reverse mode, the frequency range used in forward mode can be used. For instance, when the switching frequency is 260 kHz, output voltage is 450 V. On the other hand, when the switching frequency is 170 kHz, output voltage is 300 V.

In addition, switching losses and conduction losses of primary side MOSFETs are shown in Fig. 13 and Fig. 14, respectively. As seen in Fig. 13 and Fig. 14, the conduction losses are negligible. The main problem in this system comes from the switching losses as seen in Fig. 13 and Fig. 14. To overcome this problem (decrease switching loss), soft switching conditions are mentioned in the design procedure and simulation results confirm that the system has the soft-switching capability to reduce the switching losses (see Fig. 9 and Fig. 10).

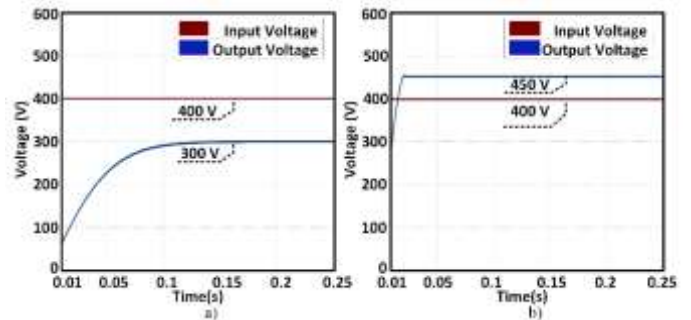


Fig.11. Input and output waveforms for forward mode a) System with maximum frequency b) System with minimum frequency

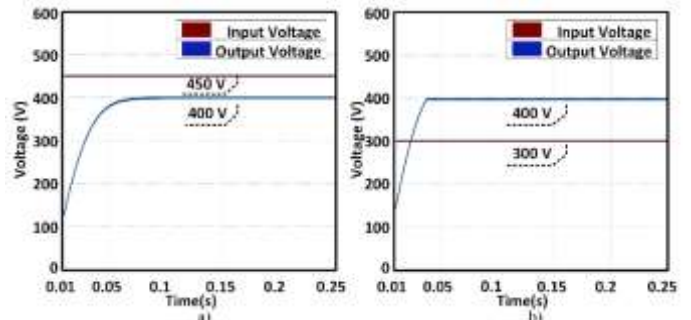


Fig.12. Input and output waveforms for reverse mode a) System with maximum frequency b) System with minimum frequency

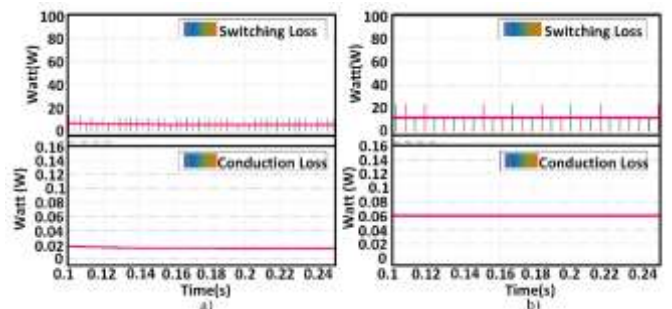


Fig.13. Switching and conduction losses for forward mode a) System with maximum frequency b) System with minimum frequency

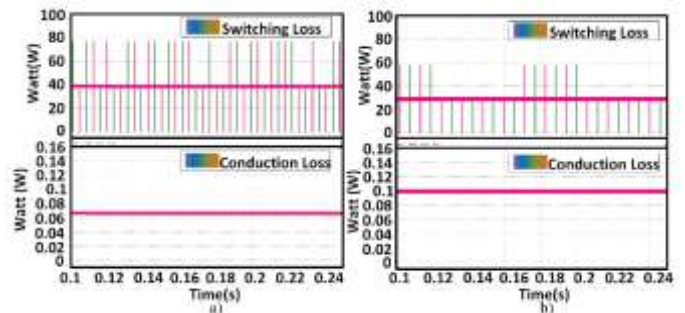


Fig.14. Switching and conduction losses for reverse mode a) System with maximum frequency b) System with minimum frequency

Results of the simulation model is shown in table 6. For a BCA, wide output load range is needed, and simulation results verified that the system has wide output load range for both modes (300 V-450 V) for a constant input voltage (400 V). Similar switching frequency range can used for the system with output power of 1 kW. Similar switching frequency range is used for both directions and the system has 1kW output power. Switching losses and conduction losses are acceptable for a 1kW system. When the resonant converter operates at 180 kHz and 310 kHz in forward mode, efficiency of the converter is 98.35 and 97.58, respectively. Similarly, the converter efficiency is 98.02/97.45 for 170 kHz/260 kHz in reverse mode.

TABLE VI  
RESULTS OF SIMULATION MODEL

Parameter	Value
Input Voltage for two Modes	400 V
Output Voltage range for two Modes	300-450 V
Switching Loss for Forward Mode	15 W
Conduction Loss for Forward Mode	0.04 W
Switching Loss for Reverse Mode	35 W
Conduction Loss for Reverse Mode	0.04 W
Operating Frequency for Forward Mode	180 kHz – 310 kHz
Operating Frequency for Reverse Mode	170 kHz – 260 kHz
Output Power	1 kW

## V. CONCLUSION

In this paper, a design method for CLLC resonant converter that is used in BCs is presented. To increase the efficiency of the system, soft switching conditions are given in design procedure. The simulation model of the resonant converter system which consists of two resonant capacitors, one resonant inductor, and one magnetizing inductor is performed using PSIM environment. Simulation model operates under wide output voltage range for a constant input voltage with rated power of 1 kW and also the model can transfer the power flow for both directions. CV and CC charging algorithms have been tested for the model with cascaded loop control and to control the output voltage to the desired value, PFM method is used. The presented system excels with the advantages of fewer components, less complexity, bidirectional power flow capability, and similar voltage gain characteristics for both directions in comparison with existing systems. In addition, another advantage of the presented system is that the converter satisfies a wide voltage range without sacrificing efficiency which is significant for BCAs. The main advantages of the presented topology are as follows:

- high efficiency,
- high energy density,
- electrical isolation,
- low electromagnetic interference and harmonic pollution,
- magnetic integration,
- wide output ranges,
- low voltage stress, and
- high operation frequency.

## REFERENCES

- [1] J. Chen, Y. Zhang and W. Su. "An anonymous authentication scheme for plug-in electric vehicles joining to charging/discharging station in vehicle-to-Grid (V2G) networks." in *China Communications*, vol. 12, no. 3, Mar. 2015, pp. 9-19, doi: 10.1109/CC.2015.7084359.
- [2] S. Amamra and J. Marco. "Vehicle-to-Grid Aggregator to Support Power Grid and Reduce Electric Vehicle Charging Cost." in *IEEE Access*, vol. 7, 2019, pp. 178528-178538, doi: 10.1109/ACCESS.2019.2958664.
- [3] M. A. Masrur, A. G. Skowronska, J. Hancock, S. W. Kolhoff, D. Z. McGrew, J. C. Vandiver, and J. Gatherer. "Military-Based Vehicle-to-Grid and Vehicle-to-Vehicle Microgrid—System Architecture and Implementation." in *IEEE Transactions on Transportation Electrification*, vol. 4, no. 1, March 2018, pp. 157-171, doi: 10.1109/TTE.2017.2779268.
- [4] B. Ray. "Bidirectional DC/DC power conversion using constant-frequency quasi-resonant topology." 1993 *IEEE International Symposium on Circuits and Systems*, vol.4, 1993, pp. 2347-2350, doi: 10.1109/ISCAS.1993.394234.
- [5] D. Ha, N. Park, K. Lee, D. Lee and D. Hyun. "Interleaved Bidirectional DC-DC Converter for Automotive Electric Systems." 2008 *IEEE Industry Applications Society Annual Meeting*, 2008, pp. 1-5, doi: 10.1109/08IAS.2008.291.
- [6] H. Li, F. Z. Peng and J. S. Lawler. "A natural ZVS medium-power bidirectional DC-DC converter with minimum number of devices." in *IEEE Transactions on Industry Applications*, vol. 39, no. 2, March-April 2003, pp. 525-535, doi: 10.1109/TIA.2003.808965.
- [7] K. W. Ma and Y. S. Lee. "An integrated flyback converter for DC uninterruptible power supply." in *IEEE Transactions on Power Electronics*, vol. 11, no. 2, March 1996, pp. 318-327, doi: 10.1109/63.486182.
- [8] P. Das, B. Laan, S. A. Mousavi and G. Moschopoulos. "A Nonisolated Bidirectional ZVS-PWM Active Clamped DC-DC Converter." in *IEEE Transactions on Power Electronics*, vol. 24, no. 2, Feb. 2009, pp. 553-558, doi: 10.1109/TPEL.2008.2006897.
- [9] D. Xu, C. Zhao and H. Fan. "A PWM plus phase-shift control bidirectional DC-DC converter." in *IEEE Transactions on Power Electronics*, vol. 19, no. 3, May 2004, pp. 666-675, doi: 10.1109/TPEL.2004.826485.
- [10] L. Zhu. "A Novel Soft-Commutating Isolated Boost Full-Bridge ZVS-PWM DC-DC Converter for Bidirectional High Power Applications." in *IEEE Transactions on Power Electronics*, vol. 21, no. 2, March 2006, pp. 422-429, doi: 10.1109/TPEL.2005.869730.
- [11] E. Hiraki, K. Yamamoto, T. Tanaka and T. Mishima. "An Isolated Bidirectional DC-DC Soft Switching Converter for Super Capacitor Based Energy Storage Systems." 2007 *IEEE Power Electronics Specialists Conference*, 2007, pp. 390-395, doi: 10.1109/PESC.2007.4342018.
- [12] G. Ma, W. Qu, G. Yu, Y. Liu, N. Liang and W. Li. "A Zero-Voltage-Switching Bidirectional DC-DC Converter With State Analysis and Soft-Switching-Oriented Design Consideration." in *IEEE Transactions on Industrial Electronics*, vol. 56, no. 6, June 2009, pp. 2174-2184, doi: 10.1109/TIE.2009.2017566.
- [13] H. Xiao and S. Xie. "A ZVS Bidirectional DC-DC Converter With Phase-Shift Plus PWM Control Scheme." in *IEEE Transactions on Power Electronics*, vol. 23, no. 2, March 2008, pp. 813-823, doi: 10.1109/TPEL.2007.915188.
- [14] L. Schuch, C. Rech, H. L. Hey, H. A. Grundlinggrundling, H. Pinheiro and J. R. Pinheiro. "Analysis and Design of a New High-Efficiency Bidirectional Integrated ZVT PWM Converter for DC-Bus and Battery-Bank Interface." in *IEEE Transactions on Industry Applications*, vol. 42, no. 5, Sept.-Oct. 2006, pp. 1321-1332, doi: 10.1109/TIA.2006.880847.
- [15] F. Z. Peng, Hui Li, Gui-Jia Su and J. S. Lawler. "A new ZVS bidirectional DC-DC converter for fuel cell and battery application." in *IEEE Transactions on Power Electronics*, vol. 19, no. 1, Jan. 2004, pp. 54-65, doi: 10.1109/TPEL.2003.820550.
- [16] S. Inoue and H. Akagi. "A Bidirectional DC-DC Converter for an Energy Storage System With Galvanic Isolation." in *IEEE Transactions on Power Electronics*, vol. 22, no. 6, Nov. 2007, pp. 2299-2306, doi: 10.1109/TPEL.2007.909248.
- [17] Y. Liu, G. Du, X. Wang and Y. Lei. "Analysis and Design of High Efficiency Bidirectional GaN-Based CLLC Resonant Converter." in *Energies*, vol. 12, no. 20, Oct. 2019, pp. 3859-3871, doi:10.3390/en12203859
- [18] Y. Wei, Q. Luo and A. Mantooh. "Comprehensive analysis and design of LLC resonant converter with magnetic control." in *CPSS Transactions on Power Electronics and Applications*, vol. 4, no. 4, Dec. 2019, pp. 265-275, doi: 10.24295/CPSS/PEA.2019.00025.
- [19] R. Yu, G. K. Y. Ho, B. M. H. Pong, B. W. Ling and J. Lam. "Computer-Aided Design and Optimization of High-Efficiency LLC Series



- Resonant Converter." in IEEE Transactions on Power Electronics, vol. 27, no. 7, July 2012, pp. 3243-3256, doi: 10.1109/TPEL.2011.2179562.
- [20] M. F. Menke, J. P. Duranti, L. Roggia, F. E. Bisogno, R. V. Tambara and A. R. Seidel. "Analysis and Design of the LLC LED Driver Based on State-Space Representation Direct Time-Domain Solution." in IEEE Transactions on Power Electronics, vol. 35, no. 12, Dec. 2020, pp. 12686-12701, doi: 10.1109/TPEL.2020.2995942.
- [21] I. Lee and G. Moon. "Analysis and Design of a Three-Level LLC Series Resonant Converter for High- and Wide-Input-Voltage Applications." in IEEE Transactions on Power Electronics, vol. 27, no. 6, June 2012, pp. 2966-2979, doi: 10.1109/TPEL.2011.2174381.
- [22] J. Deng, S. Li, S. Hu, C. C. Mi and R. Ma. "Design Methodology of LLC Resonant Converters for Electric Vehicle Battery Chargers." in IEEE Transactions on Vehicular Technology, vol. 63, no. 4, May 2014, pp. 1581-1592, doi: 10.1109/TVT.2013.2287379.
- [23] P. He and A. Khaligh. "Comprehensive Analyses and Comparison of 1 kW Isolated DC-DC Converters for Bidirectional EV Charging Systems." in IEEE Transactions on Transportation Electrification, vol. 3, no. 1, March 2017, pp. 147-156, doi: 10.1109/TTE.2016.2630927.
- [24] J. Min and M. Ordenez. "Bidirectional Resonant CLLC Charger for Wide Battery Voltage Range: Asymmetric Parameters Methodology." in IEEE Transactions on Power Electronics, vol. 36, no. 6, June 2021, pp. 6662-6673, doi: 10.1109/TPEL.2020.3033982.
- [25] J. Huang, X. Zhang, Z. Shuai, P. Wang, L. H. Koh, and X. Tong. "Robust Circuit Parameters Design for the CLLC-Type DC Transformer in the Hybrid AC-DC Microgrid." in IEEE Transactions on Industrial Electronics, vol. 66, no. 3, March 2019, pp. 1906-1918, doi: 10.1109/TIE.2018.2835373.
- [26] P. He, A. Mallik, A. Sankar and A. Khaligh. "Design of a 1-MHz High-Efficiency High-Power-Density Bidirectional GaN-Based CLLC Converter for Electric Vehicles." in IEEE Transactions on Vehicular Technology, vol. 68, no. 1, Jan. 2019, pp. 213-223, doi: 10.1109/TVT.2018.2881276.
- [27] W. Chen, P. Rong and Z. Lu. "Snubberless Bidirectional DC-DC Converter With New CLLC Resonant Tank Featuring Minimized Switching Loss." in IEEE Transactions on Industrial Electronics, vol. 57, no. 9, Sept. 2010, pp. 3075-3086, doi: 10.1109/TIE.2009.2037099.
- [28] W. Chen, S. Wang, X. Hong, Z. Lu and S. Ye. "Fully soft-switched bidirectional resonant dc-dc converter with a new CLLC tank." 2010 Twenty-Fifth Annual IEEE Applied Power Electronics Conference and Exposition (APEC), 2010, pp. 1238-1242, doi: 10.1109/APEC.2010.5433345.
- [29] J. Luo, J. Wang, Z. Shao, J. Shao, and J. Li. (2018). "Optimal Design of a High Efficiency LLC Resonant Converter with a Narrow Frequency Range for Voltage Regulation." *Energies*, 11(5), 2018, pp. 1124. doi:10.3390/en11051124.
- [30] B. Lu, W. Liu, Y. Liang, F. C. Lee and J. D. van Wyk. "Optimal design methodology for LLC resonant converter." Twenty-First Annual IEEE Applied Power Electronics Conference and Exposition, 2006. APEC '06., 2006, pp. 6 pp.-, doi: 10.1109/APEC.2006.1620590.
- [31] U. Kundu, K. Yenduri and P. Sensarma. "Accurate ZVS Analysis for Magnetic Design and Efficiency Improvement of Full-Bridge LLC Resonant Converter." in IEEE Transactions on Power Electronics, vol. 32, no. 3, March 2017, pp. 1703-1706, doi: 10.1109/TPEL.2016.2604118.
- [32] C. Zhao, Y. -H. Hsieh, F. C. Lee and Q. Li. "Design and Analysis of a High-frequency CLLC Resonant Converter with Medium Voltage insulation for Solid-State-Transformer." 2021 IEEE Applied Power Electronics Conference and Exposition (APEC), 2021, pp. 1638-1642, doi: 10.1109/APEC42165.2021.9487101.

#### BIOGRAPHIES



**BİRAND ERDOĞAN** was born in Adana, Turkey, in 1993. He is currently a Ph.D student with the Electrical and Electronics Engineering Department in Çukurova University, Adana. He has been a research assistant with the Electrical and Electronics Engineering Department, Adana Alparslan Türkeş Science and Technology University, since 2019. His current research interests include power electronics, and electric vehicles.



**ADNAN TAN** was born in Adana, Turkey, in 1985. He received the Ph.D. degree from the Electrical and Electronics Engineering Department, Çukurova University, Adana, in 2015. He has been an Assistant Professor with the Electrical and Electronics Engineering Department, Çukurova University, since 2015. His current research interests include power electronic converters, utility applications of power electronics, electrical power quality, and microgrids.



**MURAT MUSTAFA SAVRUN** was born in Osmaniye, Turkey, in 1987. He received the Ph.D. degree from the Electrical and Electronics Engineering Department, Çukurova University, Adana, Turkey, in 2017. He has been an Associate Professor with the Electrical and Electronics Engineering Department, Adana Alparslan Türkeş Science and Technology University, since 2022. His current research interests include power electronics, electrical power quality, and electric vehicles.



**MEHMET UĞRAS CUMA** was born in 1982. He received the B.Sc., M.Sc., and Ph.D. degrees in electrical and electronics engineering from Cukurova University, Adana, Turkey, in 2004, 2006, and 2010, respectively. He is currently an Associate Professor with the Electrical and Electronics Engineering Department, Cukurova University, Adana. His current research interests include power quality, power quality devices, and electric vehicles.



**MEHMET TÜMAY** received the Ph.D. degree in electrical engineering from Strathclyde University, Glasgow, U.K., in 1995. He is currently a Professor with the Department of Electrical and Electronics Engineering, and the Rector of Adana Alparslan Türkeş Science and Technology University, Adana, Turkey. His current research interests include modeling of electrical machines, power-flow controllers, power quality, and custom power devices.

# Publication Ethics

The journal publishes original papers in the extensive field of Electrical-electronics and Computer engineering. To that end, it is essential that all who participate in producing the journal conduct themselves as authors, reviewers, editors, and publishers in accord with the highest level of professional ethics and standards. Plagiarism or self-plagiarism constitutes unethical scientific behavior and is never acceptable.

By submitting a manuscript to this journal, each author explicitly confirms that the manuscript meets the highest ethical standards for authors and coauthors

**The undersigned hereby assign(s) to *Balkan Journal of Electrical & Computer Engineering* (BAJECE) copyright ownership in the above Paper, effective if and when the Paper is accepted for publication by BAJECE and to the extent transferable under applicable national law. This assignment gives BAJECE the right to register copyright to the Paper in its name as claimant and to publish the Paper in any print or electronic medium.**

Authors, or their employers in the case of works made for hire, retain the following rights:

1. All proprietary rights other than copyright, including patent rights.
2. The right to make and distribute copies of the Paper for internal purposes.
3. The right to use the material for lecture or classroom purposes.
4. The right to prepare derivative publications based on the Paper, including books or book chapters, journal papers, and magazine articles, provided that publication of a derivative work occurs subsequent to the official date of publication by BAJECE.
5. The right to post an author-prepared version or an official version ( preferred version) of the published paper on an internal or external server controlled exclusively by the author/employer, provided that (a) such posting is noncommercial in nature and the paper is made available to users without charge; (b) a copyright notice and full citation appear with the paper, and (c) a link to BAJECE's official online version of the abstract is provided using the DOI (Document Object Identifier) link.



**ISSN:** 2147- 284X  
**Year:** April 2023  
**Volume:** 11  
**Issue:** 2

### CONTENTS

Ufuk Korkmaz, Deniz Türkpençe; Stabilization and Dissipative Information Transfer of a Superconducting Kerr-Cat Qubit,.....	107-114
Hafize Nurgül Durmuş Şenyapar, Mehmet Rıda Tür; Turkey’s Domestic Car TOGG in the Framework of New Trends in Electric Vehicles and Consumer Ethnocentrism,.....	115-128
Mehmet Nergiz; Classification of Precancerous Colorectal Lesions via ConvNeXt on Histopathological Images,..	129-137
Osman Onur Akırmak, Aytaç Altan; Estimation of Extrusion Process Parameters in Tire Manufacturing Industry using Random Forest Classifier,.....	138-143
Murat Ozdemir, Eyüp Emre Ülkü, Kazım Yıldız; Analysis and Comparison of Business Intelligence Tools Most Preferred by Companies in Turkey, .....	144-155
Ahmet Kaymaz; Negative Capacitance and Abnormal Peak Behaviors in GaAs-Based MOS Devices Under Ionizing Radiation, .....	156-162
Ekrem Demir, Ozan Gülbudak, Mustafa Gökdağ; Performance Evaluation of Three-Phase Grid-Connected Inverter with Various Control Methods, .....	163-171
Nazmi Ekren, Bunyamin Sogut; DALI Compatible Smart LED Driver Controller with Wi-Fi Communication, ...	172-183
Sevilay Tüfenkçi, Gürkan Kavuran, Celeleddin Yeroğlu; An Approach for DC Motor Speed Control with Off-Policy Reinforcement Learning Method, .....	184-189
Heybet Kılıç, Musa Yılmaz; Sensor and Actuator Fault Tolerant Control of Grid-Tied Microgrid, .....	190-197
Birand Erdogan, Adnan Tan, Murat Mustafa Savrun, Mehmet Uğraş Cuma, Mehmet Tümay; Design and Analysis of a High-Efficiency Resonant Converter for EV Battery Charger, .....	198-206

## BALKAN JOURNAL OF ELECTRICAL & COMPUTER ENGINEERING

(An International Peer Reviewed, Indexed and Open Access Journal)

#### Contact

Batman University  
Department of Electrical-Electronics Engineering  
Bati Raman Campus Batman-Turkey

**Web:** <http://dergipark.gov.tr/bajece>  
<http://www.bajece.com>  
**e-mail:** [bajece@hotmail.com](mailto:bajece@hotmail.com)

